Diplomarbeit

Designing vanadium-modified photocatalysts for HER and OER using visible and UV light

ausgeführt zum Zwecke der Erlangung des akademischen Grades eines
Diplom-Ingenieurs
eingereicht an der Technischen Universität Wien, Fakultät für Technische Chemie

von

Jakob Nils Blaschke, BSc

Matr.Nr.: 01326071

unter der Anleitung von

Univ.Ass. **Ariane Giesriegl**, MSc

Univ.Ass Dr.rer.nat. **Alexey Cherevan**

Univ.Prof. Mag.rer.nat. Dr.rer.nat. **Dominik Eder**

Institut für Materialchemie
Forschungsbereich Molekulare Materialchemie
Technische Universität Wien
Getreidemarkt 9, 1060 Wien, Österreich

Wien, im Mai 2021

Unterschrift

Die approbierte gedruckte Originalversion dieser Diplomarbeit ist an der TU Wien Bibliothek verfügbar
The approved original version of this thesis is available in print at TU Wien Bibliothek.

Die approbierte gedruckte Originalversion dieser Diplomarbeit ist an der TU Wien Bibliothek verfügbar
The approved original version of this thesis is available in print at TU Wien Bibliothek.

Contents

Abstract **i**

Zusammenfassung **iii**

Acknowledgements **iv**

List of Abbreviations **v**

List of Figures **vi**

List of Tables **viii**

1 Introduction **1**
1.1 Renewable Energy and Climate Change . . . 2
1.2 Motivation and Aims . . . 4

2 Background **5**
2.1 Photocatalysis . . . 5
2.1.1 Electronic properties of semiconductors . . . 6
2.2 TiO_2 as a photocatalyst . . . 9
2.2.1 Improving the efficiency of TiO_2-photocatalysts . . . 10
2.2.2 V-modified photocatalysts . . . 11
2.3 Water splitting . . . 12
2.3.1 Sacrificial water splitting . . . 14

3 Methods **15**
3.1 Microscopy techniques . . . 15
3.1.1 Transmission Electron Microscopy (TEM) . . . 15
3.1.2 Scanning Electron Microscopy (SEM) . . . 16
3.2 Spectroscopy techniques . . . 17
3.2.1 Total Reflection X-ray Fluorescence (TXRF) . . . 17
3.2.2 X-ray Photoelectron Spectroscopy (XPS) . . . 18
3.2.3 Attenuated Total Reflectance Fourier Transform Infrared Spectroscopy (ATR-FTIR) . . . 19
3.2.4 Raman Spectroscopy . . . 19
3.2.5 Diffuse Reflectance Spectroscopy (DRS) . . . 21
3.3 Powder X-ray Diffraction (XRD) . . . 21

Die approbierte gedruckte Originalversion dieser Diplomarbeit ist an der TU Wien Bibliothek verfügbar
The approved original version of this thesis is available in print at TU Wien Bibliothek.
TU Bibliothek Your knowledge hub WIEN

3.4 Thermogravimetric Analysis (TGA) . . . 22
3.5 Gas Chromatography (GC) . . . 23

4 Experimental Part **24**
4.1 Catalyst synthesis . . . 24
4.1.1 Evaporation synthesis . . . 24
4.1.2 Filtration synthesis . . . 26
4.1.3 Reference Samples . . . 26
4.2 Photocatalytic experiments . . . 26
4.2.1 UV-HER experiments . . . 26
4.2.2 Vis-HER experiments . . . 27
4.2.3 OER experiments . . . 28

5 Results and Discussion **30**
5.1 Precursor Characterization . . . 30
5.2 Catalyst characterization . . . 31
5.2.1 Composition analysis . . . 31
5.2.2 25 at%-samples . . . 32
5.2.3 5 at%-samples . . . 45
5.2.4 1 at%-samples . . . 52
5.3 Photocatalytic experiments . . . 63
5.3.1 OER . . . 63
5.3.2 UV-HER . . . 64
5.3.3 Vis-HER . . . 67
5.4 Discussion . . . 71
5.4.1 Material characterization . . . 71
5.4.2 Photocatalytic characterization . . . 72

6 Conclusion **77**

7 Outlook **78**

References **79**

Appendix **87**

Die approbierte gedruckte Originalversion dieser Diplomarbeit ist an der TU Wien Bibliothek verfügbar
The approved original version of this thesis is available in print at TU Wien Bibliothek.
TU Bibliothek Your knowledge hub WIEN

Abstract

Photocatalytic water splitting is a promising way to produce hydrogen, which could serve as an eco-friendly fuel produced from renewable energy sources like the sun. TiO_2 is one of the most widely used photocatalysts, but it can only utilize UV light, which constitutes only a very small part of the whole spectrum of natural sunlight. To produce photocatalysts that utilize the solar spectrum more efficiently, it is necessary to modify TiO_2 and make it visible light active. In this project, vanadium-modified TiO_2 photocatalysts with 1 at%-, 5 at%- and 25 at% V were produced to investigate the role of V-species as a visible light absorber as well as their possible role as a co-catalyst. For V-concentrations of 5 at%- and 25 at%, the resulting catalysts consisted of composites between TiO_2 and V_2O_5 while no individual VO_x compounds could be detected for the low-concentration 1 at%-samples. All of the samples showed an improved visible light absorption.

The catalysts were tested for their photocatalytic activity towards OER and HER under UV light in order to investigate the ability of the V-species to act as a co-catalyst. Their role as a light absorber was analysed with HER experiments under visible light with the addition of Pt. All experiments were performed using a sacrificial agent for the respective complementary reduction and oxidation reaction. While none of the synthesized catalysts was active under UV light, the sample with 5 at% was able to produce hydrogen under visible light illumination, contrary to unmodified anatase. Due to the formation of a heterojunction between the two oxides, the V_2O_5 in the composite structure was able to act as a light absorber, transferring excited electrons into TiO_2 where they could then react with protons to form H_2.

Die approbierte gedruckte Originalversion dieser Diplomarbeit ist an der TU Wien Bibliothek verfügbar
The approved original version of this thesis is available in print at TU Wien Bibliothek.
TU Bibliothek Your knowledge hub WIEN

Die approbierte gedruckte Originalversion dieser Diplomarbeit ist an der TU Wien Bibliothek verfügbar
The approved original version of this thesis is available in print at TU Wien Bibliothek.

Zusammenfassung

Photokatalytische Wasserspaltung ist ein vielversprechender Weg um zukünftig Wasserstoff als umweltfreundlichen Treibstoff aus erneuerbaren Energiequellen wie natürlichem Sonnenlicht zu produzieren. TiO_2 ist einer der am weitesten verbreitetsten Photokatalysatoren, aber in seiner unmodifizierten Form kann TiO_2 nur UV Licht zur Photokatalyse nutzen und dieses stellt nur einen geringen Anteil am gesamten Spektrum des natürlichen Sonnenlichts dar. Um Photokatalysatoren herzustellen, die natürliches Sonnenlicht effizienter nutzen können, ist es notwendig Titandioxid zu modifizieren und es im sichtbaren Bereich des Lichts aktiv zu machen. Im Zuge dieses Projekts wurden Vanadium-modifizierte TiO_2 Photokatalysatoren mit 1 at%, 5 at% und 25 at% V hergestellt und die Rolle der V-Spezies als Ko-Katalysator sowie als Lichtabsorber wurde untersucht. Bei einer V Konzentration von 5 at% und 25 at% entstanden dabei Komposite aus TiO_2 und V_2O_5, während keine VO_x Verbindungen für die 1 at% Proben nachgewiesen werden konnten. Alle Proben wiesen eine verbesserte Absorption im sichtbaren Bereich des Lichts auf.

Die Katalysatoren wurden in OER und HER Experimenten unter UV Licht analysiert, um die Aktivität der V-Spezies als Ko-Katalysator zu untersuchen. Die Rolle als Lichtabsorber wurde mittels HER Experimenten unter sichtbarem Licht und unter der Zugabe von Pt als zusätzlichem Ko-Katalysator getestet. Alle Experimente wurden mit einem Elektronendonor/Elektronenakzeptor für die jeweilige komplementäre Reduktion oder Oxidation durchgeführt. Keiner der produzierten Katalysatoren zeigte Aktivität unter UV Licht, allerdings konnte die Probe mit 5 at% V, im Gegensatz zu unmodifiziertem Anatas, unter Beleuchtung mit sichtbarem Licht Wasserstoff produzieren. Aufgrund der Ausbildung eines Heteroübergangs zwischen den beiden Oxiden, konnte V_2O_5 als Lichtabsorber agieren und angeregte Elektronen auf TiO_2 übertragen, wo diese dann mit Protonen zu H_2 reagieren können.

Die approbierte gedruckte Originalversion dieser Diplomarbeit ist an der TU Wien Bibliothek verfügbar
The approved original version of this thesis is available in print at TU Wien Bibliothek.
TU Bibliothek Your knowledge hub WIEN

Acknowledgements

There are many people that have stood by my side and assisted me with my Masters studies and to write this Thesis. First of all, I would like to thank Prof. Dominik Eder for this wonderful opportunity to work in his group and conduct research on the exciting topic of photocatalysis and for placing his trust in me to help him with his lecture. I would also like to especially thank Ariane Giesriegl, who helped me immensely with interpreting weird research results and in proofreading my Thesis. I really enjoyed working with you. Of course I would also like to thank Alexey Cherevan and the rest of my research group for insightful advice on how to proceed with my research, for performing measurements that I couldn't do myself, for the welcoming and happy work environment that exists in the group and for the Kicker games that we had before the pandemic unfortunately drove us out of the kitchen and into our homes.

I wouldn't have come this far without the help of my friends, the Vorarlberger and the Viennese Crew. Be it short trips through the world, or just hanging out in the park or at the Danube, you made my time as a student probably the best time of my life so far. Special thanks goes out to my long time room-mate and great friend Paul. I really enjoy thinking back to study sessions for bachelor exams in the beginning, without which I probably wouldn't have come this far. I also thank Livia, whose love and comfort helped me in writing this Thesis, especially, when I just didn't feel like it at all. The desire to spend time with you, motivated me to go on, as much as it made me put off work.

And last but not least I would also like to thank my family, especially my parents. Without your support in so many ways, I couldn't have done any of this and I see myself as incredibly lucky that you believed in me and gave me this opportunity to study what I love. Thank you for being able to talk about everything, for listening, for dinner almost every Sunday and for the trips to faraway places, all of which helped me find more motivation to get trough the hard parts, when I didn't find it on my own.

Die approbierte gedruckte Originalversion dieser Diplomarbeit ist an der TU Wien Bibliothek verfügbar
The approved original version of this thesis is available in print at TU Wien Bibliothek.
TU Bibliothek Your knowledge hub WIEN

List of Abbreviations

ΔG	Gibbs free energy
ATR-FTIR	Attenuated Total Reflection - Fourier Transform Infrared Spectroscopy
BSE	Backscattered Electrons
CB	Conduction Band
DI	Deionized
DOS	Density of States
DRS	Diffuse Reflectance Spectroscopy
E_f	Fermi-level
E_g	Bandgap
$E_{VB/CB}$	Energy of the band edges
FFT	Fast Fourier Transform
FWHM	Full Width at Half Maximum
GC	Gas Chromatography
HER	Hydrogen Evolution Reaction
HOMO	Highest Occupied Molecular Orbital
IR	Infrared
LUMO	Lowest Unoccupied Molecular Orbital
OER	Oxygen Evolution Reaction
PM	Physical Mixture
SC	Semiconductor
SE	Secondary Electrons
SEM	Scanning Electron Micrsocope
SHE	Standard Hydrogen Electrode
TEM	Transmission Electron Micrsocopy
TGA	Thermogravimetric Analysis
TXRF	Total Reflection X-ray Fluorescence
UV	Ultraviolet
VB	Valence Band
XPS	X-ray Photoelectron Spectroscopy
XRD	X-ray Diffraction

Die approbierte gedruckte Originalversion dieser Diplomarbeit ist an der TU Wien Bibliothek verfügbar
The approved original version of this thesis is available in print at TU Wien Bibliothek.
TU WIEN Bibliothek Your knowledge hub

List of Figures

1.1 Evolution of the ecological footprint over time. 1
1.2 The renewable energy potential worldwide, by energy source. 2
1.3 The three main pathways how to convert light energy and store it in useful, useable forms. 3

2.1 The position of conduction and valence band and the electronic density of states for a metal, a semiconductor and an insulator. 7
2.2 The band edge and redox half-reaction potentials for a thermodynamically possible reaction. 8
2.3 General mechanism of photocatalysis with the three essential steps. 9
2.4 The band positions for TiO_2 and V_2O_5 as separate semiconductors as well as when forming a heterojunction. 12
2.5 The band positions and bandgaps for several typical semiconductors. 13

3.1 Illustration of the process of evaluating the distance of lattice fringes in TEM images. 16
3.2 Different effects produced by elastic and inelastic interactions of primary electrons with the sample surface. 16
3.3 Elastic and inelastic scattering mechanisms from the interaction of light with a powder sample. 20
3.4 Illustration of Bragg diffraction of X-rays from electrons in a lattice. 22

4.1 All the different synthesis routes used in the present master project and the resulting labels for each sample. 24
4.2 Photocatalytic reactor design for OER, HER and Vis-HER experiments. 27

5.1 TGA plots for the precursors. 30
5.2 Reference SEM images of unmodified anatase nanoparticles. 33
5.3 SEM images for the calcined 25 %-samples. 33
5.4 TEM images of the uncalcined 25 %-sample $Ti\,[25\%/RT]_E^S$. 34
5.5 TEM images of the medium calcined 25 %-sample $Ti\,[25\%/350]_E^S$. 35
5.6 TEM images of the calcined 25 %-sample $Ti\,[25\%/600]_E^S$. 35
5.7 XPS spetra of anatase and $Ti\,[25\%/600]_E^S$ core levels. 36
5.8 Powder X-ray diffraction spectra of anatase and the 25 %-samples. 38
5.9 FTIR spectra for the 25 %-samples as well as reference samples. 39
5.10 Raman spectra of the reference- and 25 %-samples. 40

Die approbierte gedruckte Originalversion dieser Diplomarbeit ist an der TU Wien Bibliothek verfügbar
The approved original version of this thesis is available in print at TU Wien Bibliothek.
TU WIEN Bibliothek Your knowledge hub

5.11 Center position and FWHM of the $E_g(1)$ band of the 25 %-samples and anatase as a reference. . . . 41
5.12 Illustration of the bandgap analysis for unmodified and modified semiconductors. 42
5.13 DRS spectra and Tauc-plots respectively for anatase, $VOSO_4$, V_2O_5 and the 25 %-samples. . . . 43
5.14 SEM images for the calcined 5 %-sample $Ti\,[5\%/600]_E^S$. . . . 45
5.15 TEM images of the uncalcined 5 %-sample. . . . 46
5.16 TEM images of the 5 %-sample, calcined at 350 °C. . . . 47
5.17 TEM images of the 5 %-samples, calcined at 600 °C. . . . 47
5.18 Powder X-ray diffraction spectra of the 5 %-samples. . . . 48
5.19 FTIR spectra for the 5 %-samples. . . . 49
5.20 Raman spectra for the 5 %-samples. . . . 49
5.21 Center position and FWHM of the $E_g(1)$ band of the 5 %-samples and anatase as a reference. . . . 50
5.22 Determination of the bandgaps for sample $PM[6\%/600]^S$. . . . 51
5.23 The DRS spectra and derived Tauc plots for the 5 %-samples. . . . 51
5.24 TEM images of the 1 %-samples with $VOSO_4$ as the precursor. . . . 53
5.25 TEM images of the 1 %-samples with NH_4VO_3 as the precursor. . . . 54
5.26 XPS spetra for the 1 %-samples. . . . 55
5.27 Powder XRD diffractograms for the 1 %-samples and Ana-600. . . . 57
5.28 FTIR spectra for the 1 %-samples. . . . 58
5.29 Raman spectra for the 1 %-samples. . . . 59
5.30 Center position and FWHM of the $E_g(1)$ band of the 1 %-samples and anatase as a reference. . . . 59
5.31 Determination of the bandgaps for sample $Ti\,[1\%/RT]_F^N$. . . . 60
5.32 DRS spectra and Tauc-plots respectively for NH_4VO_3 and the 1 %-samples. . . . 61
5.33 The oxygen evolution rates for all measured samples during the OER experiments after 30 min of illumination with UV light (365 nm). . . . 63
5.34 Hydrogen evolution rates over 30 min of light illumination with UV light (365 nm). 65
5.35 Evolution of the recorded amounts of H_2 during HER experiments under UV illumination. . . . 67
5.36 TEM images of the samples $Ti\,[5\%/600]_E^S$ and $Ti\,[5\%/600]_E^S$ (UV/Vis) after the photodeposition of Pt. . . . 69
5.37 Hydrogen evolution activities for the UV-HER experiments. . . . 73
5.38 Vis-HER activities for all tested samples with the standard deviation for the $Ti\,[5\%/600]_E^S$ experiments as an error bar. . . . 74
5.39 Difference between the anatase surface coverage of the 25 % samples vs. the 5 % samples. . . . 75

Die approbierte gedruckte Originalversion dieser Diplomarbeit ist an der TU Wien Bibliothek verfügbar
The approved original version of this thesis is available in print at TU Wien Bibliothek.
TU Bibliothek Your knowledge hub WIEN

List of Tables

4.1 List of chemicals. 25

5.1 Vanadium contents according to TXRF results. 32
5.2 X-ray transition energies of Ti and V. 32
5.3 Lattice spacings observed in the TEM images of 25 %-samples and the associated phase and crystal plane. 34
5.4 The active Raman modes for anatase and the associated Raman shifts. 40
5.5 Lattice spacings observed in the TEM images of 5 %-samples and the associated phase and crystal plane. 46
5.6 The calculated OER rates after 30 min of illumination with UV light (365 nm). . 64
5.7 The H_2 evolution rates after 30 min of illumination with UV light (365 nm). . . . 66
5.8 Amount of evolved H_2 after 60 min of illumination with visible light (445 nm). . . 68
5.9 The leached amounts of Ti, V and Pt after a Vis-HER experiment based on the total sample mass (1 mg), measured with TXRF. 69

Die approbierte gedruckte Originalversion dieser Diplomarbeit ist an der TU Wien Bibliothek verfügbar
The approved original version of this thesis is available in print at TU Wien Bibliothek.
TU Bibliothek Your knowledge hub WIEN

Introduction

One of the biggest challenges of the 21st century is an ever-increasing global energy demand, caused by rapid population growth and the industrialization and modernization of developing countries. Advancing globalization leads to increased energy consumption as more and more people are getting access to faster transportation and more consumer/luxury goods. So far, the consumption of non-renewable resources was able to cover the rising demands, however, it is clear that this strategy is not sustainable forever and is causing massive problems like climate change and overexploitation of earths resources. The Global Footprint Network collects data about the consumption of resources from many countries worldwide and summarizes the data into the ecological footprint which is a measure for how much global land area is needed to produce the required resources and take up generated waste. Fig. 1.1 shows the evolution of the worldwide ecological footprint over time [1]. It also shows the worldwide biocapacity which represents the amount of land which the ecosystems can regenerate. The graph shows that the demands for land surpassed the renewable amount in the early 1970s. Our current consumption

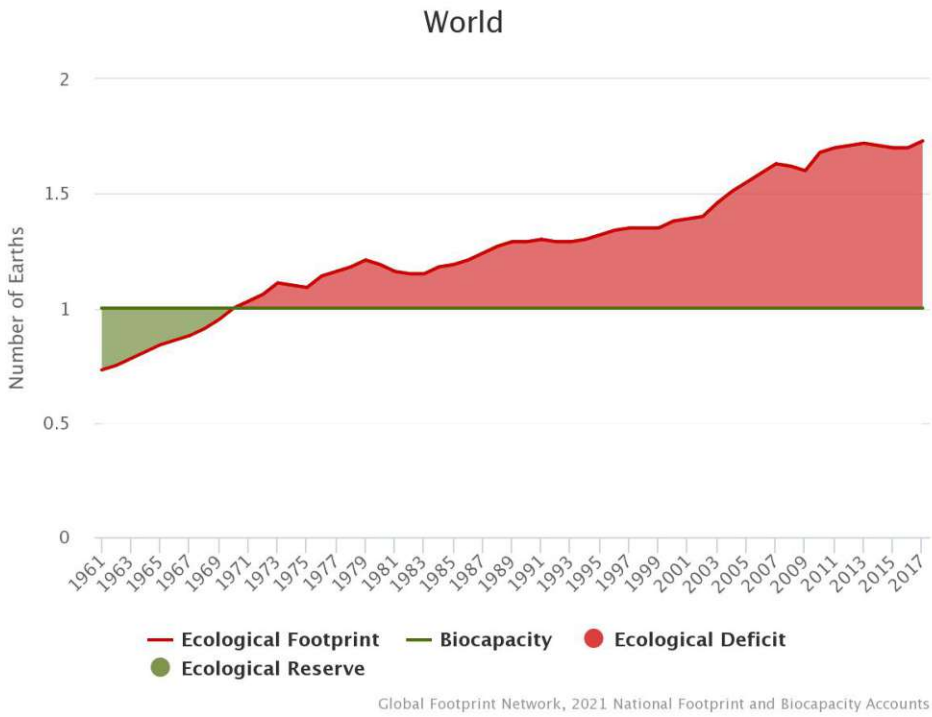

Figure 1.1: Evolution of the ecological footprint over time. Since approx. 1970 the required amount of land area exceeded the total available land area of our planet [1].

of resources would require between 1.5 and 2 whole planets to sustain long-term.

One way to decrease this ecological deficit is through the development of new, more eco-friendly and less resource-consuming technologies. In the energy sector, this can be achieved through further developing and adopting renewable energy sources like wind, water, geothermal heat or

Die approbierte gedruckte Originalversion dieser Diplomarbeit ist an der TU Wien Bibliothek verfügbar
The approved original version of this thesis is available in print at TU Wien Bibliothek.
TU Bibliothek Your knowledge hub WIEN

light from the sun in contrast to the currently predominating method of burning fossil fuels like oil, coal or gas. Additionally, the burning of these fuels has led to a strong increase of greenhouse gases in our atmosphere which is the main cause for human made climate change [2, 3].

1.1 Renewable Energy and Climate Change

Human-made climate change has caused the global average surface temperature to rise very rapidly in the last few decades compared to previous temperature changes. Since 1970, the global average temperature has increased by approx. 1 °C [2]. This causes the melting of polar ice caps, warming of the oceans and rising sea levels which in turn increases the likelihood for extreme weather events like floods, droughts, hurricanes and heat waves [2]. Big climate changes have already occured in earth's history, e.g. reoccurring ice ages, and these time periods have always been disruptive, causing extinctions or mass movements of many species. However, the human made climate change is occurring exceptionally fast, making it difficult or impossible to adapt.

The increase in global atmospheric temperature can be explained by the greenhouse effect, which is caused by the emission of greenhouse gases into the atmosphere. These gases trap infrared radiation emitted from the earth, which would normally allow it to cool down [4]. This keeps heat inside the atmosphere, causing global warming. Several gases are considered greenhouse gases, like e.g. H_2O vapour, CO_2, N_2O, CH_4 or chlorofluorocarbons, which all contribute differently depending on their persistence in the atmosphere and relative amount [5]. The biggest contributor by far is CO_2 which is mainly produced by the burning of fossil fuels [5].

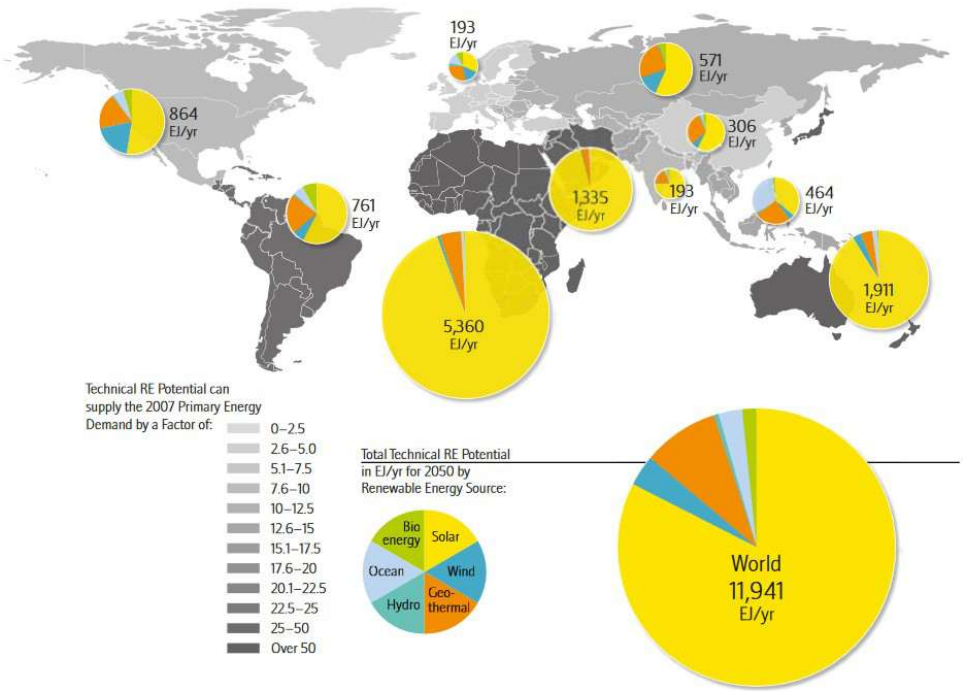

Figure 1.2: The renewable energy (RE) potential worldwide, by energy source. The gray areas represent the factor by which the potential is bigger than the demand [6].

Die approbierte gedruckte Originalversion dieser Diplomarbeit ist an der TU Wien Bibliothek verfügbar
The approved original version of this thesis is available in print at TU Wien Bibliothek.
TU Bibliothek Your knowledge hub WIEN

In order to reduce CO_2 emissions it will be necessary to move away from non-renewable energy sources and develop more eco-friendly and renewable technologies for energy production.

The main sources for renewable energy come from solar, hydro, geothermal and wind power. Fig. 1.2 shows the total renewable energy potential for different regions worldwide as estimated by the International Panel on Climate Change and based on data by Krewitt et al. [6–8]. The graphic shows that the biggest potential lies in utilizing the solar energy, radiated onto the earth.

Fig. 1.3 by Crabtree and Lewis shows the three main paths to capture solar radiation and convert it into useful energy [9]. These consist of the generation of electric power via solar cells and photovoltaics, thermal power with the use of solar thermal collectors and the synthesis of solar fuels via photocatalysis.

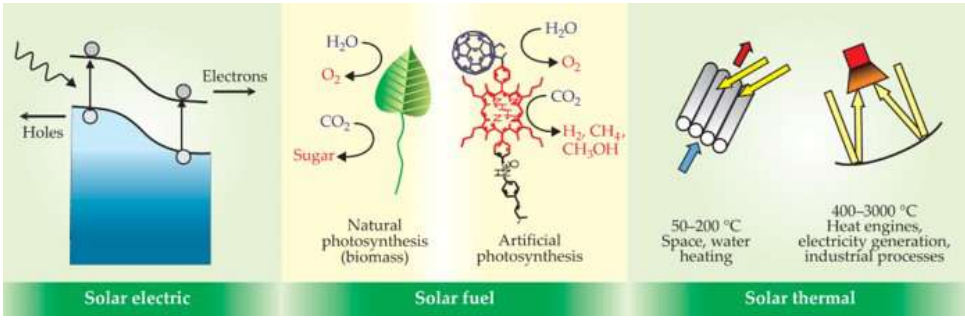

Figure 1.3: The three main pathways how to convert light energy and store it in useful, useable forms [9].

The generation of solar fuels like hydrogen via water splitting or methane gas via CO_2 reduction could deliver transportable fuels with a high energy density and therefore provide a method of powering growing energy demands in a renewable and eco-friendly way.

Die approbierte gedruckte Originalversion dieser Diplomarbeit ist an der TU Wien Bibliothek verfügbar
The approved original version of this thesis is available in print at TU Wien Bibliothek.

1.2 Motivation and Aims

The following work was performed in the field of photocatalysis/photosynthesis, two terms which are often used interchangeably, although they describe different processes. More precisely, the work focused on the hydrogen evolution reaction (HER) and oxygen evolution reaction (OER), which are the two parts of the water splitting reaction. This process utilizes water and light energy to produce hydrogen, which could be used as an alternative fuel, and oxygen. In contrast to the burning of fossil fuels, which produce harmful greenhouse gases like CO_2 or NO_2, the burning of hydrogen only produces water as a waste product.

In order to make this technology viable on an industrial scale, catalysts with a sufficient activity, meaning hydrogen production, have to be developed. TiO_2 is one of the most promising materials used in photocatalysis because it is cheap, non-toxic, chemically stable and abundant. However, the photocatalytic activity of pure TiO_2 is too low to be used in the industry, which is why a lot of studies have been performed to improve pure TiO_2 via the addition of other materials. Previous studies have found that the addition of noble metals like Pt or Pd as so called co-catalysts can significantly boost the water splitting activity of TiO_2. However, due to the rarity and cost of noble metals, efforts have been made to move away from them and develop another catalyst with a comparable activity using only abundant metals, e.g. first-row transition metals.

In the present work we chose to modify TiO_2 anatase powder with the transition metal vanadium. V has many different stable oxidation states, which could be helpful for catalysing the different oxidation and reduction reactions that can happen in the water splitting process [10]. Additionally, it was one of the few first-row transition metals which hasn't yet been studied as a co-catalyst to titanium dioxide in our research group. Our aim was to modify anatase powder using a very simple process with a V precursor without the use of organic solvents and then test the produced catalysts for their respective hydrogen and oxygen evolution activities.

To study the ability of the resulting V-species to act either as a co-catalyst or as a light-absorber, samples with different concentrations were produced. The co-catalyst role was studied by adding a low amount of V (1 at%) and to study the role as a light absorber the samples were modified with a higher V-loading (25 at%). Additionally, another sample with an intermediate amount of V (5 at%) was also synthesized to study the effect of V-concentration on the two aforementioned roles. Furthermore, the influence of V precursor and calcination temperature were examined as well.

Die approbierte gedruckte Originalversion dieser Diplomarbeit ist an der TU Wien Bibliothek verfügbar
The approved original version of this thesis is available in print at TU Wien Bibliothek.
TU Bibliothek Your knowledge hub WIEN

Background

2.1 Photocatalysis

Photocatalysis is a type of catalysis, where photons are used to drive or accelerate a chemical reaction. The wavelength of the photons typically lies in the range of ultraviolet (UV), visible or infrared (IR) light. Since natural sunlight consists of photons from this region a lot of research is conducted to create photocatalysts that are able to harness the suns energy. So called photoactive materials are able to absorb these photons and generate an excited electron (e^-), paired with a positively charged hole (h^+). These excited free charge carriers can then be used to drive a redox reaction.

Research on photoactive materials started to increase heavily with the discovery of photoelectrochemical water splitting in 1972 by Fujishima and Honda [11]. Photocatalysis can be divided into homogeneous photocatalysis, where both catalyst and reactants exist in the same phase and heterogeneous photocatalysis, where those exist in different phases. In heterogeneous photocatalysis the catalyst is most often a solid semiconductor and the interaction between reactants and catalyst happens at the interface. The work carried out for this thesis exclusively concerned the field of heterogeneous photocatalysis, so the following discussion will mainly focus on this branch of the field.

Industrial applications of photocatalysis mainly lie in the removal of pollutants from air, water or solid surfaces. Photoactive materials can oxidize and decompose organic substances, for example in waste- or groundwater or in gas exhausts [12, 13]. It can also be used for self-cleaning- and antibacterial surfaces, where the oxidation ability and superhydrophilic properties of the photocatalyst are used in conjunction [14, 15].

Another important application is photocatalytic water splitting. Here, water gets decomposed into hydrogen and oxygen, using the energy provided by the photons. Strictly speaking, pure water splitting cannot be considered catalysis, since the reaction products (H_2 and O_2) lie on a higher energy level than the reagents (H_2O). For a catalytic process to occur, the reaction needs to have a negative change in the Gibbs free energy ($\Delta G_{reaction} < 0$) and the role of a catalyst would be to lower the required energy barrier to activate the process (activation energy) without getting consumed. But many processes that are typically described as photocatalytic actually don't fulfil this criterion because the reaction in the process has a positive ΔG. These types of reactions would be better described by the term photosynthesis. Nevertheless, this fact is most often ignored and processes like water splitting are considered a part of photocatalysis in literature [16]. For the sake of simplicity, this thesis will also follow this convention and describe the discussed processes as photocatalytic and the synthesized samples as photocatalysts.

Die approbierte gedruckte Originalversion dieser Diplomarbeit ist an der TU Wien Bibliothek verfügbar
The approved original version of this thesis is available in print at TU Wien Bibliothek.
TU Bibliothek Your knowledge hub WIEN

Photocatalysis could provide yet another way of generating alternative fuels, namely via CO_2 reduction or CO_2-to-fuel conversion. In this process, CO_2 and H_2O are converted into higher hydrocarbons (i.e. solar fuels) and O_2 under the illumination of light. This technology is another promising way of tackling problems like climate change and environmental pollution, by providing ways in which closed-cycle energy systems could be engineered or it could help establish alternative and cleaner energy sources like hydrogen. In such a system the CO_2 generated through the burning of hydrocarbons in any industrial process would get captured before it is released into the atmosphere and converted back to more useful compounds by the help of sunlight or other light sources. The problems mentioned in Chapter 1, caused by the depletion of fossil fuel reserves, have made it more important than ever to understand the underlying mechanisms of photoactive materials which could help in the design of more effective photocatalysts, the establishment of hydrogen as an alternative energy source and the recycling of CO_2 emissions into the atmosphere.

2.1.1 Electronic properties of semiconductors

Semiconductors (SC) are the main materials used in heterogeneous photocataylsis and they lie at the heart of many modern technologies including transistors and diodes, which are used in all modern electronic equipment, LED's, solar cells and many more. Elements like Si, Ge and Se, but also compounds like GaAs, CN and TiO_2 can have semiconducting properties. The electronic properties of a SC are determined by it's bandgap which can be described by band theory. In a covalent bond, the orbitals of the two partners valence electrons overlap, which creates two new orbitals on a higher and lower energy level respectively. These are called the highest occupied molecular orbital (HOMO) and lowest unoccupied molecular orbital (LUMO). In a solid, however, the number of orbitals overlapping is many orders of magnitude higher than that. Because of the Pauli exclusion principle, which states that no two electrons can have the same quantum state within a quantum system, this leads to many new orbitals, all on a separate energy level. These energy levels lie so densely together, that their distribution can be regarded as quasi-continuous.

The overlapping orbitals will form distinct regions of possible energy levels, called bands. Just as in a single covalent bond the overlapping leads to a HOMO and a LUMO, there are two bands in solids which are the most relevant for photocatalytic reactions called the valence band (VB) and the conduction band (CB). The VB will be the energetically highest band which still contains electrons in the ground state and the CB will be the band above that. The energetic distance between them is called the bandgap (E_g) of the solid. The size of the bandgap and the distribution of electrons in the bands determine the electronic properties of a material and if it is considered a conductor, a semiconductor or an insulator. In a conductor, the bands either overlap ($E_g < 0\,eV$) or the valence band is not fully occupied. Semiconductors show a bandgap between 0 eV to 4 eV and insulators above 4 eV. Fig. 2.1 shows an illustration of the band positions and the electronic density of states (DOS), which is a measure of the number of possible energy levels per energy interval, in these three types of materials.

Die approbierte gedruckte Originalversion dieser Diplomarbeit ist an der TU Wien Bibliothek verfügbar
The approved original version of this thesis is available in print at TU Wien Bibliothek.
TU Bibliothek Your knowledge hub WIEN

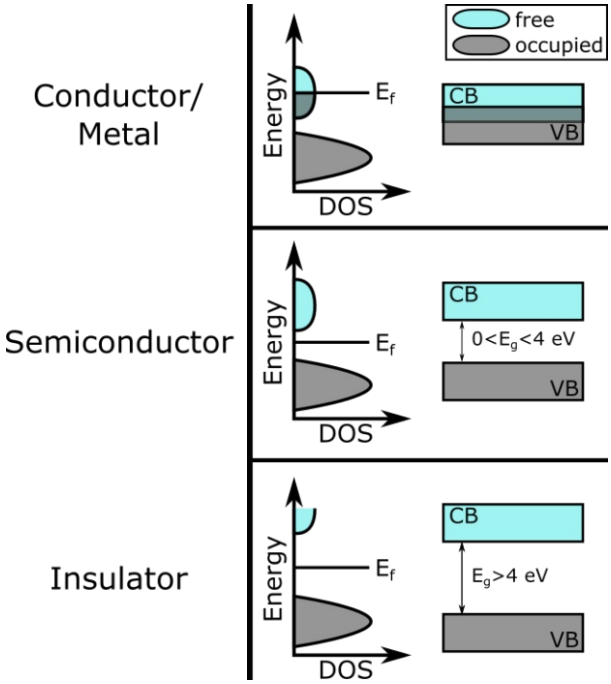

Figure 2.1: The position of conduction and valence band and the electronic density of states for a metal, a semiconductor and an insulator. E_f denotes the position of the Fermi-level.

The Fermi-level (E_f) is another way of describing the electronic structure in solid materials. It is defined as the energy for which the Fermi-Dirac distribution function, which describes the energy distribution for electrons and all other fermions, is equal to $\frac{1}{2}$ (see Eq. (2.1)).

$$f(E = E_f) = \frac{1}{2} \tag{2.1}$$

Here, it can be regarded as the hypothetical energy level of a system in thermodynamic equilibrium for which the probability of it being occupied is exactly 50 % or in other words the electrochemical potential of the material. For metals, the Fermi-level lies inside of a band, whereas for semiconductors and insulators, it typically lies in the bandgap.

Energy in the form of heat or electromagnetic waves can promote electrons from the VB to the CB provided that the incoming energy exceeds the band gap. In the VB, electrons are called localized because they are bound strongly to the atoms, however, in the CB they are called de-localized or free charge carriers because they can move freely through the lattice. This is because electrons in any partially filled band (VB in conductors or CB in semiconductors) can be promoted to higher energy states with way less energy than electrons in a completely filled band, because of the quasi-continuous distribution of energy levels. So if an electric field is applied, the electrons in a partially filled band can use the potential from the electric field to accelerate, which we perceive as an electric current. For semiconductors this means that promoting electrons to the conduction band increases their electric conductivity. Photocatalysis and photoactive materials in general utilize photons in this process, called photoexcitation, to generate free charge carriers and then utilize these for the oxidation or reduction of reactants.

Die approbierte gedruckte Originalversion dieser Diplomarbeit ist an der TU Wien Bibliothek verfügbar
The approved original version of this thesis is available in print at TU Wien Bibliothek.
TU Bibliothek Your knowledge hub WIEN

Some SC require phonon assistance in order to allow for photoexcitation to occur, because the crystal momentum (quasimomentum) is different in the ground state and the excited state. This means that in order to fulfil the conservation of momentum, the transition from CB to VB (and vice versa) requires a change in the crystal wave vector k which can be achieved with the help of a phonon. These types of SC, where the VB maximum and CB minimum lie at different values for k, are called indirect SC, in contrast to direct SC, where the opposite is the case. The typical representation of the bandgap doesn't account for this and just displays the values of the global VB maximum and CB minimum irrespective of k. Due to the fact that an additional phonon is needed for electron excitation as well as recombination, indirect SC have slower band transitions which is important for the specific application of the SC (e.g. LED's are typically made from direct SC's).

For a typical semiconductor the bandgap can be overcome by visible or UV radiation. The excited electron leaves behind a hole in the valence band, which can be described as a positively charged quasiparticle. Together the electron and the hole form an exciton and since the negative electron and the positive hole attract each other, an additional energy, the exciton binding energy, needs to be overcome to produce actual freely moving electrons. But electrons and holes can also recombine in a process called recombination, thereby giving off the stored energy in the form of heat (i.e. thermalization losses) or radiation. The mean distance that the charge carriers can travel inside a specific material before recombination happens is called the diffusion length and it depends on the lifetime and mobility of the carriers in the material. To increase the fraction of carriers that reach the surface of the semiconductor the size of the semiconductor particles is often reduced down to the nanoregime, e.g. nanoparticles or nanorods.

The size of the bandgap determines which photons can be used to generate excitons, but the absolute energy levels of the band edge positions determine which reactions can be catalysed. The excited electrons in the conduction band can reduce adsorbed molecules only if the redox potential of the adsorbed species is more positive than the potential of the conduction band edge of the semiconductor (Fig. 2.2). The opposite is true for holes, where, in order to oxidise

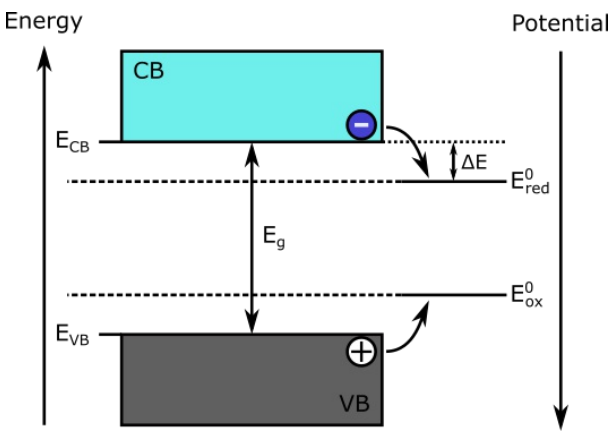

Figure 2.2: The band edge and redox half-reaction potentials for a thermodynamically possible reaction. ΔE marks the overpotential which is needed to improve the kinetics of the reaction.

an adsorbed species, the redox potential of adsorbed species has to be more negative than the potential of the valence band edge. This means that in Fig. 2.2 the redox potentials of the

Die approbierte gedruckte Originalversion dieser Diplomarbeit ist an der TU Wien Bibliothek verfügbar
The approved original version of this thesis is available in print at TU Wien Bibliothek.
TU Bibliothek Your knowledge hub WIEN

oxidation- and reduction half-reactions of a particular reaction have to lie in between the band edges (E_{VB} and E_{CB}). But this only considers the thermodynamic point of view. Kinetically, to achieve high reaction rates, big overpotentials are needed (ΔE in Fig. 2.2). This increases the need for larger bandgap semiconductors, but which unfortunately need higher energy photons to generate excitons, so a trade-off needs to be considered.

Generally speaking, a photocatalytic reaction can be divided into three main steps. The first is light harvesting, where electromagnetic radiation is used to generate excited electron-hole pairs, the excitons. The second step is the separation of these two charge carriers and their transfer to the surface of the catalyst, and the third step is the actual surface reaction of some reactants consuming the energetic charge carriers (see Fig. 2.3). To keep the diffusion path to the surface low and thereby reduce the probability for recombination and thermalization losses, the photocatalytic materials are typically scaled down to the nanoregime. Additionally, these morphologies provide a high surface area, which can enhance the third step in the process, the surface reaction, through an increased amount of adsorption sites which are the active sites for photocatalysis.

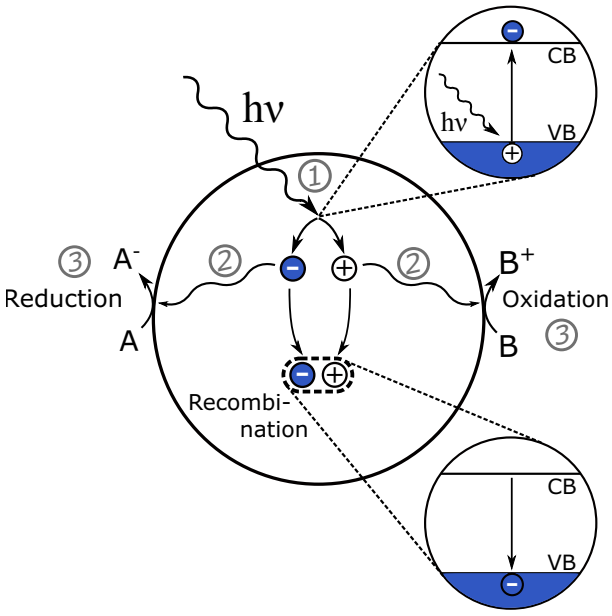

Figure 2.3: General mechanism of photocatalysis with the three essential steps: (1) Light harvesting, (2) Charge separation and diffusion to the catalyst surface and (3) Surface reaction. Additionally, the process of recombination is illustrated.

2.2 TiO_2 as a photocatalyst

TiO_2 is a very well-known photoactive material. There are three important modifications: rutile, anatase and brookite. All three forms are semiconductors with bandgaps between 3.0 eV and 3.3 eV but anatase and brookite are metastable modifications. Since anatase is the most studied and photocatalytically active modification and also the one used during the experiments in this work, the following discussion will focus mainly on this modification.

Die approbierte gedruckte Originalversion dieser Diplomarbeit ist an der TU Wien Bibliothek verfügbar
The approved original version of this thesis is available in print at TU Wien Bibliothek.
TU Bibliothek Your knowledge hub WIEN

Anatase has a bandgap of 3.2 eV [17] which means that it can only generate an exciton by irradiation with UV light. Advantages of TiO_2 anatase are its high chemical stability, high availability, inexpensiveness and non-toxicity [18]. Because of these reasons it is one of the best studied photoactive materials. It is most often used in the form of nanoparticles, however, the issue of reclaiming the catalyst after the reaction has lead to the development of supported systems, where the catalyst is attached to some kind of support. Pure anatase shows two main drawbacks: first it has a high recombination rate and second it's bandgap is very large, meaning that it can only absorb UV light and not visible light. This means that anatase could not be efficiently used with sunlight where only approx. 4 % of the photons lie in the UV range.

2.2.1 Improving the efficiency of TiO_2-photocatalysts

Several approaches have been developed to improve the effectiveness of TiO_2 or photocatalysts in general. One approach to address the insufficient light absorption of anatase would be to directly alter the properties of the bandgap. This can be done in several ways, but probably the most common one is doping the material with other cations or anions [19–21]. This produces so called extrinsic SC, in contrast to undoped SC which are called intrinsic. Through doping, inter-bandgap states are introduced and depending on whether the doped species is an electron donor or acceptor, these additional levels lie close to the conduction (n-type SC) or valence band (p-type SC) respectively. The additional energy states also shift the Fermi-level of the material. For n-type SC E_f moves closer to the CB and vice versa. This reduces the required energy for an electron to be promoted to a higher energetic state, but the doped species also introduce lattice defects, which can act as recombination centers. There is usually an optimal dopant concentration to increase the photon harvesting efficiency while still keeping the recombination rate low [22]. Other options include valence band control [23], where a big part of O^{2-}-anions are substituted to completely shift the energy level of the valence band, or photosensitization [24], where the TiO_2 is combined with a visible light active dye that injects excited electrons into the solid TiO_2.

A different strategy to improve the overall efficiency is via the introduction of a second material, creating so called heterojunctions. Typically, heterojunctions are interfaces between the primary photocatalyst and another SC, a metal or some form of nanocarbon. When a heterojunction forms, the Fermi-levels of the two materials align, leading to band bending and shifts in the relative positions of the bands [25]. A difference in the CB-levels could lead to the physical separation of excited electrons and holes if one species will preferentially move to one material while the other stays behind. This can allow for an improved extraction of the electrons and thereby reduce recombination. E.g. in the case of TiO_2 it was discovered that a mixture of anatase and rutile is more active than the individual components [26]. The heterojunction between anatase ($E_g = 3.2$ eV) and rutile ($E_g = 3.0$ eV) helps in the separation between charge carriers and thereby enhances the lifetime of excitons.

Co-catalysts are another often-used strategy to improve the catalytic properties of anatase or other semiconductors [27, 28]. For example Pt is often used to improve the water splitting activity of TiO_2 [29]. The Pt is added as small nanoparticles on the surface of TiO_2 and these

Die approbierte gedruckte Originalversion dieser Diplomarbeit ist an der TU Wien Bibliothek verfügbar
The approved original version of this thesis is available in print at TU Wien Bibliothek.
TU Bibliothek Your knowledge hub WIEN

particles can trap electrons out of the substrate and provide active reduction sites for protons in the reaction mixture. In general co-catalysts can provide active sites for the separate oxidation and reduction reactions, through lowering the activation energy required for a specific reaction, or they can extract charge carriers out of the primary semiconductor, thereby increasing the lifetime of excited states.

Alternatively, the activity of a pure SC can generally be improved by improving the availability of active reaction sites, meaning to increase the available surface area [30, 31]. Since all reactions with the photocatalyst have to happen on its surface, increasing the surface area, leads to an increase in available reaction sites. In addition to that, the increase in surface area will reduce the diffusion length of excited electrons and thereby reduce recombination.

2.2.2 V-modified photocatalysts

Titanium and vanadium are neighbours in the periodic table (atomic number Ti: 22 / V: 23) and their electronegativities (Ti: 1.54/ V: 1.63) as well as ionic radii (Ti^{4+}: 61 pm / V^{4+}: 58 pm / V^{5+}: 54 pm [32]) are quite similar. The TiO_2-catalysts used in the present work were modified with vanadium in several ways, so the following section will present a few examples of work that has previously been done on V-modified catalysts. Vanadium oxide based catalysts are well known in thermal catalysis. One prominent example is the production of sulfuric acid which is industrially realized with the help of a V_2O_5-based catalyst in the so called contact process, where the vanadium oxide oxidizes SO_2 to SO_3 under the formation of V_2O_4, which is then oxidized with oxygen back to V_2O_5. But also other industrially relevant processes like the oxidation of chlorinated organics or reduction of NO_x with NH_3 use vanadium oxide catalysts to increase selectivity or efficiency [33, 34]. In the examples above, the catalysts are most often supported on semiconductors, like for example V_2O_5 on TiO_2 [35, 36]. Depending on the amount of V in the catalyst, it typically forms either two-dimensional layers of vanadium oxide species (sub-monolayer coverage) or it can also form crystalline V_2O_5 (over monolayer coverage). The oxidation reactions typically involve the surface oxygen of the catalyst which is later replenished by gaseous oxygen and supports that can enhance the ability of the supported vanadium to form oxygen defects will improve the catalytic activity [33, 36, 37] .

In addition to thermal catalysis, vanadium-containing materials have also been used in the field of photocatalysis. Here, the most studied materials include $BiVO_4$ and vanadium-doped TiO_2, which seem to show photocatalytic activity under the illumination with visible light, but also pure vanadium oxides have been used, especially for the oxygen evolution reaction [38–42]. Vanadium is stable in several different oxidation states (+II to +V) which is reflected in the many different stable or metastable oxides that exist (VO, VO_2, V_2O_3, V_2O_4, V_2O_5). This gives the element a rich chemistry with many different possible crystal phases of the oxides, which all have different bandgaps and band positions. For example the bandgap of $BiVO_4$ and V_2O_5 are 2.5 eV and approx. 2.3 eV respectively, which both lie in the visible light range [43, 44]. In general, V is often used to produce visible light active photocatalysts, either through the addition of a vanadium containing SC [39, 45–47], that itself has a visible light bandgap or through doping which introduces inter-bandgap states and thereby makes the absorption

Die approbierte gedruckte Originalversion dieser Diplomarbeit ist an der TU Wien Bibliothek verfügbar
The approved original version of this thesis is available in print at TU Wien Bibliothek.
TU Bibliothek Your knowledge hub WIEN

of photons with a higher wavelength possible [40, 48, 49]. In the former case, the V species were able to absorb visible light and the formation of a heterojunction lead to a separation of the charge carriers. Fig. 2.4 shows the situation of the two semiconductors TiO_2 anatase and V_2O_5 as separate particles and when forming a heterojunction. The Fermi-levels for both these semiconductors lie closer to the CB since both are n-type semiconductors due to oxygen vacancies leaving electrons behind in the valence band. The resulting band structure allows for lower frequency photons to be absorbed in the V_2O_5 and the generated excitons are separated more easily because excited electrons can transfer to anatase, where they are on a lower energy level, while the holes remain in the V_2O_5.

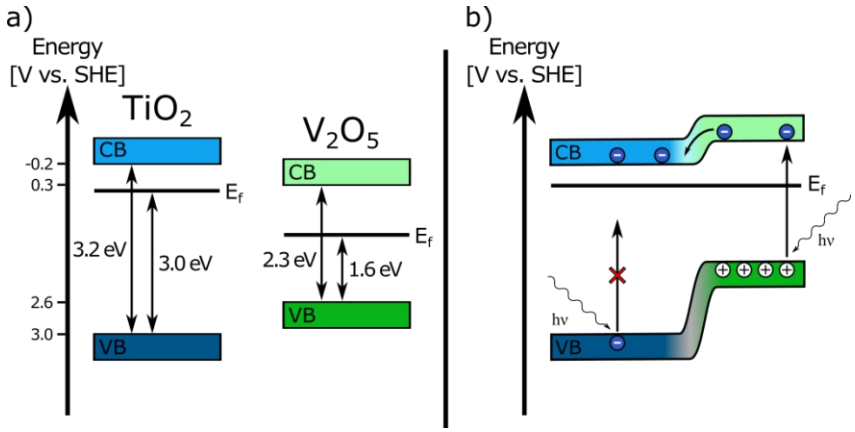

Figure 2.4: The band positions for TiO_2 and V_2O_5 as (a) separate semiconductors as well as (b) the new situation arising when the two materials are forming a heterojunction. The CB of V_2O_5 now lies higher than the CB of TiO_2 due to the equalizaion of the E_f. [46, 47]

2.3 Water splitting

Water splitting is one of the most studied photocatalytic reactions. Reaction {1} shows the overall reaction equation and it can be seen that it has a positive ΔG, meaning that the back reaction is thermodynamically favoured.

$$2\,H_2O \longrightarrow 2\,H_2 + O_2 \qquad \Delta G^0 = 237.2\,\mathrm{kJ/mol} \qquad \{1\}$$

Because it has a positive ΔG it is an example of artificial photosynthesis, however, it is still most often described as a photocatalytic process. The produced hydrogen gas can be used as a fuel source which makes water splitting a promising technology in the search for non-fossil and sustainable energy sources. The total reaction can be split into a reduction and an oxidation half-reaction which are called the hydrogen evolution reaction (HER) and oxygen evolution reaction (OER) respectively. The equations for these half-reactions are given in Reactions {2} and {3}.

$$2\,H^+ + 2\,e^- \longrightarrow H_2 \qquad E^0{}_{red} = 0.00\,\mathrm{V} \qquad \{2\}$$

$$2\,H_2O \longrightarrow O_2 + 4\,H^+ + 4\,e^- \qquad E^0{}_{ox} = 1.23\,\mathrm{V} \qquad \{3\}$$

Die approbierte gedruckte Originalversion dieser Diplomarbeit ist an der TU Wien Bibliothek verfügbar
The approved original version of this thesis is available in print at TU Wien Bibliothek.
TU Bibliothek Your knowledge hub WIEN

Reaction {3} can also be written as:

$$2\,H_2O + 4\,h^+ \longrightarrow O_2 + 4\,H^+ \qquad \{4\}$$

The redox potentials above are given for pH 0, for which the potential of the standard hydrogen electrode (SHE) is defined. In fact, all other redox potentials are defined in relation to the SHE, which is a theoretical electrochemical half-cell where an inert Pt metal is immersed in a 1 mol/L solution of H^+ ions that do not interact with themselves. However, because both half-reactions include protons, these values are pH-dependent and at pH 7 the reduction potential of H_2 decreases to -0.41 V and the oxidation potential for O_2 becomes 0.82 V. A photocatalyst would need a VB-edge higher than the oxidation potential and a CB-edge lower than the reduction potential to theoretically be able to facilitate the complete water splitting reaction. Many typical semiconductors, e.g. TiO_2 or CdS, fulfil these criteria, and a few can be seen in Fig. 2.5.

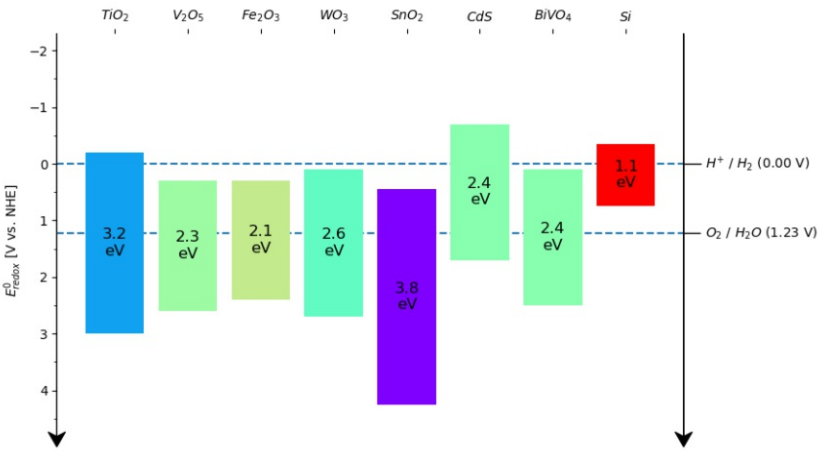

Figure 2.5: The band positions and bandgaps for several typical semiconductors. The two dotted lines represent the standard potentials for the hydrogen and oxygen evolution potentials at pH 0.

The minimal theoretical bandgap for this reaction is 1.23 eV but due to overpotentials at the interface between the semiconductor and water the actual required bandgap is usually larger. In fact, the HER has such a large, required overpotential for the bare surface of TiO_2 that it is often considered inactive [50]. This problem is often solved with the usage of noble metal co-catalysts like Pt or Pd, where Pt requires the lowest activation energy and therefore shows the highest activity towards HER [29].

For the relatively simple HER, a proton has to adsorb onto the catalyst surface, get reduced by the excited electrons and then combine with another reduced hydrogen atom on the surface or with another proton and an additional electron to form a molecule of H_2 [51]. This molecule has to desorb again to make the surface available again for further reactions.

Problems with water splitting lie mainly in the more complex OER, where many holes have to react at the same time and location to create O_2. The process invovles a concerted reaction mechanism of several like-charged species which greatly reduces the probability for the process and results in large required overpotentials. The exact prevalent mechanism is still subject to debate in the literature. It has been suggested that H_2O_2 plays a role as an intermediate

Die approbierte gedruckte Originalversion dieser Diplomarbeit ist an der TU Wien Bibliothek verfügbar
The approved original version of this thesis is available in print at TU Wien Bibliothek.
TU Bibliothek Your knowledge hub WIEN

product for the OER [52, 53] but more recent results have suggested a different mechanism involving surface peroxides [54, 55]. Typical co-catalysts for the OER on TiO_2 include noble- and transition metal oxides like IrO_2, RuO_2, CoO_x, MnO_x or FeO_x [56, 57].

2.3.1 Sacrificial water splitting

To design catalysts that are specifically tuned to enhance one half-reaction, sacrificial agents can be used to scavenge the electrons or holes that aren't consumed in the reaction. These sacrificial agents provide alternative half-reactions with different redox-potentials and lower overpotentials, so that the reaction can happen more easily. E.g. methanol or other alcohols can be used for HER catalysts to scavenge holes thereby reduce the recombination of electrons, which enhances the HER [58]. The sacrificial agent is oxidised and in the case of methanol it forms CO_2 and leaves the system, preventing a back reaction. For the OER, easily reducible ions like Ag^+ can be used to scavenge the electrons [59, 60]. This system can be used to study one half-reaction individually while reducing the influence of the counter reaction. As said before, many co-catalysts are only able to enhance one half-reaction and they are typically studied using sacrifial water splitting. To later enhance the overall reaction, it is possible to use two separate co-catalysts on a single SC, each designed for either the oxidation or reduction half reaction [61].

Die approbierte gedruckte Originalversion dieser Diplomarbeit ist an der TU Wien Bibliothek verfügbar
The approved original version of this thesis is available in print at TU Wien Bibliothek.
TU Bibliothek Your knowledge hub WIEN

Methods

3.1 Microscopy techniques

3.1.1 Transmission Electron Microscopy (TEM)

Transmission Electron Microscopy is a very high resolution (approx. 0.2 nm) microscopy technique. In a TEM-microscope, an electron source generates free electrons in a vacuum, that get accelerated with voltages of several hundred kV towards the sample. Electromagnetic lenses allow the beam to be focused onto a small spot with a diameter below 1 nm. The electrons can hit and pass through the sample, while interacting elastically and inelastically with the atoms and the crystal lattice (see Fig. 3.2). After the electrons have passed through the sample, the TEM works analogously to an optical microscope in the sense that the electrons get projected onto the detector by lenses. A typical detector contains a scintillator, to convert the incoming electrons into photons which subsequently get transferred onto a charge coupled device (CCD) camera to be viewed on a PC screen. A big advantage of electron microscopy compared to optical is that electrons have a much smaller wavelength than lightwaves (400 nm - 800 nm). This means that much smaller details can be resolved, even up to individual atoms. Also, the lenses are electromagnetic which means that their properties can be changed and errors can be corrected during a measurement. Chemical information can also be obtained from characteristic X-rays, generated from inelastic interactions of the electrons with the sample (energy-dispersive X-ray spectroscopy, EDX). However, because the electrons have to pass through the sample to reach the detector, only relatively thin samples like NP's or thin films can be analysed with TEM (max. thickness between several hundred nm and a few µm [62]).

TEM is especially useful for crystalline materials, since it can depict the crystal structure on an atomic scale. If the crystal lattice aligns correctly with the electron beam, so-called lattice fringes appear in the image which hold information about the spacing of the particular lattice planes that are visible. For measuring the distance between these lattice planes, it is convenient to transform the image with the Fast Fourier Transform (FFT) algorithm [63].

For this project TEM measurements were performed on a *FEI* Tecnai F20. To prepare the samples a small amount of powder was placed on a special copper grid with amorphous carbon sputtered onto, without the use of any solvents. On some of the images, lattice fringes are visible. In these cases, the distance between them was measured by calculating the Fourier transform of the concerning region of the image. The resulting image showed periodic, light spots in the orthogonal direction to the lattice fringes. By masking everything except the two innermost spots and calculating the reverse Fourier transformation of the image, the lattice fringes were much more clearly visible than before the transformations. This process can schematically be seen in Fig. 3.1.

Die approbierte gedruckte Originalversion dieser Diplomarbeit ist an der TU Wien Bibliothek verfügbar
The approved original version of this thesis is available in print at TU Wien Bibliothek.
TU Bibliothek Your knowledge hub WIEN

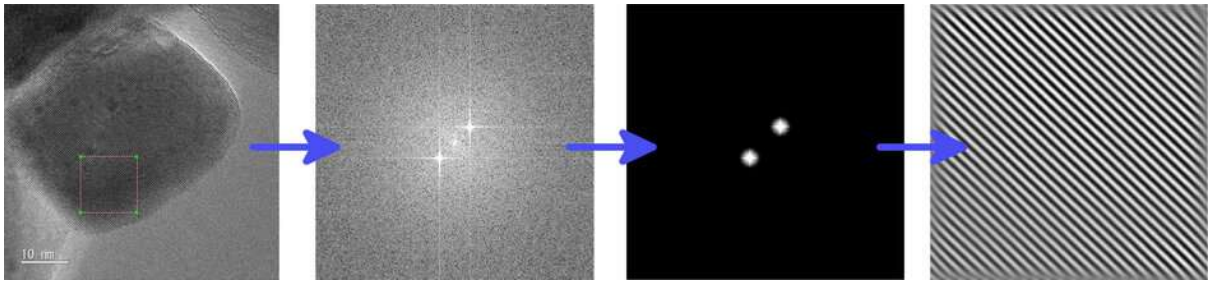

Figure 3.1: Illustration of the process of evaluating the distance of lattice fringes in TEM images. The area of interest is processed with a FFT and then everything except the two innermost spots are masked. After the reverse FFT process, the lattice fringes are more clearly visible.

3.1.2 Scanning Electron Microscopy (SEM)

Scanning electron microscopy is a different electron microscopy technique, where, in contrast to TEM, the image is generated from secondary and backscattered electrons instead of transmitted ones. Electrons from an electron gun are accelerated towards the sample with voltages in the range of 10 kV or lower. Upon impact, the electrons interact elastically and inelastically with the specimen and depending on the acceleration voltage they penetrate the sample up to a specific depth. Inelastic collisions with atoms of the sample can create a wide range of effects like Auger electrons, characteristic X-rays, or eject weakly bound valence electrons called secondary electrons (SE) (see Fig. 3.2). SE have very low kinetic energy which means only the ones

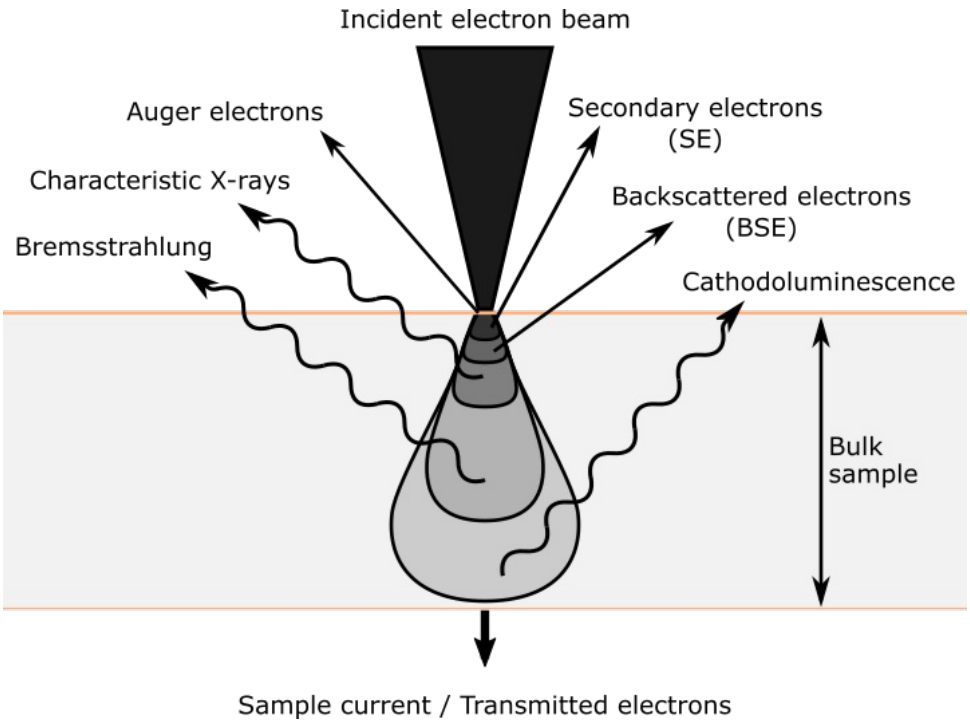

Figure 3.2: Different effects produced by elastic and inelastic interactions of primary electrons with the sample surface. The individual types of radiation and electrons can come from different levels meaning they contain information from different depths.

generated near the surface are able to escape and travel to the detector. They mainly give information about sample topology due to an increased SE ejection at higher incidence angles which leads to a brightness contrast at particular surface features. Elastic interaction with the sample atoms can lead to backscattered electrons (BSE). BSE get generated from deeper layers

Die approbierte gedruckte Originalversion dieser Diplomarbeit ist an der TU Wien Bibliothek verfügbar
The approved original version of this thesis is available in print at TU Wien Bibliothek.
TU Bibliothek Your knowledge hub WIEN

of the sample and they mainly contain information about sample composition since heavier elements are more likely to reflect the incoming electrons elastically. This means that heavy elements appear brighter when looking at the signal coming from the BSE.

Typically the images generated from SE or BSE can be viewed individually depending on whether the compositional or topological information is required. Compared to TEM, thicker samples can be analysed but because many of the incoming electrons don't leave the sample, it has to be conductive. Insulating samples can be made conductive by sputtering a thin metal layer onto the surface. Similarly to TEM, the inner part of the instrument has to be evacuated to allow electrons to travel far enough to hit the sample.

SEM images for this project were taken on a *FEI* Quanta 250 FEGSEM. For the sample preparation, a little bit of powder was placed on a sticky carbon film and evacuated. Only the SE signal was recorded and all images were taken with an accelerating voltage of 10 kV.

3.2 Spectroscopy techniques

3.2.1 Total Reflection X-ray Fluorescence (TXRF)

TXRF is a non-destructive, qualitative and quantitative analytical technique to analyse sample composition. Solid powders as well as liquid solutions of analytes can be measured with this technique. For the measurement the sample is irradiated with X-rays at a very low angle of incidence. The high-energy photons can knock out inner shell electrons of atoms in the sample which leaves the atom in an excited state. This state decays very rapidly via the relaxation of an electron from a higher shell to fill up the lower shell. During this process, the atom emits secondary X-rays which are characteristic for the element. Qualitative information can then be extracted from the energy of the secondary X-rays and quantitative information from the intensity of specific energies. Also, due to the low angle of incidence, the incoming beam is scattered very little which reduces the noise on the detector from the primary radiation.

Since X-rays can travel through the atmosphere, the technique can be employed in atmospheric conditions, however, to reduce noise from the measurement it is still often performed under vacuum. During this master thesis project an *ATOMIKA* 8030C X-ray fluorescence analyzer was used. The sample was excited, utilizing a Mo X-ray tube (monochromatized K_α-line) at 50 kV and 47 mA for 100 s, using the total reflection geometry and an energy-dispersive Si(Li)-detector. For solid measurements 1 mg of the powder sample was placed at the centre of a quartz reflector and 5 µL of a 1 % polyvinyl alcohol solution were added and dried off, using a hot plate. The bare reflectors were measured as blanks before and between each set of measurements to check for possible contaminations in the analyzer. Ti was set as the matrix and the concentrations of other elements were determined as relative amounts. For liquid measurements, 1 mL of the sample were mixed with 10 µL of an internal Y standard with a concentration of 1000 ppm in an Eppendorf tube. These were then vortexed for 1 min and 5 µL of the sample were then pipetted onto the reflector and dried on a hot plate. After cooling, the reflectors with the dried samples were measured.

Die approbierte gedruckte Originalversion dieser Diplomarbeit ist an der TU Wien Bibliothek verfügbar
The approved original version of this thesis is available in print at TU Wien Bibliothek.
TU Bibliothek Your knowledge hub WIEN

3.2.2 X-ray Photoelectron Spectroscopy (XPS)

The measurement technique of XPS utilizes monochromatic X-ray radiation to excite and eject electrons from the analysed sample. The energy of these electrons contains information about the amount, identity and chemical surrounding of the atoms. Especially information about the oxidation state of present elements can be extracted. In order to extend the mean free path of the emitted electrons, the technique is preferentially performed under ultra high vacuum atmosphere.

When an X-ray photon gets absorbed by an electron in the sample it gets excited and if the photon energy was high enough it is elevated to the vacuum level and ejected from the sample with some leftover kinetic energy. This kinetic energy (E_{kin}) is connected with the original binding energy ($E_{binding}$) of the electron in the atom through Eq. (3.1)

$$E_{binding} = E_{photon} - (E_{kin} + \phi) \tag{3.1}$$

E_{photon} describes the energy of the incoming X-ray photon, ϕ is the work function of the detector and E_{kin} is measured by the spectrometer. Because Eq. (3.1) includes the photon energy it is important to utilize monochromatic radiation.

Emitted electrons can interact with surrounding atoms via inelastic collisions. This leads to an increased background signal and some electrons can also be reabsorbed, which means that only surface-near electrons will have a high chance of being able to escape completely and reach the detector. The obtained binding energy of the electrons is dependent on a few different factors. First and foremost, it depends on the element from which the electron was emitted. Second, it also depends on the specific shell out of which the electron was emitted. Since electrons from several different shells can get emitted, one element typically produces several different signals. Third, the binding energy also depends on the chemical surrounding of the atom, specifically the chemical bonds and its oxidation state. Changes in the oxidation state typically results in binding energy shifts of a few eV.

For this master thesis, the measurements were performed on a custom-built *SPECS* XPS-spectrometer equipped with a monochromatised Al-Kα X-ray source (µ-Focus 350) and a hemispherical WAL-150 analyser (acceptance angle: 60°). All samples were mounted onto the sample holder using double-sided carbon tape. Pass energies of 100 eV and 30 eV and energy resolutions of 1 eV and 100 meV were used for survey and detail spectra respectively (excitation energy: 1486.6 eV, beam energy and spot size: 70 W onto 400 µm, angle: 51° to sample surface normal, base pressure: 5×10^{-10} mbar, pressure during measurements: 2×10^{-9} mbar). Data analysis was performed using the CASA XPS software, employing transmission corrections (as per the instrument vendor's specifications), Shirley/Tougaard backgrounds [64, 65] and Scofield sensitivity factors [66]. Charge correction was applied so the adventitious carbon peak (C-C peak) was shifted to 284.80 eV binding energy. A broad-spot low energy electron source (SPECS FG 22 flood gun) was used for charge compensation (5 eV/25 µA) to reduce potential charging effects.

Die approbierte gedruckte Originalversion dieser Diplomarbeit ist an der TU Wien Bibliothek verfügbar
The approved original version of this thesis is available in print at TU Wien Bibliothek.
TU Bibliothek Your knowledge hub WIEN

3.2.3 Attenuated Total Reflectance Fourier Transform Infrared Spectroscopy (ATR-FTIR)

Infrared Spectroscopy uses (typically mid-) IR radiation to excite molecular rotations and vibrations in the tested sample. Like in other absorption spectroscopy techniques, the sample is illuminated with light of a specific wavelength and a specific intensity and the transmitted intensity is measured, to obtain information about the absorbed wavelengths. Infrared radiation has less energy than UV or visible light, so it cannot excite electronic energy levels. Instead it excites rotational or vibrational states of molecules or individual bonds from the sample. Specific structures (e.g. a C=O-bond or a Ti−O-bond) have characteristic vibrational modes that get excited by the absorption of infrared radiation, so IR-Spectroscopy can be used to identify structures existing in the sample. Most organic molecules also display absorption in the so-called "fingerprint region", which is a wavelength region between $1500\,\mathrm{cm}^{-1}$ and $500\,\mathrm{cm}^{-1}$. This region contains absorptions of bigger structures, or the molecule as a whole and it can be used to identify the molecule through comparison of the spectrum with spectra from a database.

There are several measurement techniques for different samples like transmission-mode or the fabrication of a compact KBr-sample mixture, but for powder samples ATR requires the least amount of sample-preparation. In this technique, the powder is pressed against a special ATR-crystal and the infrared light is sent through the crystal while getting reflected through total internal reflection. When the lightwave hits the interface of the crystal and the sample, part of the wave travels out of the crystal into the sample as an evanescent wave (penetration depth between 0.5 and a few µm). Here, absorption happens and afterwards the light gets reflected back internally and sent to the detector. Since IR radiation is absorbed when travelling through the sample, and the evanescent wave doesn't travel far out of the crystal, this technique is useful for analysing the sample surface only up to a depth of a few µm.

FTIR stands for Fourier-Transform- Infrared and it also describes a special technique of Infrared spectroscopy. Here, the whole spectrum is measured all at once and the signal is then generated using a Fourier transform. This poses a significant time advantage compared to dispersive IR-Spectroscopy, where each wavelength has to measured individually.

In this work, ATR-FTIR measurements were performed using a Tensor 27 FTIR from *Bruker* with a ZnSe crystal. Spectra were recorded from $400\,\mathrm{cm}^{-1}$ to $4000\,\mathrm{cm}^{-1}$ with a resolution of $4\,\mathrm{cm}^{-1}$ and 32 scans. For each measurement the FTIR crystal was covered with a few mg of sample and then compressed using a metallic pin. Before each measurement a background spectrum of air was collected which was then subtracted from the actual sample spectrum.

3.2.4 Raman Spectroscopy

Raman spectroscopy is a technique that uses monochromatic light which interacts with molecular vibrations in the sample. From these interactions informations about chemical structures, present phases or intrinsic stress/strain can be extracted. Typically a visible light laser illuminates the sample and scattered light is caught by a detector. In contrast to IR spectroscopy, where the information comes from the absorption of IR photons, Raman spectroscopy utilizes scattered

Die approbierte gedruckte Originalversion dieser Diplomarbeit ist an der TU Wien Bibliothek verfügbar
The approved original version of this thesis is available in print at TU Wien Bibliothek.
TU Bibliothek Your knowledge hub WIEN

photons to extract the information. Most of the incoming light scatters elastically via Rayleigh scattering but a small fraction interacts with phonons in the sample and gets scattered inelastically via either Stokes Raman scattering or Anti-Stokes Raman scattering. Fig. 3.3 shows an illustration of the process. The incoming photon elevates an electron to a virtual energy state that decays after a very short time by emitting another photon. If the electron falls back to a different energy state than where it was originally at, the resulting radiation will be of a different wavelength. This shift is called the Raman shift and it is typically given as a wavenumber shift instead of a wavelength shift. In Eq. (3.2) $\Delta\nu$ denotes the Raman shift, λ_1 the excitation wavelength and λ_2 the outgoing Raman wavelength.

$$\Delta\nu = \left(\frac{1}{\lambda_1} - \frac{1}{\lambda_2}\right) \tag{3.2}$$

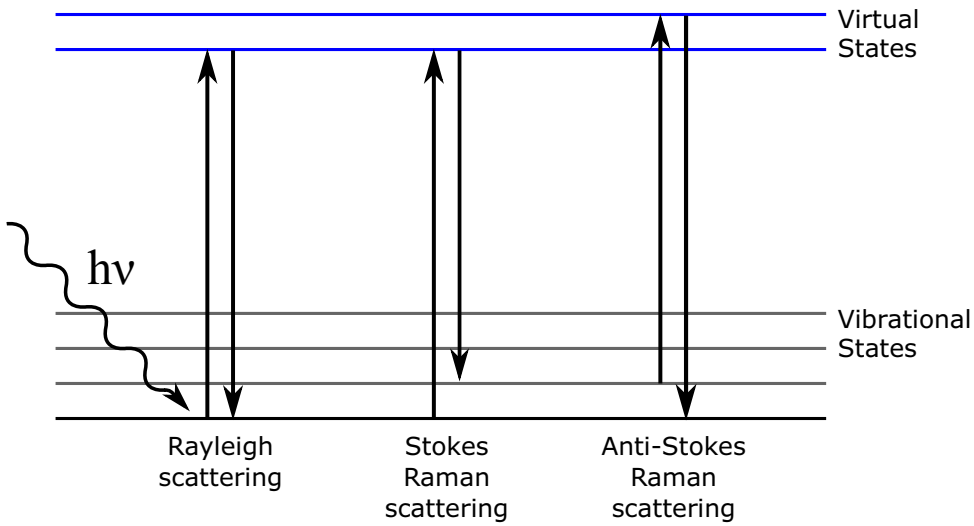

Figure 3.3: Elastic and inelastic scattering mechanisms from the interaction of light with a powder sample. Photons scattered via Stokes Raman or Anti-Stokes Raman scattering carry information about rotational and vibrational energy levels in the sample.

For a vibrational energy state to be Raman-active, the vibration needs to change the polarizability of the molecule. This can make it a complementary technique to IR-spectroscopy where the vibration needs to change the dipole-moment of the molecule to be IR-active.

The Raman shifts of a particular sample can be used to identify present phases by comparing it with a database of known spectra or it can be used to identify particular structure fragments. When comparing different spectra of the same compound, the change in Raman shift can also give information about intrinsic properties like stress/strain or temperature.

Raman spectra were measured on a *Horiba* Jobin-Yvon LabRAM 800HR spectrometer equipped with an edge filter, an external frequency-doubled Nd:YAG laser (Oxxius LMX 532 nm, maximum power output < 55 mW) as monochromatic light source, a Synapse Open-Electrode-CCD detector with a grating of $1800\,\mathrm{mm}^{-1}$ and an optical microscope (*Olympus* BX40) with a motorized xyz-stage (*Märzhäuser*). Spectra were recorded with an acquisition time of 0.5 s and 50 accumulations from $100\,\mathrm{cm}^{-1}$ to $1000\,\mathrm{cm}^{-1}$. For calibration a pure Si wafer was measured and the peak was set to be at a Raman shift of $520\,\mathrm{cm}^{-1}$. The samples were measured by placing a few mg of

Die approbierte gedruckte Originalversion dieser Diplomarbeit ist an der TU Wien Bibliothek verfügbar
The approved original version of this thesis is available in print at TU Wien Bibliothek.
TU Bibliothek Your knowledge hub WIEN

powder on a microscope glass slide and flattening them with another piece of glass. After the measurement the sample was recovered.

3.2.5 Diffuse Reflectance Spectroscopy (DRS)

Diffuse Reflectance Spectroscopy can be used to obtain reflectance spectra of powder samples. In contrast to specular reflectance, where light is being reflected in such a way, that the incident angle equals the reflected angle, diffuse reflectance scatters the incoming light in all directions. This type of reflectance can typically be seen with rough samples, like for example powders, whereas specular reflectance can be observed with smooth or polished surfaces, where the typical scale of surface roughness inhomogeneities is smaller than the incident wavelength. Like in other absorption spectroscopy techniques, the sample absorbs absorbs photons of a specific energy and this can be used to obtain information about the sample. Typically, DRS is performed with wavelengths between the UV and mid-IR regions, where the technique using light in the UV-vis region is called UV-vis-DRS.

DRS was used to examine the optical absorption properties of different catalysts in powder form. A *Jasco* V-670 Spectrophotometer with a special sample holder for powder samples and an insert including an integrating sphere was used for DRS measurements. Approx. 20 mg of a powder-sample were inserted into the sample holder and gently compacted. The reflectance was then measured for wavelengths between 200 nm and 800 nm.

3.3 Powder X-ray Diffraction (XRD)

Powder XRD is an analytical technique used to determine phase composition, texture or exact lattice parameters of a solid powder sample. The term diffraction is used to describe a number of phenomena that happen when a wave hits an obstacle. In the case of X-ray diffraction, incoming X-rays get scattered by the electrons from atoms inside a crystal lattice. Due to the regularity of the lattice, the scattered waves cancel each other out in most directions due to destructive interference. But depending on the lattice plane, some angles show constructive interference and thereby generate outcoming waves from the sample, as can be seen in Fig. 3.4. For constructive interference to occur, the distance δ in Fig. 3.4 has to be a halfinteger multiple of the wavelength.

The angles for which this occurs can be calculated with Bragg's law (Eq. (3.3)), where d denotes the lattice plane spacing, θ the incidence angle, λ the wavelength of the radiation and n any integer.

$$2d \sin\theta = n\lambda \tag{3.3}$$

For a typical measurement the sample is milled into a fine powder, placed on a spinning sample table and illuminated with parallel, monochromatic X-ray radiation. The detector then records the signal intensity depending on the incidence angle and the diffractogram is given as a graph of intensity vs. 2θ.

The resulting peak positions depend on the crystal structure and each present phase gives its characteristic diffractogram which is why this technique is most often used to determine the

Die approbierte gedruckte Originalversion dieser Diplomarbeit ist an der TU Wien Bibliothek verfügbar
The approved original version of this thesis is available in print at TU Wien Bibliothek.
TU Bibliothek Your knowledge hub WIEN

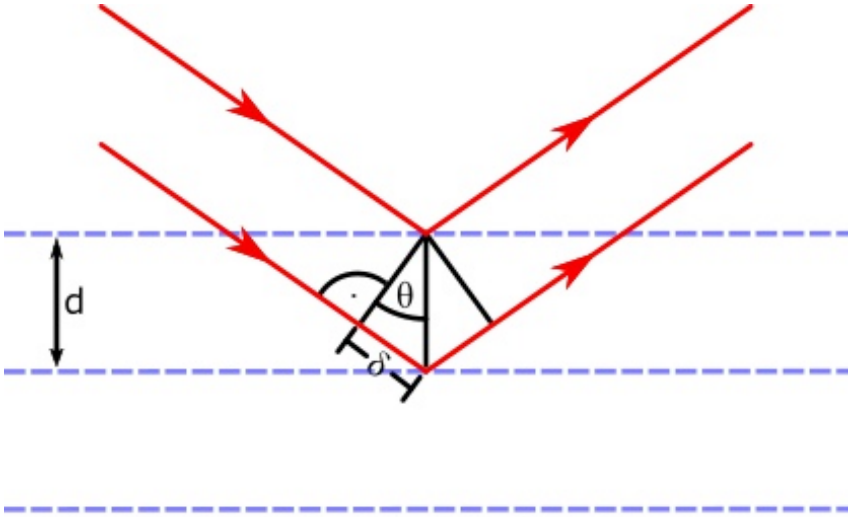

Figure 3.4: Illustration of Bragg diffraction of X-rays from electrons in a lattice. d is the lattice plane spacing and θ the incidence angle

phase composition of a sample, by comparing the found peaks with a database of reference diffractograms. Quantitative information can also be extracted from the relative intensities of the signals.

However, they can also be influenced by the texture of the sample, which is a preferred orientation of the crystallites in the powder and leads to an increase in intensity for some diffraction peaks. This information can also be used to study preferred growth directions of the crystal which is especially interesting for biological samples or material properties.

The related technique of single-crystal XRD is mainly used to determine the structure of sample but, as the name suggests, requires a large enough single crystal, which can be difficult to grow. In contrast, powder XRD can give information about the whole sample instead of an individual crystal and be used with almost any crystalline material.

For this master project powder XRD measurements were carried out using a XPERT II:PANalytical XPert Pro MPD ($\Theta - \Theta$ Diffractometer). Sample irradiation was performed using a Cu X-ray source (8.04 keV, 1.5406 Å) with Bragg-Brentano geometry. A few mg of the powder sample were placed on a Si sample holder and inserted into the machine which was equipped with an autosampler. Each specimen was scanned between 5° and 80° while rotating the sample. The background of the recorded signal was analyzed and removed using the open-source package 'peakutils' for the Python programming language [67].

3.4 Thermogravimetric Analysis (TGA)

In TGA a typically solid sample is heated up while its weight is recorded. The temperature dependent weight loss of the sample can be used to gain information about volatile compounds in the sample (e.g. crystal- or adsorbed water) and about reactions happening in the examined temperature range. By using different atmospheres, different reactions like the oxidation or reduction of metals and organic compounds can be observed.

Die approbierte gedruckte Originalversion dieser Diplomarbeit ist an der TU Wien Bibliothek verfügbar
The approved original version of this thesis is available in print at TU Wien Bibliothek.
TU Bibliothek Your knowledge hub WIEN

The experiment can be performed either with a constant heating rate (dynamic method), at a fixed temperature (isothermal method) or a combination of both. In a dynamic measurement the heating rate should be chosen small enough to not induce more than one reaction at a time, so that every individual reaction step can be resolved.

The TGA measurements for this project were performed on a *PerkinElmer* Thermogravimetric Analyser TGA 8000. For each measurement between 5 mg to 10 mg of the sample were loaded into a small ceramic weighing dish and inserted into the autosampler of the machine. Precursor substances were analysed dynamically from 30 °C to 800 °C with a heating rate of 10 °C/min. Catalyst samples were analysed slightly differently. To remove any adsorbed water, the catalysts were first heated to 120 °C with a heating rate of 40 °C/min and kept at that temperature until constant weight. After that the samples were again heated up to 800 °C with a rate of 10 °C/min.

3.5 Gas Chromatography (GC)

Gas chromatography is an analytical technique to analyse the composition of gaseous or liquid and volatile samples. Every chromatographic technique has a stationary and a mobile phase. In gas chromatography the sample is inserted into a constant carrier gas stream which constitutes the mobile phase and which carries the mixture into a column filled with the stationary phase. In the column, the different components are separated depending on their strength of interaction with the stationary phase. Behind the column the gases are detected and identified via their retention time, meaning the total time it takes the substance to travel through the column and to the detector.

In the present project, a Nexis GC-2030 from *Shimadzu* was used in combination with a ShinCarbon ST 2.0 m x 1.0 mm ID micropacked column by *Restek* to analyse gas mixtures that were produced from HER experiments. He 6.0 was used as carrier gas and kept at a constant flow rate of 7.0 mL. For each injection, 200 µL were taken from the reactor headspace and inserted into the GC injector, which was kept at 150 °C. The split ratio for the split injection was set to 4 so that only 1/5 of the total sample amount flowed into the column. The temperature of the column was held constant at 100 °C. For the detection a barrier ionization discharge detector was used which generates a He plasma that ionizes all incoming gases (except neon) and detects them via changes in conductivity of the plasma. During the measurement, the detector was kept at 280 °C.

For the quantitative analysis of the gas components, a calibration was performed with gas mixtures of known concentration. For this purpose a round bottom flask with one opening and an additional valve was closed with a septum and evacuated while heating the glass with a heat gun. Using a three-way valve the flask was then filled with the gas mixture directly from the gas bottle. The process of evacuating and filling up with a gas mixture was repeated four times. The gas mixtures consisted of H_2, O_2, CO and CO_2 in an Ar Matrix in concentrations of 5 Vol ppm, 25 Vol ppm, 100 Vol ppm, 1000 Vol ppm and 10 000 Vol ppm each.

Die approbierte gedruckte Originalversion dieser Diplomarbeit ist an der TU Wien Bibliothek verfügbar
The approved original version of this thesis is available in print at TU Wien Bibliothek.
TU Bibliothek Your knowledge hub WIEN

Experimental Part

The catalysts used in this master project were synthesized with two different synthetic routes and two different V-precursors. Anatase nanopowder was mixed with a V-precursor in aqueous solution. The water of the dispersion was either evaporated (evaporation synthesis), which led to the recrystallization of the complete amount of precursor, or the particles were filtered (filtration synthesis) which kept only the precursor that adsorbed to the surface of the anatase particles. Additionally, several concentrations were used as well as different calcination temperatures, which resulted in different products on the catalysts. The utilized precursors were ammonium metavanadate (NH_4VO_3) and vanadyl sulfate ($VOSO_4 \cdot 4\,H_2O$). Fig. 4.1 shows all synthesis routes schematically and the labels for each sample.

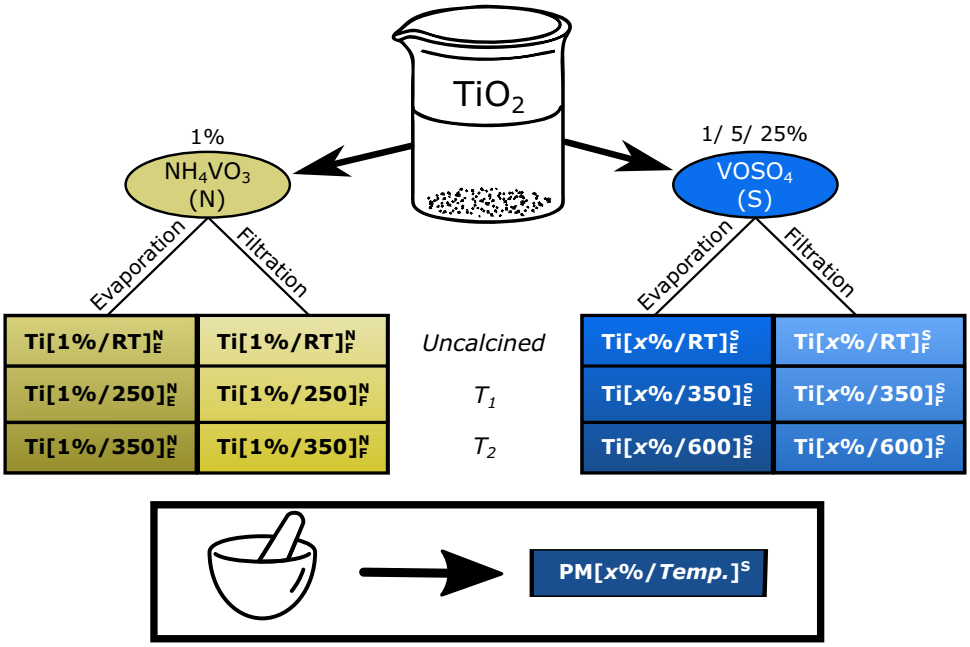

Figure 4.1: All the different synthesis routes used in the present master project and the resulting labels for each sample (PM: physical mixture).

Informations about the used chemicals are given in Table 4.1.

4.1 Catalyst synthesis

4.1.1 Evaporation synthesis

For this synthesis, 400 mg (5 mmol) TiO_2 anatase nanoparticles were dispersed in 100 mL of deionized (DI) water while stirring with a magnetic stirrer. After 5 min, 294 mg (1.25 mmol) of $VOSO_4 \cdot 4\,H_2O$ were dissolved in 25 mL of DI water and added to the dispersion so that the finished sample would have 25 at% of V in relation to Ti. The dispersion was then ultrasonicated

Die approbierte gedruckte Originalversion dieser Diplomarbeit ist an der TU Wien Bibliothek verfügbar
The approved original version of this thesis is available in print at TU Wien Bibliothek.

Table 4.1: List of chemicals.

Name	Chemical formula	CAS number	Supplier	Purity
Anatase	TiO_2	1317-70-0	Sigma Aldrich	99.7 % *
Ammonium-metavanadate	NH_4VO_3	7803-55-6	Carl Roth	≥ 99.8 %
Vanadylsulfate hydrate	$VOSO_4 \cdot 4\,H_2O$	12439-96-2	Acros Organics	17 - 23 %V
Silvernitrate	$AgNO_3$	7761-88-8	-	-
Vanadium(V)-pentoxide	V_2O_5	1314-62-1	ABCR	99.5 %
Chloroplatinic acid solution	H_2PtCl_6	16941-12-1	Sigma Aldrich	8 % in water
Methanol	CH_3OH	67-56-1	VWR	HPLC grade

* Mean particle size: <25 nm; Surface Area: $74\,m^2\,g^{-1}$

for 15 min and stirred for another 30 min. Afterwards, the water was evaporated under vacuum (20 mbar) at a temperature of 45 °C, which resulted in a dark blue, wet solid, which was dried at 60 °C.

The catalysts were then calcined in a muffle oven in air at two different temperatures: 350 °C and 600 °C. The heating rate was set to $5\,°C\,min^{-1}$ and the maximum temperature was held for 1 h.

For additional characterization of the samples, some catalysts with different V-concentrations of 5 at% and 1 at% were produced. The 5 %-sample was produced analogous to the above described procedure, using only 59 mg (0.25 mmol) of $VOSO_4 \cdot 4\,H_2O$. For the 1 %-sample, however, only 200 mg (2.5 mmol) TiO_2 anatase powder were dispersed in 49 mL of DI water and after 5 min, 1 mL of a precursor stock solution ($5.89\,g\,L^{-1}$) was added whose concentration was set so that the finished sample would have 1 at% of V in relation to Ti. The rest of the procedure was equal to the one described above. The resulting samples are blue (5 %) and yellow (1 %) coloured powders.

Additional 1 %-samples were also produced with a second precursor, ammoniummetavanadate (NH_4VO_3), to investigate the influence of the precursor on the resulting catalyst. In this case the precursor stock solution had a concentration of $2.92\,g\,L^{-1}$, but otherwise the synthesis was performed the same way. Due to the low solubility of NH_4OV_3 in water, no samples with a higher V-concentration were produced with this precursor.

After 5 min, 1 mL of a precursor stock solution was added whose concentration was set so that the finished sample would have 1 at% of V in relation to Ti ($0.025\,mol\,L^{-1}$; $2.92\,g\,L^{-1}$ for NH_4VO_3 and $5.89\,g\,L^{-1}$ for $VOSO_4 \cdot 4\,H_2O$). The catalysts were then calcined in a muffle oven in air at two different temperatures per precursor: 250 °C and 350 °C for NH_4VO_3 or 350 °C and 600 °C

Die approbierte gedruckte Originalversion dieser Diplomarbeit ist an der TU Wien Bibliothek verfügbar
The approved original version of this thesis is available in print at TU Wien Bibliothek.
TU Bibliothek Your knowledge hub WIEN

for $VOSO_4$. The heating rate was set to 5 °C min^{-1} and the maximum temperature was held for 1 h.

4.1.2 Filtration synthesis

This route was only performed with 1 %-samples and differs mainly in the separation process of the catalysts from the dispersion. Like in Section 4.1.1, 200 mg (2.5 mmol) of TiO_2 anatase nanoparticles were mixed with 49 mL of DI water. But in this route, 1 mL of the precursor solution was added after 10 min of ultrasonication, followed by another 5 min of sonication. Afterwards, the dispersion was magnetically stirred for 1 h.

The solid powder was then vacuum filtered from the solution and washed three times with 50 mL of DI water. The yellow powders were dried and then calcined with the same procedure as described in Section 4.1.1.

4.1.3 Reference Samples

A few additional samples were synthesized as a reference. A physical mixture of the two components was produced by first calcining the dry anatase powder and $VOSO_4 \cdot 4\,H_2O$ at 600 °C for 1 h separately and only afterwards mixing the calcined anatase with the calcined $VOSO_4$. Depending on the concentration and calcination temperature these samples were given the label $PM[x\%/temp.]^S$. The molecular weight of V_2O_5 was used to calculate the concentration of V.

Pure anatase powder and the pure precursors were also calcined separately at 250 °C, 350 °C and 600 °C using the same procedure as above, and labelled *"Material-Calc.Temp"* (e.g. Ana-350, $VOSO_4$-600).

4.2 Photocatalytic experiments

4.2.1 UV-HER experiments

Sacrificial UV-HER experiments were performed in a photocatalytic glass reactor, which can be seen in Fig. 4.2a. In this watercooled reactor the catalyst was dispersed in a water/methanol mixture and illuminated from above, through a quartz window. The lightsource was a LED lamp with a wavelength of 365 nm ± 20 nm (SOLIS 365-C from *Thorlabs*). All evolved gases were picked up by an Ar stream that runs through the reactor and carries the analytes to a detector. A $CaCl_2$ trap was installed after the reactor to absorb any remaining water or methanol from the gases. To measure the hydrogen content of the gas stream, a Rosemount XStream XEGP detector from *Emerson* was used. The detection was performed via thermal conductivity of the gas stream and the detector was calibrated using gas mixtures of hydrogen in argon with different concentrations.

For each experiment 10 mg of the catalyst was dispersed in a mixture of 20 mL of DI water and 20 mL of methanol, which was used as a sacrificial agent. The dispersion was ultrasonicated in a plastic beaker for 1 min and then transferred into the reactor, which was placed in a intransparent

Die approbierte gedruckte Originalversion dieser Diplomarbeit ist an der TU Wien Bibliothek verfügbar
The approved original version of this thesis is available in print at TU Wien Bibliothek.
TU Bibliothek Your knowledge hub WIEN

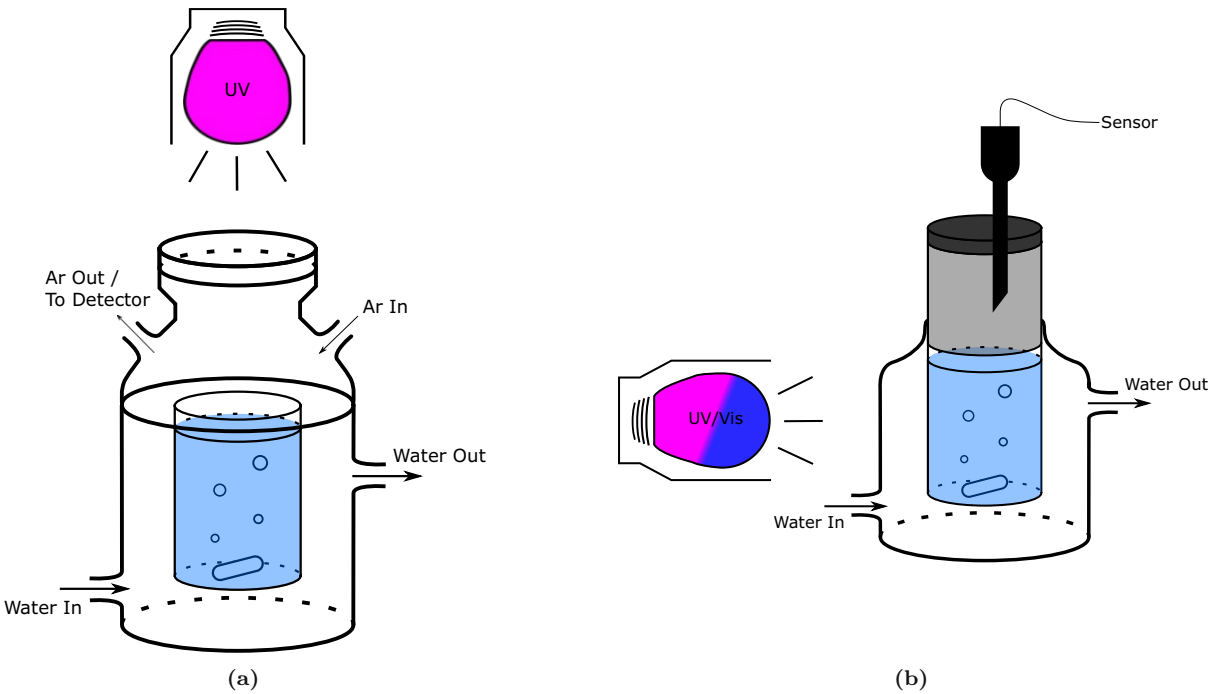

Figure 4.2: Photocatalytic reactor design for (a) HER experiments and (b) OER and Vis-HER experiments.

photobox. While stirring, the dispersion was cooled to 15 °C and purged for 5 min with Ar at a flow rate of 100 mL min^{-1}. The reactor was then sealed, except for the Ar-inlet and outlet to the detector and the Ar flow was reduced to 30 mL min^{-1}. The detection was started and after 30 min the light was turned on. The experiment was then stopped after another 30 min. A blank experiment without the addition of a catalyst was also performed.

Since the detector measured in-flow, the resulting data was directly converted to the H_2 production rate using Eq. (4.1) with the activity, flowrate, the pressure p, temperature T and the ideal gas constant R.

$$Rate\left[\frac{\mu\text{mol}}{\text{h}}\right] = \frac{activity[ppm] * flowrate * p}{T * R} \tag{4.1}$$

4.2.2 Vis-HER experiments

In addition to HER with UV light, some samples were also tested under illumination with visible light. Due to the expected lower yields with this lightsource, the setup was different to the UV-HER setup and detection of evolved hydrogen was performed with a GC "Nexis GC-2030" by *Shimadzu* (see Section 3.5). Additionally, the experiments were performed with the addition of a platinum precursor solution which, upon illumination, resulted in Pt nanoparticles being deposited on the catalysts surface. This precursor was prepared by diluting a 8 % solution of H_2PtCl_6 in water from Sigma Aldrich further to a concentration of 4.1×10^{-3} mol L^{-1}. A schematic of the reactor is given in Fig. 4.2b. However, instead of an O_2 sensor, a gastight syringe for extracting a gas sample is inserted through a septum at the top.

Similarly to the reactor from the UV-HER experiments, this one also had a watercooled outer shell but only a single opening at the top. As a light source, a monochromatic visible light LED lamp with a wavelength of 445 nm ± 20 nm (SOLIS 445-C from Thorlabs) was used

Die approbierte gedruckte Originalversion dieser Diplomarbeit ist an der TU Wien Bibliothek verfügbar
The approved original version of this thesis is available in print at TU Wien Bibliothek.
TU Bibliothek Your knowledge hub WIEN

and illumination was performed from the side instead of the top. For each reaction 1 mg of the catalyst was weighed into a small glass vial and mixed with 2 mL of a 50 vol%/50 vol% methanol/water mixture. The dispersion was then placed in an ultrasound bath for 1 min to create a well dispersed suspension. Afterwards it was transferred to the reactor and 6.3 µL of the platinum precursor solution was added. This resulted in a Pt concentration of 0.5 wt% relative to the catalyst's weight. The reactor was sealed with a septum and placed in an intransparent photobox. While stirring the dispersion at 300 rpm and cooling it to 15 °C, Ar was bubbled through the solution at a flow rate of 100 mL min^{-1}. After 5 min the Ar flow was stopped and 200 µL of the gas volume above the reaction were taken with a gastight syringe. The box was closed, the light turned on and the first gas sample was injected into the GC, to measure the H_2 concentration of the baseline value. After that, gas samples were taken approx. every 10 min and the gas concentrations were recorded. The detected peak areas for H_2 were calibrated beforehand and, using the volume of the reactor gas phase, could be converted into the total volume of hydrogen created. Under the assumption that hydrogen behaves nearly ideal, the volume could be converted to an amount in mol, with the molar volume at the reaction temperature of 15 °C of 23.6 L mol^{-1}. A blank experiment was also carried out without the addition of a catalyst.

4.2.3 OER experiments

OER experiments were performed in the same watercooled, quartz-glass reactor already described in Section 4.2.2. Fig. 4.2b shows a schematic representation of the design. In contrast to the UV-HER experiments illumination was performed from the side instead of the top and also the detection of oxygen wasn't performed in flow, but through an oxygen sensor, which recorded the O_2-concentration above the catalyst dispersion. As a light source the same UV-LED lamp with a wavelength of 365 nm ± 20 nm as in the UV-HER experiments was used. The utilized detector was a needle-type, optical oxygen sensor (FireSting Pro from *pyroscience*).

For a typical measurement 1 mg of catalyst was dispered in 2 mL of a 0.01 mol L^{-1} $AgNO_3$ solution. Silver nitrate was used as a sacrificial agent. The reactor was filled with the suspension and sealed tightly using a septum, through which the detector needle could be pierced. The gas space above the dispersion, where the sensor measured the oxygen content was shielded from the lamp using black tape, to minimize any interactions between the UV light and the sensor. When the reactor was set up, the gas space was flushed with Ar using two needles, until the measured O_2 signal was minimized, and then the flushing needles were removed. After another few minutes, where it was confirmed that the baseline didn't increase indicating that the reactor was sealed, the stable baseline was recorded for 30 min. Then the UV lamp was turned on for 30 min during which the O_2 concentration started to increase. Afterwards the lamp was switched off and the signal was recorded for another 30 min to confirm that the O_2 concentration stayed stable without any illumination. The detector signal was calibrated using a known amount of oxygen which was inserted into the reactor. This resulted in Eq. (4.2) which was used to convert the detector concentration to the amount of produced oxygen.

$$c[\mu mol] = c[\%] * x[\frac{\mu mol}{\%}] \tag{4.2}$$

Die approbierte gedruckte Originalversion dieser Diplomarbeit ist an der TU Wien Bibliothek verfügbar
The approved original version of this thesis is available in print at TU Wien Bibliothek.
TU Bibliothek Your knowledge hub WIEN

The recorded concentrations were transformed to an O_2 evolution rate by derivation of the recorded graph. To further confirm that the O_2 was produced by the catalyst, a blank experiment was performed without the addition of any sample.

Die approbierte gedruckte Originalversion dieser Diplomarbeit ist an der TU Wien Bibliothek verfügbar
The approved original version of this thesis is available in print at TU Wien Bibliothek.
TU WIEN Bibliothek Your knowledge hub

Results and Discussion

5.1 Precursor Characterization

Before synthesizing the samples, the precursors were analysed with TGA to investigate their degradation behaviour. The precursors were first heated to 100 °C until constant weight to remove any adsorbed water. Afterwards, they were heated up to 800 °C at a constant heating rate. The plots and relative weight losses can be seen in Fig. 5.1.

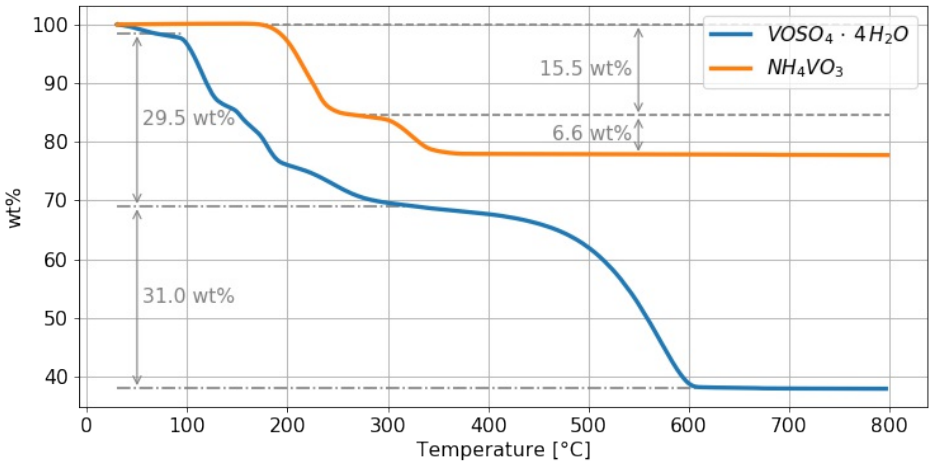

Figure 5.1: TGA plots for the precursors NH_4VO_3 and $VOSO_4 \cdot 4\,H_2O$ with the relative weight losses for each major degradation step.

NH_4VO_3 didn't have any physically adsorbed water nor chemically bound crystal water and had two onset temperatures of 190 °C and 305 °C with a total relative weight loss of 22.1 wt%. This weight loss would fit best with a degradation to V_2O_5 since this would result in a theoretical loss of 22.3 wt%, which is very close to the actual value. All other stable oxides of V would have resulted in a bigger relative weight reduction. This precursor also showed an intermediate degradation step that started around 200 °C with a mass loss of 15.5 wt%. Brown and Stewart measured a similar degradation and assigned it to the formation of $NH_4V_3O_8$ which would have had a theoretical weight loss of 14.8 wt% [68].

$VOSO_4 \cdot 4\,H_2O$ seemed to have adsorbed water in addition to the four crystal water molecules which evaporated while heating up to 100 °C. While heating up further, four degradation steps can be observed where each step could correspond to the evaporation of one unit of crystal water. Between approx. 450 °C to 600 °C the final degradation step appeared which resulted in a total weight loss of 59.5 wt%. When comparing this value with the theoretical weight losses for VO, V_2O_3, VO_2, V_6O_{13} or V_2O_5 the observed value is again closest to the degradation to V_2O_5 which would result in an expected weight reduction by 61.3 wt%. The difference between the

Die approbierte gedruckte Originalversion dieser Diplomarbeit ist an der TU Wien Bibliothek verfügbar
The approved original version of this thesis is available in print at TU Wien Bibliothek.
TU Bibliothek Your knowledge hub WIEN

theoretical and the observed value could come from inaccuracies from the scale of the machine or from inaccuracies at determining the starting and stopping values for the weight loss.

Since each precursor appeared to have at least two distinct steps during degradation, two calcination temperatures were chosen for each one. The temperatures for NH_4VO_3 were 250 °C and 350 °C and for $VOSO_4 \cdot 4\,H_2O$ 350 °C and 600 °C. The higher calcination temperature for each precursor leads to the formation of V_2O_5.

5.2 Catalyst characterization

Catalysts with different concentrations of V were produced during this project. Starting with 25 at% and then reducing the concentration to 5 at% and finally to 1 at% of V in the sample, shifting the role of the V-species from acting as a light absorber to acting as a co-catalyst. The 1 %-samples were produced with $VOSO_4$ and NH_4VO_3 as precursors, however, due to the lower solubility of NH_4VO_3 in water, the higher percentage samples were only synthesized with $VOSO_4$. The following section will first present the results obtained from compositional analysis of all samples. Afterwards, microscopic, structural and optical analysis of the catalysts are presented for each V-concentration separately, starting with the samples with higher loadings, because not all characterization methods were performed for all samples and it allowed for better comparison of the samples in the following discussion.

5.2.1 Composition analysis

5.2.1.1 TXRF

TXRF analysis was performed to measure the actual concentrations of V on the catalysts and analyse the influence of the different synthesis techniques, namely the evaporation and filtration synthesis. For the 1 %-samples with NH_4VO_3 as the precursor the two samples calcined at the highest temperature of 350 °C, $Ti\,[1\%/350]_F^N$ and $Ti\,[1\%/350]_E^N$, were compared. For the samples with $VOSO_4$ as the precursor, the 1 % uncalcined samples were analysed in addition to the ones calcined at 600 °C ($Ti\,[1\%/RT]_F^S$, $Ti\,[1\%/600]_F^S$, $Ti\,[1\%/RT]_E^S$, $Ti\,[1\%/600]_E^S$). Two calcined samples with higher concentrations were analysed as well ($Ti\,[5\%/600]_E^S$, $Ti\,[25\%/600]_E^S$). The results can be seen in Table 5.1.

Due to their similarity in electron configuration (V has only one d electron more than Ti), the X-ray transition energies of Ti and V are close to each other (see Table 5.2). This lead to the overlapping of the $K\beta_1$ peak of Ti with the $K\alpha_1$ peak of V which is why the lower intensity V $K\beta_1$ peak had to be used for quantification, which makes the method less accurate at determining the exact concentrations. Unfortunately, a lot of methods for quantifying elements are based on element-specific X-ray radiation, where the signals of Ti and V are difficult to separate. The TXRF spectra are shown in the Appendix (see Section 9.5).

The results suggest that most of the added V precursor amounts stayed on the sample and the measured concentrations of V fit well with the nominal amounts. Additionally, there seems to be only a very small difference between the two different synthesis routes (evaporation vs. filtration)

Die approbierte gedruckte Originalversion dieser Diplomarbeit ist an der TU Wien Bibliothek verfügbar
The approved original version of this thesis is available in print at TU Wien Bibliothek.
TU Bibliothek Your knowledge hub WIEN

Table 5.1: Vanadium contents according to TXRF results. The mean error of the method is 10 %.

Sample	Measured amount [at%]	Nominal amount [at%]
$Ti\,[1\%/350]_F^N$	0.95	1
$Ti\,[1\%/350]_E^N$	0.98	1
$Ti\,[1\%/RT]_F^S$	0.92	1
$Ti\,[1\%/600]_F^S$	0.98	1
$Ti\,[1\%/RT]_E^S$	1.07	1
$Ti\,[1\%/600]_E^S$	1.25	1
$Ti\,[5\%/600]_E^S$	5.86	5
$Ti\,[25\%/600]_E^S$	26.03	25

Table 5.2: X-ray transition energies of Ti and V.

Spectral line	Energy keV
Ti $K\alpha_1$	4.512
Ti $K\beta_1$	4.933
V $K\alpha_1$	4.953
V $K\beta_1$	5.428

for both precursors. The filtration samples $Ti\,[1\%/350]_F^N$, $Ti\,[1\%/RT]_F^S$ and $Ti\,[1\%/600]_F^S$ have a slightly lower amount of V as their evaporation counterparts, $Ti\,[1\%/350]_E^N$, $Ti\,[1\%/RT]_E^S$ and $Ti\,[1\%/600]_E^S$ respectively. This means that both of the dissolved precursors had a high affinity to the anatase particles and adsorbed well on the surface, so that they weren't significantly removed during the washing process in the filtration route.

5.2.2 25 at%-samples

5.2.2.1 SEM - 25 at%

SEM images were recorded to study the shape of the catalyst particles after the synthesis. As a reference for the initial shape of the particles, the pure anatase powder was also analysed (see Fig. 5.2).

The images show that although the size of individual particles lies in the range of tens of nm together they form larger agglomerates.

Fig. 5.3 shows the recorded SEM images of the 25 %-samples calcined at two different temperatures, $Ti\,[25\%/350]_E^S$ and $Ti\,[25\%/600]_E^S$.

Die approbierte gedruckte Originalversion dieser Diplomarbeit ist an der TU Wien Bibliothek verfügbar
The approved original version of this thesis is available in print at TU Wien Bibliothek.
TU Bibliothek Your knowledge hub WIEN

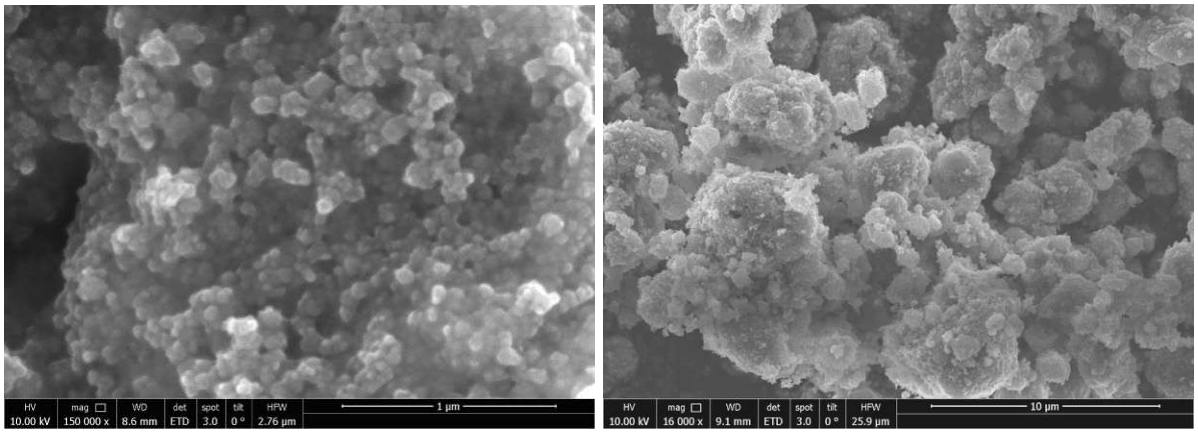

(a): Anatase nanoparticles, magn. x150 000 **(b):** Anatase nanoparticles, magn. x16 000

Figure 5.2: Reference SEM images of unmodified anatase nanoparticles that were used for the synthesis of the catalysts.

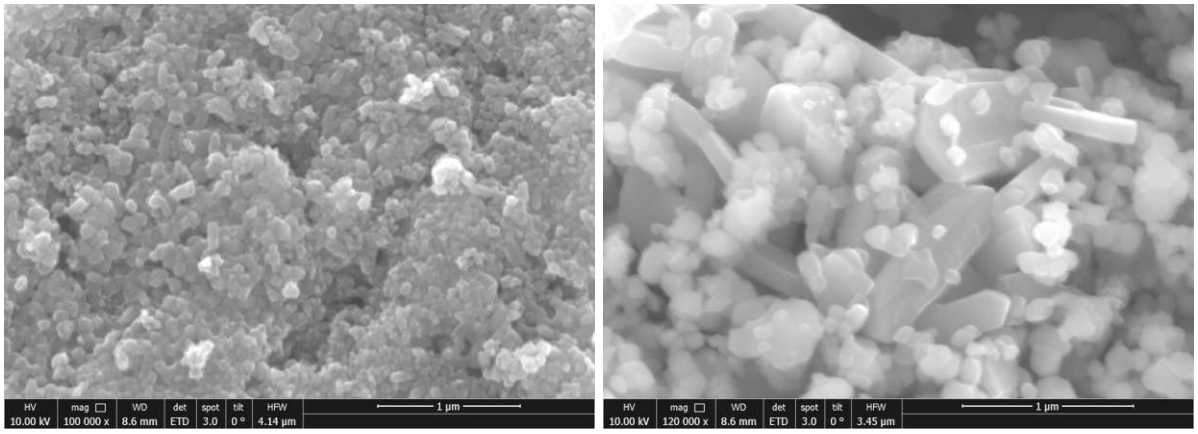

(a): $Ti\,[25\%/350]_E^S$, magn. x100 000 **(b):** $Ti\,[25\%/600]_E^S$, magn. x120 000

Figure 5.3: SEM images for the calcined 25 %-samples. (a) shows the sample after the medium calcination at 350 °C, where cylindrical particles, likely belonging to the undecomposed precursor $VOSO_4$, can be seen. (b) shows the sample after the high calcination at 600 °C. Bigger plate-like particles, most likely belonging to V_2O_5, can be seen in the image.

Sample $Ti\,[25\%/350]_E^S$ in Fig. 5.3a shows rod-like, cylindrical particles that aren't visible in the anatase powder in addition to the round particles that can be seen in the anatase reference measurement. Fig. 5.3b of sample $Ti\,[25\%/600]_E^S$ shows some plate-like, bigger particles in addition to the smaller anatase particles.

TGA of the precursors (see Fig. 5.1) revealed that $VOSO_4 \cdot 4\,H_2O$ loses crystal water during the heat treatment at 350 °C and decomposes to V_2O_5 when the calcination temperature is increased to 600 °C. This suggests that the cylindrical particles from $Ti\,[25\%/350]_E^S$ (Fig. 5.3a) consist of the precursor $VOSO_4$ after removal of the crystal water while the bigger, plate-like particles in $Ti\,[25\%/600]_E^S$ (Fig. 5.3b) are crystalline V_2O_5.

In addition to the newly formed crystals, the SEM images revealed that the anatase particles increased in size after the calcination at 600 °C. At 350 °C no significant difference could be detected. This could be either because of a layer of V-species covering part of the particles or because of particle sintering during the heat treatment. The bigger size also leads to a smaller

Die approbierte gedruckte Originalversion dieser Diplomarbeit ist an der TU Wien Bibliothek verfügbar
The approved original version of this thesis is available in print at TU Wien Bibliothek.
TU Bibliothek Your knowledge hub WIEN

active surface area, which is typically detrimental to the catalytic activity. No increase was visible after the calcination at 350 °C.

Some additional SEM images that were recorded can be seen in the Appendix in Section 9.2.

5.2.2.2 TEM - 25 at%

To further investigate the structure of the synthesized catalysts, TEM images were recorded. The analysed 25 %-samples showed lattice fringes which can be seen in Fig. 5.4 to 5.6. The observed lattice spacings with the assigned phase and crystal plane are listed in Table 5.3.

Table 5.3: Lattice spacings observed in the TEM images of 25 %-samples and the associated phase and crystal plane. All powder diffraction files from [69]

Observed lattice spacing [nm]	Phase & Crystal plane
0.35	Anatase (101) [a]
0.63	$VOSO_4$ (010) [b]
0.43	V_2O_5 (010) [c]
0.59	V_2O_5 (200) [c]

[a] PDF 04-007-0701
[b] PDF 04-008-1941
[c] PDF 04-012-3680

The uncalcined sample $Ti\,[25\%/RT]_E^S$ (Fig. 5.4) as well as the sample calcined at the medium temperature of 350 °C, $Ti\,[25\%/350]_E^S$ (Fig. 5.5), show anatase particles with a layer of an amorphous material covering the surface. Additionally, particles with distinct lattice spacings

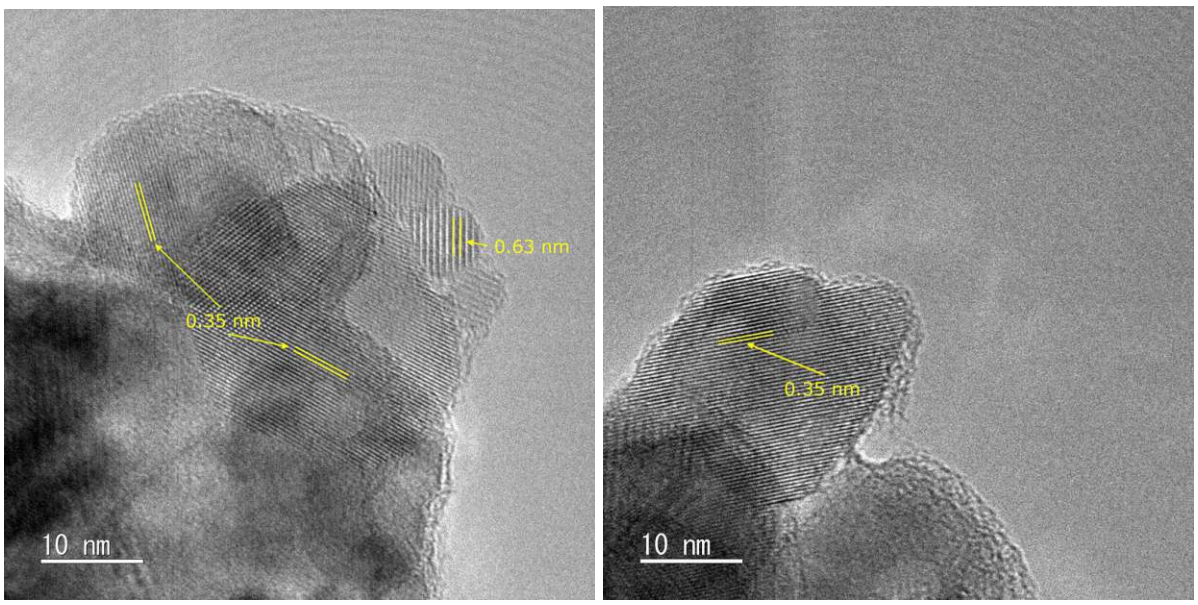

(a): $Ti\,[25\%/RT]_E^S$ **(b):** $Ti\,[25\%/RT]_E^S$

Figure 5.4: TEM images of the uncalcined 25 %-sample $Ti\,[25\%/RT]_E^S$. (a) An amorphous layer and individual particles of precursor are visible. (b) An amorphous layer covering the anatase particles.

Die approbierte gedruckte Originalversion dieser Diplomarbeit ist an der TU Wien Bibliothek verfügbar
The approved original version of this thesis is available in print at TU Wien Bibliothek.
TU Bibliothek Your knowledge hub WIEN

form anatase appear in the TEM images of the uncalcined sample. Both the layer and the new particles presumably consist of the precursor $VOSO_4$.

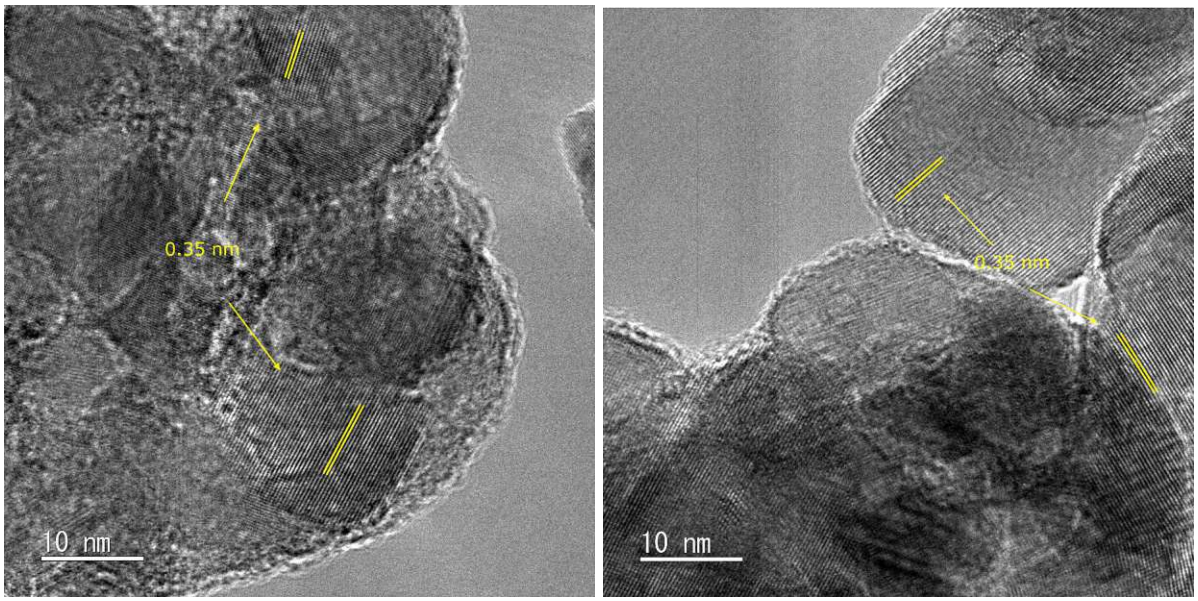

(a): $Ti\,[25\%/350]_E^S$ **(b):** $Ti\,[25\%/350]_E^S$

Figure 5.5: TEM images of the medium calcined 25 %-sample $Ti\,[25\%/350]_E^S$. Both images (a) and (b) show an amorphous layer of the precursor covering the anatase particles.

After the calcination at 600 °C, the layer covering the anatase particles is not visible anymore and large crystals of a new material are visible (Fig. 5.6). From the observed lattice spacings and the precursor characterization, the new material consists of V_2O_5. These particles were

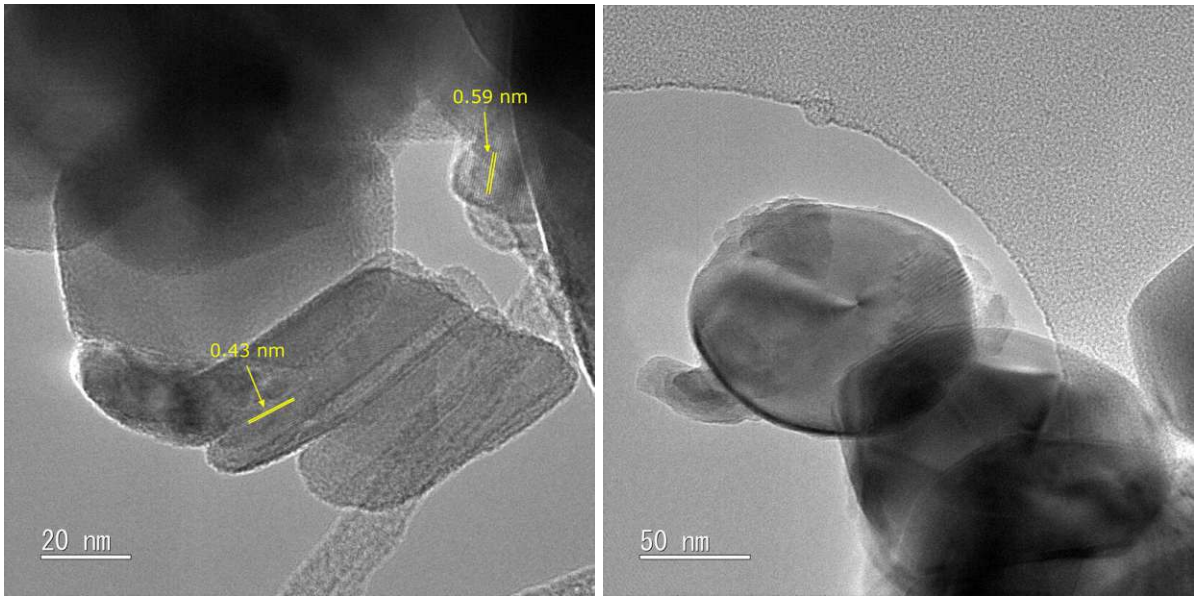

(a): $Ti\,[25\%/600]_E^S$ **(b):** $Ti\,[25\%/600]_E^S$

Figure 5.6: TEM images of the calcined 25 %-sample $Ti\,[25\%/600]_E^S$. (a) Large crystals of V_2O_5 are visible after the calcination. (b) Another view of newly formed particles after the calcination.

already observed in SEM analysis which can be seen in Fig. 5.3.

Die approbierte gedruckte Originalversion dieser Diplomarbeit ist an der TU Wien Bibliothek verfügbar
The approved original version of this thesis is available in print at TU Wien Bibliothek.
TU Bibliothek Your knowledge hub WIEN

In conclusion, the TEM analysis of the 25 % samples revealed that the precursor formed a layer on top of the TiO_2 before calcination, which then disappeared during the calcination at 600 °C to form particles of V_2O_5 attached to the anatase surface. More TEM images for the samples shown above can be seen in the Appendix in Section 9.3.

5.2.2.3 XPS - 25 at%

XPS spectra were recorded to analyze the chemical state of the near surface elements. The binding energy plots of anatase and the calcined 25 %-sample $Ti\,[25\%/600]_E^S$ can be seen in Fig. 5.7. The sample $Ti\,[25\%/350]_E^S$ was also measured with XPS, however, due to strong charging of the sample, no information about the chemical state of the analysed elements could be extracted (see Appendix Fig. 9.21).

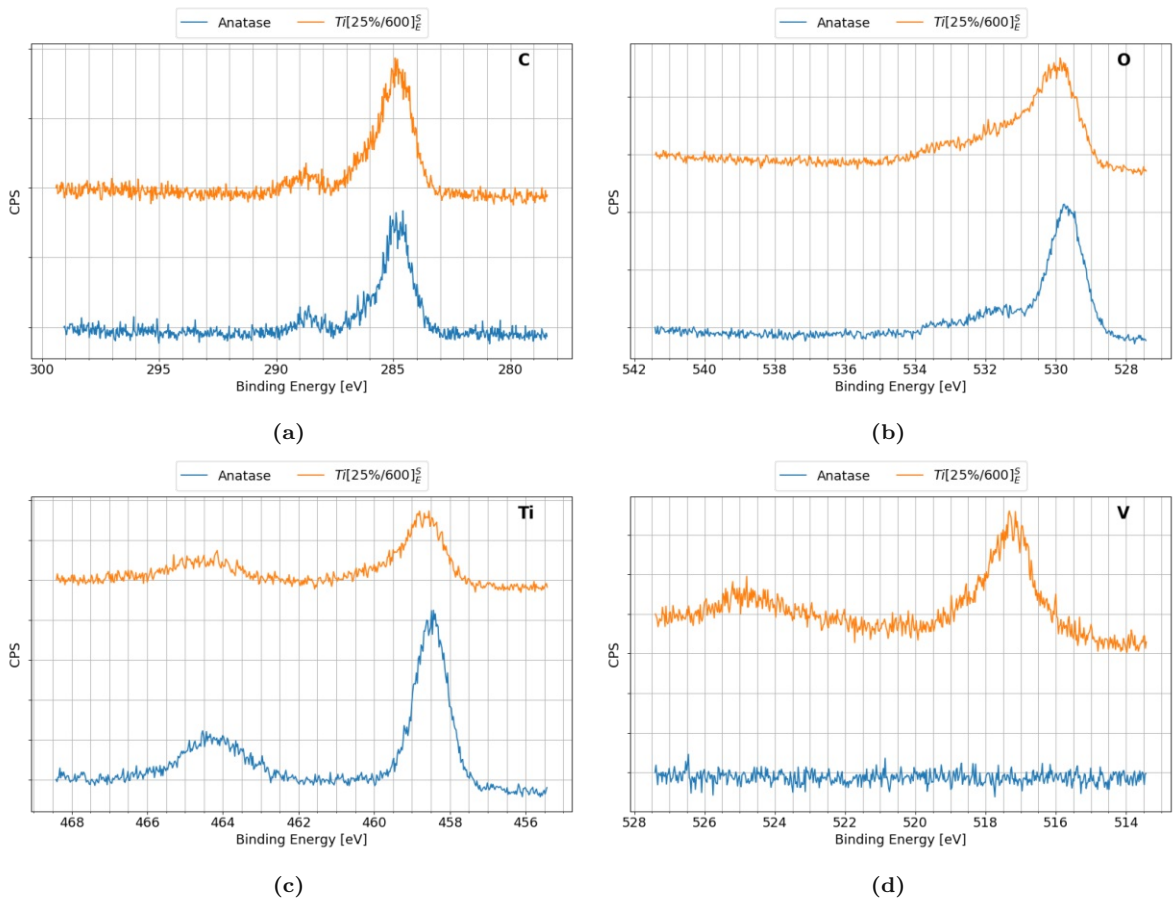

Figure 5.7: XPS spetra of anatase (blue) and $Ti\,[25\%/600]_E^S$ (orange) core levels. (a) shows the binding energy region for carbon (C 1s), (b) for oxygen (O 1s), (c) for titanium (Ti 2p) and (d) for vanadium (V 2p).

Fig. 5.7a shows the binding energy region for carbon (C 1s) which shows the typical C 1s peak from adventitious carbon. This signal usually appears on all samples, because carbon sources from the atmosphere can attach to the surface while handling the sample during sample preparation [70]. The carbon signal was used to calibrate the energy levels and was set to 284.80 eV.

Die approbierte gedruckte Originalversion dieser Diplomarbeit ist an der TU Wien Bibliothek verfügbar
The approved original version of this thesis is available in print at TU Wien Bibliothek.

The binding region for oxygen (O 1s) can be seen in Fig. 5.7b. Both spectra show a peak at about 530 eV which belongs to the metal oxide and an additional shoulder at higher binding energies, belonging to other oxygen species like hydroxyl groups, water or organics [71, 72]. For both TiO_2 and V_2O_5, the metal oxide peak appears at the same binding energy [73, 74].

The titanium (Ti 2p) spectra in Fig. 5.7c show two peaks at approx. 458.7 eV and 464.4 eV belonging to Ti^{+4} $2p_{3/2}$ and Ti^{+4} $2p_{1/2}$ respectively [73]. The addition of the V-precursor led to a reduction in the intensity of the Ti signal, compared to the pure anatase, due to the lower Ti-content in the sample.

Vanadium (V 2p) spectra are shown in Fig. 5.7d. While the pure anatase didn't show any V, sample $Ti\,[25\%/600]_E^S$ shows a peak at 517.3 eV which can be assigned to V^{+5} $2p_{3/2}$ and another peak at 524.7 eV which belongs to V^{+5} $2p_{1/2}$ [45, 73, 75]. No V^{+4}, which would have a binding energy of approx. 516 eV [75], could be detected, which would mean that the whole precursor was calcined and oxidised to form V_2O_5 with an oxidation number of +5. However, since the V^{+5} peak overlaps with the region for V^{+4} it cannot be excluded that a small amount of V^{+4} still remains, especially since the V could be reduced under the vacuum of the XPS conditions [76].

The binding energy region for sulphur (S 2p) was also recorded but no signal could be detected for anatase and sample $Ti\,[25\%/600]_E^S$, which was calcined at the higher temperature. Only $Ti\,[25\%/350]_E^S$ (calcined at medium temperature) showed some remaining sulphur in the sample, but due to strong charging of the sample, the exact sulphur species or oxidation state could not be determined (see Appendix Fig. 9.21e). The TGA results suggested that the calcination at 350 °C only removed crystal water from the original $VOSO_4 \cdot 4\,H_2O$ and didn't lead to the complete degradation, so the appearance of sulphur in this sample fits well with this result. The absence of sulphur from the sample calcined at the higher temperature $Ti\,[25\%/600]_E^S$ is another sign for the complete degradation of the precursor and the formation of the fully oxidised species V_2O_5.

The XPS analysis of the two calcined samples ($Ti\,[25\%/350]_E^S$ and $Ti\,[25\%/600]_E^S$) suggests that the precursor was decomposed fully only after the calcination at 600 °C. For this sample ($Ti\,[25\%/600]_E^S$) the prevailing oxidation state of V was V^{+5}, which matches V_2O_5.

5.2.2.4 Powder XRD - 25 at%

To analyse the phase composition in the prepared catalysts, powder XRD was performed for the calcined catalysts as well as the pure anatase powder for reference. Fig. 5.8 shows the recorded diffractograms.

In Fig. 5.8a the anatase powder calcined at 600 °C shows a very small rutile (PDF 04-008-7645) peak at 27.5° (rutile peaks labelled 'R' and anatase peaks labelled 'A'), indicating that the pure powder partially transforms to the thermodynamically stable rutile phase during the calcination [69, 77]. This sample also shows much sharper peaks than the uncalcined powder which is a sign for the growth of the crystallites during the temperature treatment [78].

Die approbierte gedruckte Originalversion dieser Diplomarbeit ist an der TU Wien Bibliothek verfügbar
The approved original version of this thesis is available in print at TU Wien Bibliothek.
TU Bibliothek Your knowledge hub WIEN

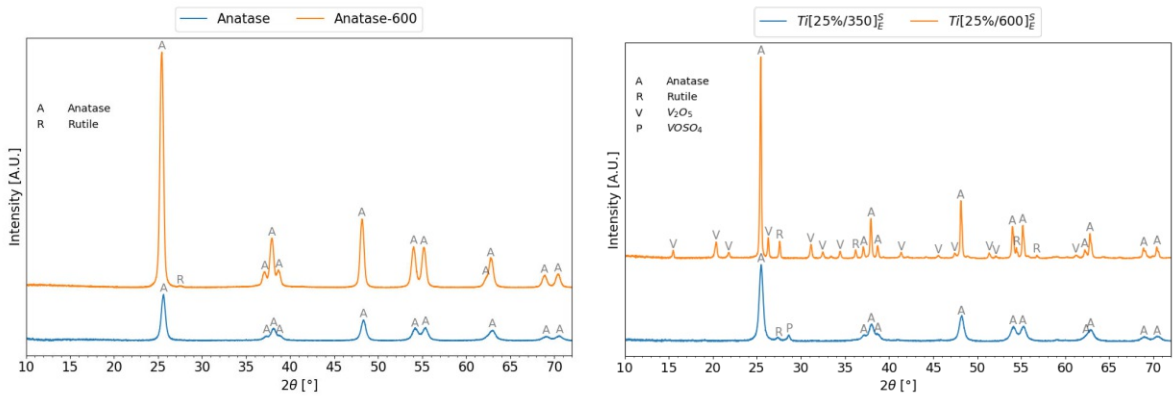

(a): XRD diffractograms of pure anatase powder as well as anatase calcined at 600 °C for 1 h.

(b): XRD diffractograms of the 25 %-samples $Ti\,[25\%/350]_E^S$ and $Ti\,[25\%/600]_E^S$.

Figure 5.8: Powder X-ray diffraction spectra of anatase and the 25 %-samples. Peaks are marked with the corresponding crystal phase.

The 25 %-samples show new peaks at both calcination temperatures. The medium calcined sample $Ti\,[25\%/350]_E^S$ shows two additional peaks at 27.4° and 28.6°, which were assigned to rutile and the crystal-water-free precursor $VOSO_4$ (labelled 'P' in Fig. 5.8b) (PDF 04-008-1941) respectively [69].

After the calcination at 600 °C a lot of new peaks appear which were assigned to fully oxidised V_2O_5 (labelled 'V' in Fig. 5.8b) (PDF 04-012-3680 [69]). Additionally, more rutile peaks appear and at a higher intensity compared to the sample calcined at 350 °C and also to the pure Ana-600 sample, which indicates that the presence of the V species facilitates the phase transformation to rutile. It is known in literature that the addition of foreign ions, such as V-dopants or even the addition of V_2O_5, can lead to the transformation of anatase to rutile, thereby changing the required phase transition temperature [79–82].

To summarize, V_2O_5 could be detected with XRD in the sample calcined at 600 °C ($Ti\,[25\%/600]_E^S$) but not in the sample calcined at 350 °C ($Ti\,[25\%/350]_E^S$). The addition of V also led to an increase in the amount of rutile which formed during the calcination.

5.2.2.5 ATR-FTIR - 25 at%

Fig. 5.9 shows an overview and a cut-out of the low-wavenumber region for the ATR-FTIR spectra recorded of the 25 % calcined catalyst sample $Ti\,[25\%/600]_E^S$ and the physical mixture of the individually calcined powders $PM[25\%/600]^S$. For reference, the spectra of anatase powder and the pure precursor, both calcined at 600 °C, as well as V_2O_5 are also shown. The spectra of V_2O_5 and the calcined precursor show almost no difference which is another sign that the precursor was decomposed to V_2O_5 during the calcination at 600 °C.

The anatase spectrum only shows absorption below approx. 900 cm^{-1} which belong to Ti−O−Ti stretching vibrations from the Ti−O network [83, 84]. Similarly, the references V_2O_5 and $VOSO_4$-600 also show strong absorptions in the same region (in particular the large peak at 812 cm^{-1} in Fig. 5.9b) belonging to analogous V−O−V stretching and bending vibrations in the V_2O_5 structure [85, 86]. These spectra show another broad peak at 1010 cm^{-1} with a small

Die approbierte gedruckte Originalversion dieser Diplomarbeit ist an der TU Wien Bibliothek verfügbar
The approved original version of this thesis is available in print at TU Wien Bibliothek.
TU Bibliothek Your knowledge hub WIEN

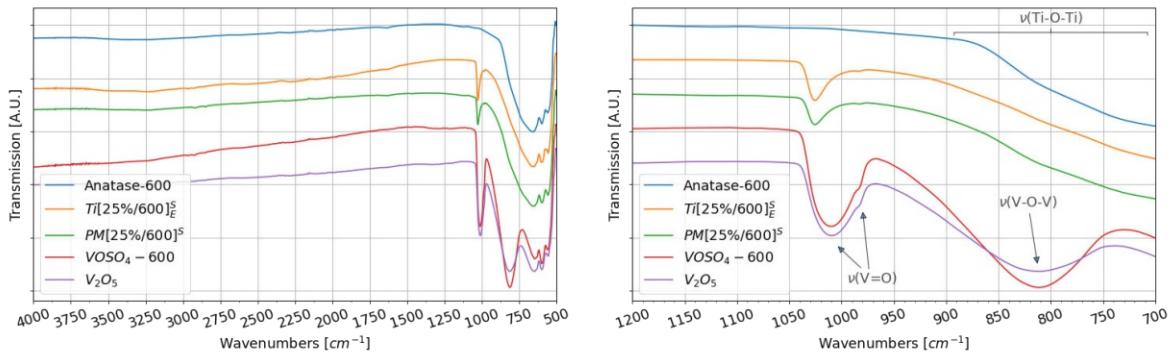

(a): Overview

(b): Low-wavenumver region

Figure 5.9: FTIR spectra for the 25 %-sample $Ti\,[25\%/600]_E^S$ as well as the physical mixture with 25 at% of V $PM[25\%/600]^S$ and reference samples, all calcined at 600 °C.

shoulder at 983 cm^{-1}. Both peaks can be assigned to stretching vibrations of V=O double bonds (terminal O bound to V in the bulk V_2O_5 structure) [85, 87, 88].

The sample $Ti\,[25\%/600]_E^S$ shows the same peak at 983 cm^{-1}, however, the other peak appears narrowed and the maximum now lies at 1026 cm^{-1}. The higher wavenumber could be assigned to surface V=O which has been reported to have an absorption approx. 10 cm^{-1} higher than the absorption for crystalline V_2O_5 [89, 90]. The higher amount of surface V=O could be a sign of smaller crystallites, which have a higher surface fraction per volume, or of the presence of polymeric vanadia species spread out on the anatase surface [91]. However, the peak also appears shifted in the physical mixture sample $PM[25\%/600]^S$, where the same crystals as in the calcined precursor $VOSO_4$-600 are present. This means that a structural difference is unlikely and the shift is probably caused by the difference in concentration and the presence of TiO_2 with the V_2O_5 crystals.

It was not possible to detect absorption peaks for a potential Ti−O−V bond since this peak would be expected somewhere below 900 cm^{-1} where it overlaps strongly with the Ti−O−Ti peak of the anatase phase [83]. The samples $Ti\,[25\%/600]_E^S$ and $PM[25\%/600]^S$ show a slight shoulder at 815 cm^{-1} but this shoulder can also be seen in anatase, as part of the Ti−O−Ti peaks and also in V_2O_5 from the V−O−V peak at 812 cm^{-1}.

In conclusion, the IR analysis further confirms the presence of V_2O_5 on the surface of anatase.

5.2.2.6 Raman Spectroscopy - 25 at%

In addition to FTIR spectra, Raman spectra were also recorded to identify and characterize the vanadium species present on the TiO_2 surface. Fig. 5.10 shows the recorded spectra of the 25 %-samples and the ones of pure anatase as well as V_2O_5. Anatase has six Raman active modes ($A_{1g} + 2B_{1g} + 3E_g$) which appear in five bands listed in Table 5.4 (see Fig. 5.10a).

The spectrum for pure anatase was only recorded up to 1000 cm^{-1} because it doesn't show any bands above that value.

Die approbierte gedruckte Originalversion dieser Diplomarbeit ist an der TU Wien Bibliothek verfügbar
The approved original version of this thesis is available in print at TU Wien Bibliothek.
TU Bibliothek Your knowledge hub WIEN

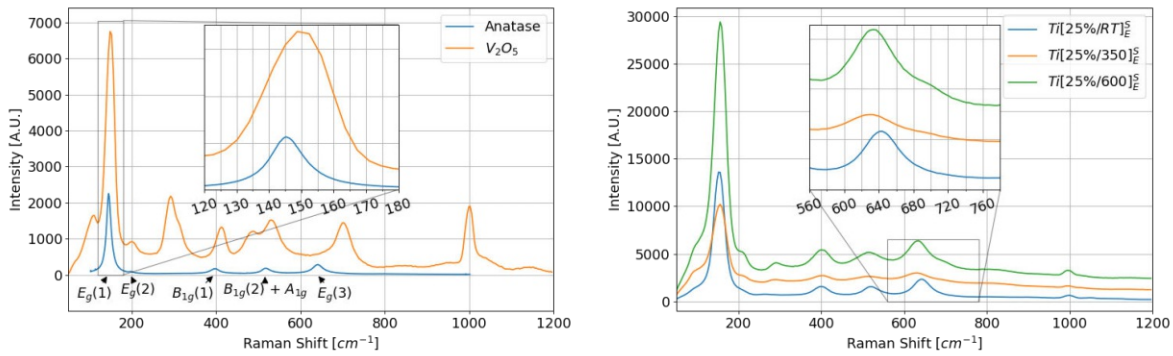

(a): References anatase and V_2O_5

(b): Samples $Ti\,[25\%/RT]_E^S$, $Ti\,[25\%/350]_E^S$ and $Ti\,[25\%/600]_E^S$

Figure 5.10: Raman spectra of the reference and 25 %-samples. The high calcined sample $Ti\,[25\%/600]_E^S$ shows bands belonging to crystalline V_2O_5.

Fig. 5.10b shows the Raman spectra of the catalyst samples containing 25 at% V. The sample calcined at high temperature $Ti\,[25\%/600]_E^S$ shows additional bands at 290 cm^{-1}, 704 cm^{-1} and 995 cm^{-1}. The absorption at 995 cm^{-1} is also clearly visible in the V_2O_5 reference and it can be assigned to the stretching mode of terminal V=O [94]. The band at 704 cm^{-1} is also observed in pure V_2O_5 and according to Julien et al. it can be assigned to a stretching mode of bridging oxygen in O−V−O in V_2O_5. The band at 290 cm^{-1} can be assigned to the bending mode of V−O bonds [94]. This band seems to also appear in the sample calcined at medium temperature $Ti\,[25\%/350]_E^S$, which would indicate that part of the $VOSO_4$ could have already formed some vanadium oxide, which contains V−O bonds. The uncalcined sample shows two additional bands at 270 cm^{-1} and 998 cm^{-1} which belong to the precursor $VOSO_4$.

Fig. 5.11 shows the center positions as well as the FWHM (full width at half maximum) of the $E_g(1)$ bands of each spectrum. Both values increase significantly with the addition of the V-species and then only change slightly during the calcination.

A blue shift of the anatase peak is often associated with a reduction in crystal size [95, 96], however since the biggest part of the peak shift already happens for the uncalcined sample and XRD and TEM results suggested that the anatase crystals grew during the calcination this effect

Table 5.4: The active Raman modes for anatase and the associated Raman shifts [92, 93].

Mode	Raman shift [cm^{-1}]
$E_g(1)$	145
$E_g(2)$	198
$B_{1g}(1)$	397
$B_{1g}(2) + A_{1g}$*	517
$E_g(3)$	641

* not resolvable at room temperature

Die approbierte gedruckte Originalversion dieser Diplomarbeit ist an der TU Wien Bibliothek verfügbar
The approved original version of this thesis is available in print at TU Wien Bibliothek.

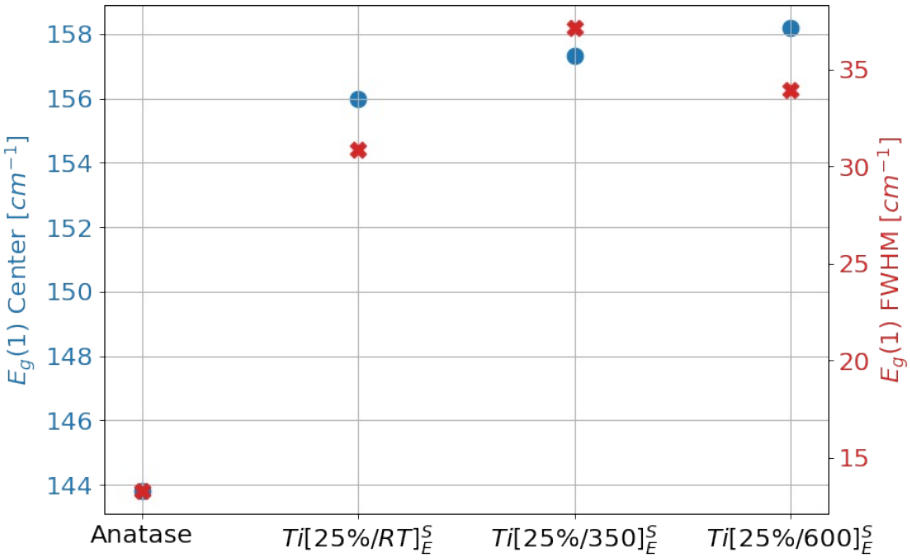

Figure 5.11: Center position and FWHM of the $E_g(1)$ band of the 25 %-samples and anatase as a reference. Both increased a lot upon addition of the V precursor and then increased slightly during calcination.

probably doesn't affect the $E_g(1)$ band position. Another explanation could be that the addition of the V species applied an elastic strain to the TiO_2 surface, which caused the reduction in the band position [97, 98]. However, it is also possible that the blue shift is caused by the formation of defects like doping of the TiO_2 lattice with V ions [99] or O-vacancies [100]. The latter effect has also been associated with an increase in the FWHM of the $E_g(1)$ band of TiO_2 [100, 101].

Considering the similarity of the additional bands from the high calcined 25 %-sample $Ti\,[25\%/600]_E^S$ and the pure V_2O_5 the Raman results indicate that it consists at least partly of crystalline V_2O_5. No bands belonging to the rutile phase could be observed, although they were detected in the XRD analysis. The blue shift and increasing FWHM of the anatase $E_g(1)$ band also fit well with the addition of surface species onto the anatase particles resulting in a close interaction between V_2O_5 and TiO_2. The Raman results also agree well with the IR analysis of sample $Ti\,[25\%/600]_E^S$. Both methods show an absorption for bridging V−O as well as terminal V=O which are both present in the V_2O_5 structure.

5.2.2.7 DRS - 25 at%

To study the optoelectronic properties of the synthesized samples diffuse reflectance spectra were recorded. The DRS of a semiconductor nanopowder can be used to construct the Tauc-plot, from which the bandgap of the material can be determined [102, 103]. The construction of the Tauc-plot is different for direct vs. indirect semiconductors and depends on their absorption coefficient α ($[\alpha E]^2$ *vs.* E for direct SC; $[\alpha E]^{\frac{1}{2}}$ *vs.* E for indirect SC). This difference cannot be used to distinguish between direct and indirect semiconductors but since anatase and V_2O_5 both have an indirect bandgap transition, the plots will be constructed for indirect semiconductors [44, 104].

Die approbierte gedruckte Originalversion dieser Diplomarbeit ist an der TU Wien Bibliothek verfügbar
The approved original version of this thesis is available in print at TU Wien Bibliothek.
TU Bibliothek Your knowledge hub WIEN

The absorption coefficient of the powder samples can be calculated from the reflectance spectra with the Kubelka-Munk formula [102, 105]:

$$F(R_\infty) = \frac{(1 - R_\infty)^2}{2R_\infty} \propto \alpha(E) \tag{5.1}$$

where R_∞ is the diffuse reflectance and F a function proportional to the absorption coefficient $\alpha(E)$. F can be used in good approximation to construct the Tauc-plot.

For an unmodified semiconductor, the bandgap is determined by extending the linear portion of the Tauc plot to the abcissa. This procedure is illustrated in Fig. 5.12a for pure anatase. However, in the case of modified or mixtures of semiconductors which show a significant absorption at sub-bandgap energies, the method has to be adjusted. Makuła et al. have described a procedure how the bandgap can be determined in this case [106]. Here the linear part of the Tauc plot has to be extended, only up to an elevated baseline, which can be extrapolated from the absorption at sub-bandgap energies. The analogous process from Fig. 5.12a for a mixture of semiconductors is illustrated in Fig. 5.12b. All samples except for pure anatase, calcined at different temperatures, were evaluated using the latter approach, where a baseline was extended from the linear region below the bandgap.

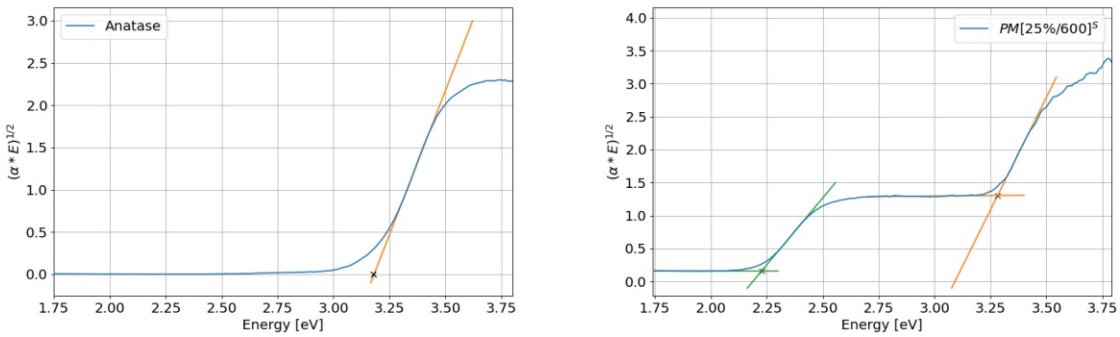

(a): Determination of the bandgap for anatase.

(b): Determination of the bandgaps for the physical mixture $PM[25\%/600]^S$.

Figure 5.12: Illustration of the bandgap analysis for unmodified and modified semiconductors. While the bandgap for pure semiconductors (a) can be determined by extending the linear section of the Tauc plot to the abscissa, the baseline for modified semiconductors (b) has to be extrapolated from the sub-bandgap energy region.

Fig. 5.13 shows the original diffuse reflectance spectra and the calculated Tauc-plots for the 25 %-samples as well as reference spectra of anatase and the pure $VOSO_4$ precursor. The photon energy E was calculated from the wavelength according to Eq. (5.2).

$$E = \frac{hc}{\lambda} \tag{5.2}$$

with h as Planck's constant, c as the speed of light and λ as the wavelength.

The bandgap for the anatase samples determined from the Tauc plot in Fig. 5.13b lies at 3.2 eV which is in accordance with the literature [17, 104, 107].

Die approbierte gedruckte Originalversion dieser Diplomarbeit ist an der TU Wien Bibliothek verfügbar
The approved original version of this thesis is available in print at TU Wien Bibliothek.

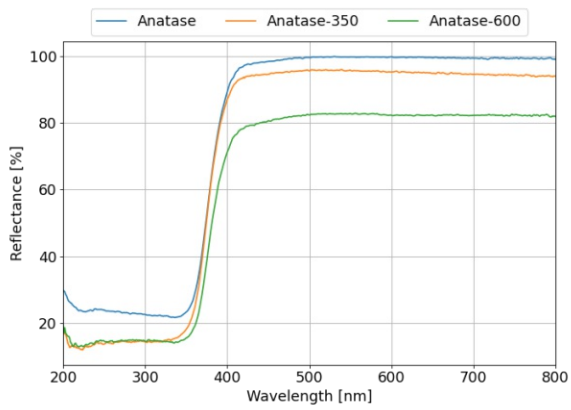

(a): Reflectance: Anatase calcined at different temperatures.

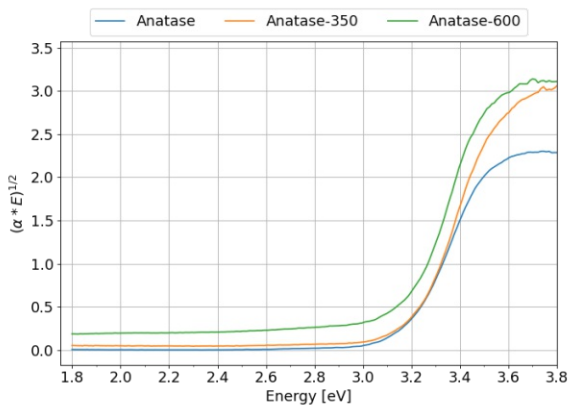

(b): Tauc plot: Anatase calcined at different temperatures.

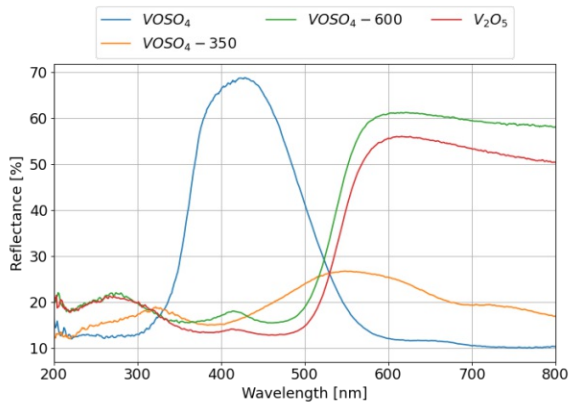

(c): Reflectance: $VOSO_4$ calcined at different temperatures and V_2O_5.

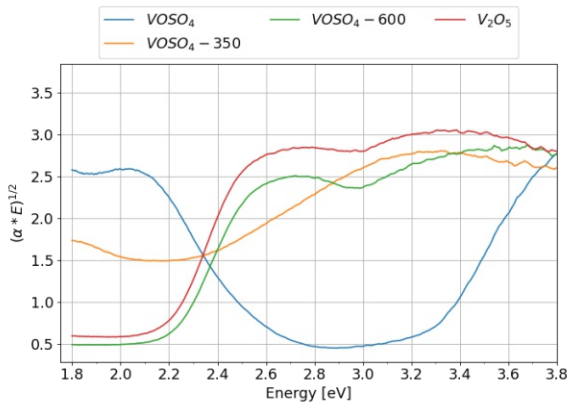

(d): Tauc plot: $VOSO_4$ calcined at different temperatures and V_2O_5.

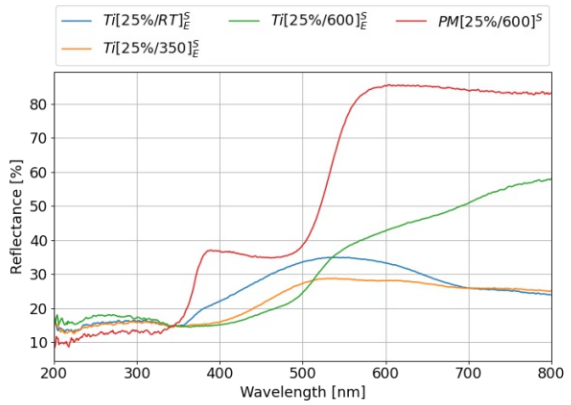

(e): Reflectance: 25 %-samples.

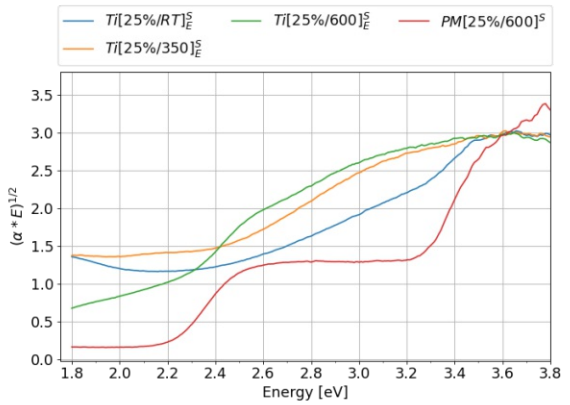

(f): Tauc plot: 25 %-samples.

Figure 5.13: DRS spectra and Tauc-plots respectively for: (a)/(b) anatase, calcined at different temperatures; (c)/(d) pure $VOSO_4$ calcined at different temperatures and V_2O_5; (e)/(f) the 25 %-samples and the physical mixture $PM[25\%/600]^S$.

Fig. 5.13c shows that the precursor calcined at higher temperature $VOSO_4$-600 has a very similar spectrum to commercially purchased V_2O_5 and its Tauc plot (Fig. 5.13d) shows a bandgap that was determined to be at around 2.2 eV. The reported values for V_2O_5 lie between 2.2 eV and 2.4 eV which is reasonably close to the value measured here [44, 47, 108]. Compared to anatase, V_2O_5 absorbs light of higher wavelengths in the visible range starting from just below 600 nm, whereas TiO_2 starts absorbing light only below 400 nm. The uncalcined precursor $VOSO_4$ has a

Die approbierte gedruckte Originalversion dieser Diplomarbeit ist an der TU Wien Bibliothek verfügbar
The approved original version of this thesis is available in print at TU Wien Bibliothek.
TU Bibliothek Your knowledge hub WIEN

strong blue colour due to the very stable vanadyl ion VO^{2+} which shows a strong adsorption in the visible region around 775 nm [109]. Both $VOSO_4$ and $VOSO_4$-350 didn't show any regions in the Tauc plot which could be extrapolated to indicate a bandgap.

The uncalcined as well as medium calcined 25 %-samples $Ti\,[25\%/RT]_E^S$ and $Ti\,[25\%/350]_E^S$ in Fig. 5.13e show a low reflectance at high wavenumbers. This is due to remaining $VOSO_4$ which absorbs strongly around 775 nm as can be seen in Fig. 5.13c. $Ti\,[25\%/600]_E^S$ shows a much increased reflectance at this wavelength which probably means that most of the V was oxidised to V^{+5}. The reflectance spectrum of the physical mixture $PM[25\%/600]^S$ shows a very different spectrum compared to the synthesised samples, which is strong evidence for the formation of heterojunction-based composites in the samples synthesized via the evaporation route. The spectrum shows two big drops in the reflectance at 600 nm and 400 nm which correspond to the absorption edges already seen in V_2O_5 and anatase respectively.

The Tauc plot of $PM[25\%/600]^S$ in Fig. 5.13f also shows two clearly distinct bandgaps at 3.3 eV for anatase and 2.2 eV for V_2O_5. It is unlikely that the bandgap of TiO_2 was actually increased during the synthesis since the addition of a lower bandgap semiconductor or ions typically only leads to a decrease in the bandgap [40, 46, 48, 110]. The apparent increase is more likely caused by the variation from the manual determination of the linear region in the Tauc plot or the difference in the evaluation methods of pure anatase and modified anatase (see Fig. 5.12).

The determination of bandgaps for all of the synthesized samples only yielded a value for the uncalcined sample $Ti\,[25\%/RT]_E^S$ (3.3 eV) and the high temperature calcined sample $Ti\,[25\%/600]_E^S$ (2.3 eV) which correspond to the respective TiO_2 or V_2O_5 components. It is difficult to determine bandgap values for these samples and also the sample calcined at medium temperature $Ti\,[25\%/350]_E^S$, due to the more continuous DRS profiles. To determine a bandgap using the Tauc model, the DRS spectrum needs to show a sharp edge in order to get clear slopes in the Tauc plot. The absence of such an edge in the synthesized samples can be attributed either to low absorption of TiO_2 or a high absorption of V-species.

However, the spectra and Tauc plots of the synthesized samples (especially $Ti\,[25\%/600]_E^S$) stand in clear contrast to the DRS analysis of the physical mixture $PM[25\%/600]^S$. This confirms a closer interaction between the V-species in the synthesized samples, compared to a physical mixture of the two components. The synthesis and calcination probably led to the formation of heterojunctions between V_2O_5 and TiO_2 in the sample $Ti\,[25\%/600]_E^S$, where the vanadium oxide forms surface species on top of anatase.

It needs to be said that the Tauc-plot method of determining the bandgap (Eq. (5.1)) is strictly only valid for samples whose particles are smaller or comparable to the wavelength of the incoming light [102]. These prerequisites aren't necessarily fulfilled by the V_2O_5 particles or the calcined precursors, since their particle size is not precisely known. The size of the anatase particles, however, is in the range of a few nm which is smaller than the wavelength of the incoming light and therefore fulfils the requirements of the Tauc-plot analysis.

Die approbierte gedruckte Originalversion dieser Diplomarbeit ist an der TU Wien Bibliothek verfügbar
The approved original version of this thesis is available in print at TU Wien Bibliothek.
TU Bibliothek Your knowledge hub WIEN

5.2.3 5 at%-samples

5.2.3.1 SEM - 5 at%

To compare the morphology of the 5 %-samples with the 25 %-samples, SEM images were recorded of sample $Ti\,[5\%/600]_E^S$, which can be seen in Fig. 5.14. Both samples were sythesized with $VOSO_4$ as the precursor.

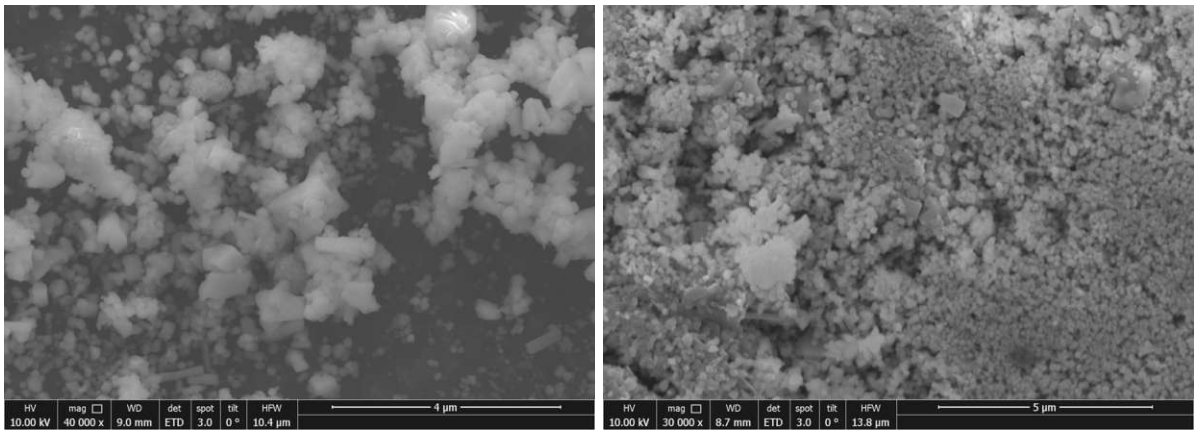

(a): $Ti\,[5\%/600]_E^S$, magn. x40 000 **(b):** $Ti\,[5\%/600]_E^S$, magn. x30 000

Figure 5.14: SEM images for the calcined 5 %-sample $Ti\,[5\%/600]_E^S$.

Similar to the 25 %-samples (see Fig. 5.3) the images show small, round anatase particles as well as bigger particles belonging to V_2O_5. The V_2O_5 shows long and cylindrical particles as well as bigger ones without a defined shape, however, less particles are visible than for the 25 %-sample.

Compared to the uncalcined anatase particles it can also be seen, that the TiO_2 grew due to the calcination treatment at 600 °C.

Die approbierte gedruckte Originalversion dieser Diplomarbeit ist an der TU Wien Bibliothek verfügbar
The approved original version of this thesis is available in print at TU Wien Bibliothek.

5.2.3.2 TEM - 5 at%

TEM images were also recorded for the 5 %-sample. The new lattice spacings and the assigned phases are listed in Table 5.5. Fig. 5.15 shows the uncalcined sample after the synthesis and, similar to the 25 %-samples, a layer of an amorphous material can be seen on the anatase particles. However, no individual particles of precursor could be detected. Compared to the 25 %-sample, the layer appears thinner.

Table 5.5: Lattice spacings observed in the TEM images of 5 %-samples and the associated phase and crystal plane. All powder diffraction files from [69].

Observed lattice spacing [nm]	Phase & Crystal plane
0.35	Anatase (101) [a]
0.28	V_2O_5 (011) [b]
0.41	V_2O_5 (110) [b]
0.33	Rutile (110) [c]

[a] PDF 04-007-0701
[b] PDF 04-012-3680
[c] PDF 04-008-7645

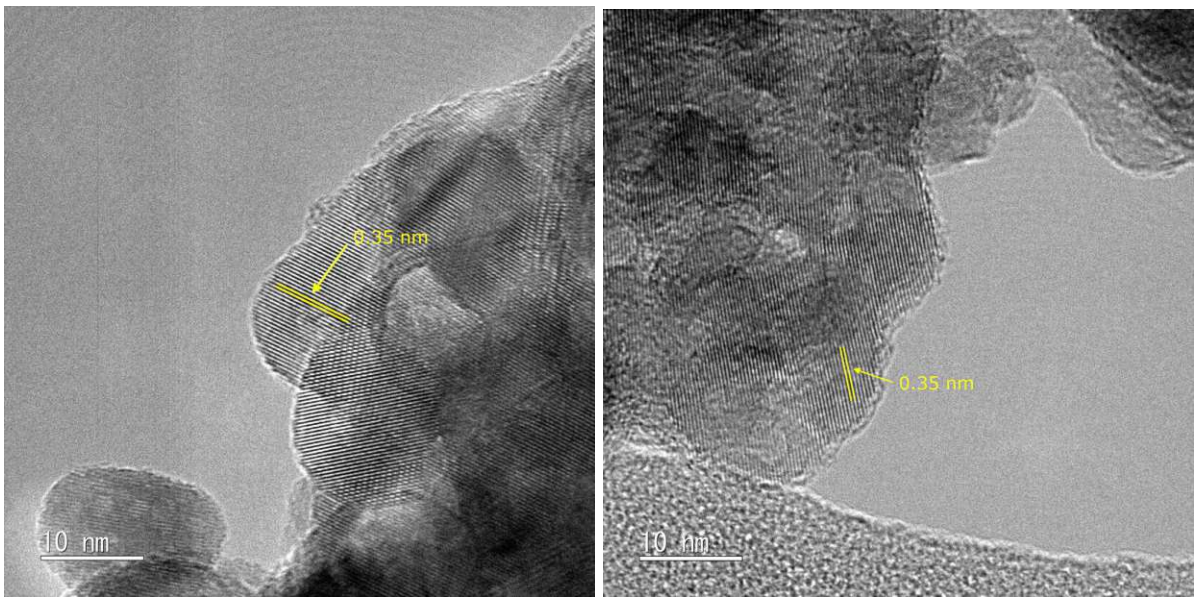

(a): $Ti\,[5\%/RT]_E^S$ **(b):** $Ti\,[5\%/RT]_E^S$

Figure 5.15: TEM images of the uncalcined 5 %-sample. Both images show an amorphous layer of the precursor $VOSO_4$, which is covering the anatase particles.

In contrast to the 25 %-samples, the layer is no longer visible after the calcination at 350 °C as can be seen in Fig. 5.16. This indicates that the precursor can diffuse and move at a temperature of 350 °C to form bigger particles. However, only after the calcination at 600 °C new particles with different lattice spacings appear, which belong to V_2O_5 and rutile.

Fig. 5.17 shows that the amorphous layer, which was seen on the uncalcined catalyst, formed V_2O_5 particles on the surface of anatase during the calcination at 600 °C.

Die approbierte gedruckte Originalversion dieser Diplomarbeit ist an der TU Wien Bibliothek verfügbar
The approved original version of this thesis is available in print at TU Wien Bibliothek.
TU Bibliothek Your knowledge hub WIEN

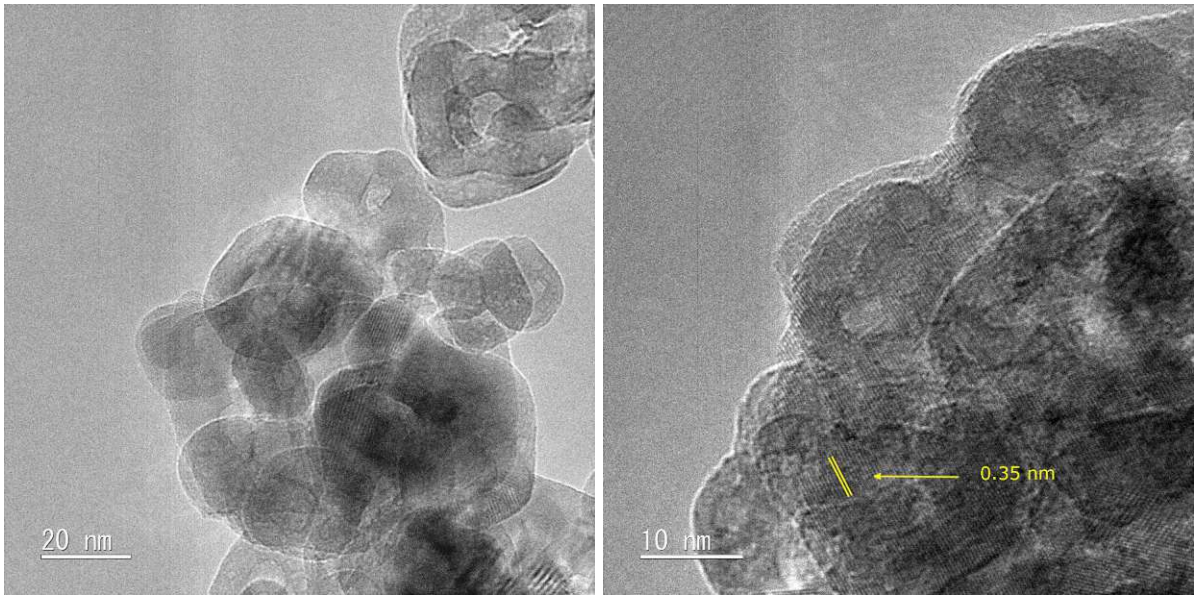

(a): $Ti\,[5\%/350]_E^S$ **(b):** $Ti\,[5\%/350]_E^S$

Figure 5.16: TEM images of the 5 %-sample, calcined at 350 °C. The amorphous layer, which was observed in the uncalcined sample, is no longer visible.

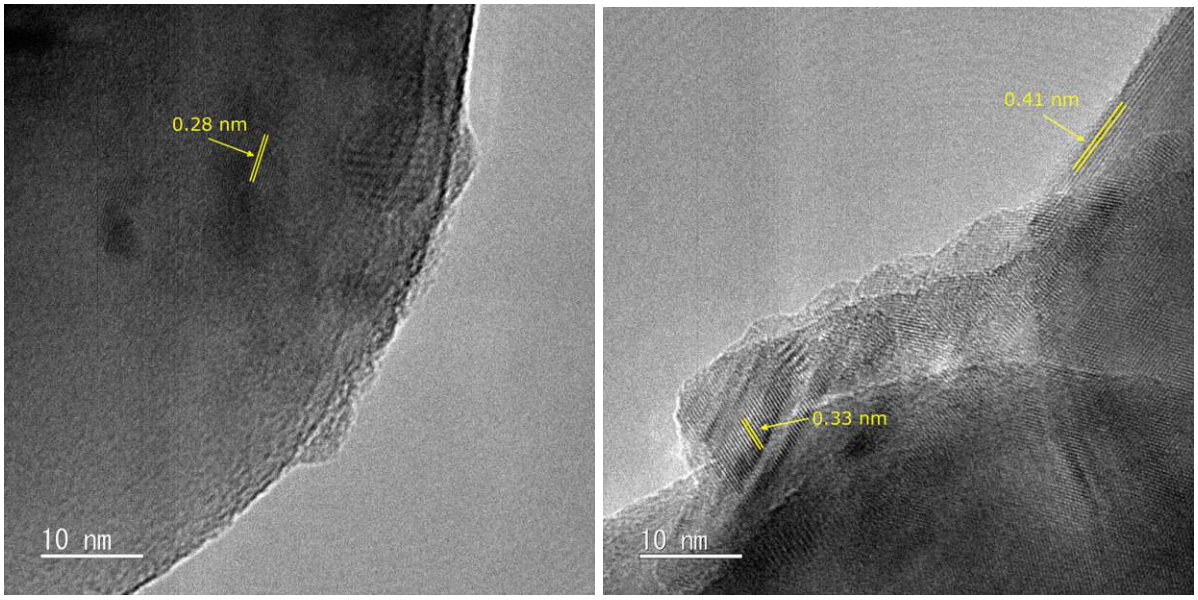

(a): $Ti\,[5\%/600]_E^S$ **(b):** $Ti\,[5\%/600]_E^S$

Figure 5.17: TEM images of the 5 %-samples, calcined at 600 °C. (a) shows lattice spacings belonging to newly formed V_2O_5 on the anatase surface and (b) shows spacings which were assigned to V_2O_5 and rutile TiO_2.

5.2.3.3 Powder XRD - 5 at%

The calcined 5 %-samples can be seen in Fig. 5.18 together with the diffractogram of calcined anatase. As mentioned above, the calcined anatase shows an additional peak at 27.5°, which belongs to the rutile modification which is the thermodynamically stable phase of TiO_2 and which evolves at elevated temperatures [81].

The catalyst $Ti\,[5\%/350]_E^S$ only shows peaks belonging to the anatase phase. The absence of any additional peaks due to a VO_x phase could be because the concentration is too small to

Die approbierte gedruckte Originalversion dieser Diplomarbeit ist an der TU Wien Bibliothek verfügbar
The approved original version of this thesis is available in print at TU Wien Bibliothek.
TU Bibliothek Your knowledge hub WIEN

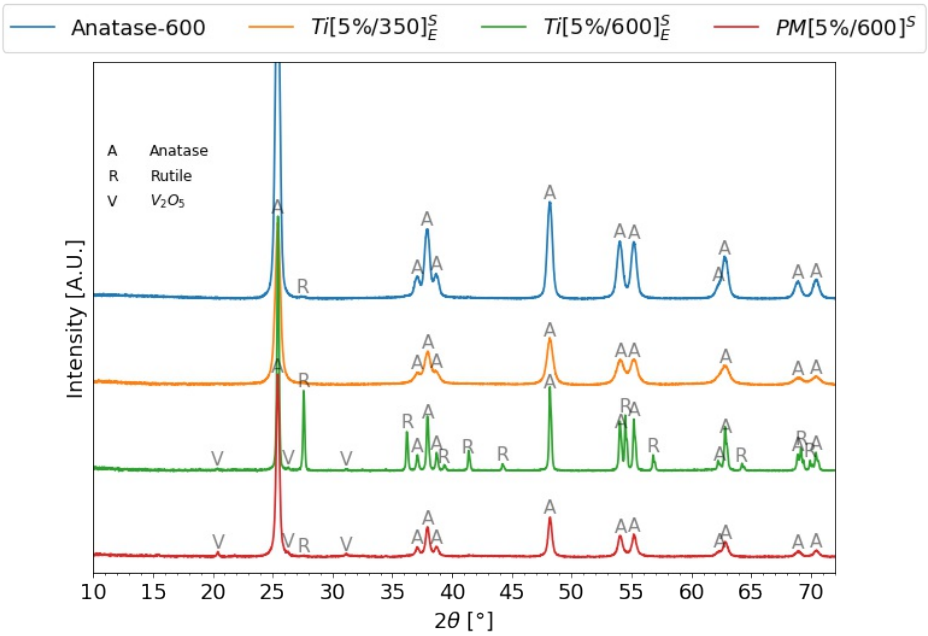

Figure 5.18: Powder X-ray diffraction spectra of the 5 %-samples. The letters indicate which phase each peak was assigned to.

be detected by powder XRD or because the V-species are dispersed very strongly so that no crystallites big enough for diffraction have formed or they exist as an amorphous layer on the anatase particles [111]. However, the peaks don't appear as sharp as for the Ana-600 sample, which is caused by the lower calcination temperature and therefore smaller crystallite growth.

The 5 %-sample calcined at higher temperature $Ti\,[5\%/600]_E^S$ shows very intense rutile peaks next to the anatase peaks. Comparing the diffractograms of $Ti\,[5\%/600]_E^S$ and the physical mixture $PM[5\%/600]^S$ which both contain the same amount of V it is clear that the synthesis affected the rutilation, because $PM[5\%/600]^S$ shows almost no rutile in the powder XRD diffractogram. $Ti\,[5\%/600]_E^S$ also shows peaks which were assigned to V_2O_5 with a small intensity. The physical mixture $PM[5\%/600]^S$ produced the same peaks with almost the same intensities.

These results are similar to the XRD analysis of the 25 % sample. V_2O_5 could be detected in the sample calcined at the higher temperature of 600 °C, but not after calcination at 350 °C. Also the amount of rutile that formed was increased compared to the physical mixture.

5.2.3.4 ATR-FTIR - 5 at%

The FTIR spectra of the catalyst sample $Ti\,[5\%/600]_E^S$ and the physical mixture $PM[5\%/600]^S$ can be seen in Fig. 5.19 with the spectra of Ana-600 and the pure calcined precursor $VOSO_4$-600 as a reference. These spectra are very similar to the spectra of their respective counterparts $Ti\,[25\%/600]_E^S$ and $PM[25\%/600]^S$ which can be seen in Fig. 5.9.

Both samples $Ti\,[5\%/600]_E^S$ and $PM[5\%/600]^S$ show the Ti−O−Ti stretching vibrations of the TiO_2 network which produce the intense peaks below approx. 900 cm^{-1} [83, 84]. They also show a peak at 1026 cm^{-1} which was assigned to the V=O stretching vibration of terminal O in the

Die approbierte gedruckte Originalversion dieser Diplomarbeit ist an der TU Wien Bibliothek verfügbar
The approved original version of this thesis is available in print at TU Wien Bibliothek.
TU Bibliothek Your knowledge hub WIEN

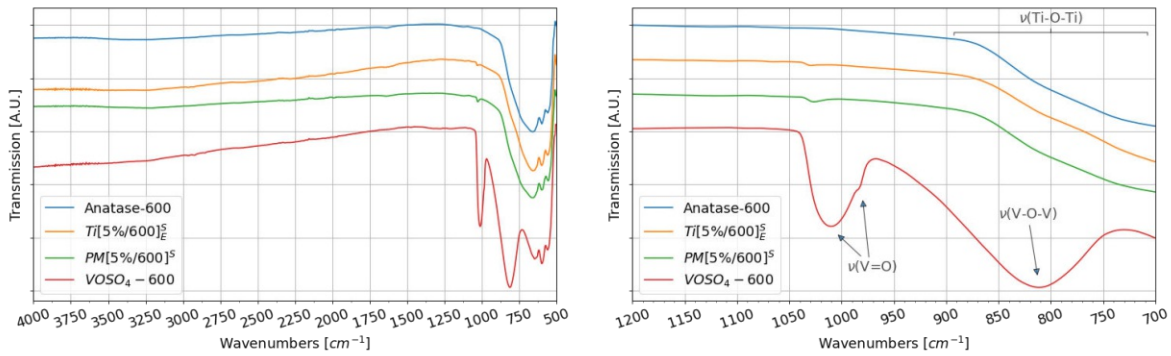

(a): Overview **(b):** Low-wavenumver region

Figure 5.19: FTIR spectra for the 5 %-sample $Ti\,[5\%/600]_E^S$ as well as the physical mixture with 5% of V $PM[5\%/600]^S$, Ana-600 and $VOSO_4$.

V_2O_5 structure and which again appears shifted from the same peak in the reference sample $VOSO_4$-600 (V=O at 1010 cm^{-1}) [85, 87]. However, since it appears at the same position for the synthesized sample, as well as the physical mixture of the components, the shift could also be caused by the chemical environment of V_2O_5, meaning the TiO_2 matrix in the sample.

The large peak at 812 cm^{-1} from the reference $VOSO_4$-600 belongs to V−O−V lattice vibrations [85, 86].

The IR results of the 5 % samples again confirm the presence of V_2O_5 in the sample.

5.2.3.5 Raman Spectroscopy - 5 at%

Fig. 5.20 shows the plots of the Raman spectra of the 5 %-samples $Ti\,[5\%/RT]_E^S$, $Ti\,[5\%/350]_E^S$ and $Ti\,[5\%/600]_E^S$. The sample calcined at 600 °C $Ti\,[5\%/600]_E^S$ shows two very low intensity bands at 291 cm^{-1} and 997 cm^{-1} which belong to crystalline V_2O_5. The sample calcined at

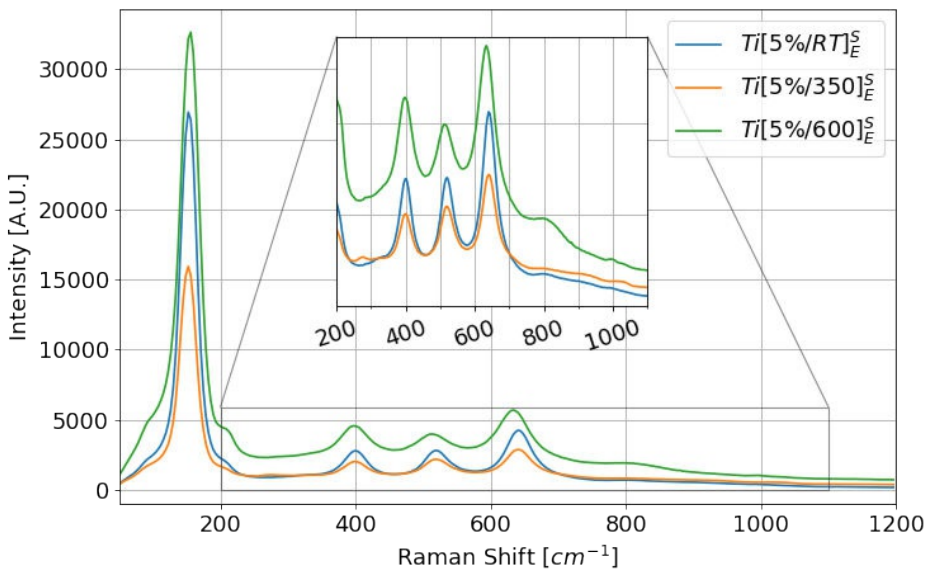

Figure 5.20: Raman spectra for the 5 %-samples. Only the samples calcined at 350 °C and 600 °C showed additional bands belonging to $VOSO_4$ and V_2O_5 respectively.

Die approbierte gedruckte Originalversion dieser Diplomarbeit ist an der TU Wien Bibliothek verfügbar
The approved original version of this thesis is available in print at TU Wien Bibliothek.

medium temperature $Ti\,[5\%/350]_E^S$ shows two bands at 277 cm^{-1} and 1030 cm^{-1} which already appeared in the uncalcined 25 %-sample $Ti\,[25\%/RT]_E^S$ (see Fig. 5.10b). These bands most likely belong to uncalcined $VOSO_4$, however, it is not visible in the uncalcined 5 %-sample $Ti\,[5\%/RT]_E^S$. One possible explanation could be the unequal distribution of the precursor on the anatase particles, as was seen in the TEM analysis of the 5 %-samples. In the uncalcined sample, the precursor was distributed as a layer on the particles, which disappeared after the calcination at 350 °C, indicating that the $VOSO_4$ could have sintered together to form bigger crystallites.

Fig. 5.21 shows the change of center position and FWHM of the $E_g(1)$ band for the 5 %-samples. There is a big shift towards higher wavenumbers (blue shift) from the unmodified anatase sample to the catalysts. Additionally, the peak width increased as well. Between the three 5 %-catalysts there is only little change in peak center as well as the FWHM. As mentioned in the 25 at%-section (Section 5.2.2.6), the shift from pure anatase to the catalysts could be caused by some elastic strain on the TiO_2 lattice, applied by the V-species on the surface, doping with V-ions or the formation of O-vacancies [97, 99–101].

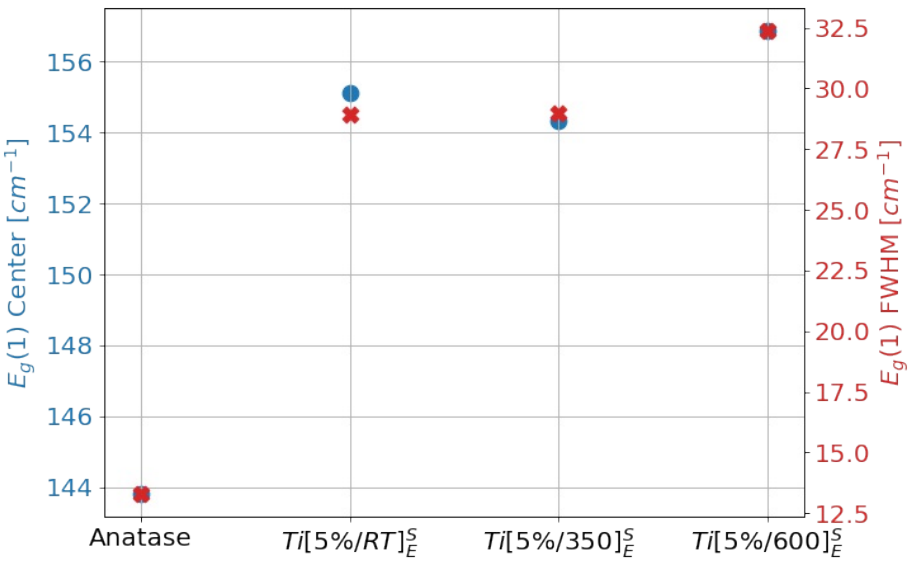

Figure 5.21: Center position and FWHM of the $E_g(1)$ band of the 5 %-samples and anatase as a reference. Both increased a lot upon addition of the V precursor and then changed again slightly after calcination.

Similar to the 25 % samples, the Raman results fit well with the IR analysis and further help confirm the structure of the V-species as V_2O_5. The shift in the $E_g(1)$ band of anatase also suggests a close interaction of V_2O_5 and the anatase particles.

5.2.3.6 DRS - 5 at%

Fig. 5.23 shows the reflectance spectra and Tauc-plots for the 5 %-samples. The process for determining the bandgap was described in detail in the 25 at% section but Fig. 5.22 illustrates how the bandgap was determined for the 5 %-samples.

Die approbierte gedruckte Originalversion dieser Diplomarbeit ist an der TU Wien Bibliothek verfügbar
The approved original version of this thesis is available in print at TU Wien Bibliothek.
TU Bibliothek Your knowledge hub WIEN

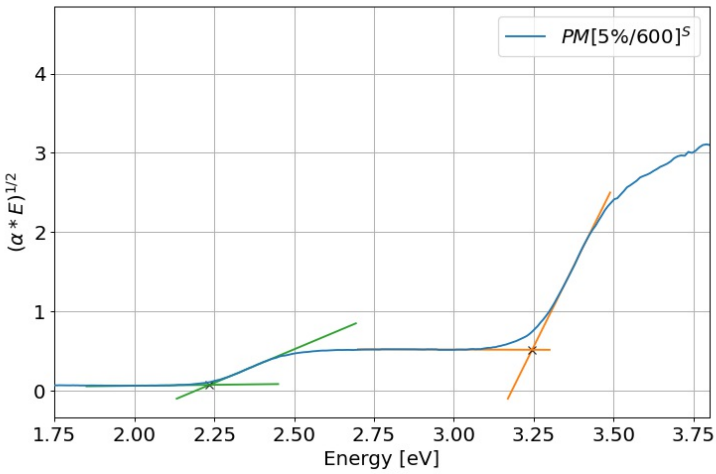

Figure 5.22: Determination of the bandgaps for sample $PM[6\%/600]^S$. For modified semiconductors, the bandgap is determined by the intersection of the linear section of the Tauc plot and the baseline extrapolated from the sub-bandgap energy region.

Similar to the physical mixture with 25 at% V (see Fig. 5.13e), the sample $PM[5\%/600]^S$ shows two distinct absorption edges which resulted in the bandgaps 3.2 eV for anatase and 2.2 eV for V_2O_5.

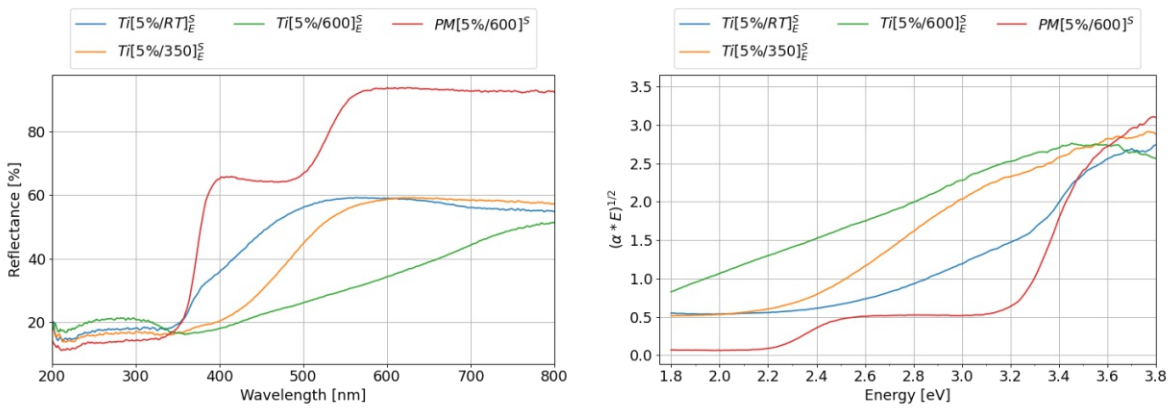

(a): Reflectance: 5 %-samples.

(b): Tauc-plot: 5 %-samples.

Figure 5.23: The DRS spectra and derived Tauc plots for the 5 %-samples $Ti\,[5\%/RT]^S_E$, $Ti\,[5\%/350]^S_E$ and $Ti\,[5\%/600]^S_E$.

The uncalcined sample $Ti\,[5\%/RT]^S_E$ shows a slight absorption edge for TiO_2 which yields a bandgap of 3.2 eV in the Tauc plot analysis, but the calcined samples $Ti\,[5\%/350]^S_E$ and $Ti\,[5\%/600]^S_E$ do not show a clear decline in the Tauc plot to be evaluated.

The difference of the DRS profiles between the sythesized samples and the physical mixture is confirmation of a close interaction between the V-species and the TiO_2 in the synthesized samples.

Die approbierte gedruckte Originalversion dieser Diplomarbeit ist an der TU Wien Bibliothek verfügbar
The approved original version of this thesis is available in print at TU Wien Bibliothek.

5.2.4 1 at%-samples

In contrast to the 5 %- and 25 %-samples, catalysts with 1 % of V were produced with two different precursors ($VOSO_4$ and NH_4VO_3) and two different synthesis methods (filtration and evaporation).

5.2.4.1 TEM - 1 at%

For the 1 %-samples TEM images were recorded for the samples prepared with $VOSO_4$ as the precursor as well as the samples with NH_4VO_3. Fig. 5.24 shows images of the samples with the precursor $VOSO_4$. The first two images Fig. 5.24a and 5.24b show the filtration samples in uncalcined and calcined form and Fig. 5.24c and 5.24d show analogous samples synthesized via the evaporation route. Both of these uncalcined samples show an outer layer around anatase particles, which were identified by the lattice spacing of 0.35 nm belonging to the (101) crystal plane of anatase (see Table 5.3). After the calcination of $Ti\,[1\%/RT]_F^S$ into $Ti\,[1\%/600]_F^S$ the sample shows a new monolayer on the anatase particles with a lattice spacing of >0.5 nm as can be seen in Fig. 5.24b. This lattice spacing couldn't be attributed to any phase with certainty. Similarly, the outer layer of sample $Ti\,[1\%/RT]_E^S$ in Fig. 5.24c disappears upon calcination and instead irregularly shaped particles appear on the anatase particles in sample $Ti\,[1\%/600]_E^S$ (see arrow in Fig. 5.24d).

The TEM images of samples with NH_4VO_3 as the precursor can be seen in Fig. 5.25. Again, the first two images Fig. 5.25a and 5.25b show the samples synthesized via the filtration method and Fig. 5.25c and 5.25d show the evaporation samples, each before and after calcination. In contrast to the $VOSO_4$ samples, the catalysts with NH_4VO_3 as the precursor, show big clusters of particles that appeared different to pure anatase. Also no outer layer covering anatase could be observed. For the filtration samples, these clusters can be seen before ($Ti\,[1\%/RT]_F^N$) and after ($Ti\,[1\%/350]_F^N$) the calcination (see Fig. 5.25a and 5.25b). The evaporation sample only shows clusters after the calcination $Ti\,[1\%/350]_E^N$ in Fig. 5.25d and there were no clusters visible in the TEM analysis of $Ti\,[1\%/RT]_E^N$.

In conclusion, the precursor $VOSO_4$ appeared as a layer on the anatase particles, irrespective of the synthesis method. After the calcination at 600 °C the layer disappeared and new particles with an irregular shape formed. Similar results also were found for the other two concentrations (5 and 25 %). In the case of the precursor NH_4VO_3, however, the TEM images showed clusters of small particles in the uncalcined filtration sample as well as both samples, calcined at 350 °C (filtration and evaporation sample). In the case of the precursor $VOSO_4$ this leads to an increased interface between the TiO_2 and the VO_x, compared to the samples synthesized with NH_4VO_3.

Die approbierte gedruckte Originalversion dieser Diplomarbeit ist an der TU Wien Bibliothek verfügbar
The approved original version of this thesis is available in print at TU Wien Bibliothek.
TU Bibliothek Your knowledge hub WIEN

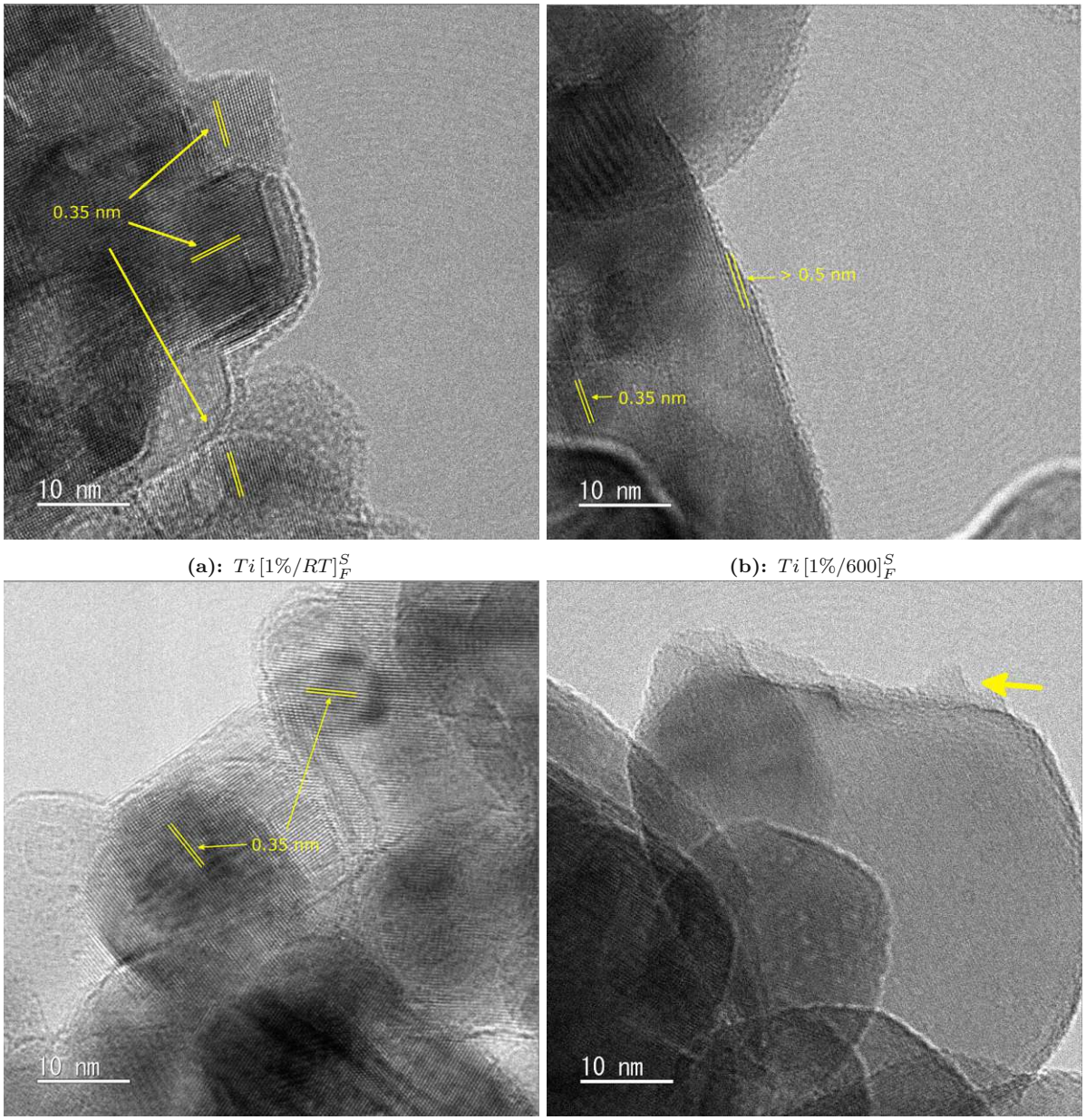

(a): $Ti\,[1\%/RT]_F^S$ **(b):** $Ti\,[1\%/600]_F^S$

(c): $Ti\,[1\%/RT]_E^S$ **(d):** $Ti\,[1\%/600]_E^S$

Figure 5.24: TEM images of the 1 %-samples with $VOSO_4$ as the precursor. (a)/(b) Filtration samples before and after the calcination at600 °C. Before the calcination, an amorphous layer appeared on top of the anatase particles. After the calcination the layer was still present, however, it showed a lattice spacing of > 0.5 nm which couldn't be attributed to any phase; (c)/(d) Evaporation samples before and after calcination at 600 °C. Again, a layer appeared on the anatase particles which turned into irregular shaped particles during the calcination (see arrow in (d)).

Die approbierte gedruckte Originalversion dieser Diplomarbeit ist an der TU Wien Bibliothek verfügbar
The approved original version of this thesis is available in print at TU Wien Bibliothek.
TU Bibliothek Your knowledge hub WIEN

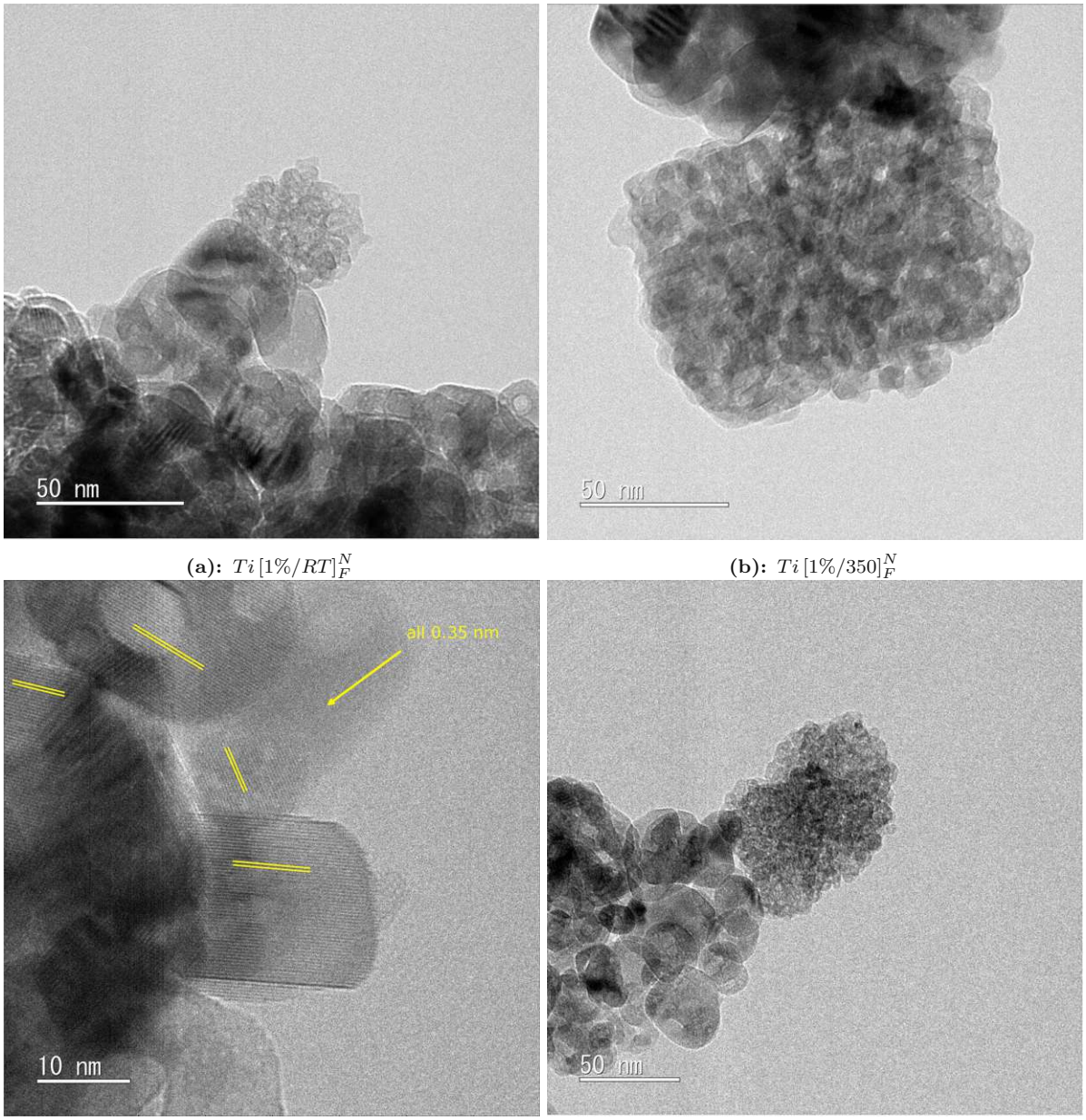

(a): $Ti\,[1\%/RT]_F^N$ **(b):** $Ti\,[1\%/350]_F^N$

(c): $Ti\,[1\%/RT]_E^N$ **(d):** $Ti\,[1\%/350]_E^N$

Figure 5.25: TEM images of the 1 %-samples with NH_4VO_3 as the precursor. (a)/(b) Filtration samples before and after the calcination at 350 °C. Both samples show clusters of particles which were not visible in the TEM analysis of pure anatase; (c)/(d) Evaporation samples before and after the calcination at 350 °C. No clusters were found before the calcination, however, afterwards they were again visible.

Die approbierte gedruckte Originalversion dieser Diplomarbeit ist an der TU Wien Bibliothek verfügbar
The approved original version of this thesis is available in print at TU Wien Bibliothek.
TU Bibliothek Your knowledge hub WIEN

5.2.4.2 XPS - 1 at%

Fig. 5.26 shows XPS spectra for the 1 %-samples $Ti\,[1\%/350]_E^N$, $Ti\,[1\%/350]_E^S$ and $Ti\,[1\%/600]_E^S$. All peaks of $Ti\,[1\%/600]_E^S$ show a higher FWHM which can be attributed to a slight charging of the sample.

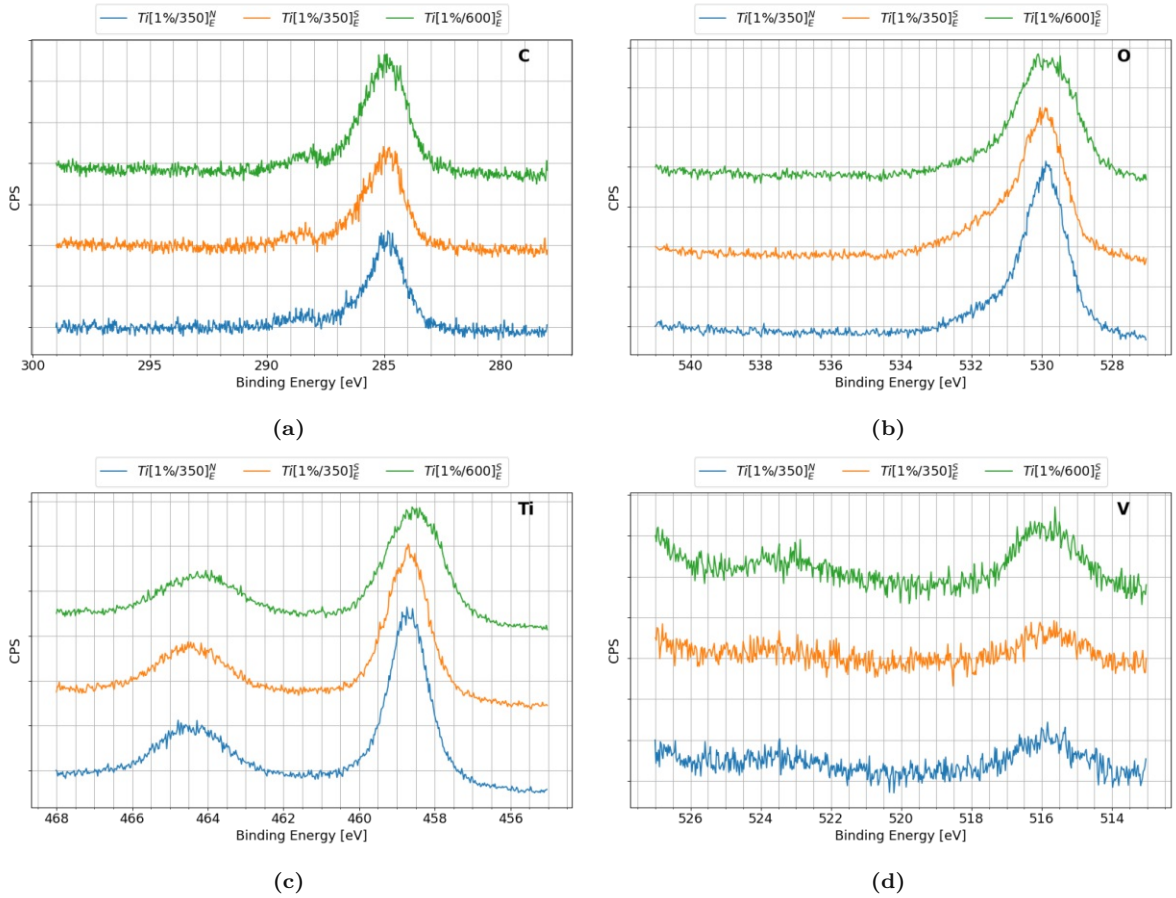

Figure 5.26: XPS spetra for the 1 %-samples $Ti\,[1\%/350]_E^N$, $Ti\,[1\%/350]_E^S$ and $Ti\,[1\%/600]_E^S$. (a) shows the binding energy region for carbon (C 1s), (b) for oxygen (O 1s), (c) for titanium (Ti 2p) and (d) for vanadium (V 2p). $Ti\,[1\%/600]_E^S$ (green spectra) shows a larger FWHM than the other two samples, which can be attributed to charging of the sample.

The carbon signal form adventitious carbon (C 1s) can be seen in Fig. 5.26a [70]. As mentioned above in the XPS part of Section 5.2.2, it was set to 284.80 eV and used to calibrate the energy scale.

The oxygen (O 1s) spectra can be seen in Fig. 5.26b. All spectra show a big peak around 530 eV with a small shoulder towards higher binding energies. The bigger peak was assigned to the metal oxides Ti−O and V−O for all synthesized samples [73, 74]. The shoulder at higher energies was assigned to other oxygen species like like hydroxyl groups, water or organics [71, 72].

For the titanium (Ti 2p) spectra, no significant difference in the position of the peaks was observed between the synthesized samples and anatase (see Fig. 5.7c). Two peaks at 458.7 eV and 464.4 eV belonging to Ti^{+4} $2p_{3/2}$ and Ti^{+4} $2p_{1/2}$ respectively [73] were detected for all samples.

Die approbierte gedruckte Originalversion dieser Diplomarbeit ist an der TU Wien Bibliothek verfügbar
The approved original version of this thesis is available in print at TU Wien Bibliothek.
TU Bibliothek Your knowledge hub WIEN

The vanadium spectra (V 2p) are given in Fig. 5.26d. All samples show a bigger peak at 515.7 eV and a very small peak at about 523.5 eV which were assigned to the V $2p_{3/2}$ and V $2p_{1/2}$ of V^{+4} respectively [75]. This would be expected for the sample $Ti\,[1\%/350]_E^S$, because the TGA suggested that the precursor $VOSO_4$ looses its crystal water upon calcination at 350 °C, but doesn't get oxidized to V_2O_5 and the V in $VOSO_4$ has an oxidation state of +4. However, upon calcination at 600 °C, the TGA suggested that $VOSO_4$ turns into V_2O_5, where V has an oxidation state of +5. Additionally, the V in the samples with NH_4VO_3 as the precursor ($Ti\,[1\%/350]_E^N$) must have even been reduced during the synthesis since it is present as V^{+5} in the uncalcined precursor. The V-species of both precursors could be reduced by Ti^{+3}, which forms at oxygen vacancies on the TiO_2 surface, especially since TiO_2 is a more stable oxide than V_2O_5 [112]. This would also means that the V cannot be present as V_2O_5 on the surface of anatase because there, the V would have an oxidation number of +5.

However, it is also possible that V was reduced under the vacuum conditions in the XPS analysis chamber. The reduction of V^{+5} to V^{+4} due to the XPS vacuum has been reported in the literature, but the degree of reduction depends on the support [76]. Because V_2O_5 is less stable than TiO_2 it would also be expected to get reduced before TiO_2 [112].

Due to the possibility of the reduction under the XPS conditions and the low concentration it is difficult to say, which oxidation state is actually present on the synthesized samples.

5.2.4.3 XRD - 1 at%

Powder XRD measurements were done for the high-temperature calcined catalysts $Ti\,[1\%/350]_E^N$ and $Ti\,[1\%/600]_E^S$. The diffractograms for these samples and calcined anatase Ana-600 can be seen in Fig. 5.27.

Sample $Ti\,[1\%/350]_E^N$ only showed peaks belonging to anatase and no additional peaks that could be attributed to any VO_x phase. Similarly, the sample $Ti\,[1\%/600]_E^S$ mostly showed peaks belonging to anatase, except for two more peaks at 27.5° and 31.1°. The first one at 27.5° had a very low intensity and it was attributed to the formation of rutile during the calcination at the higher temperature [77]. This peak was also found in pure anatase when calcined at 600 °C. The other peak at 31.1° was attributed to measurement error, although it seems to match with a peak from V_2O_5. Since it is the only unassigned peak at a comparatively high intensity it is unlikely to be coming from a VO_x phase, since they typically show many different peaks in a powder diffractogram, as can be seen in Fig. 5.8b.

Fig. 5.27 clearly shows that the samples, calcined at a higher temperature have sharper peaks, which is a sign for crystallite growth. The same effect can also be seen in the other graphs in Fig. 5.8b and 5.18. However, due to the low concentration of V in these samples, no peaks belonging to a VO_x phase could be detected.

Die approbierte gedruckte Originalversion dieser Diplomarbeit ist an der TU Wien Bibliothek verfügbar
The approved original version of this thesis is available in print at TU Wien Bibliothek.
TU Bibliothek Your knowledge hub WIEN

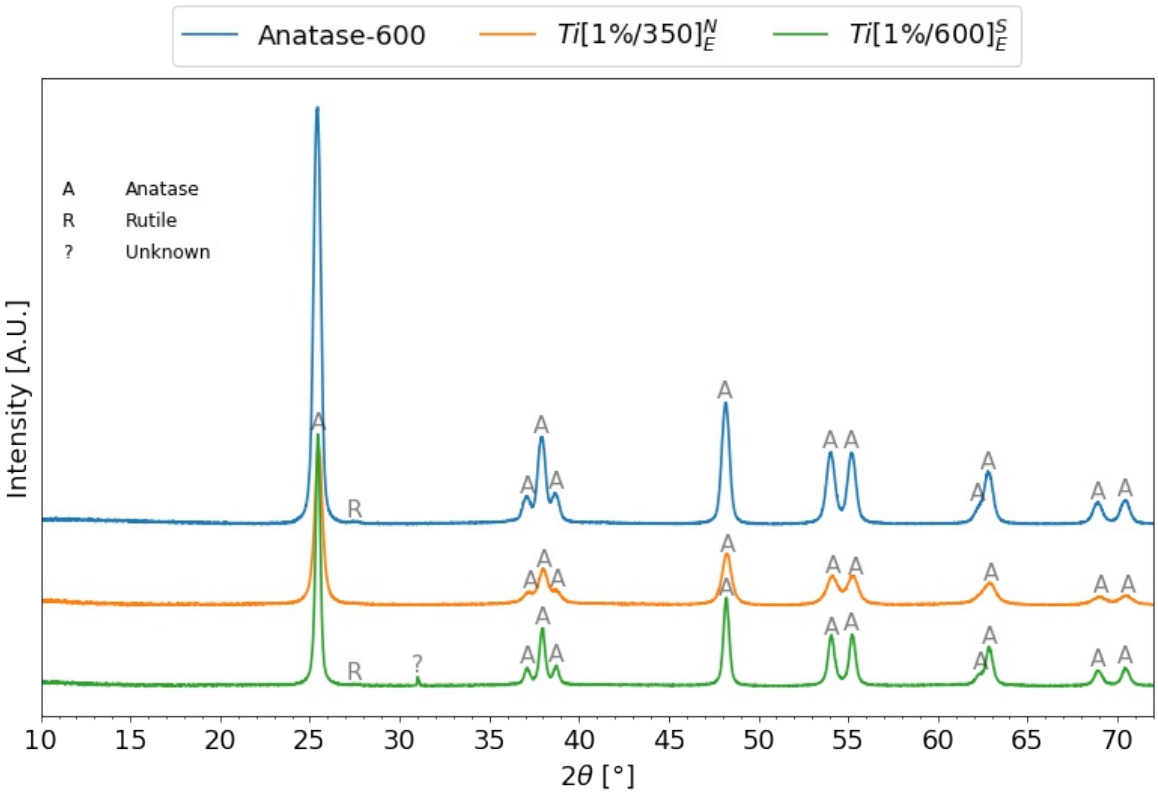

Figure 5.27: Powder XRD diffractograms for the 1 %-samples $Ti\,[1\%/350]_E^N$, $Ti\,[1\%/600]_E^S$ and anatase, calcined at 600 °C for 1 h (Ana-600).

5.2.4.4 ATR-FTIR - 1 at%

The FTIR spectra for the 1 %-samples can be seen in Fig. 5.28. Only the spectra of the uncalcined sample $Ti\,[1\%/RT]_E^S$ and the sample calcined at 350 °C $Ti\,[1\%/350]_E^S$ of the evaporation synthesis with $VOSO_4$ as the precursor show two additional peaks at 1130 cm^{-1} and 1042 cm^{-1}. Both peaks were also observed in the IR spectrum of the uncalcined precursor (see Appendix Fig. 9.35) and most likely belong to a stretching vibration of SO_4^{2-} [113]. However, due to the low concentration of the precursor, the catalysts show no characteristic V_2O_5-related bands.

Die approbierte gedruckte Originalversion dieser Diplomarbeit ist an der TU Wien Bibliothek verfügbar
The approved original version of this thesis is available in print at TU Wien Bibliothek.

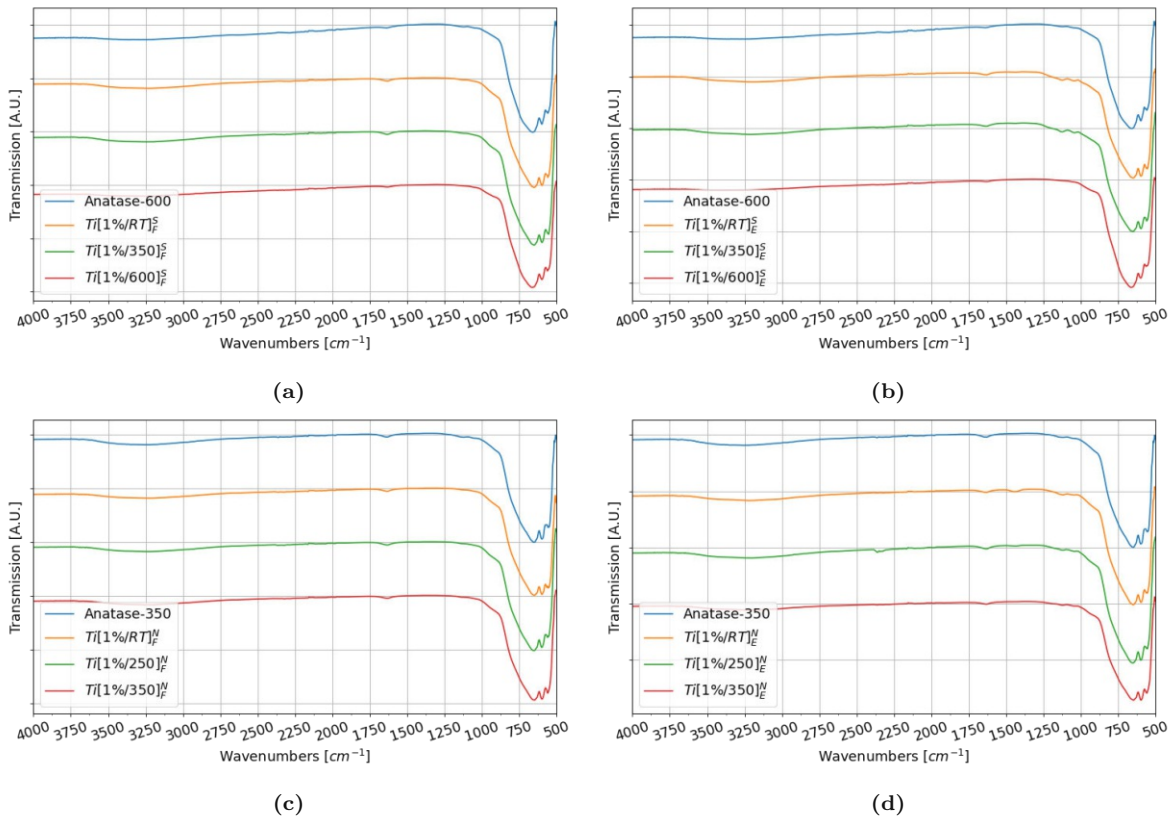

Figure 5.28: FTIR spectra for the 1 %-samples. Most of the spectra show no significant differences to the anatase spectrum. Only the uncalcined sample $Ti\,[1\%/RT]_E^S$ as well as the sample calcined at medium temperature $Ti\,[1\%/350]_E^S$ show two peaks at 1130 cm^{-1} and 1042 cm^{-1} which belong to uncalcined $VOSO_4$.

5.2.4.5 Raman Spectroscopy - 1 at%

Similarly to the FTIR results, the Raman spectra also didn't show any characteristic bands from V_2O_5 or other VO_x species. The spectra can be seen in Fig. 5.29.

Fig. 5.30 shows the change in center position and FWHM of the $E_g(1)$ band for all the 1 %-samples. Most of the spectra show a shift of $< 1\,cm^{-1}$ and no consistent trend could be determined. The position and FWHM of the $E_g(1)$ peak are not affected by the addition of 1 % vanadium.

Die approbierte gedruckte Originalversion dieser Diplomarbeit ist an der TU Wien Bibliothek verfügbar
The approved original version of this thesis is available in print at TU Wien Bibliothek.
TU Bibliothek Your knowledge hub WIEN

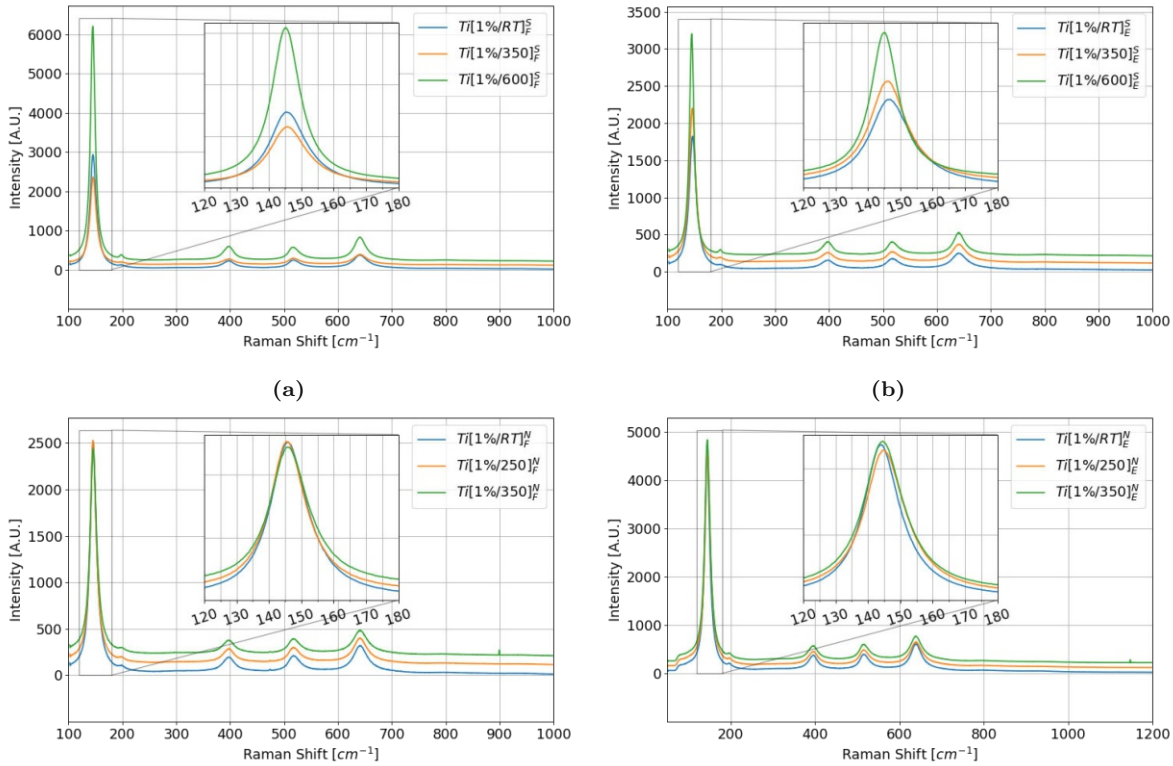

(a) (b) (c) (d)

Figure 5.29: Raman spectra for the 1 %-samples. All spectra show no significant differences to the anatase spectrum.

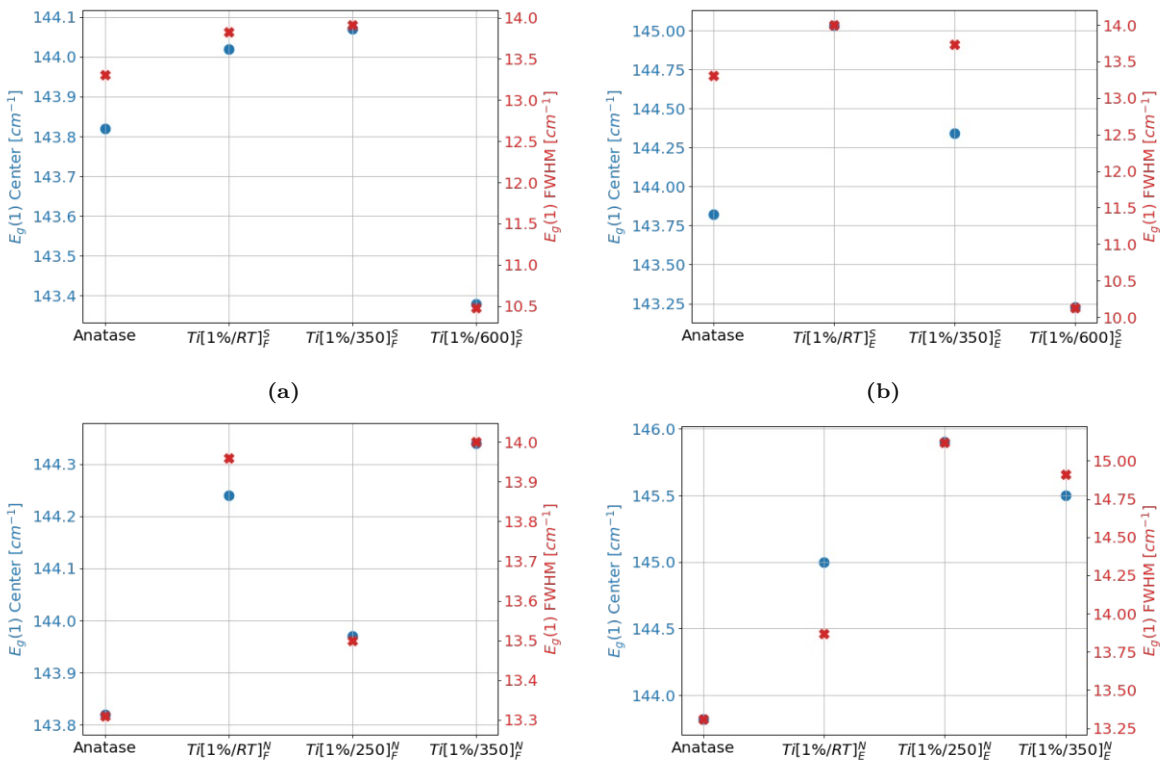

(a) (b) (c) (d)

Figure 5.30: Center position and FWHM of the $E_g(1)$ band of the 1 %-samples and anatase as a reference. The addition of the V precursors seems to have no significant effect on the $E_g(1)$ band.

Die approbierte gedruckte Originalversion dieser Diplomarbeit ist an der TU Wien Bibliothek verfügbar
The approved original version of this thesis is available in print at TU Wien Bibliothek.
TU Bibliothek Your knowledge hub WIEN

5.2.4.6 DRS - 1 at%

All DRS reflectance spectra and the calculated Tauc plots of the 1 %-samples can be seen in Fig. 5.32. Fig. 5.31 exemplarily shows how the bandgap was determined for all V-modified samples.

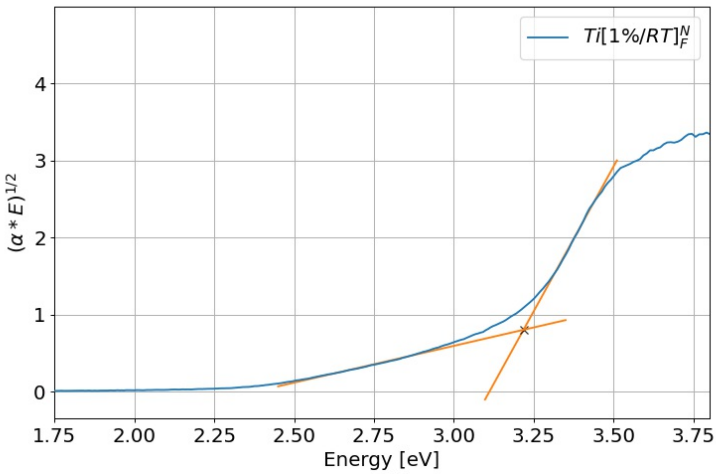

Figure 5.31: Determination of the bandgaps for sample $Ti\,[1\%/RT]_F^N$. For modified semiconductors, the bandgap is determined by the intersection of the linear section of the Tauc plot and the baseline extrapolated from the sub-bandgap energy region.

Additionally, Fig. 5.32a and Fig. 5.32b show the reflectance and Tauc plots of the NH_4VO_3 precursor and V_2O_5. The same plots for the precursor $VOSO_4$ can be seen in Fig. 5.13c and Fig. 5.13d respectively. Here, the bandgaps were determined analogous to the procedure shown in Fig. 5.31.

Fig. 5.32a shows that NH_4VO_3, calcined at 350 °C, has a very similar reflectance spectrum to V_2O_5 and both bandgaps from the Tauc plots were determined at 2.2 eV.

All of the 1 %-samples show a similar behaviour. In all cases, the addition of the precursor and the calcination led to a decreased reflectance between 350 nm to 550 nm, meaning a shift in the absorption edge. All bandgaps were determined to be 3.2 eV.

The bandgap of pure anatase was not modified by the addition of 1 at% of V however the absorption of the whole sample shifted towards the visible light region, which could correspond to either absorption by VO_x centres or modification of the electronic structure of TiO_2 by interbandgap states.

Die approbierte gedruckte Originalversion dieser Diplomarbeit ist an der TU Wien Bibliothek verfügbar
The approved original version of this thesis is available in print at TU Wien Bibliothek.

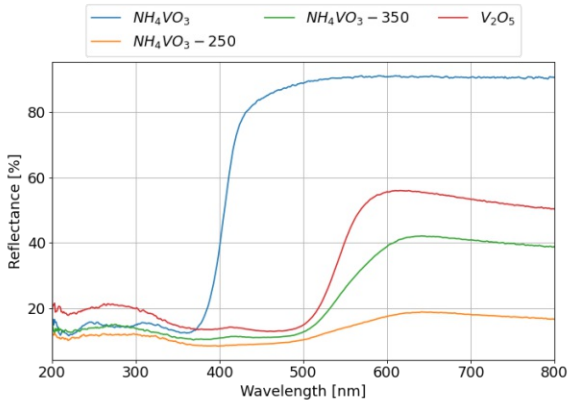

(a): Reflectance: NH_4VO_3 calcined at different temperatures and V_2O_5.

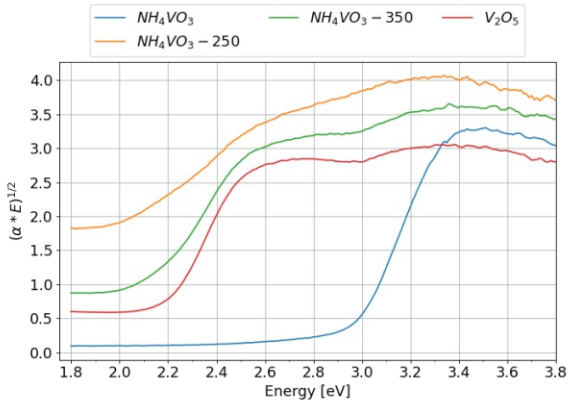

(b): Tauc: NH_4VO_3 calcined at different temperatures and V_2O_5.

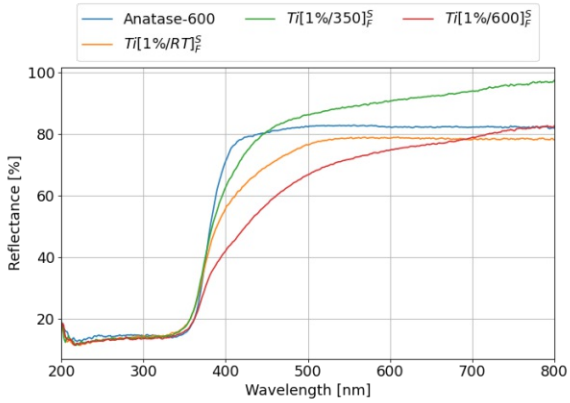

(c): Reflectance: $Ti\,[1\%/RT]_F^S$ calcined at different temperatures.

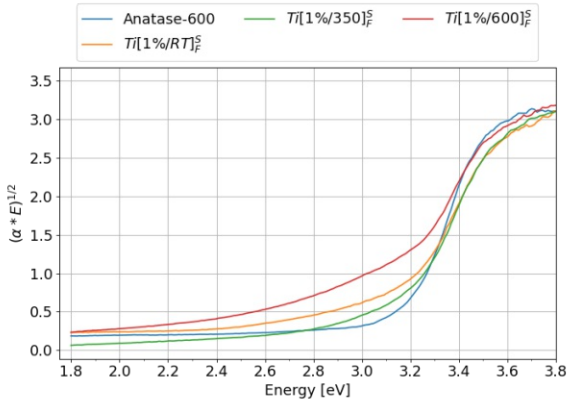

(d): Tauc: $Ti\,[1\%/RT]_F^S$ calcined at different temperatures.

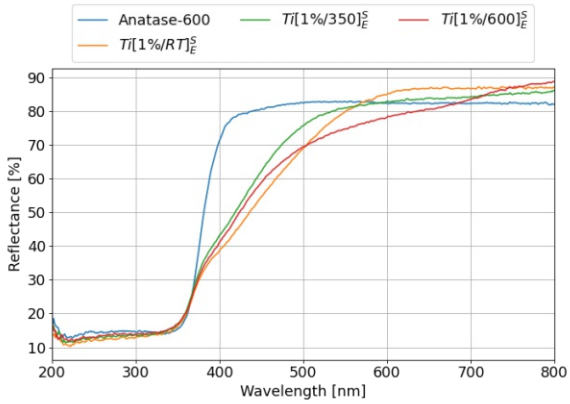

(e): Reflectance: $Ti\,[1\%/RT]_E^S$ calcined at different temperatures.

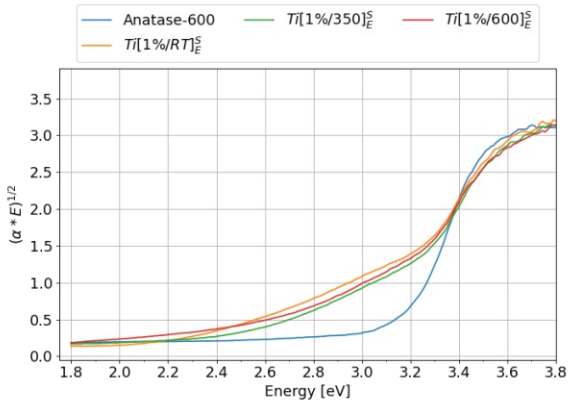

(f): Tauc: $Ti\,[1\%/RT]_E^S$ calcined at different temperatures.

Figure 5.32: DRS spectra and Tauc-plots respectively for: (a)/(b) NH_4VO_3, (c)/(d) $Ti\,[1\%/RT]_F^S$, (e)/(f) $Ti\,[1\%/RT]_E^S$, (g)/(h) $Ti\,[1\%/RT]_F^N$ and (i)/(j) $Ti\,[1\%/RT]_E^N$ all calcined at different temperatures.

Die approbierte gedruckte Originalversion dieser Diplomarbeit ist an der TU Wien Bibliothek verfügbar
The approved original version of this thesis is available in print at TU Wien Bibliothek.
TU Bibliothek Your knowledge hub WIEN

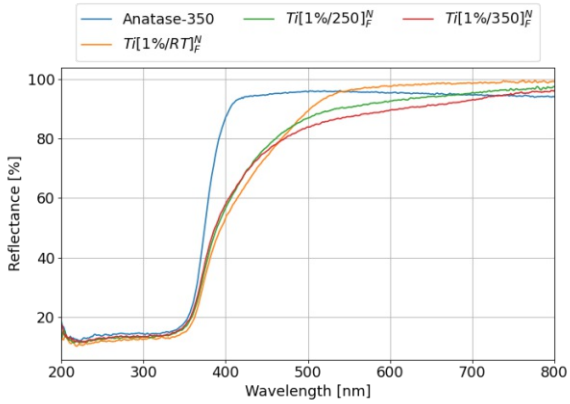

(g): Reflectance: $Ti\,[1\%/RT]_F^N$ calcined at different temperatures.

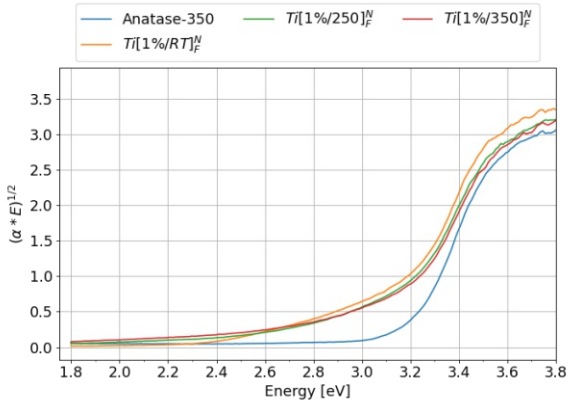

(h): Tauc: $Ti\,[1\%/RT]_F^N$ calcined at different temperatures.

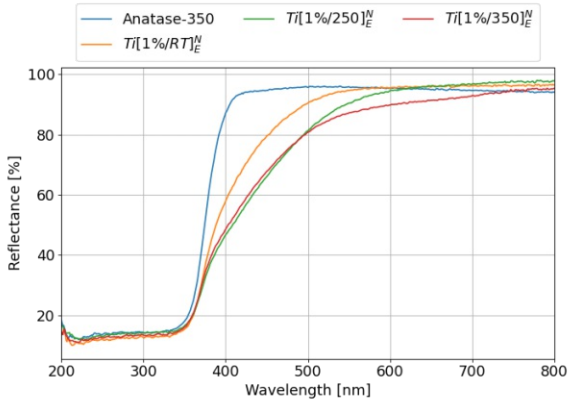

(i): Reflectance: $Ti\,[1\%/RT]_E^N$ calcined at different temperatures.

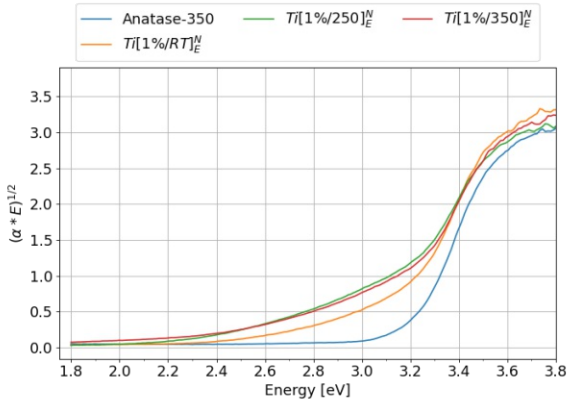

(j): Tauc: $Ti\,[1\%/RT]_E^N$ calcined at different temperatures.

Figure 5.32: DRS spectra and Tauc-plots respectively for: (a)/(b) NH_4VO_3, (c)/(d) $Ti\,[1\%/RT]_F^S$, (e)/(f) $Ti\,[1\%/RT]_E^S$, (g)/(h) $Ti\,[1\%/RT]_F^N$ and (i)/(j) $Ti\,[1\%/RT]_E^N$ all calcined at different temperatures.

Die approbierte gedruckte Originalversion dieser Diplomarbeit ist an der TU Wien Bibliothek verfügbar
The approved original version of this thesis is available in print at TU Wien Bibliothek.
TU Bibliothek Your knowledge hub WIEN

5.3 Photocatalytic experiments

The hydrogen evolution reaction is one of the most studied photocatalytic reactions since it could produce hydrogen gas as a "green" fuel source from water with energy provided from absorbed photons. After the characterization, the catalysts were tested for their photocatalytic activity in sacrificial HER and OER experiments. The DRS results suggested that pure anatase doesn't significantly absorb photons with a wavelength higher than 400 nm and that this absorption is only slightly improved for the 1 %-samples (see Fig. 5.13 and 5.32). The 5 %- and 25 %-samples, however, did show a much improved absorption in this range most likely owing to the formation of V_2O_5 on the sample surface which has a smaller bandgap, as was seen in the DRS results, and thus is able to absorb photons with a higher wavelength. For this reason HER experiments were also performed using visible light ($\lambda = 445$ nm) to test whether the addition of V_2O_5 could enhance light absorption, compared to the UV-HER and OER experiments.

5.3.1 OER

OER experiments were performed with all synthesized samples under illumination with UV light (365 nm) for 30 min. Ag^+ ions were used as a sacrificial agent to scavenge excited electrons and no additional co-catalyst was added to the reaction mixture. The O_2-concentration in the reactor was measured continuously during the experiment. This data could be converted to a rate by calculating the derivative of the plot. The recorded data as well as the calculated derivative can be seen in the Appendix in Section 9.7. The maximum of the derivative was then taken to be the oxygen evolution rate (see Fig. 5.33 and Table 5.6).

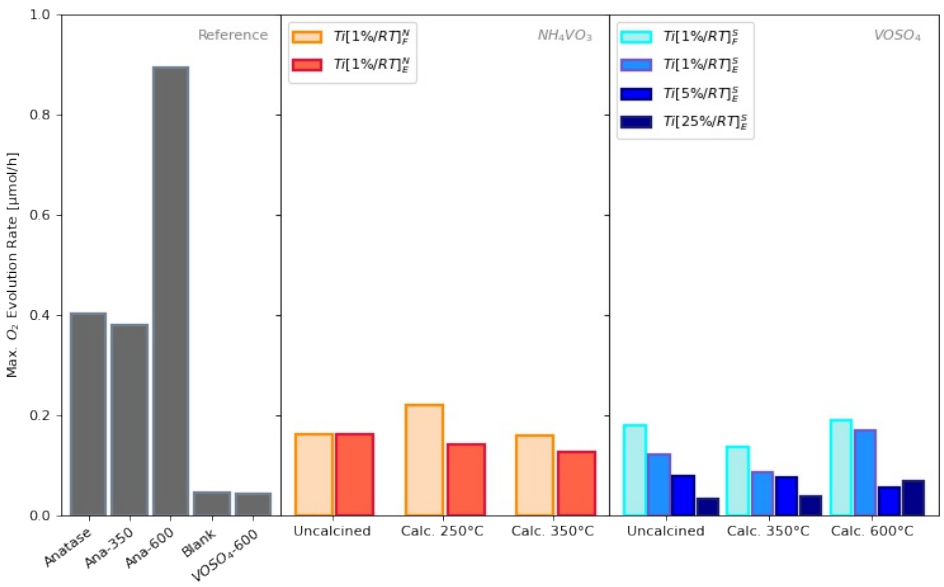

Figure 5.33: The oxygen evolution rates for all measured samples during the OER experiments after 30 min of illumination with UV light (365 nm).

The results show that no improvement in the OER activity could be achieved through the modification of the anatase powder with the vanadium precursors. In fact, it seems as though the opposite is the case, where the addition of more vanadium precursor decreased the activity,

Die approbierte gedruckte Originalversion dieser Diplomarbeit ist an der TU Wien Bibliothek verfügbar
The approved original version of this thesis is available in print at TU Wien Bibliothek.
TU Bibliothek Your knowledge hub WIEN

up to the calcined precursor $VOSO_4$-600 which showed as much activity as the blank experiment. The V species don't provide better active sites for the OER, compared to the anatase surface.

Table 5.6: The calculated OER rates after 30 min of illumination with UV light (365 nm).

Sample	O_2 Evolution Rate [$\mu mol\, h^{-1}$]
Anatase	0.40
Ana-350	0.38
Ana-600	0.89
Blank	0.04
$VOSO_4$-600	0.04
$Ti\,[1\%/RT]_F^N$	0.16
$Ti\,[1\%/250]_F^N$	0.22
$Ti\,[1\%/350]_F^N$	0.16
$Ti\,[1\%/RT]_E^N$	0.16
$Ti\,[1\%/250]_E^N$	0.14
$Ti\,[1\%/350]_E^N$	0.13
$Ti\,[1\%/RT]_F^S$	0.18
$Ti\,[1\%/350]_F^S$	0.14
$Ti\,[1\%/600]_F^S$	0.19
$Ti\,[1\%/RT]_E^S$	0.12
$Ti\,[1\%/350]_E^S$	0.09
$Ti\,[1\%/600]_E^S$	0.17
$Ti\,[5\%/RT]_E^S$	0.08
$Ti\,[5\%/350]_E^S$	0.08
$Ti\,[5\%/600]_E^S$	0.06
$Ti\,[25\%/RT]_E^S$	0.03
$Ti\,[25\%/350]_E^S$	0.04
$Ti\,[25\%/600]_E^S$	0.07

5.3.2 UV-HER

In the UV-HER experiments the catalysts were screened for activity in short experiments, with 30 min of light illumination (365 nm) in order to see if any of the catalysts would show significant activity. Methanol was used as a sacrificial agent for the oxidizing holes and no additional

Die approbierte gedruckte Originalversion dieser Diplomarbeit ist an der TU Wien Bibliothek verfügbar
The approved original version of this thesis is available in print at TU Wien Bibliothek.
TU Bibliothek Your knowledge hub WIEN

co-catalyst was added to the reaction mixture. The experiments were carried out for all samples synthesized via the filtration or evaporation synthesis and a few of the tested samples produced small amounts of hydrogen. Fig. 5.34 shows the hydrogen evolution rates for those samples for which hydrogen evolution could be detected, as well as for the pure anatase samples, calcined at different temperatures. All the reaction rates which where measured in the experiments are given in Table 5.7. The samples for which no activity could be detected are shown in the Appendix in Section 9.8.

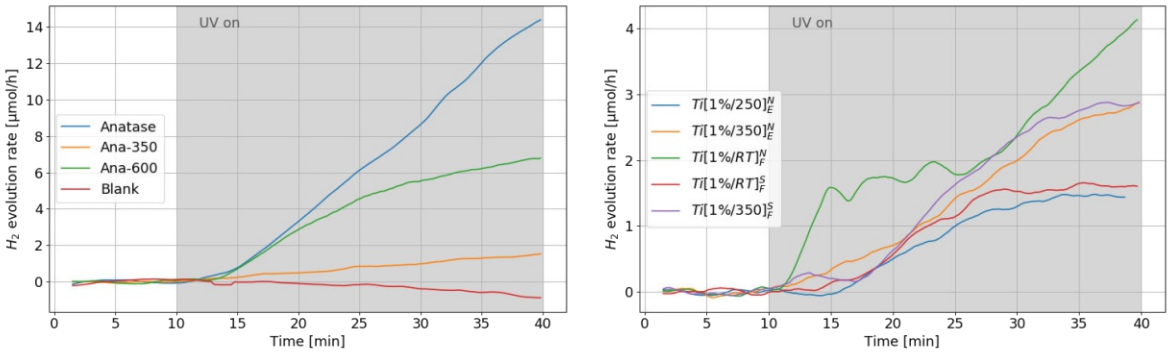

(a) **(b)**

Figure 5.34: Hydrogen evolution rates over 30 min of light illumination with UV light (365 nm). (a) shows the blank experiment and activities of pure anatase, calcined at different temperatures and (b) shows the activities of all the active samples. It should be noted that the scales of the two y-axes are different due to the lower activity of the synthesized catalysts.

When comparing the activities of the anatase samples with the synthesized samples it is clear that none of the produced catalysts shows improved hydrogen evolution efficiency compared to pure anatase. The most active sample is pure anatase followed by anatase calcined at 600 °C.

Looking only at the pure anatase samples, there is a decrease in activity between the uncalcined and the calcined samples which could be explained by an increase in particle size during the calcination, as was seen in the TEM images and XRD diffractograms. The crystal growth can lead to a decreased surface area and therefore a decreased number of active sites for the UV-HER, which causes the lower activity. However, the overall activty of anatase without a co-catalyst is low, so the difference might not be significant.

No sample with a higher V-concentration, nor any sample calcined at 600 °C shows any activity toward UV-HER. So, similar to the OER results the V-species didn't provide better active sites for the HER, compared to the anatase surface.

Die approbierte gedruckte Originalversion dieser Diplomarbeit ist an der TU Wien Bibliothek verfügbar
The approved original version of this thesis is available in print at TU Wien Bibliothek.
TU Bibliothek Your knowledge hub WIEN

Table 5.7: The H_2 evolution rates after 30 min of illumination with UV light (365 nm).

Sample	Max. H_2 Rate [µmol/h]
Anatase	14.6
Ana-350	1.6
Ana-600	6.9
$Ti\,[1\%/RT]_F^N$	4.2
$Ti\,[1\%/250]_F^N$	-
$Ti\,[1\%/350]_F^N$	-
$Ti\,[1\%/RT]_E^N$	-
$Ti\,[1\%/250]_E^N$	1.5
$Ti\,[1\%/350]_E^N$	3.0
$Ti\,[1\%/RT]_F^S$	1.7
$Ti\,[1\%/350]_F^S$	2.9
$Ti\,[1\%/600]_F^S$	-
$Ti\,[1\%/RT]_E^S$	-
$Ti\,[1\%/350]_E^S$	-
$Ti\,[1\%/600]_E^S$	-
$Ti\,[5\%/RT]_E^S$	-
$Ti\,[5\%/350]_E^S$	-
$Ti\,[5\%/600]_E^S$	-
$Ti\,[25\%/RT]_E^S$	-
$Ti\,[25\%/350]_E^S$	-
$Ti\,[25\%/600]_E^S$	-

Die approbierte gedruckte Originalversion dieser Diplomarbeit ist an der TU Wien Bibliothek verfügbar
The approved original version of this thesis is available in print at TU Wien Bibliothek.
TU Bibliothek Your knowledge hub WIEN

5.3.3 Vis-HER

Only those samples which were calcined at the highest temperature (350 °C for samples with NH_4VO_3 or 600 °C for samples with $VOSO_4$) were tested for Vis-HER activity because these samples showed the highest absorption in the visible region. Since the expected yield for hydrogen was very low using only visible light, the detection was performed discontinuously via several injections of gas phase aliquots from the gas volume above the reaction into a GC. The samples were illuminated with a wavelength of 445 nm for at least 80 min and again methanol was used as a sacrificial agent. It should be mentioned again that these experiments were performed with Pt as an additional co-catalyst.

The evolution of the measured H_2 amounts for these samples as well as for pure anatase, a blank sample and pure V_2O_5 powder can be seen in Fig. 5.35. The results of all other tested samples are given in the Appendix in Section 9.9. In order to estimate the standard deviation of the results, the experiment with $Ti\,[5\%/600]_E^S$ was repeated three times consecutively, which can be seen in Fig. 5.35b.

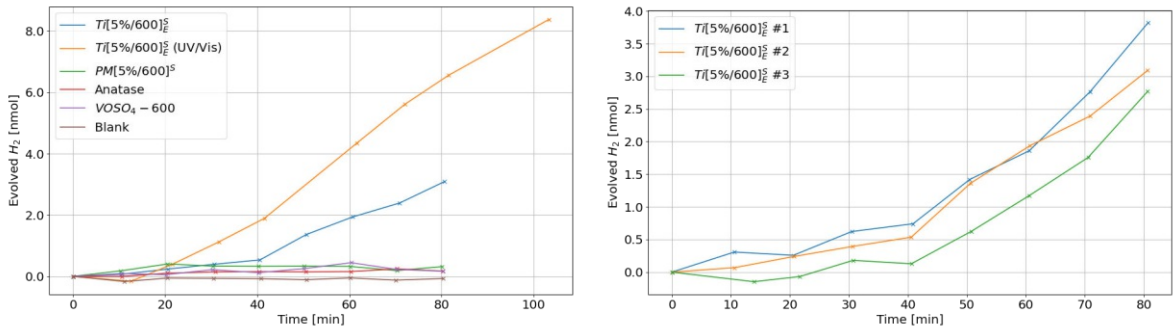

(a) (b)

Figure 5.35: Evolution of the recorded amounts of H_2 during HER experiments under UV illumination. (a) shows a comparison of the active and reference samples, excluding all inactive catalysts and (b) shows a comparison of three repetitions of the experiment performed with the catalyst $Ti\,[5\%/600]_E^S$.

To compare the hydrogen evolution of the samples, the amount of evolved H_2 after 60 min can be seen in Table 5.8. The three values for $Ti\,[5\%/600]_E^S$ were used to calculate the standard deviation of this measurement ($\sigma = 0.4\,\mathrm{nmol\,h^{-1}}$).

The only sample with significant activity was the 5 %-sample $Ti\,[5\%/600]_E^S$ with $VOSO_4$ as the precursor. It shows a mean hydrogen production of $1.7\,\mathrm{nmol\,h^{-1}}$. Since the photodeposition of Pt is dependent on the wavelength of the radiation, an additional experiment with this sample was performed, where the reaction mixture was irradiated with UV light (365 nm) for 10 min and then the illumination wavelength was switched to 445 nm. This sample is labelled "$Ti\,[5\%/600]_E^S$ (UV/Vis)" to indicate the usage of both UV and visible light. This treatment was able to approximately double the hydrogen production to $4\,\mathrm{nmol\,h^{-1}}$. Neither anatase, the pure calcined precursor $VOSO_4$-600, nor the physical mixture $PM[5\%/600]^S$ show any activity, indicating that both semiconductors are involved in the mechanism and that the synthesis introduced electronic interactions at the interface of TiO_2 and V_2O_5 leading to band bending and charge carrier separation after absorption of visible light through the light absorber V_2O_5.

Die approbierte gedruckte Originalversion dieser Diplomarbeit ist an der TU Wien Bibliothek verfügbar
The approved original version of this thesis is available in print at TU Wien Bibliothek.
TU Bibliothek Your knowledge hub WIEN

Table 5.8: Amount of evolved H_2 after 60 min of illumination with visible light (445 nm).

Sample	H_2 Rate [nmol/h]
Anatase	0.2
Blank	-0.1
$VOSO_4$-600	0.4
$Ti\,[1\%/350]_E^N$	-0.1
$Ti\,[1\%/600]_E^S$	0.2
$Ti\,[5\%/350]_E^S$	0.1
$Ti\,[5\%/600]_E^S$ #1	1.9 ± 0.4
$Ti\,[5\%/600]_E^S$ #2	1.9 ± 0.4
$Ti\,[5\%/600]_E^S$ #3	1.2 ± 0.4
$Ti\,[5\%/600]_E^S$ (UVVis)	4.3
$Ti\,[25\%/600]_E^S$	0.2
$PM[5\%/600]^S$	0.3

No 1 %-sample nor the 25 %-sample showed any activity towards hydrogen production under visible light irradiation. Because $Ti\,[5\%/600]_E^S$ was able to produce hydrogen, the sample $Ti\,[5\%/350]_E^S$ was also tested. However, it also didn't show significant activity, indicating that the presence of V_2O_5 is necessary for visible light HER.

The photodeposition of the Pt was confirmed by analyzing the sample via TEM, after centrifuging the reaction mixture and separating the solid catalyst. Images recorded for both samples can be seen in Fig. 5.36 and in the Appendix in Section 9.9.

Both images in Fig. 5.36 show a lot of Pt nanoparticles on the surface of the TiO_2 with diameters between 1.0 nm to 2.5 nm. Comparing the two images reveals that the deposition in visible light lead to denser and bigger particles then the deposition under UV light, however, it was not possible to see if Pt was deposited preferentially on TiO_2 or V_2O_5. The illumination with UV light ($\lambda = 365\,\text{nm} \equiv 3.4\,\text{eV}$) can generate excitons in anatase ($E_g = 3.2\,\text{eV}$) and V_2O_5 ($E_g \approx 2.3\,\text{eV}$) and thereby electrons throughout the whole sample which can then reduce Pt-ions and generate the deposited particles. With visible light irradiation ($\lambda = 445\,\text{nm} \equiv 2.8\,\text{eV}$) the energy of incoming photons is no longer enough to generate excitons in anatase, however, it is still capable of creating electron-hole pairs in V_2O_5. Since the V_2O_5 is more localized at particular areas on the anatase particles, it would be expected that the Pt-ions are likely reduced in the vicinity of the V_2O_5 clusters, leading to more reductions in a smaller area and thereby bigger particles.

Die approbierte gedruckte Originalversion dieser Diplomarbeit ist an der TU Wien Bibliothek verfügbar
The approved original version of this thesis is available in print at TU Wien Bibliothek.
TU Bibliothek Your knowledge hub WIEN

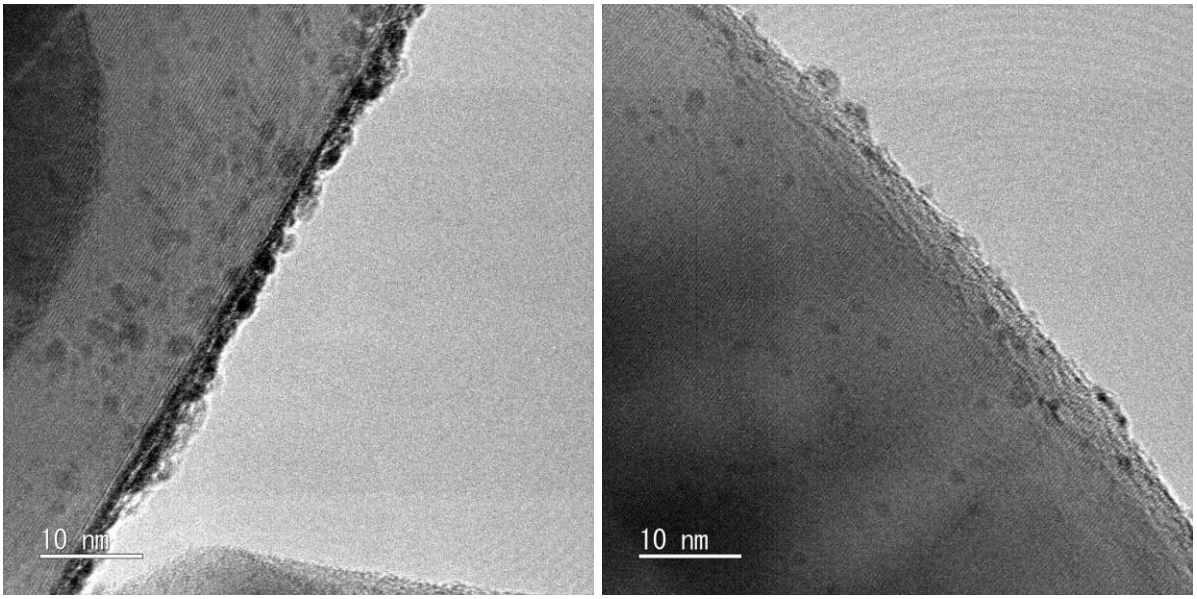

(a) (b)

Figure 5.36: TEM images of the samples (a) $Ti\,[5\%/600]_E^S$ and (b) $Ti\,[5\%/600]_E^S$ (UV/Vis) after the photodeposition of Pt.

5.3.3.1 Leaching

To study the leaching of V and Pt during a Vis-HER experiment, TXRF analysis was performed on a few reaction solutions. After the Vis-HER experiments of the samples $Ti\,[1\%/600]_E^S$, $Ti\,[5\%/600]_E^S$, $Ti\,[5\%/600]_E^S$ (UV/Vis) and $Ti\,[25\%/600]_E^S$ (all samples with $VOSO_4$ as the precursor), the solid catalyst was centrifuged and TXRF was performed on the solution. Table 5.9 shows the percentages of the total sample mass (1 mg) for each leached element and the TXRF spectra can be seen in the Appendix (see Section 9.5).

Table 5.9: The leached amounts of Ti, V and Pt after a Vis-HER experiment based on the total sample mass (1 mg), measured with TXRF.

Sample	Ti[wt%]	V[wt%]	Pt[wt%]
$Ti\,[1\%/600]_E^S$	0.1	10.8	0.0
$Ti\,[5\%/600]_E^S$	0.1	6.5	9.4
$Ti\,[5\%/600]_E^S$ (UV/Vis)	0.0	14.1	38.4
$Ti\,[25\%/600]_E^S$	0.1	20.0	70.2

While almost no Ti was present in the reaction solution, not all of the V stayed on the particles. V_2O_5 is slightly soluble in water (0.8 g/L) which could explain the high amounts of leached vanadium [114]. The amount of Pt, which was still present in the solution after the experiment, increased with the amount of V and also for the UVVis sample. This could also be related to

Die approbierte gedruckte Originalversion dieser Diplomarbeit ist an der TU Wien Bibliothek verfügbar
The approved original version of this thesis is available in print at TU Wien Bibliothek.
TU Bibliothek Your knowledge hub WIEN

the higher amounts of leached V in the UVVis and 25 % sample, because Pt, that was deposited onto V_2O_5, would also be removed from the sample if the V_2O_5 dissolves.

Die approbierte gedruckte Originalversion dieser Diplomarbeit ist an der TU Wien Bibliothek verfügbar
The approved original version of this thesis is available in print at TU Wien Bibliothek.
TU WIEN Bibliothek Your knowledge hub

5.4 Discussion

5.4.1 Material characterization

The characterization of the catalysts revealed that the calcination of samples with 5 at% and 25 at% vanadium led to the formation of heterojunctions between TiO_2 and V_2O_5 particles. The TEM images show that part of the uncalcined catalyst particles are covered with a layer of the precursor, which, after calcination, turned into V_2O_5 interfacing with the TiO_2 particles (e.g. see Fig. 5.4 and 5.6). Also the SEM, XRD, IR and Raman results confirm that the precursor turned into V_2O_5 for the 5 % and 25 % samples after the calcination at 600 °C.

The situation is different for the 1 % samples. Although the TEM analysis revealed distinct structures of the precursor on the anatase particles, IR, Raman and XRD were not able to detect any signals belonging to a VO_x phase. This is probably caused by the low concentration, however, it could also mean that the V didn't form oxides here, but is rather present as surface or bulk dopants in the anatase.

Influence of V on the rutile transformation

The XRD results show that the addition of the precursor led to an increased rutilation during calcination (see Fig. 5.8b and 5.18). The promotion of the phase transformation by foreign ions is explained through the generation of oxygen vacancies, e.g. via substitutional doping of small ions with a lower valence than four [77, 115]. Transformation to rutile happens via ionic transport and is associated with a lattice contraction. The oxygen vacancies destabilise the large and rigid oxygen sublattice and thereby promote the ionic transfer and decrease the transformation temperature [116]. In contrast to substitutional doping, interstitial doping of any ions seems to stabilise the lattice and therefore only hinder the transformation [79]. Another reason for the phase transformation at lower temperatures could be heterogeneous nucleation of V_2O_5. Vejux and Courtine explained the increased rutilation with elastic stress, excerted onto the anatase surface by loaded V_2O_5, thereby increasing the surface energy of TiO_2 and decreasing the activation barrier for the transformation [117].

This was also observed in the Raman analysis (see Fig. 5.11 and 5.21). Both, the 25 %- as well as the 5 %-samples exhibit peak broadening and a blue shift of the anatase $E_g(1)$ peak of about $12\,cm^{-1}$ and $10\,cm^{-1}$ respectively. The intensity of the shift also increases after the calcination at 600 °C. The blue shift of this anatase band is usually associated with size-confinement in TiO_2 nanoparticles [96]. However, since the nanoparticles didn't undergo any heat treatment during the first synthesis step, the size of the anatase particles can be assumed to be unchanged in the unmodified catalysts. The shift is rather attributed to surface strain, caused by the formation of a vanadium-oxide layer and possibly the incorporation of V^{+4} into the lattice [80, 97, 118, 119]. The 1 at%-samples don't exhibit this blue shift in the Raman spectra and the XRD spectra also didn't show an increased amount of rutile compared to unmodified anatase (see Fig. 5.27 and 5.30).

Die approbierte gedruckte Originalversion dieser Diplomarbeit ist an der TU Wien Bibliothek verfügbar
The approved original version of this thesis is available in print at TU Wien Bibliothek.
TU Bibliothek Your knowledge hub WIEN

Influence of the V-concentration on its oxidation state

The XPS analysis of the 25 %-sample $Ti\,[25\%/600]_E^S$ showed that the V on this sample is mostly present as V^{+5}. But because of the very broad V^{+5} peak it cannot be excluded that a small amount of V^{+4} is also present. This means that most of the V exists as V_2O_5 oxide with possibly defect V_2O_5 near the interface of the two SC. IR and Raman experiments revealed that this oxide is also present in the 5 %-samples. The XPS analysis of the 1 %-samples $Ti\,[1\%/350]_E^N$, $Ti\,[1\%/350]_E^S$ and $Ti\,[1\%/600]_E^S$, however, revealed that the vanadium could be present as V^{+4} on these samples, even though vanadium is present as V^{+5} in the precursor NH_4VO_3. Bañares et al. have observed that for low V contents on TiO_2, V^{+4} is the preferred oxidation state due to a strong stabilization of V^{+4} ions by hydroxyl groups on the TiO_2 surface, which is favoured because of the very similar ionic radii of Ti^{+4} (61 pm) and V^{+4} (58 pm) [32, 118]. This suggests that the V on the 1 %-samples is dispersed on the TiO_2 surface, through interactions with the hydroxyl groups on the anatase surface and that the interface between V_2O_5 and TiO_2 in the 5 % and 25 % samples probably also contains V^{+4}.

5.4.2 Photocatalytic characterization

Role of V as a co-catalyst

None of the produced catalysts were active during OER or UV-HER, suggesting that the V-species that were produced on the anatase aren't active co-catalysts for these reactions. The DRS results showed that all samples, as well as the calcined precursor alone, strongly absorb UV light with a wavelength of 365 nm, leading to the generation of excitons in anatase as well as in V_2O_5. However, the heterojunction between anatase and V_2O_5 leads to charge separation where the holes stay in V_2O_5.

For the OER, this means that the holes now lie at a lower energy level, thereby reducing the energy difference between the holes and the oxidation potential for the water oxidation. Since this reaction is typically kinetically hindered due to it being a four-hole process, this strongly affects the oxygen evolution rate [120, 121]. The OER results exhibit this trend as well, where the catalyst activity decreases with increasing vanadium content because of an increased amount of holes has a reduced potential. The highest activity by far was achieved by the anatase powder calcined at 600 °C, which could have been caused by the formation of rutile, as was seen in the XRD results. Calcined anatase has been reported to be more photocatalytically active due to the formation of the rutile phase (E_g = 3.0 eV) [26, 122–124].

Fig. 5.37 shows the H_2 evolution activities measured during the UV-HER experiments. The results show that all samples modified with V show a lower activity than pure anatase and no 5 at% nor any 25 at% sample were able to produce any measurable amount of hydrogen.

The presence of the vanadium species seems to hinder the hydrogen evolution. This suggests that V_2O_5 is not a suitable co-catalyst for anatase for photocatalytic hydrogen evolution. From the bandgaps in Fig. 2.4 and the DRS analysis it is expected that, under UV light, both semiconductors can produce excitons. Due to the energy difference in the band positions, the electrons will then jump to the conduction band of anatase whereas the holes will move to

Die approbierte gedruckte Originalversion dieser Diplomarbeit ist an der TU Wien Bibliothek verfügbar
The approved original version of this thesis is available in print at TU Wien Bibliothek.
TU Bibliothek Your knowledge hub WIEN

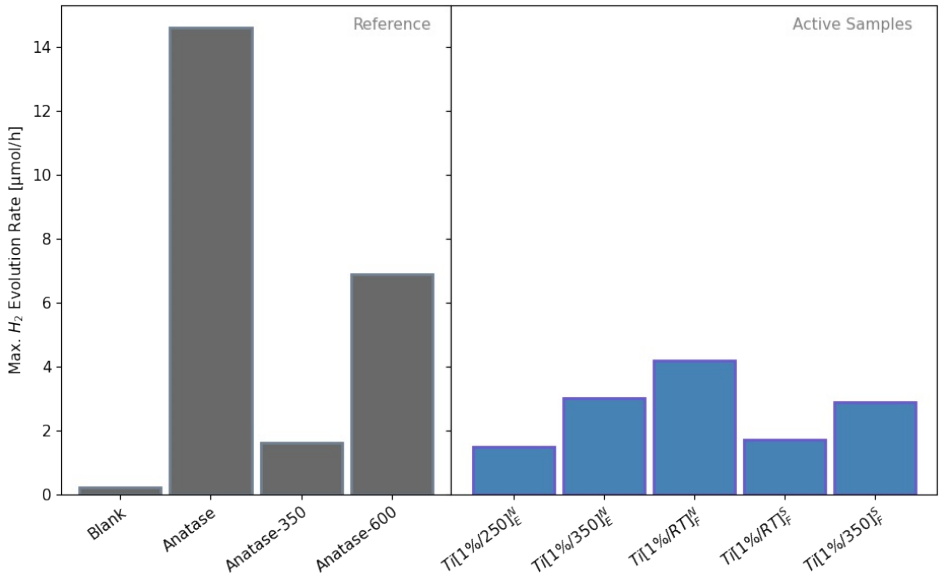

Figure 5.37: Hydrogen evolution activities for the UV-HER experiments. Only those samples which were able to produce some amount of H_2 are shown. Uncalcined and unmodified anatase shows the highest HER activity.

V_2O_5, leading to charge separation. This usually improves the photocatalytic activity, but the vanadium species also covers part of the surface area of the anatase nanoparticles. The UV-HER experiments suggest that the coverage of the anatase surface is detrimental to the hydrogen evolution rate, because the samples with higher V-concentrations show no activity towards hydrogen production anymore. This phenomenon is also known to occur with other co-catalysts, e.g. Pt, where an increased concentration of the co-catalyst leads to the blocking of light via the coverage of active catalyst surface or where the co-catalyst starts to act as a charge recombination centre [125–127]. There is typically an optimal surface concentration for a given co-catalyst, that results in an improved activity due to the effects mentioned in Section 2.2.1 but where the concentration still doesn't significantly affect the light absorption and the availability of active sites. Since the uncalcined precursors are soluble in water and the experiment was performed in a water/methanol mixture the precursors of the uncalcined samples may have dissolved in the reaction mixture.

Similarly, the intermediate vanadium species on the samples calcined at medium temperatures (250 °C for NH_4VO_3 leading to $NH_4V_3O_8$, and 350 °C for $VOSO_4$ leaving the precursor mostly unmodified, see Section 5.1) could also have been still soluble in the water/methanol mixture leading to mostly unmodified anatase in a solution of the precursor species in both cases. This could explain the small activity of the few samples which were able to produce hydrogen.

Role of V as a light absorber

Contrary to the photocatalytic activity under UV light, the synthesized catalysts were able to improve the activity of anatase when illuminated with visible light. The sample $Ti\,[5\%/600]_E^S$ (5 at% V with $VOSO_4$ as the precursor and calcined at 600 °C) was able to produce hydrogen at a rate of approx. 2 nmol h^{-1} which increased to about 4 nmol h^{-1} when the deposition of Pt as the co-catalyst was performed under UV illumination prior to the visible light HER experiment.

Die approbierte gedruckte Originalversion dieser Diplomarbeit ist an der TU Wien Bibliothek verfügbar
The approved original version of this thesis is available in print at TU Wien Bibliothek.
TU Bibliothek Your knowledge hub WIEN

Fig. 5.38 shows a bar plot with the activities of all analysed catalysts and the standard deviation of sample $Ti\,[5\%/600]_E^S$ as error bars. The results clearly shows, that V_2O_5 is able to work as a light absorber for TiO_2, since neither pure TiO_2 nor the calcined precursor on its own ($VOSO_4$-600) were able to produce H_2 under illumination with visible light. Only when the two SCs are forming a heterojunction, can the calcined precursor inject excited electrons into anatase, thereby enabling the HER.

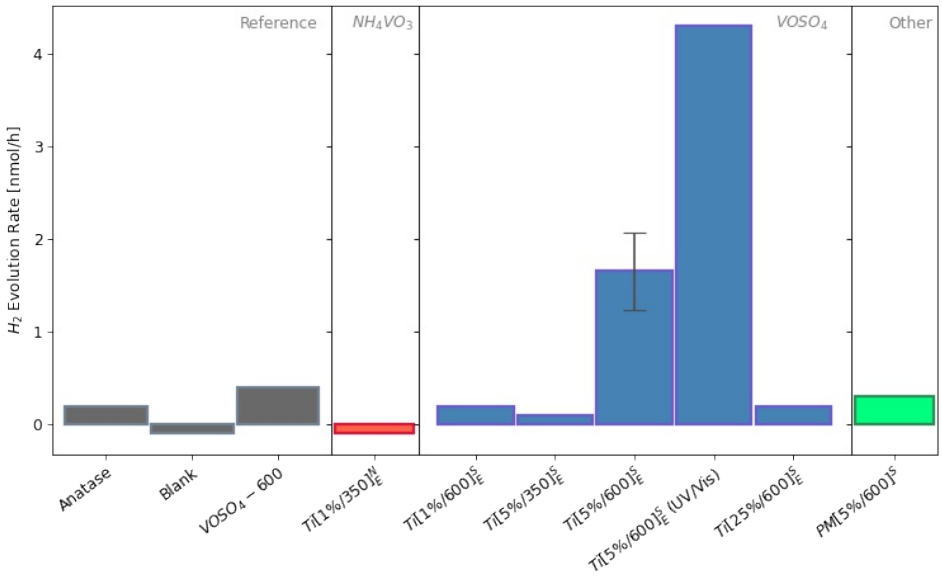

Figure 5.38: Vis-HER activities for all tested samples with the standard deviation for the $Ti\,[5\%/600]_E^S$ experiments as an error bar. The results show that V_2O_5 was able to work as a light absorber for TiO_2, allowing for HER activity under visible light illumination.

The DRS results revealed that the visible light absorption increased with the V-content. The band positions of pure anatase and V_2O_5 would make an electron transfer unlikely, since the CB of pure V_2O_5 lies at a lower energy level than the CB of TiO_2. However, the heterojunction between the two semiconductors leads to the equalization of the Fermi-levels (E_f) and, as a consequence, also to band bending of the CB and VB of both semiconductors. This elevates the band position of V_2O_5 over the required potential for the HER, making it a suitable light absorber (see Fig. 2.4 in Section 2.2.2). Additionally, it means that excited e^- generated in V_2O_5 transfer to the anatase conduction band while the holes stay behind, leading to charge separation. This, for one, improves the lifetime of excited charge carriers and thereby also the photoactivity and second, it populates the CB of anatase with excited electrons which can then further travel to the Pt co-catalyst. These can then react with protons to form H_2 while the holes in V_2O_5 are used to oxidise methanol.

The sample $Ti\,[5\%/600]_E^S$ (UVVis) where the Pt deposition was performed under UV light showed even better results than $Ti\,[5\%/600]_E^S$, where the deposition was performed under visible light. The TEM analysis of the Pt deposition indicated that the pre-illumination with UV light led to denser and bigger Pt clusters. This could lead to a reduced surface area of Pt, which could be detrimental to the activity. Additionally, the photodeposition of Pt with UV light would lead to a higher percentage of Pt being deposited on the TiO_2 surface since excited electrons can be

Die approbierte gedruckte Originalversion dieser Diplomarbeit ist an der TU Wien Bibliothek verfügbar
The approved original version of this thesis is available in print at TU Wien Bibliothek.
TU Bibliothek Your knowledge hub WIEN

generated directly in TiO_2, whereas under visible light illumination, they are only generated in V_2O_5. This can also contribute to a higher activity of $Ti\,[5\%/600]_E^S$ (UVVis) since under visible light illumination V_2O_5 acts as a light absorber injecting the excited electrons into TiO_2. However, the analysis of Pt content in the reaction mixture after the experiment, showed that for sample $Ti\,[5\%/600]_E^S$ (UVVis) more Pt was still present in solution compared to $Ti\,[5\%/600]_E^S$ which was illuminated only with visible light. This means that either less Pt was deposited on the sample, or that Pt was more easily removed from the surface in the case of the (UVVis) sample. The higher activity of $Ti\,[5\%/600]_E^S$ (UVVis) which had less Pt on the surface could indicate that a higher concentration of Pt could already act as recombination centers for excitons or block the surface of the catalyst for light illumination [128].

The calcined precursor $VOSO_4$-600 with Pt as a co-catalyst didn't show any activity, indicating that TiO_2 is needed to produce hydrogen. This could be because of missing active sites due to a smaller surface area, since the precursor didn't form nanoparticles, or due to increased recombination of excited charge carriers. Also, the conduction band position of V_2O_5 is approx. 0.3 V which lies below the required potential for the HER (0.0 V at pH0 and −0.41 V at pH7). The physical mixture sample $PM[5\%/600]^S$ also didn't show any activity, most likely because for band bending to occur, the two semiconductors have to form a heterojunction, meaning a close contact of the crystal structures, which was not achieved by simply mixing the two powders.

Influence of the V-concentration on the Vis-HER activity

The lower activity of the 25 %-sample can be explained by a higher surface coverage of the anatase by the vanadium oxide. Since the electrons are first transferred onto anatase at the heterojunction and then travel to the Pt nanoparticles, the protons for the HER need to access Pt on the anatase surface in order to be reduced (see Fig. 5.39). The TEM results showed that

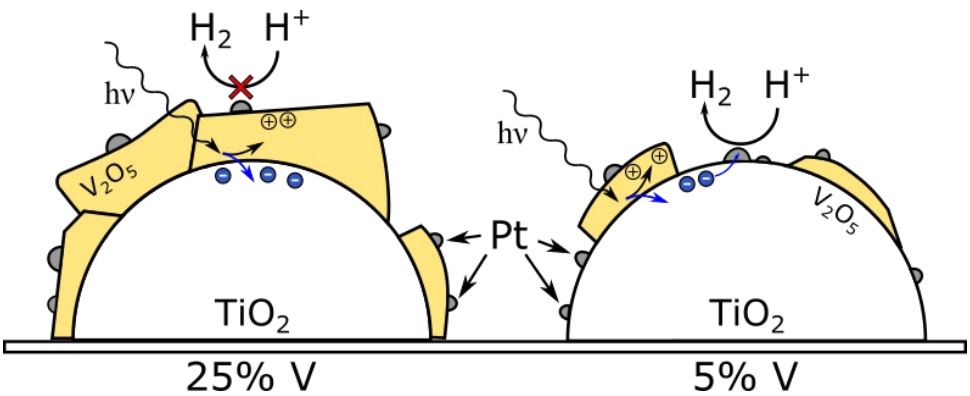

Figure 5.39: Difference between the anatase surface coverage of the 25 % samples vs. the 5 % samples. In order for the HER to occur, protons need to have access to Pt nanoparticles on the anatase surface, since excited electrons, forming at the heterojunction, are transferred to anatase first and then onto the Pt nanoparticles.

the anatase particles were partly covered by a layer which could block the surface and inhibit hydrogen production. The 25 %-sample, where the layer was most pronounced, likely blocks more of this surface thereby hindering the hydrogen production.

Compared to the 5 % sample, it could also be that less of the formed V_2O_5 is in close proximity to the TiO_2 surface due to the formation of bigger V_2O_5 particles. This could reduce the activity

Die approbierte gedruckte Originalversion dieser Diplomarbeit ist an der TU Wien Bibliothek verfügbar
The approved original version of this thesis is available in print at TU Wien Bibliothek.
TU Bibliothek Your knowledge hub WIEN

since V_2O_5 can only act as a light absorber, through the formation of a heterojunction with TiO_2 at an interface between the two SC. A bigger particle size reduced the relative amount of V_2O_5 that is in close contact with TiO_2 and also would require larger diffusion lengths of excited electrons. Additionally, the co-catalyst Pt needs to be deposited onto the anatase surface instead of onto V_2O_5, since only the interface between anatase and Pt is able to promote the HER. The leaching analysis also showed that approx. 70 % of the Pt was still dissolved in the solution after the experiment, indicating that the deposition couldn't happen effectively under the illumination with visible light.

The 1 %-samples were also not active during Vis-HER. The amount of V-species in these catalysts is probably too low to lead to significant visible light absorption.

This means that the 5 % sample $Ti\,[5\%/600]_E^S$ has the optimal V-concentration from the different amounts that were investigated in this thesis. With 5 at% of V, enough V_2O_5 has formed for the formation of heterojunctions between TiO_2 and V_2O_5 and compared to the higher concentration of 25 at%, most of it is still in close interaction with TiO_2 while still leaving the anatase surface available for the actual HER to happen.

Die approbierte gedruckte Originalversion dieser Diplomarbeit ist an der TU Wien Bibliothek verfügbar
The approved original version of this thesis is available in print at TU Wien Bibliothek.
TU Bibliothek Your knowledge hub WIEN

Conclusion

V-modified TiO_2 samples with 25 at%, 5 at% and 1 at% of V were synthesized, using a very simple, solvent-free impregnation method and tested for their photocatalytic activity toward HER and OER. The initial structural and optical characterization revealed that the 25 at%- and 5 at%-samples consisted of composites between TiO_2 and V_2O_5 while the 1 at%-samples contained mostly V^{+4} from vanadium species on the TiO_2 surface or doped in the TiO_2 lattice. However, in both cases, the synthesized samples showed an increased absorption in the visible light range, while the bandgaps stayed mostly unaffected. Additionally, the addition of vanadium in the 5 at%- and 25 at%-samples has led to an increased amount of rutile which formed during the calcination at 600 °C.

While the catalysts were not photocatalytically active under UV light illumination, the sample $Ti\,[5\%/600]_E^S$ with 5 at% V was able to produce hydrogen at a rate of approx. 4 nmol h^{-1} with 1 mg of catalyst. The measured hydrogen production rates under visible light illumination can be seen in Fig. 5.38. While unmodified anatase wasn't active at all under the applied experimental conditions, the achieved activity is still way less than e.g. the hydrogen production rate reported by Martha et al. who prepared a visible light responsive V_2O_5/N,S-TiO_2 composite photocatalyst which achieved an activity for H_2 evolution of almost 3000 µmol h^{-1} g^{-1} during sacrificial water splitting [129]. This means that V_2O_5 was not able to work as a co-catalyst that provides active sites for the HER or OER reaction, but instead it worked as a visible light absorber, injecting electrons into anatase. These excited electrons could then get transferred onto Pt which worked as the co-catalyst for HER. The hydrogen production could be improved by performing the photodeposition of the Pt under UV light, which led to more distributed and smaller Pt clusters on the TiO_2 surface. However, an optimal V concentration for the light absorption exists, since neither the 1 at%-samples nor the 25 at%-samples didn't show any activity in the Vis-HER experiments. The concentration of 1 at% was probably too low to form significant amounts of V_2O_5, while most of the V_2O_5 in the 25 at%-samples wasn't in close enough interaction with the TiO_2 or blocked its surface for the HER.

Die approbierte gedruckte Originalversion dieser Diplomarbeit ist an der TU Wien Bibliothek verfügbar
The approved original version of this thesis is available in print at TU Wien Bibliothek.
TU Bibliothek Your knowledge hub WIEN

Outlook

During this project, catalysts with three different V-concentrations have been synthesized, all starting from the precursor $VOSO_4$. The photocatalytic experiments revealed that the V-species were not active as a co-catalyst, but were able to function as a light absorber for TiO_2. Further studies should be done to investigate the exact mechanism and the optimization of the V-concentration and morphology. Only the 1 at%-samples were synthesized with an additional precursor to study the effect of a different precursor oxidation state, because further studies would have exceeded the boundaries of the current project. Further studies with NH_4VO_3 with higher concentrations could be done in order to better compare the two precursors and the influence of the oxidation state of vanadium. Here, additional XPS studies of the 5 % sample as well as samples, calcined at different intermediate temperatures could enhance our understanding of the processes occurring at the TiO_2 surface.

It would also be interesting to further study the difference between bulk V_2O_5 and the V-species present on the surface of TiO_2. The IR analysis revealed a difference in the V=O band absorption between pure bulk V_2O_5 and the same band in the synthesized samples. However, also the physical mixture showed the same difference in the V=O absorption, which cannot be explained by a structural difference. Further IR studies and Raman studies of the physical mixture could elucidate the structure of the V_2O_5 on the synthesized samples, compared to the physical mixture.

Additionally, it would be interesting to see if the hydrogen production could be optimized by varying the V concentration near 5 at%. Since this was the only active sample, nothing can be said about a possible correlation between the hydrogen production and increasing or decreasing the V concentration. The Pt deposition could also be optimized. The experiments revealed that ex-situ deposition under UV light increased the hydrogen production, however, approx. 40 % of the added Pt weren't deposited under these conditions.

Finally, additional photocatalytic experiments, like the degradation of organic molecules or CO_2 reduction, could be performed with the synthesized catalysts.

Die approbierte gedruckte Originalversion dieser Diplomarbeit ist an der TU Wien Bibliothek verfügbar
The approved original version of this thesis is available in print at TU Wien Bibliothek.
TU Bibliothek Your knowledge hub WIEN

References

[1] *Global Footprint Network National Footprint and Biocapacity Accounts, 2021 Edition*. Open Data Platform. URL: https://data.footprintnetwork.org/#/ (visited on 02/14/2021).

[2] *Evidence & Causes of Climate Change | Royal Society*. URL: https://royalsociety.org/topics-policy/projects/climate-change-evidence-causes/ (visited on 02/20/2021).

[3] *Causes of Climate Change*. Climate Action - European Commission. Nov. 23, 2016. URL: https://ec.europa.eu/clima/change/causes_en (visited on 02/20/2021).

[4] A. Raval and V. Ramanathan. "Observational Determination of the Greenhouse Effect". In: *Nature* 342.6251 (6251 Dec. 1989), pp. 758–761. ISSN: 1476-4687. DOI: 10.1038/342758a0.

[5] H. Rodhe. "A Comparison of the Contribution of Various Gases to the Greenhouse Effect". In: *Science* 248.4960 (June 8, 1990), pp. 1217–1219. ISSN: 0036-8075, 1095-9203. DOI: 10.1126/science.248.4960.1217. pmid: 17809907.

[6] *2017 Renewables Global Futures Report*. REN21. June 14, 2019. URL: https://www.ren21.net/2017-renewables-global-futures-report/ (visited on 02/15/2021).

[7] W. Krewitt, K. Nienhaus, C. Kleßmann, C. Capone, E. Stricker, W. Graus, M. Hoogwijk, N. Supersberger, U. von Winterfeld, and S. Samadi. "Role and Potential of Renewable Energy and Energy Efficiency for Global Energy Supply". In: (2009).

[8] M. Fischedick, R. Schaeffer, A. Adedoyin, M. Akai, T. Bruckner, L. Clarke, V. Krey, I. Savolainen, S. Teske, D. Ürge-Vorsatz, and R. Wright. "Mitigation Potential and Costs". In: *IPCC Special Report on Renewable Energy Sources and Climate Change Mitigation*. Ed. by O. Edenhofer, R. Pichs-Madruga, Y. Sokona, K. Seyboth, P. Matschoss, S. Kadner, T. Zwickel, P. Eickemeier, G. Hansen, S. Schlömer, and C. von Stechow. Cambridge, United Kingdom and New York, NY, USA: Cambridge University Press, 2011.

[9] G. W. Crabtree and N. S. Lewis. "Solar Energy Conversion". In: *Physics Today* 60.3 (Mar. 1, 2007), pp. 37–42. ISSN: 0031-9228. DOI: 10.1063/1.2718755.

[10] R. R. Langeslay, D. M. Kaphan, C. L. Marshall, P. C. Stair, A. P. Sattelberger, and M. Delferro. "Catalytic Applications of Vanadium: A Mechanistic Perspective". In: *Chemical Reviews* 119.4 (Feb. 27, 2019), pp. 2128–2191. ISSN: 0009-2665. DOI: 10.1021/acs.chemrev.8b00245.

[11] A. Fujishima and K. Honda. "Electrochemical Photolysis of Water at a Semiconductor Electrode". In: *Nature* 238.5358 (5358 July 1972), pp. 37–38. ISSN: 1476-4687. DOI: 10.1038/238037a0.

[12] M. R. Hoffmann, S. T. Martin, W. Choi, and D. W. Bahnemann. "Environmental Applications of Semiconductor Photocatalysis". In: *Chemical Reviews* 95.1 (Jan. 1995), pp. 69–96. ISSN: 0009-2665. DOI: 10.1021/cr00033a004.

[13] O. Carp, C. Huisman, and A. Reller. "Photoinduced Reactivity of Titanium Dioxide". In: *Progress in Solid State Chemistry* 32.1-2 (Jan. 2004), pp. 33–177. ISSN: 0079-6786. DOI: 10.1016/J.PROGSOLIDSTCHEM.2004.08.001.

[14] N. S. Leyland, J. Podporska-Carroll, J. Browne, S. J. Hinder, B. Quilty, and S. C. Pillai. "Highly Efficient F, Cu Doped TiO 2 Anti-Bacterial Visible Light Active Photocatalytic Coatings to Combat Hospital-Acquired Infections". In: *Scientific Reports* 6.1 (1 Apr. 21, 2016), pp. 1–10. ISSN: 2045-2322. DOI: 10.1038/srep24770.

[15] N. Sakai, A. Fujishima, T. Watanabe, and K. Hashimoto. "Quantitative Evaluation of the Photoinduced Hydrophilic Conversion Properties of TiO2 Thin Film Surfaces by the Reciprocal of Contact Angle". In: *The Journal of Physical Chemistry B* 107.4 (Jan. 1, 2003), pp. 1028–1035. ISSN: 1520-6106. DOI: 10.1021/jp022105p.

[16] F. E. Osterloh. "Photocatalysis versus Photosynthesis: A Sensitivity Analysis of Devices for Solar Energy Conversion and Chemical Transformations". In: *ACS Energy Letters* 2.2 (Feb. 10, 2017), pp. 445–453. DOI: 10.1021/acsenergylett.6b00665.

[17] D. Reyes-Coronado, G. Rodríguez-Gattorno, M. E. Espinosa-Pesqueira, C. Cab, R. de Coss, and G. Oskam. "Phase-Pure TiO2 Nanoparticles: Anatase, Brookite and Rutile". In: *Nanotechnology* 19.14 (Apr. 2008), p. 145605. DOI: 10.1088/0957-4484/19/14/145605.

[18] K. Hashimoto, H. Irie, and A. Fujishima. "TiO2 Photocatalysis: A Historical Overview and Future Prospects". In: *Japanese Journal of Applied Physics* 44.12 (Dec. 2005), pp. 8269–8285. ISSN: 0021-4922. DOI: 10.1143/JJAP.44.8269.

Die approbierte gedruckte Originalversion dieser Diplomarbeit ist an der TU Wien Bibliothek verfügbar
The approved original version of this thesis is available in print at TU Wien Bibliothek.
TU Bibliothek Your knowledge hub WIEN

[19] S. A. Ansari, M. M. Khan, M. O. Ansari, and M. H. Cho. "Nitrogen-Doped Titanium Dioxide (N-Doped TiO2) for Visible Light Photocatalysis". In: *New Journal of Chemistry* 40.4 (Apr. 11, 2016), pp. 3000–3009. ISSN: 1369-9261. DOI: 10.1039/C5NJ03478G.

[20] C. Di Valentin, E. Finazzi, G. Pacchioni, A. Selloni, S. Livraghi, M. C. Paganini, and E. Giamello. "N-Doped TiO2: Theory and Experiment". In: *Chemical Physics*. Doping and Functionalization of Photoactive Semiconducting Metal Oxides 339.1 (Oct. 15, 2007), pp. 44–56. ISSN: 0301-0104. DOI: 10.1016/j.chemphys.2007.07.020.

[21] X. Kang, S. Liu, Z. Dai, Y. He, X. Song, Z. Tan, X. Kang, S. Liu, Z. Dai, Y. He, X. Song, and Z. Tan. "Titanium Dioxide: From Engineering to Applications". In: *Catalysts* 9.2 (Feb. 2019), p. 191. ISSN: 2073-4344. DOI: 10.3390/catal9020191.

[22] J. Z. Bloh, R. Dillert, and D. W. Bahnemann. "Zinc Oxide Photocatalysis: Influence of Iron and Titanium Doping and Origin of the Optimal Doping Ratio". In: *ChemCatChem* 5.3 (Mar. 1, 2013), pp. 774–778. ISSN: 1867-3880. DOI: 10.1002/cctc.201200558.

[23] K. Maeda and K. Domen. "New Non-Oxide Photocatalysts Designed for Overall Water Splitting under Visible Light". In: *The Journal of Physical Chemistry C* 111.22 (June 1, 2007), pp. 7851–7861. ISSN: 1932-7447. DOI: 10.1021/jp070911w.

[24] W. J. Youngblood, S.-H. A. Lee, Y. Kobayashi, E. A. Hernandez-Pagan, P. G. Hoertz, T. A. Moore, A. L. Moore, D. Gust, and T. E. Mallouk. "Photoassisted Overall Water Splitting in a Visible Light-Absorbing Dye-Sensitized Photoelectrochemical Cell". In: *Journal of the American Chemical Society* 131.3 (Jan. 28, 2009), pp. 926–927. ISSN: 0002-7863. DOI: 10.1021/ja809108y.

[25] Z. Zhang and J. T. Yates. "Band Bending in Semiconductors: Chemical and Physical Consequences at Surfaces and Interfaces". In: *Chemical Reviews* 112.10 (Oct. 10, 2012), pp. 5520–5551. ISSN: 0009-2665. DOI: 10.1021/cr3000626.

[26] D. O. Scanlon, C. W. Dunnill, J. Buckeridge, S. A. Shevlin, A. J. Logsdail, S. M. Woodley, C. R. A. Catlow, M. J. Powell, R. G. Palgrave, I. P. Parkin, G. W. Watson, T. W. Keal, P. Sherwood, A. Walsh, and A. A. Sokol. "Band Alignment of Rutile and Anatase TiO 2". In: *Nature Materials* 12.9 (9 Sept. 2013), pp. 798–801. ISSN: 1476-4660. DOI: 10.1038/nmat3697.

[27] J. Yang, D. Wang, H. Han, and C. Li. "Roles of Cocatalysts in Photocatalysis and Photoelectrocatalysis". In: *Accounts of Chemical Research* 46.8 (Aug. 20, 2013), pp. 1900–1909. ISSN: 0001-4842. DOI: 10.1021/ar300227e.

[28] D. Y. C. Leung, X. Fu, C. Wang, M. Ni, M. K. H. Leung, X. Wang, and X. Fu. "Hydrogen Production over Titania-Based Photocatalysts". In: *ChemSusChem* 3.6 (June 21, 2010), pp. 681–694. ISSN: 1864-5631. DOI: 10.1002/cssc.201000014.

[29] Y. Z. Yang, C. .-H. Chang, and H. Idriss. "Photo-Catalytic Production of Hydrogen Form Ethanol over M/TiO2 Catalysts (M=Pd, Pt or Rh)". In: *Applied Catalysis B: Environmental* 67.3 (Oct. 5, 2006), pp. 217–222. ISSN: 0926-3373. DOI: 10.1016/j.apcatb.2006.05.007.

[30] W. C. Hao, S. K. Zheng, C. Wang, and T. M. Wang. "Comparison of the Photocatalytic Activity of TiO2 Powder with Different Particle Size". In: *Journal of Materials Science Letters* 21.20 (Oct. 1, 2002), pp. 1627–1629. ISSN: 1573-4811. DOI: 10.1023/A:1020386019893.

[31] D. S. Kim, S. J. Han, and S.-Y. Kwak. "Synthesis and Photocatalytic Activity of Mesoporous TiO2 with the Surface Area, Crystallite Size, and Pore Size". In: *Journal of Colloid and Interface Science* 316.1 (Dec. 1, 2007), pp. 85–91. ISSN: 0021-9797. DOI: 10.1016/j.jcis.2007.07.037.

[32] R. D. Shannon. "Revised Effective Ionic Radii and Systematic Studies of Interatomic Distances in Halides and Chalcogenides". In: *Acta Crystallographica Section A: Crystal Physics, Diffraction, Theoretical and General Crystallography* 32.5 (5 Sept. 1, 1976), pp. 751–767. ISSN: 0567-7394. DOI: 10.1107/S0567739476001551.

[33] J. Lichtenberger and M. D. Amiridis. "Catalytic Oxidation of Chlorinated Benzenes over V2O5/TiO2 Catalysts". In: *Journal of Catalysis* 223.2 (Apr. 25, 2004), pp. 296–308. ISSN: 0021-9517. DOI: 10.1016/j.jcat.2004.01.032.

[34] G. Tuenter, W. F. van Leeuwen, and L. Snepvangers. "Kinetics and Mechanism of the NOx Reduction with NH3 on V2O5 - WO3-TiO2 Catalyst". In: *Industrial & Engineering Chemistry Product Research and Development* 25.4 (Dec. 1, 1986), pp. 633–636. ISSN: 0196-4321. DOI: 10.1021/i300024a607.

[35] F. Roozeboom, T. Fransen, P. Mars, and P. J. Gellings. "Vanadium Oxide Monolayer Catalysts. I. Preparation, Characterization, and Thermal Stability". In: *Zeitschrift für*

Die approbierte gedruckte Originalversion dieser Diplomarbeit ist an der TU Wien Bibliothek verfügbar
The approved original version of this thesis is available in print at TU Wien Bibliothek.
TU Bibliothek Your knowledge hub WIEN

anorganische und allgemeine Chemie 449.1 (Feb. 1979), pp. 25–40. ISSN: 0044-2313, 1521-3749. DOI: 10.1002/zaac.19794490102.

[36] I. E. Wachs. "Catalysis Science of Supported Vanadium Oxide Catalysts". In: *Dalton Transactions* 42.33 (Aug. 2, 2013), pp. 11762–11769. ISSN: 1477-9234. DOI: 10.1039/C3DT50692D.

[37] H. Y. Kim, H. M. Lee, R. G. S. Pala, V. Shapovalov, and H. Metiu. "CO Oxidation by Rutile TiO2(110) Doped with V, W, Cr, Mo, and Mn". In: *The Journal of Physical Chemistry C* 112.32 (Aug. 1, 2008), pp. 12398–12408. ISSN: 1932-7447. DOI: 10.1021/jp802296g.

[38] S.-W. Cao, Z. Yin, J. Barber, F. Y. C. Boey, S. C. J. Loo, and C. Xue. "Preparation of Au-BiVO4 Heterogeneous Nanostructures as Highly Efficient Visible-Light Photocatalysts". In: *ACS Applied Materials & Interfaces* 4.1 (Jan. 25, 2012), pp. 418–423. ISSN: 1944-8244. DOI: 10.1021/am201481b.

[39] N. Wetchakun, S. Chaiwichain, B. Inceesungvorn, K. Pingmuang, S. Phanichphant, A. I. Minett, and J. Chen. "BiVO4/CeO2 Nanocomposites with High Visible-Light-Induced Photocatalytic Activity". In: *ACS Applied Materials & Interfaces* 4.7 (July 25, 2012), pp. 3718–3723. ISSN: 1944-8244. DOI: 10.1021/am300812n.

[40] J. C.-S. Wu and C.-H. Chen. "A Visible-Light Response Vanadium-Doped Titania Nanocatalyst by Sol–Gel Method". In: *Journal of Photochemistry and Photobiology A: Chemistry* 163.3 (May 2004), pp. 509–515. ISSN: 10106030. DOI: 10.1016/j.jphotochem.2004.02.007.

[41] T. F.-R. Shen, M.-H. Lai, T. C.-K. Yang, I.-P. Fu, N.-Y. Liang, and W.-T. Chen. "Photocatalytic Production of Hydrogen by Vanadium Oxides under Visible Light Irradiation". In: *Journal of the Taiwan Institute of Chemical Engineers* 43.1 (Jan. 2012), pp. 95–101. ISSN: 18761070. DOI: 10.1016/j.jtice.2011.06.004.

[42] J. M. Gonçalves, M. Ireno da Silva, L. Angnes, and K. Araki. "Vanadium-Containing Electro and Photocatalysts for the Oxygen Evolution Reaction: A Review". In: *Journal of Materials Chemistry A* 8.5 (2020), pp. 2171–2206. ISSN: 2050-7488, 2050-7496. DOI: 10.1039/C9TA10857B.

[43] H. Luo, A. H. Mueller, T. M. McCleskey, A. K. Burrell, E. Bauer, and Q. X. Jia. "Structural and Photoelectrochemical Properties of BiVO4 Thin Films". In: *The Journal of Physical Chemistry C* 112.15 (Apr. 1, 2008), pp. 6099–6102. ISSN: 1932-7447. DOI: 10.1021/jp7113187.

[44] M. Kang, S. W. Kim, Y. Hwang, Y. Um, and J.-W. Ryu. "Temperature Dependence of the Interband Transition in a V2O5 Film". In: *AIP Advances* 3.5 (May 1, 2013), p. 052129. DOI: 10.1063/1.4808021.

[45] J. Sun, X. Li, Q. Zhao, J. Ke, and D. Zhang. "Novel V2O5/BiVO4/TiO2 Nanocomposites with High Visible-Light-Induced Photocatalytic Activity for the Degradation of Toluene". In: *The Journal of Physical Chemistry C* 118.19 (May 15, 2014), pp. 10113–10121. ISSN: 1932-7447, 1932-7455. DOI: 10.1021/jp5013076.

[46] Y. Wang, Y. R. Su, L. Qiao, L. X. Liu, Q. Su, C. Q. Zhu, and X. Q. Liu. "Synthesis of One-Dimensional TiO2/V2O5branched Heterostructures and Their Visible Light Photocatalytic Activity towards Rhodamine B". In: *Nanotechnology* 22.22 (Apr. 2011), p. 225702. ISSN: 0957-4484. DOI: 10.1088/0957-4484/22/22/225702.

[47] M. Gurulakshmi, M. Selvaraj, A. Selvamani, P. Vijayan, N. R. Sasi Rekha, and K. Shanthi. "Enhanced Visible-Light Photocatalytic Activity of V2O5/S-TiO2 Nanocomposites". In: *Applied Catalysis A: General* 449 (Dec. 27, 2012), pp. 31–46. ISSN: 0926-860X. DOI: 10.1016/j.apcata.2012.09.039.

[48] D.-E. Gu, B.-C. Yang, and Y.-D. Hu. "A Novel Method for Preparing V-Doped Titanium Dioxide Thin Film Photocatalysts with High Photocatalytic Activity Under Visible Light Irradiation". In: *Catalysis Letters* 118.3-4 (Sept. 24, 2007), pp. 254–259. ISSN: 1011-372X, 1572-879X. DOI: 10.1007/s10562-007-9179-5.

[49] W.-C. Lin and Y.-J. Lin. "Effect of Vanadium(IV)-Doping on the Visible Light-Induced Catalytic Activity of Titanium Dioxide Catalysts for Methylene Blue Degradation". In: *Environmental Engineering Science* 29.6 (June 2012), pp. 447–452. ISSN: 1092-8758, 1557-9018. DOI: 10.1089/ees.2010.0350. pmid: 22693413.

[50] A. L. Linsebigler, G. Lu, and J. T. Yates. "Photocatalysis on TiO2 Surfaces: Principles, Mechanisms, and Selected Results". In: *Chemical Reviews* 95.3 (May 1, 1995), pp. 735–758. ISSN: 0009-2665. DOI: 10.1021/cr00035a013.

Die approbierte gedruckte Originalversion dieser Diplomarbeit ist an der TU Wien Bibliothek verfügbar
The approved original version of this thesis is available in print at TU Wien Bibliothek.
TU Bibliothek Your knowledge hub WIEN

[51] T. Hisatomi, K. Takanabe, and K. Domen. "Photocatalytic Water-Splitting Reaction from Catalytic and Kinetic Perspectives". In: *Catalysis Letters* 145.1 (Jan. 1, 2015), pp. 95–108. ISSN: 1572-879X. DOI: 10.1007/s10562-014-1397-z.

[52] P. Salvador and F. Decker. "The Generation of Hydrogen Peroxide during Water Photoelectrolysis at N-Titanium Dioxide". In: *The Journal of Physical Chemistry* 88.25 (1984), pp. 6116–6120.

[53] R. Cai, Y. Kubota, and A. Fujishima. "Effect of Copper Ions on the Formation of Hydrogen Peroxide from Photocatalytic Titanium Dioxide Particles". In: *Journal of Catalysis* 219.1 (Oct. 1, 2003), pp. 214–218. ISSN: 0021-9517. DOI: 10.1016/S0021-9517(03)00197-0.

[54] R. Nakamura and Y. Nakato. "Primary Intermediates of Oxygen Photoevolution Reaction on TiO2 (Rutile) Particles, Revealed by in Situ FTIR Absorption and Photoluminescence Measurements". In: *Journal of the American Chemical Society* 126.4 (Feb. 1, 2004), pp. 1290–1298. ISSN: 0002-7863. DOI: 10.1021/ja0388764.

[55] R. Nakamura, T. Okamura, N. Ohashi, A. Imanishi, and Y. Nakato. "Molecular Mechanisms of Photoinduced Oxygen Evolution, PL Emission, and Surface Roughening at Atomically Smooth (110) and (100) n-TiO2 (Rutile) Surfaces in Aqueous Acidic Solutions". In: *Journal of the American Chemical Society* 127.37 (Sept. 1, 2005), pp. 12975–12983. ISSN: 0002-7863. DOI: 10.1021/ja053252e.

[56] J. Ran, J. Zhang, J. Yu, M. Jaroniec, and S. Z. Qiao. "Earth-Abundant Cocatalysts for Semiconductor-Based Photocatalytic Water Splitting". In: *Chemical Society Reviews* 43.22 (Oct. 20, 2014), pp. 7787–7812. ISSN: 1460-4744. DOI: 10.1039/C3CS60425J.

[57] L. Liu, Z. Ji, W. Zou, X. Gu, Y. Deng, F. Gao, C. Tang, and L. Dong. "In Situ Loading Transition Metal Oxide Clusters on TiO2 Nanosheets As Co-Catalysts for Exceptional High Photoactivity". In: *ACS Catalysis* 3.9 (Sept. 6, 2013), pp. 2052–2061. DOI: 10.1021/cs4002755.

[58] C. R. López, E. P. Melián, J. A. Ortega Méndez, D. E. Santiago, J. M. Doña Rodríguez, and O. González Díaz. "Comparative Study of Alcohols as Sacrificial Agents in H2 Production by Heterogeneous Photocatalysis Using Pt/TiO2 Catalysts". In: *Journal of Photochemistry and Photobiology A: Chemistry* 312 (Nov. 1, 2015), pp. 45–54. ISSN: 1010-6030. DOI: 10.1016/j.jphotochem.2015.07.005.

[59] A. Kudo and I. Mikami. "New In2O3(ZnO)m Photocatalysts with Laminal Structure for Visible Light-Induced H2 or O2 Evolution from Aqueous Solutions Containing Sacrificial Reagents". In: *Chemistry Letters* 27.10 (Oct. 1, 1998), pp. 1027–1028. ISSN: 0366-7022. DOI: 10.1246/cl.1998.1027.

[60] A. Kudo, K. Ueda, H. Kato, and I. Mikami. "Photocatalytic O2 Evolution under Visible Light Irradiation on BiVO4 in Aqueous AgNO3 Solution". In: *Catalysis Letters* 53.3 (Aug. 1, 1998), pp. 229–230. ISSN: 1572-879X. DOI: 10.1023/A:1019034728816.

[61] B. Ma, F. Wen, H. Jiang, J. Yang, P. Ying, and C. Li. "The Synergistic Effects of Two Co-Catalysts on Zn2GeO4 on Photocatalytic Water Splitting". In: *Catalysis Letters* 134.1 (Jan. 1, 2010), pp. 78–86. ISSN: 1572-879X. DOI: 10.1007/s10562-009-0220-8.

[62] S. Sadamatsu, M. Tanaka, K. Higashida, and S. Matsumura. "Transmission Electron Microscopy of Bulk Specimens over 10µm in Thickness". In: *Ultramicroscopy* 162 (Mar. 1, 2016), pp. 10–16. ISSN: 0304-3991. DOI: 10.1016/j.ultramic.2015.09.001.

[63] P. G. Self, H. K. D. H. Bhadeshia, and W. M. Stobbs. "Lattice Spacings from Lattice Fringes". In: *Ultramicroscopy* 6.1 (Jan. 1, 1981), pp. 29–40. ISSN: 0304-3991. DOI: 10.1016/S0304-3991(81)80175-1.

[64] S. Tougaard. "Universality Classes of Inelastic Electron Scattering Cross-Sections". In: *Surface and Interface Analysis* 25.3 (1997), pp. 137–154. ISSN: 1096-9918. DOI: 10.1002/(SICI)1096-9918(199703)25:3<137::AID-SIA230>3.0.CO;2-L.

[65] D. A. Shirley. "High-Resolution X-Ray Photoemission Spectrum of the Valence Bands of Gold". In: *Physical Review B* 5.12 (June 15, 1972), pp. 4709–4714. DOI: 10.1103/PhysRevB.5.4709.

[66] J. H. Scofield. "Hartree-Slater Subshell Photoionization Cross-Sections at 1254 and 1487 eV". In: *Journal of Electron Spectroscopy and Related Phenomena* 8.2 (Jan. 1, 1976), pp. 129–137. ISSN: 0368-2048. DOI: 10.1016/0368-2048(76)80015-1.

[67] L. H. Negri and C. Vestri. *Lucashn/Peakutils: V1.1.0*. Version v1.1.0. Zenodo, Sept. 2017. DOI: 10.5281/zenodo.887917.

[68] M. E. Brown and B. V. Stewart. "The Thermal Decomposition of Ammonium Metavanadate, I: The Stoichiometry of the Decomposition". In: *Journal of Thermal Analysis* 2.3 (Sept. 1970), pp. 287–299. ISSN: 0022-5215, 1572-8943. DOI: 10.1007/BF01911410.

Die approbierte gedruckte Originalversion dieser Diplomarbeit ist an der TU Wien Bibliothek verfügbar
The approved original version of this thesis is available in print at TU Wien Bibliothek.
TU Bibliothek Your knowledge hub WIEN

[69] S. Gates-Rector and T. Blanton. "The Powder Diffraction File: A Quality Materials Characterization Database". In: *Powder Diffraction* 34.4 (Dec. 2019), pp. 352–360. ISSN: 0885-7156, 1945-7413. DOI: 10.1017/S0885715619000812.

[70] P. Swift. "Adventitious Carbon—the Panacea for Energy Referencing?" In: *Surface and Interface Analysis* 4.2 (1982), pp. 47–51. ISSN: 1096-9918. DOI: 10.1002/sia.740040204.

[71] T. K. Sham and M. S. Lazarus. "X-Ray Photoelectron Spectroscopy (XPS) Studies of Clean and Hydrated TiO2 (Rutile) Surfaces". In: *Chemical Physics Letters* 68.2 (Dec. 15, 1979), pp. 426–432. ISSN: 0009-2614. DOI: 10.1016/0009-2614(79)87231-0.

[72] A. Lu, J. Liu, D. Zhao, Y. Guo, Q. Li, and N. Li. "Photocatalysis of V-Bearing Rutile on Degradation of Halohydrocarbons". In: *Catalysis Today*. Environmental Catalysis and Eco-Materials 90.3 (July 1, 2004), pp. 337–342. ISSN: 0920-5861. DOI: 10.1016/j.cattod.2004.04.044.

[73] G. Silversmit, H. Poelman, D. Depla, N. Barrett, G. B. Marin, and R. D. Gryse. "A Comparative XPS and UPS Study of VOx Layers on Mineral TiO2(001)-Anatase Supports". In: *Surface and Interface Analysis* 38.9 (2006), pp. 1257–1265. ISSN: 1096-9918. DOI: 10.1002/sia.2384.

[74] Z. Zhang and V. E. Henrich. "Electronic Interactions in the Vanadium/TiO2(110) and Vanadia/TiO2(110) Model Catalyst Systems". In: *Surface Science* 277.3 (Oct. 20, 1992), pp. 263–272. ISSN: 0039-6028. DOI: 10.1016/0039-6028(92)90767-Z.

[75] G. Silversmit, D. Depla, H. Poelman, G. B. Marin, and R. De Gryse. "Determination of the V2p XPS Binding Energies for Different Vanadium Oxidation States (V5+ to V0+)". In: *Journal of Electron Spectroscopy and Related Phenomena* 135.2 (Apr. 1, 2004), pp. 167–175. ISSN: 0368-2048. DOI: 10.1016/j.elspec.2004.03.004.

[76] Y. Suchorski, L. Rihko-Struckmann, F. Klose, Y. Ye, M. Alandjiyska, K. Sundmacher, and H. Weiss. "Evolution of Oxidation States in Vanadium-Based Catalysts under Conventional XPS Conditions". In: *Applied Surface Science* 249.1 (Aug. 15, 2005), pp. 231–237. ISSN: 0169-4332. DOI: 10.1016/j.apsusc.2004.11.083.

[77] R. D. Shannon and J. A. Pask. "Kinetics of the Anatase-Rutile Transformation". In: *Journal of the American Ceramic Society* 48.8 (1965), pp. 391–398. ISSN: 1551-2916. DOI: 10.1111/j.1151-2916.1965.tb14774.x.

[78] J. F. Porter, Y.-G. Li, and C. K. Chan. "The Effect of Calcination on the Microstructural Characteristics and Photoreactivity of Degussa P-25 TiO2". In: *Journal of Materials Science* 34.7 (Apr. 1, 1999), pp. 1523–1531. ISSN: 1573-4803. DOI: 10.1023/A:1004560129347.

[79] D. A. H. Hanaor and C. C. Sorrell. "Review of the Anatase to Rutile Phase Transformation". In: *Journal of Materials Science* 46.4 (Feb. 1, 2011), pp. 855–874. ISSN: 1573-4803. DOI: 10.1007/s10853-010-5113-0.

[80] G. C. Bond, A. J. Sárkány, and G. D. Parfitt. "The Vanadium Pentoxide-Titanium Dioxide System: Structural Investigation and Activity for the Oxidation of Butadiene". In: *Journal of Catalysis* 57.3 (May 1, 1979), pp. 476–493. ISSN: 0021-9517. DOI: 10.1016/0021-9517(79)90013-7.

[81] J. Choi, H. Park, and M. R. Hoffmann. "Effects of Single Metal-Ion Doping on the Visible-Light Photoreactivity of TiO2". In: *The Journal of Physical Chemistry C* 114.2 (Jan. 21, 2010), pp. 783–792. ISSN: 1932-7447. DOI: 10.1021/jp908088x.

[82] Y.-H. Zhang and A. Reller. "Phase Transformation and Grain Growth of Doped Nanosized Titania". In: *Materials Science and Engineering: C* 19.1 (2002), pp. 323–326. ISSN: 0928-4931. DOI: 10.1016/S0928-4931(01)00409-X.

[83] I. E. Wachs. "Raman and IR Studies of Surface Metal Oxide Species on Oxide Supports: Supported Metal Oxide Catalysts". In: *Catalysis Today*. Vibrational Spectroscopy of Adsorbed Molecules and Surface Species on Metal Oxides 27.3 (Feb. 26, 1996), pp. 437–455. ISSN: 0920-5861. DOI: 10.1016/0920-5861(95)00203-0.

[84] G. J. d. A. A. Soler-Illia, A. Louis, and C. Sanchez. "Synthesis and Characterization of Mesostructured Titania-Based Materials through Evaporation-Induced Self-Assembly". In: *Chemistry of Materials* 14.2 (Feb. 1, 2002), pp. 750–759. ISSN: 0897-4756. DOI: 10.1021/cm011217a.

[85] L. Abello, E. Husson, Y. Repelin, and G. Lucazeau. "Vibrational Spectra and Valence Force Field of Crystalline V2O5". In: *Spectrochimica Acta Part A: Molecular Spectroscopy* 39.7 (Jan. 1, 1983), pp. 641–651. ISSN: 0584-8539. DOI: 10.1016/0584-8539(83)80040-3.

[86] W. G. Menezes, D. M. Reis, T. M. Benedetti, M. M. Oliveira, J. F. Soares, R. M. Torresi, and A. J. G. Zarbin. "V2O5 Nanoparticles Obtained from a Synthetic Bariandite-like Vanadium Oxide: Synthesis, Characterization and Electrochemical Behavior in an Ionic

Die approbierte gedruckte Originalversion dieser Diplomarbeit ist an der TU Wien Bibliothek verfügbar
The approved original version of this thesis is available in print at TU Wien Bibliothek.
TU Bibliothek Your knowledge hub WIEN

Liquid". In: *Journal of Colloid and Interface Science* 337.2 (Sept. 15, 2009), pp. 586–593. ISSN: 0021-9797. DOI: 10.1016/j.jcis.2009.05.050.

[87] X. Zhang and R. Frech. "Vibrational Spectroscopic Study of Lithium Vanadium Pentoxides". In: *Electrochimica Acta* 42.3 (Jan. 1, 1997), pp. 475–482. ISSN: 0013-4686. DOI: 10.1016/S0013-4686(96)00268-X.

[88] A. Z. Moshfegh and A. Ignatiev. "Formation and Characterization of Thin Film Vanadium Oxides: Auger Electron Spectroscopy, X-Ray Photoelectron Spectroscopy, X-Ray Diffraction, Scanning Electron Microscopy, and Optical Reflectance Studies". In: *Thin Solid Films* 198.1 (Mar. 20, 1991), pp. 251–268. ISSN: 0040-6090. DOI: 10.1016/0040-6090(91)90344-W.

[89] F. Hatayama, T. Ohno, T. Maruoka, T. Ono, and H. Miyata. "Structure and Acidity of Vanadium Oxide Layered on Titania (Anatase and Rutile)". In: *Journal of the Chemical Society, Faraday Transactions* 87.16 (Jan. 1, 1991), pp. 2629–2633. ISSN: 1364-5455. DOI: 10.1039/FT9918702629.

[90] M. A. Centeno, J. J. Benítez, P. Malet, I. Carrizosa, and J. A. Odriozola. "In Situ Temperature-Programmed Diffuse Reflectance Infrared Fourier Transform Spectroscopy (TPDRIFTS) of V2O5/TiO2 Catalysts". In: *Applied Spectroscopy* 51.3 (Mar. 1, 1997), pp. 416–422. ISSN: 0003-7028. DOI: 10.1366/0003702971940305.

[91] G. T. Went, L.-j. Leu, and A. T. Bell. "Quantitative Structural Analysis of Dispersed Vanadia Species in TiO2(Anatase)-Supported V2O5". In: *Journal of Catalysis* 134.2 (Apr. 1, 1992), pp. 479–491. ISSN: 0021-9517. DOI: 10.1016/0021-9517(92)90336-G.

[92] O. Frank, M. Zukalova, B. Laskova, J. Kürti, J. Koltai, and L. Kavan. "Raman Spectra of Titanium Dioxide (Anatase, Rutile) with Identified Oxygen Isotopes (16, 17, 18)". In: *Physical Chemistry Chemical Physics* 14.42 (2012), p. 14567. ISSN: 1463-9076, 1463-9084. DOI: 10.1039/c2cp42763j.

[93] M. Scepanovic, S. Aškrabić, V. Berec, G. Aleksandar, Z. Dohčević-Mitrović, A. Kremenovic, and Z. Popovic. "Characterization of La-Doped TiO2 Nanopowders by Raman Spectroscopy". In: *Acta Physica Polonica Series a* 115 (Apr. 2009), pp. 771–774. DOI: 10.12693/APhysPolA.115.771.

[94] C. Julien, G. A. Nazri, and O. Bergström. "Raman Scattering Studies of Microcrystalline V6O13". In: *physica status solidi (b)* 201.1 (1997), pp. 319–326. ISSN: 1521-3951. DOI: 10.1002/1521-3951(199705)201:1<319::AID-PSSB319>3.0.CO;2-T.

[95] D. Bersani, P. P. Lottici, and X.-Z. Ding. "Phonon Confinement Effects in the Raman Scattering by TiO2 Nanocrystals". In: *Applied Physics Letters* 72.1 (Jan. 5, 1998), pp. 73–75. ISSN: 0003-6951. DOI: 10.1063/1.120648.

[96] K.-R. Zhu, M.-S. Zhang, Q. Chen, and Z. Yin. "Size and Phonon-Confinement Effects on Low-Frequency Raman Mode of Anatase TiO2 Nanocrystal". In: *Physics Letters A* 340.1 (June 6, 2005), pp. 220–227. ISSN: 0375-9601. DOI: 10.1016/j.physleta.2005.04.008.

[97] C. Y. Xu, P. X. Zhang, and L. Yan. "Blue Shift of Raman Peak from Coated TiO2 Nanoparticles". In: *Journal of Raman Spectroscopy* 32.10 (2001), pp. 862–865. ISSN: 1097-4555. DOI: 10.1002/jrs.773.

[98] D. Eder and A. H. Windle. "Carbon–Inorganic Hybrid Materials: The Carbon-Nanotube/TiO2 Interface". In: *Advanced Materials* 20.9 (2008), pp. 1787–1793. ISSN: 1521-4095. DOI: 10.1002/adma.200702835.

[99] X. Cheng, X. Yu, Z. Xing, and L. Yang. "Synthesis and Characterization of N-Doped TiO2 and Its Enhanced Visible-Light Photocatalytic Activity". In: *Arabian Journal of Chemistry* 9 (Nov. 1, 2016), S1706–S1711. ISSN: 1878-5352. DOI: 10.1016/j.arabjc.2012.04.052.

[100] J. C. Parker and R. W. Siegel. "Calibration of the Raman Spectrum to the Oxygen Stoichiometry of Nanophase TiO2". In: *Applied Physics Letters* 57.9 (Aug. 27, 1990), pp. 943–945. ISSN: 0003-6951. DOI: 10.1063/1.104274.

[101] J. S. Schubert, J. Popovic, G. M. Haselmann, S. P. Nandan, J. Wang, A. Giesriegl, A. S. Cherevan, and D. Eder. "Immobilization of Co, Mn, Ni and Fe Oxide Co-Catalysts on TiO2 for Photocatalytic Water Splitting Reactions". In: *Journal of Materials Chemistry A* 7.31 (Aug. 6, 2019), pp. 18568–18579. ISSN: 2050-7496. DOI: 10.1039/C9TA05637H.

[102] A. R. Zanatta. "Revisiting the Optical Bandgap of Semiconductors and the Proposal of a Unified Methodology to Its Determination". In: *Scientific Reports* 9.1 (1 Aug. 2, 2019), p. 11225. ISSN: 2045-2322. DOI: 10.1038/s41598-019-47670-y.

[103] J. Tauc, R. Grigorovici, and A. Vancu. "Optical Properties and Electronic Structure of Amorphous Germanium". In: *physica status solidi (b)* 15.2 (1966), pp. 627–637. ISSN: 1521-3951. DOI: 10.1002/pssb.19660150224.

Die approbierte gedruckte Originalversion dieser Diplomarbeit ist an der TU Wien Bibliothek verfügbar
The approved original version of this thesis is available in print at TU Wien Bibliothek.
TU Bibliothek Your knowledge hub WIEN

[104] L. Kavan, M. Grätzel, S. E. Gilbert, C. Klemenz, and H. J. Scheel. "Electrochemical and Photoelectrochemical Investigation of Single-Crystal Anatase". In: *Journal of the American Chemical Society* 118.28 (Jan. 1, 1996), pp. 6716–6723. ISSN: 0002-7863. DOI: 10.1021/ja954172l.

[105] P. Kubelka. "New Contributions to the Optics of Intensely Light-Scattering Materials. Part I". In: *JOSA* 38.5 (May 1, 1948), pp. 448–457. DOI: 10.1364/JOSA.38.000448.

[106] P. Makuła, M. Pacia, and W. Macyk. "How To Correctly Determine the Band Gap Energy of Modified Semiconductor Photocatalysts Based on UV–Vis Spectra". In: *The Journal of Physical Chemistry Letters* 9.23 (Dec. 6, 2018), pp. 6814–6817. DOI: 10.1021/acs.jpclett.8b02892.

[107] N. Hosaka, T. Sekiya, C. Satoko, and S. Kurita. "Optical Properties of Single-Crystal Anatase TiO2". In: *Journal of the Physical Society of Japan* 66.3 (Mar. 1997), pp. 877–880. ISSN: 0031-9015. DOI: 10.1143/JPSJ.66.877.

[108] M. Benmoussa, E. Ibnouelghazi, A. Bennouna, and E. Ameziane. "Structural, Electrical and Optical Properties of Sputtered Vanadium Pentoxide Thin Films". In: *Thin Solid Films* 265.1 (1995), pp. 22–28. ISSN: 0040-6090. DOI: 10.1016/0040-6090(95)06617-9.

[109] C. J. Ballhausen and H. B. Gray. "The Electronic Structure of the Vanadyl Ion". In: *Inorganic Chemistry* 1.1 (Feb. 1, 1962), pp. 111–122. ISSN: 0020-1669. DOI: 10.1021/ic50001a022.

[110] Q. Zhang, L. Gao, and J. Guo. "Effects of Calcination on the Photocatalytic Properties of Nanosized TiO2 Powders Prepared by TiCl4 Hydrolysis". In: *Applied Catalysis B: Environmental* 26.3 (May 8, 2000), pp. 207–215. ISSN: 0926-3373. DOI: 10.1016/S0926-3373(00)00122-3.

[111] S. R. G. Carrazan and V. Rives. "An FT-IR Spectroscopy and X-Ray Diffraction Characterization of V2O5TiO2 (Anatase and Rutile) Mechanical Mixtures". In: *Materials Chemistry and Physics* 28.2 (June 1, 1991), pp. 227–235. ISSN: 0254-0584. DOI: 10.1016/0254-0584(91)90066-4.

[112] U. Diebold. "The Surface Science of Titanium Dioxide". In: *Surface Science Reports* 48.5 (Jan. 1, 2003), pp. 53–229. ISSN: 0167-5729. DOI: 10.1016/S0167-5729(02)00100-0.

[113] S. Boghosian, K. M. Eriksen, R. Fehrmann, K. Nielsen, C. P. Tønseth, K. R. Seddon, and L. Bao-Sheng. "Synthesis, Crystal Structure Redetermination and Vibrational Spectra of Beta-VOSO4." In: *Acta Chemica Scandinavica* 49 (1995), pp. 703–708. ISSN: 0904-213X. DOI: 10.3891/acta.chem.scand.49-0703.

[114] *ICSC 0596 - VANADIUM PENTOXIDE*. URL: https://www.ilo.org/dyn/icsc/showcard.display?p_version=2&p_card_id=0596 (visited on 02/28/2021).

[115] D. Eder, M. S. Motta, and A. H. Windle. "Nanoengineering with Residual Catalyst from CNT Templates". In: *Acta Materialia* 58.13 (Aug. 1, 2010), pp. 4406–4413. ISSN: 1359-6454. DOI: 10.1016/j.actamat.2010.04.037.

[116] A. Moya, A. Cherevan, S. Marchesan, P. Gebhardt, M. Prato, D. Eder, and J. J. Vilatela. "Oxygen Vacancies and Interfaces Enhancing Photocatalytic Hydrogen Production in Mesoporous CNT/TiO2 Hybrids". In: *Applied Catalysis B: Environmental* 179 (Dec. 1, 2015), pp. 574–582. ISSN: 0926-3373. DOI: 10.1016/j.apcatb.2015.05.052.

[117] A. Vejux and P. Courtine. "Interfacial Reactions between V2O5 and TiO2 (Anatase): Role of the Structural Properties". In: *Journal of Solid State Chemistry* 23.1 (1978), pp. 93–103. ISSN: 0022-4596. DOI: 10.1016/0022-4596(78)90055-5.

[118] M. A. Bañares, L. J. Alemany, M. Jiménez, M. Larrubia, F. Delgado, M. L. Granados, A. Martıinez-Arias, J. Blasco, and J. L. G. Fierro. "The Role of Vanadium Oxide on the Titania Transformation under Thermal Treatments and Surface Vanadium States". In: *Journal of Solid State Chemistry* 124.1 (June 1996), pp. 69–76. ISSN: 00224596. DOI: 10.1006/jssc.1996.0209.

[119] R. Y. Saleh, I. E. Wachs, S. S. Chan, and C. C. Chersich. "The Interaction of V2O5 with Ti02(Anatase): Catalyst Evolution with Calcination Temperature and O-Xylene Oxidation". In: *Journal of Catalysis* 98.1 (Mar. 1, 1986), pp. 102–114. ISSN: 0021-9517. DOI: 10.1016/0021-9517(86)90300-3.

[120] L. C. Seitz, C. F. Dickens, K. Nishio, Y. Hikita, J. Montoya, A. Doyle, C. Kirk, A. Vojvodic, H. Y. Hwang, J. K. Norskov, and T. F. Jaramillo. "A Highly Active and Stable IrOx/SrIrO3 Catalyst for the Oxygen Evolution Reaction". In: *Science* 353.6303 (Sept. 2, 2016), pp. 1011–1014. ISSN: 0036-8075, 1095-9203. DOI: 10.1126/science.aaf5050. pmid: 27701108.

Die approbierte gedruckte Originalversion dieser Diplomarbeit ist an der TU Wien Bibliothek verfügbar
The approved original version of this thesis is available in print at TU Wien Bibliothek.
TU Bibliothek Your knowledge hub WIEN

[121] M. S. Burke, L. J. Enman, A. S. Batchellor, S. Zou, and S. W. Boettcher. "Oxygen Evolution Reaction Electrocatalysis on Transition Metal Oxides and (Oxy)Hydroxides: Activity Trends and Design Principles". In: *Chemistry of Materials* 27.22 (Nov. 24, 2015), pp. 7549–7558. ISSN: 0897-4756. DOI: 10.1021/acs.chemmater.5b03148.

[122] G. Yudoyono, N. Ichzan, V. Zharvan, R. Daniyati, H. Santoso, B. Indarto, Y. H. Pramono, M. Zainuri, and Darminto. "Effect of Calcination Temperature on the Photocatalytic Activity of TiO2 Powders Prepared by Co-Precipitation of TiCl3". In: *AIP Conference Proceedings* 1725.1 (Apr. 19, 2016), p. 020099. ISSN: 0094-243X. DOI: 10.1063/1.4945553.

[123] J. He, Y.-e. Du, Y. Bai, J. An, X. Cai, Y. Chen, P. Wang, X. Yang, and Q. Feng. "Facile Formation of Anatase/Rutile TiO2 Nanocomposites with Enhanced Photocatalytic Activity". In: *Molecules* 24.16 (16 Jan. 2019), p. 2996. DOI: 10.3390/molecules24162996.

[124] A. Li, Z. Wang, H. Yin, S. Wang, P. Yan, B. Huang, X. Wang, R. Li, X. Zong, H. Han, and C. Li. "Understanding the Anatase–Rutile Phase Junction in Charge Separation and Transfer in a TiO2 Electrode for Photoelectrochemical Water Splitting". In: *Chemical Science* 7.9 (Aug. 16, 2016), pp. 6076–6082. ISSN: 2041-6539. DOI: 10.1039/C6SC01611A.

[125] G. R. Bamwenda, S. Tsubota, T. Nakamura, and M. Haruta. "Photoassisted Hydrogen Production from a Water-Ethanol Solution: A Comparison of Activities of Au-TiO2 and Pt-TiO2". In: *Journal of Photochemistry and Photobiology A: Chemistry* 89.2 (July 12, 1995), pp. 177–189. ISSN: 1010-6030. DOI: 10.1016/1010-6030(95)04039-I.

[126] Y. Ikuma and H. Bessho. "Effect of Pt Concentration on the Production of Hydrogen by a TiO2 Photocatalyst". In: *International Journal of Hydrogen Energy*. International Conference on Materials for Hydrogen Energy: Solar Hydrogen (ICMHE 2004) 32.14 (Sept. 1, 2007), pp. 2689–2692. ISSN: 0360-3199. DOI: 10.1016/j.ijhydene.2006.09.024.

[127] N.-T. Nguyen, D.-D. Zheng, S.-S. Chen, and C.-T. Chang. "Preparation and Photocatalytic Hydrogen Production of Pt-Graphene/TiO2 Composites from Water Splitting". In: *Journal of Nanoscience and Nanotechnology* 18.1 (Jan. 1, 2018), pp. 48–55. DOI: 10.1166/jnn.2018.14556.

[128] D. Benz, K. M. Felter, J. Köser, J. Thöming, G. Mul, F. C. Grozema, H. T. Hintzen, M. T. Kreutzer, and J. R. van Ommen. "Assessing the Role of Pt Clusters on TiO2 (P25) on the Photocatalytic Degradation of Acid Blue 9 and Rhodamine B". In: *The Journal of Physical Chemistry C* 124.15 (Apr. 16, 2020), pp. 8269–8278. ISSN: 1932-7447. DOI: 10.1021/acs.jpcc.0c00926.

[129] S. Martha, D. P. Das, N. Biswal, and K. M. Parida. "Facile Synthesis of Visible Light Responsive V 2 O 5 /N,S–TiO 2 Composite Photocatalyst: Enhanced Hydrogen Production and Phenol Degradation". In: *Journal of Materials Chemistry* 22.21 (2012), pp. 10695–10703. DOI: 10.1039/C2JM30462G.

Die approbierte gedruckte Originalversion dieser Diplomarbeit ist an der TU Wien Bibliothek verfügbar
The approved original version of this thesis is available in print at TU Wien Bibliothek.
TU WIEN Bibliothek Your knowledge hub

Appendix

9.1 TGA

TGA analysis was performed for the uncalcined samples $Ti\,[1\%/RT]_E^N$, $Ti\,[1\%/RT]_E^S$, $Ti\,[1\%/RT]_F^N$ and $Ti\,[1\%/RT]_F^S$ and the plots can be seen in Fig. 9.1.

All samples still had a lot of adsorbed water which was removed by heating up to 120 °C (or 190 °C in the case of anatase) and holding the temperature until constant weight. Afterwards the samples were heated further to 800 °C. No stepwise degradation could be observed until 550 °C. At this temperature the sample $Ti\,[1\%/RT]_E^S$ started to lose weight more quickly and at 600 °C the other samples did as well. However, this weight loss at around 600 °C can also be observed with pure anatase so it probably doesn't come from a degradation reaction by the precursors. With a concentration of 1 at% the expected weight loss for the degradation of the precursors to V_2O_5 would be 0.3 wt% for NH_4VO_3 and 1.8 wt% for $VOSO_4 \cdot 4\,H_2O$. The large weight loss by $Ti\,[1\%/RT]_E^S$ could come from this degradation but the overlapping with other weight reductions makes it difficult to determine a clear start and end point.

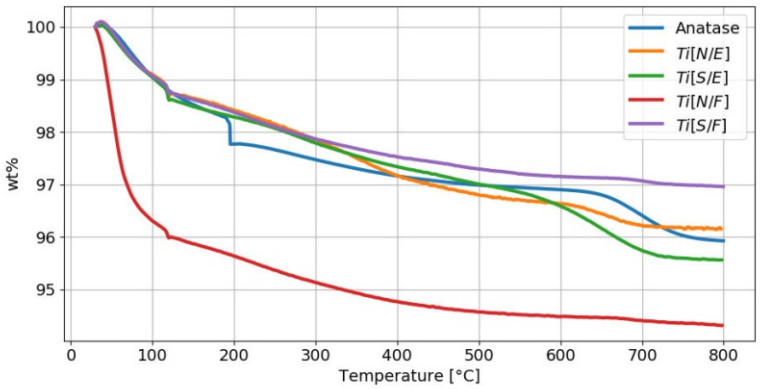

Figure 9.1: TGA plots for the uncalcined samples $Ti\,[1\%/RT]_E^N$, $Ti\,[1\%/RT]_E^S$, $Ti\,[1\%/RT]_F^N$ and $Ti\,[1\%/RT]_F^S$ as well as anatase as a reference.

Die approbierte gedruckte Originalversion dieser Diplomarbeit ist an der TU Wien Bibliothek verfügbar
The approved original version of this thesis is available in print at TU Wien Bibliothek.

9.2 SEM

Anatase

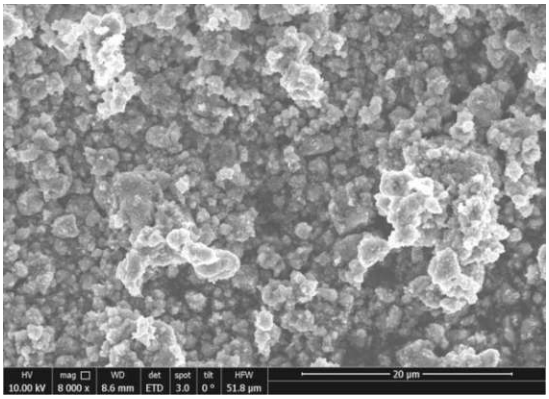

(a): 8000 x

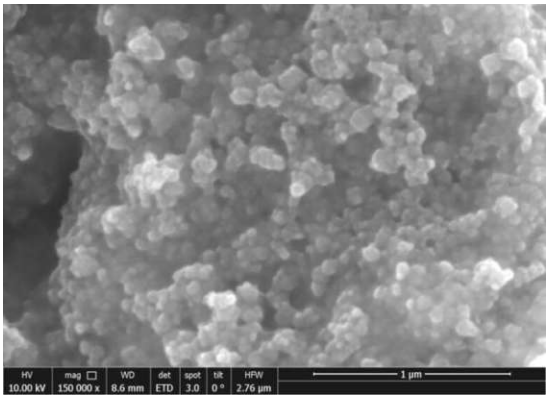

(b): 150 000 x

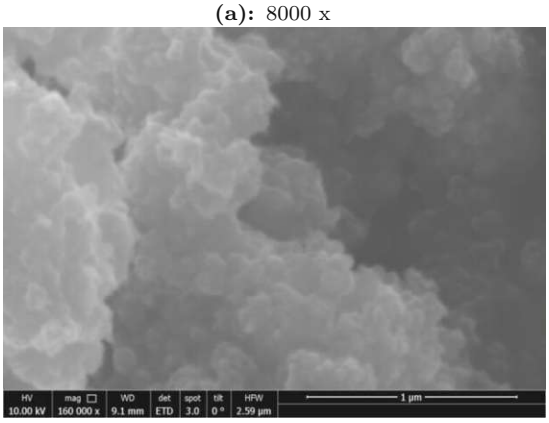

(c): 160 000 x

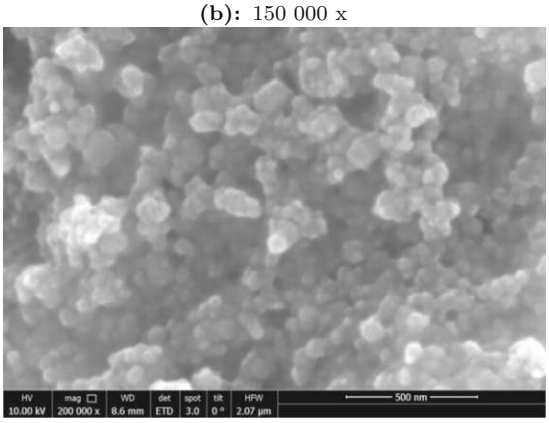

(d): 200 000 x

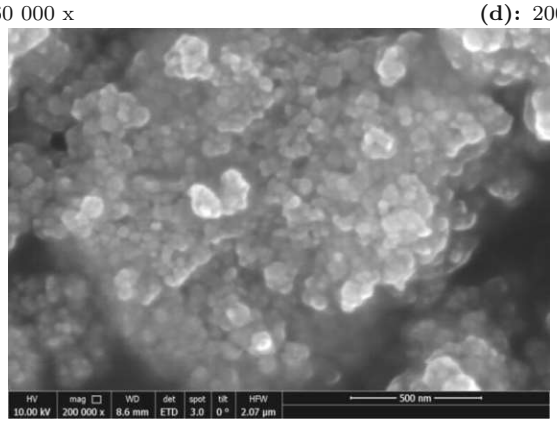

(e): 200 000 x

Figure 9.2: Anatase

Die approbierte gedruckte Originalversion dieser Diplomarbeit ist an der TU Wien Bibliothek verfügbar
The approved original version of this thesis is available in print at TU Wien Bibliothek.

$Ti\,[5\%/600]_E^S$

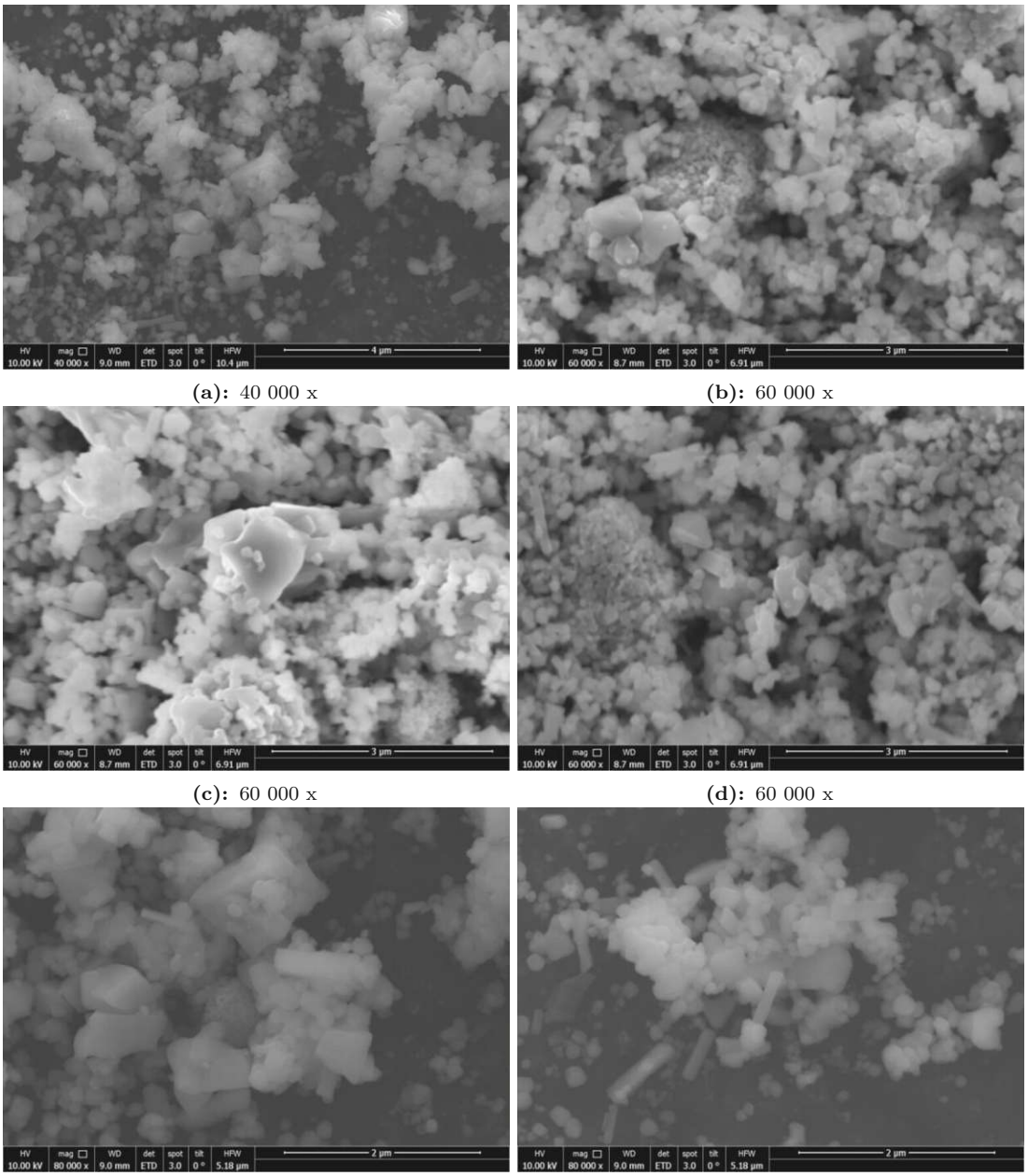

(a): 40 000 x **(b):** 60 000 x

(c): 60 000 x **(d):** 60 000 x

(e): 80 000 x **(f):** 80 000 x

Figure 9.3: $Ti\,[5\%/600]_E^S$

Die approbierte gedruckte Originalversion dieser Diplomarbeit ist an der TU Wien Bibliothek verfügbar
The approved original version of this thesis is available in print at TU Wien Bibliothek.

$Ti\,[25\%/350]_E^S$

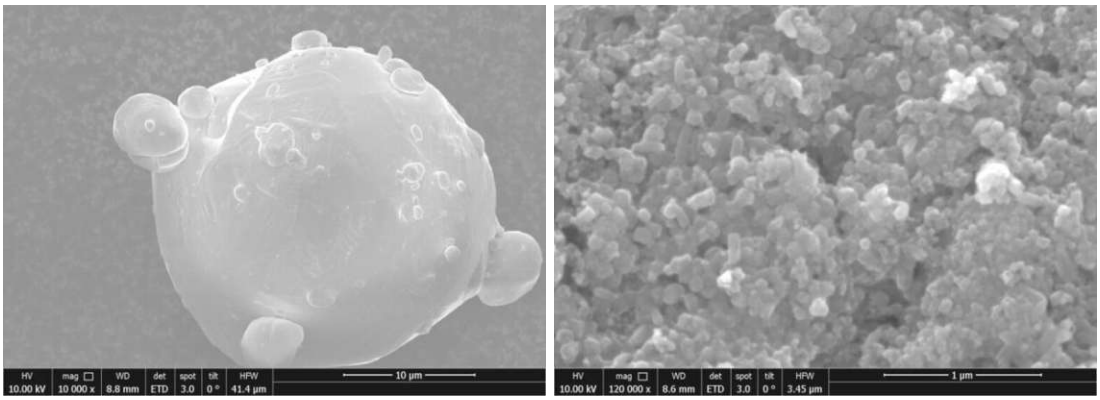

(a): 10 000 x **(b):** 120 000 x

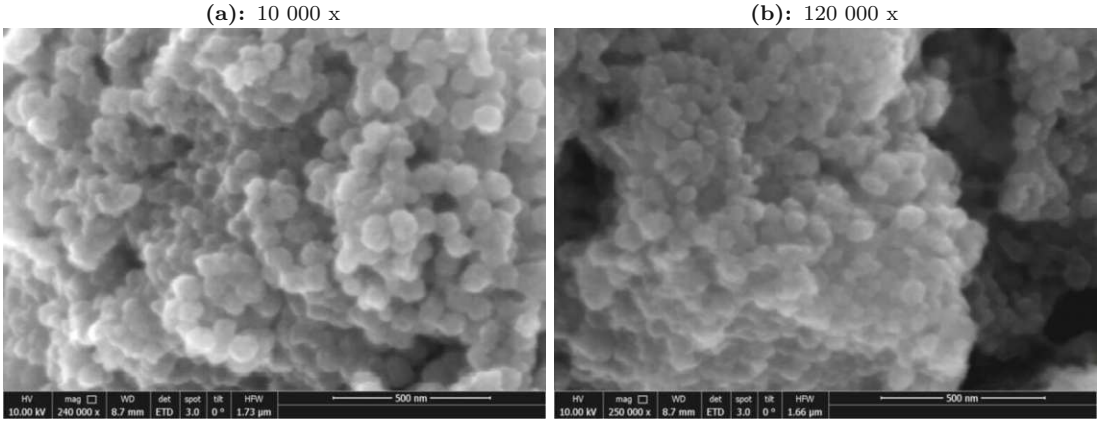

(c): 240 000 x **(d):** 250 000 x

Figure 9.4: $Ti\,[25\%/350]_E^S$

Die approbierte gedruckte Originalversion dieser Diplomarbeit ist an der TU Wien Bibliothek verfügbar
The approved original version of this thesis is available in print at TU Wien Bibliothek.

$Ti\,[25\%/600]_E^S$

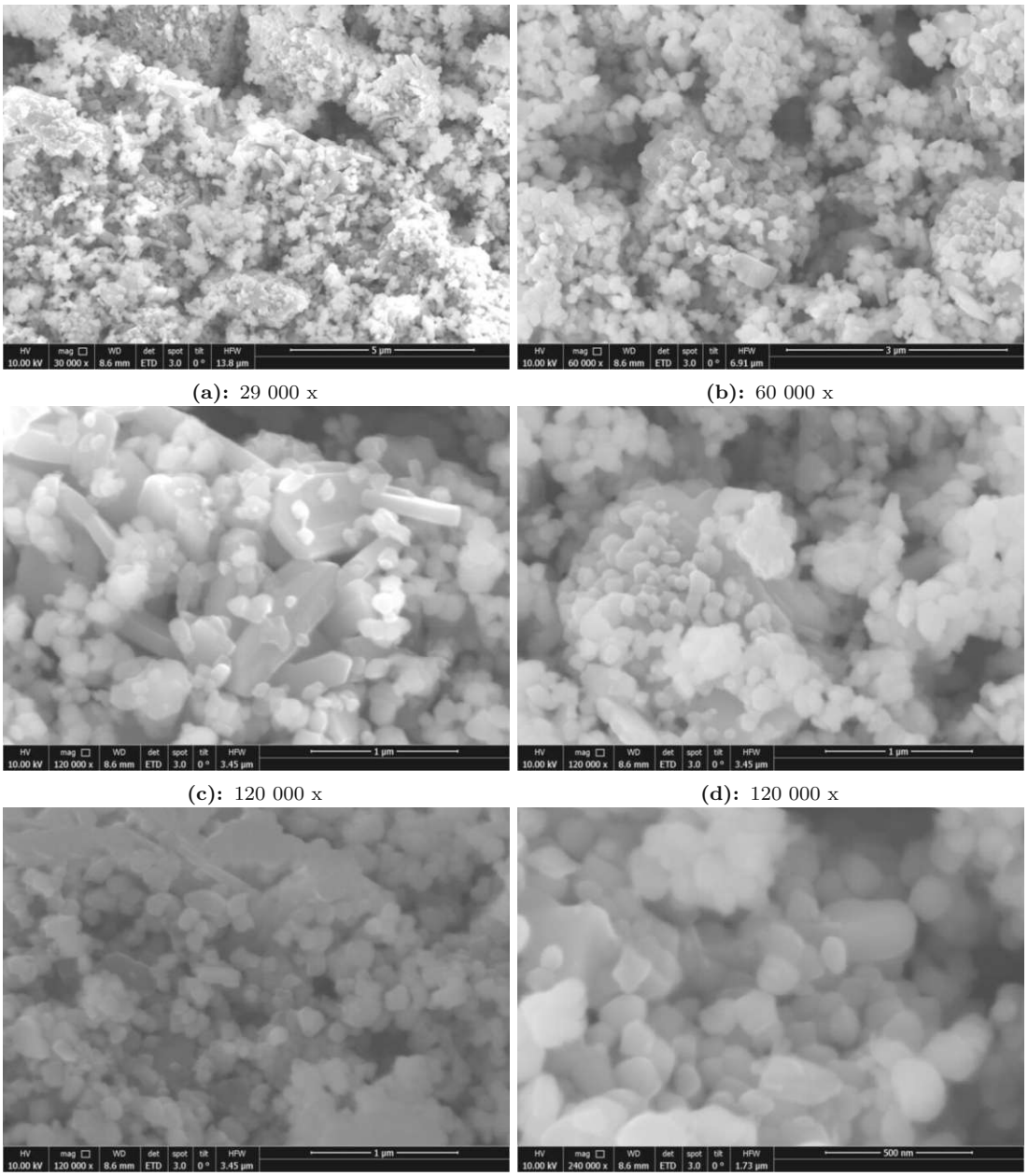

(a): 29 000 x **(b):** 60 000 x

(c): 120 000 x **(d):** 120 000 x

(e): 120 000 x **(f):** 240 000 x

Figure 9.5: $Ti\,[25\%/600]_E^S$

Die approbierte gedruckte Originalversion dieser Diplomarbeit ist an der TU Wien Bibliothek verfügbar
The approved original version of this thesis is available in print at TU Wien Bibliothek.
TU WIEN Bibliothek Your knowledge hub

9.3 TEM

$Ti\,[1\%/RT]_F^N$

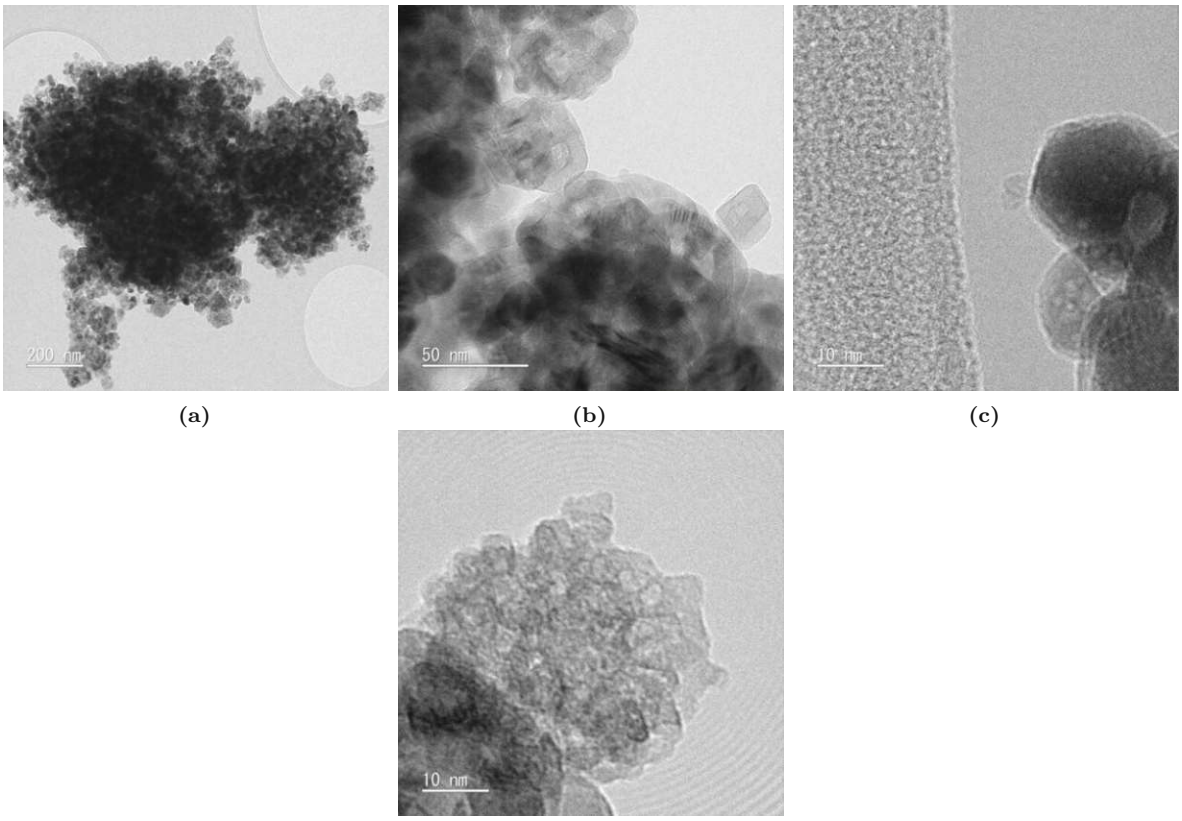

(a) (b) (c) (d)

Figure 9.6: $Ti\,[1\%/RT]_F^N$

$Ti\,[1\%/350]_F^N$

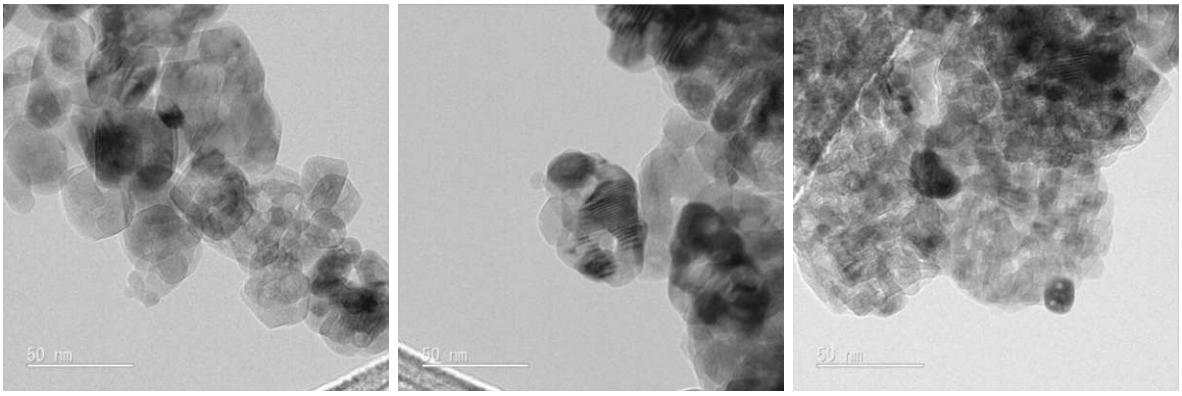

(a) (b) (c)

Figure 9.7: $Ti\,[1\%/350]_F^N$

Die approbierte gedruckte Originalversion dieser Diplomarbeit ist an der TU Wien Bibliothek verfügbar
The approved original version of this thesis is available in print at TU Wien Bibliothek.
TU Bibliothek Your knowledge hub WIEN

$Ti\,[1\%/RT]_E^N$

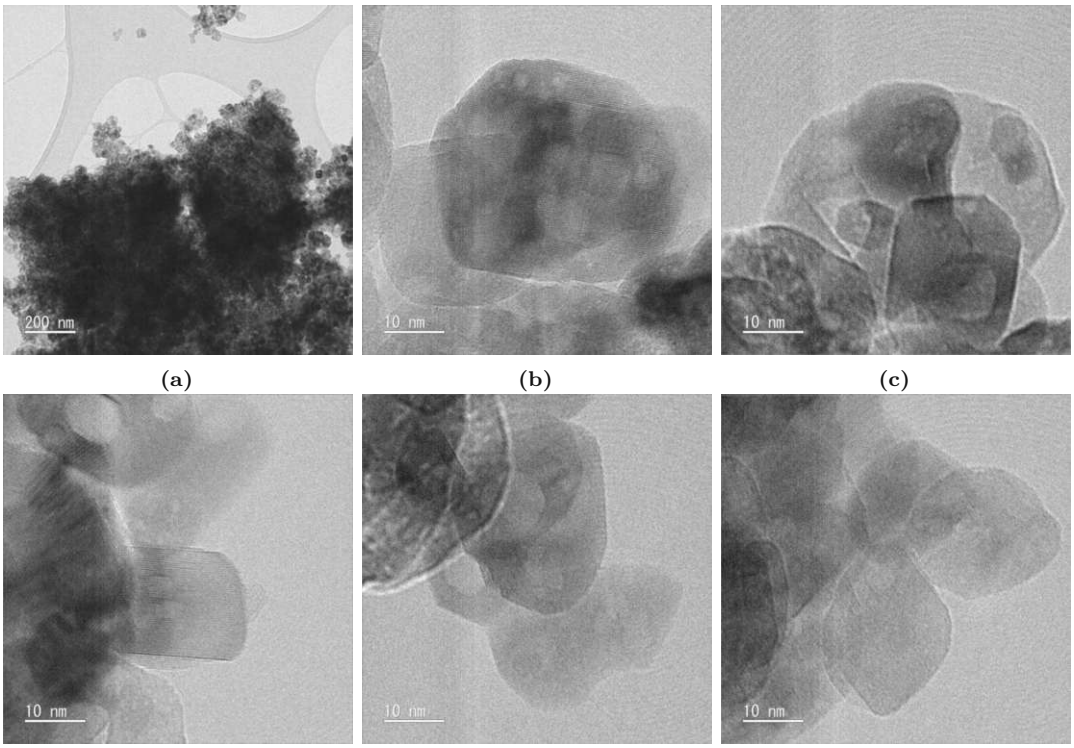

(a) (b) (c)

(d) (e) (f)

Figure 9.8: $Ti\,[1\%/RT]_E^N$

$Ti\,[1\%/350]_E^N$

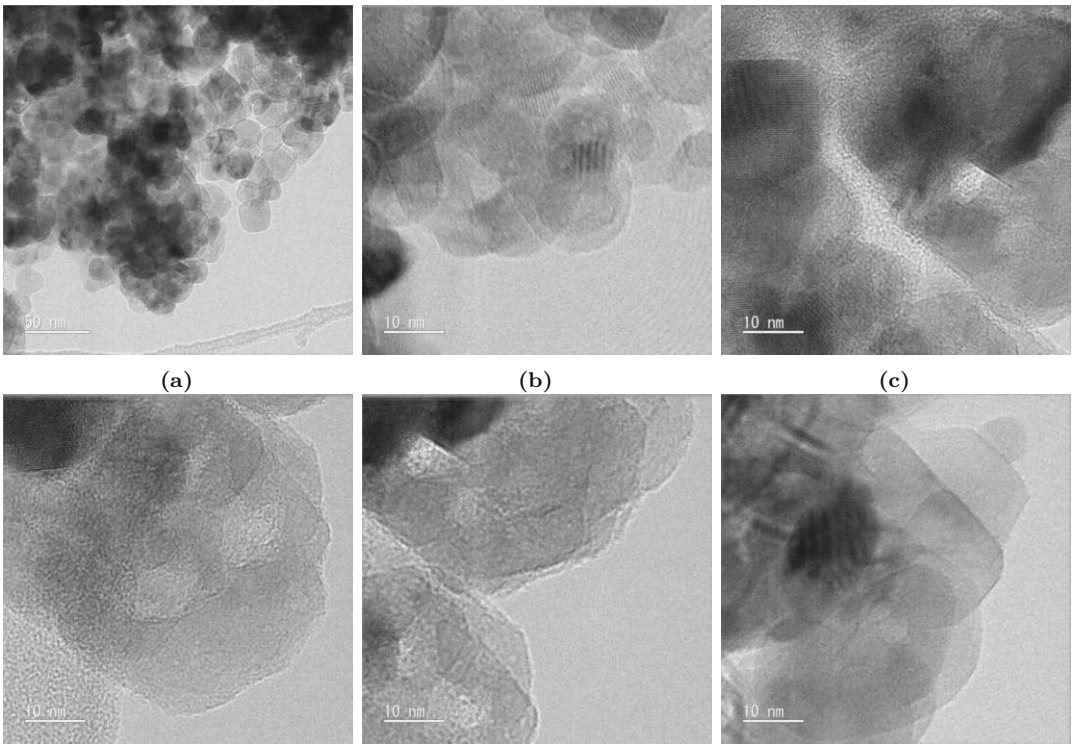

(a) (b) (c)

(d) (e) (f)

Figure 9.9: $Ti\,[1\%/350]_E^N$

Die approbierte gedruckte Originalversion dieser Diplomarbeit ist an der TU Wien Bibliothek verfügbar
The approved original version of this thesis is available in print at TU Wien Bibliothek.
TU Bibliothek Your knowledge hub WIEN

$Ti\,[1\%/RT]_F^S$

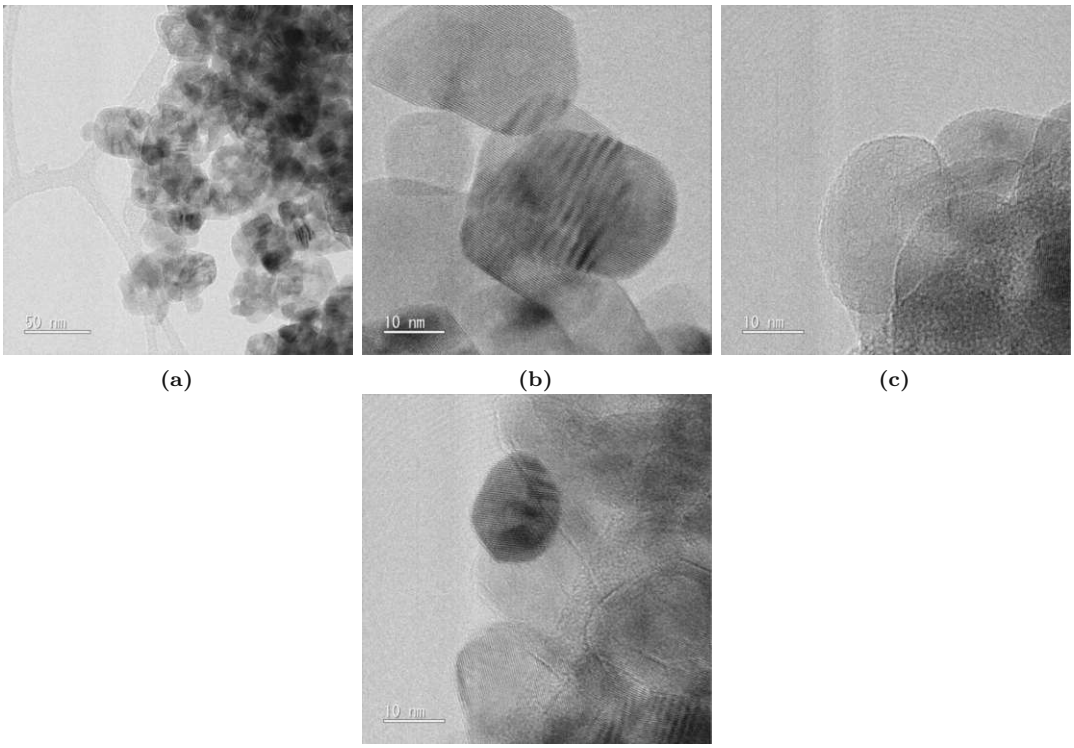

(a) (b) (c)

(d)

Figure 9.10: $Ti\,[1\%/RT]_F^S$

$Ti\,[1\%/600]_F^S$

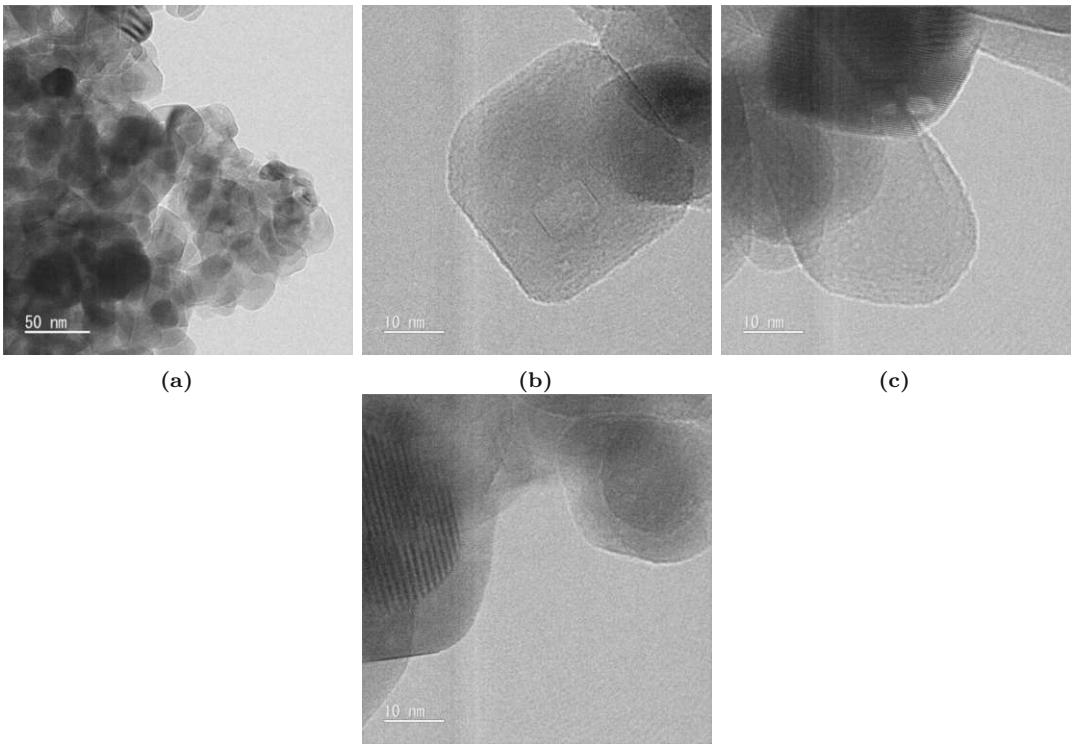

(a) (b) (c)

(d)

Figure 9.11: $Ti\,[1\%/600]_F^S$

Die approbierte gedruckte Originalversion dieser Diplomarbeit ist an der TU Wien Bibliothek verfügbar
The approved original version of this thesis is available in print at TU Wien Bibliothek.

$Ti\,[1\%/RT]_E^S$

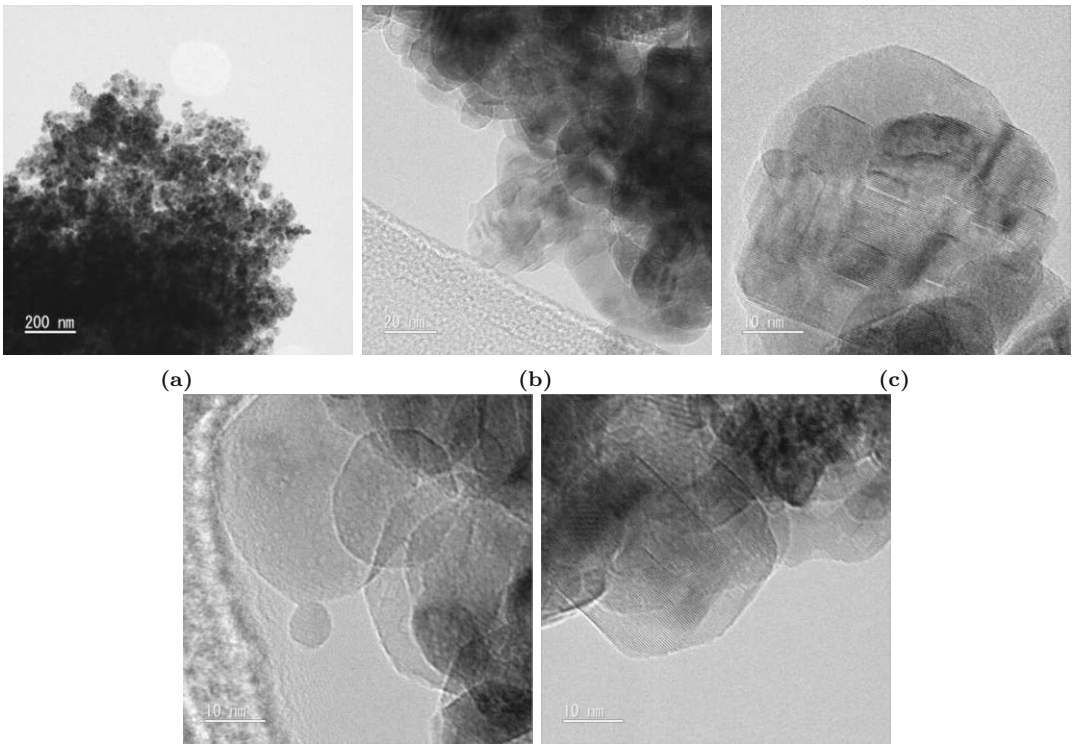

(a) (b) (c) (d) (e)

Figure 9.12: $Ti\,[1\%/RT]_E^S$

$Ti\,[1\%/350]_E^S$

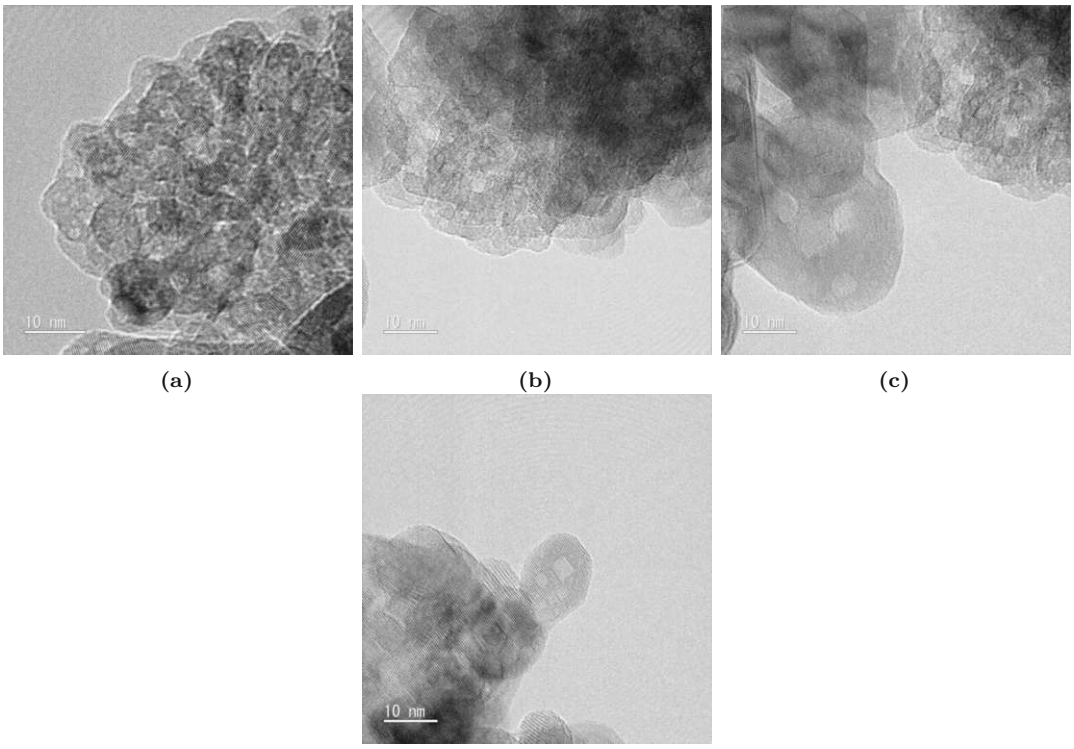

(a) (b) (c) (d)

Figure 9.13: $Ti\,[1\%/350]_E^S$

Die approbierte gedruckte Originalversion dieser Diplomarbeit ist an der TU Wien Bibliothek verfügbar
The approved original version of this thesis is available in print at TU Wien Bibliothek.

$Ti\,[1\%/600]_E^S$

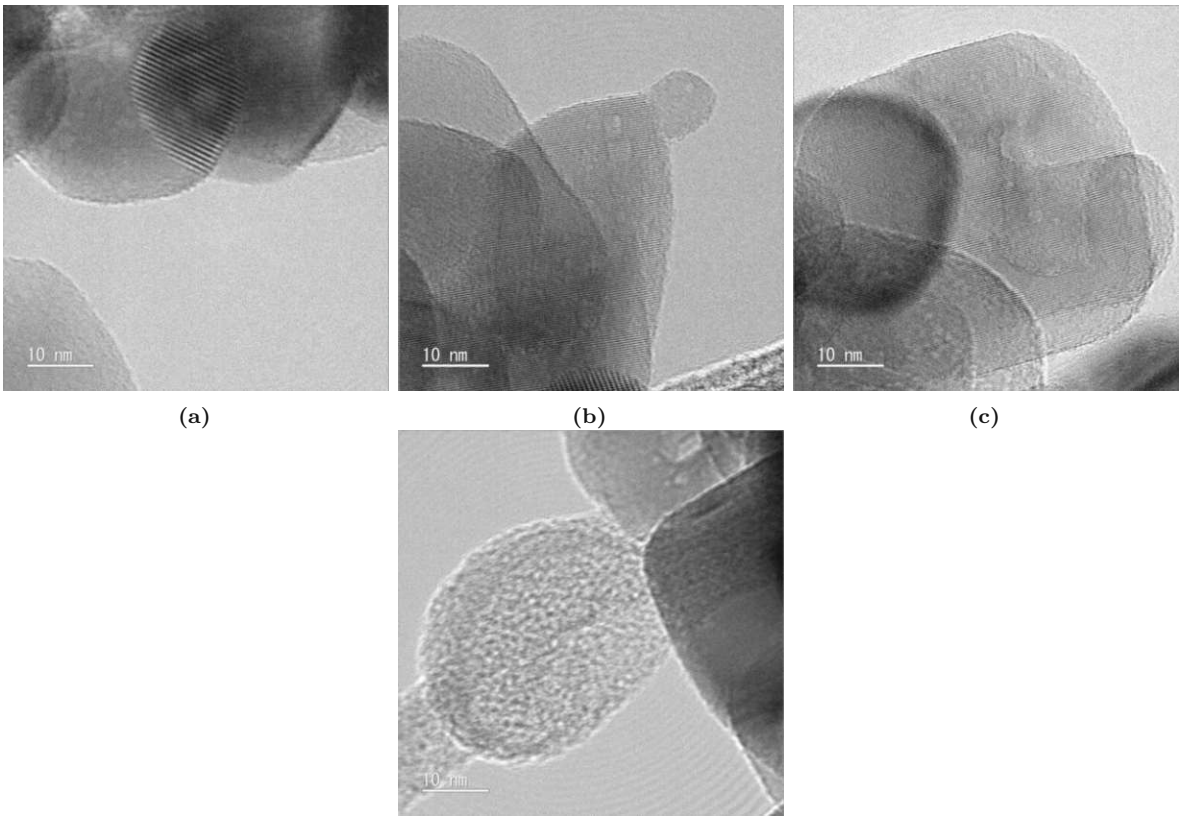

(a) (b) (c)

(d)

Figure 9.14: $Ti\,[1\%/600]_E^S$

$Ti\,[5\%/RT]_E^S$

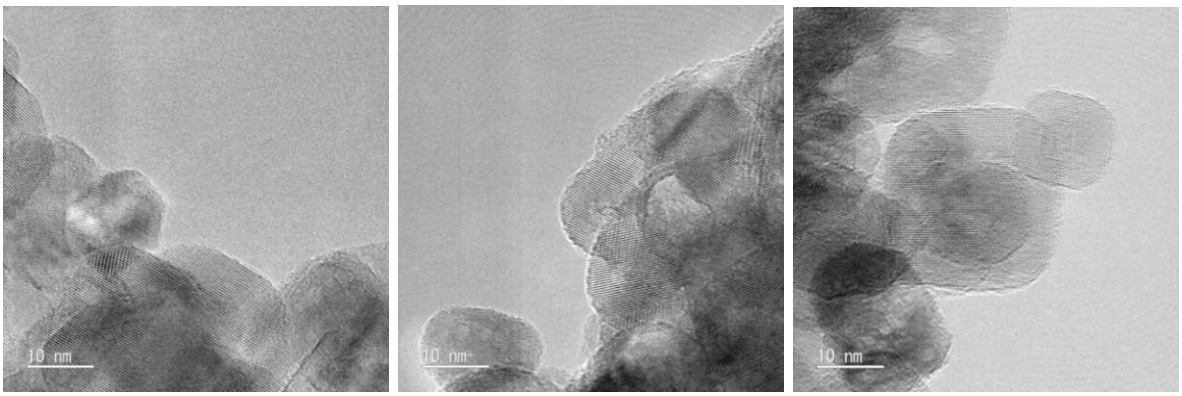

(a) (b) (c)

Figure 9.15: $Ti\,[5\%/RT]_E^S$

Die approbierte gedruckte Originalversion dieser Diplomarbeit ist an der TU Wien Bibliothek verfügbar
The approved original version of this thesis is available in print at TU Wien Bibliothek.

$Ti\,[5\%/350]_E^S$

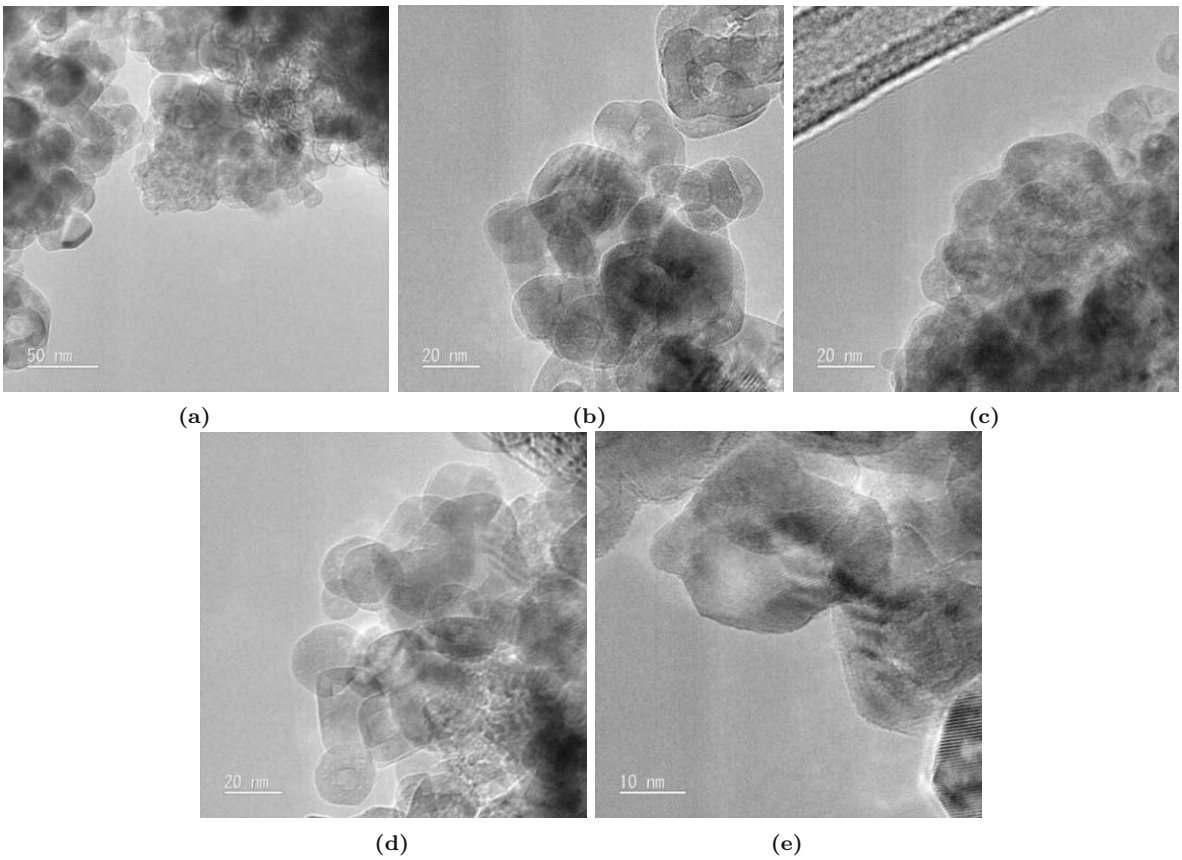

Figure 9.16: $Ti\,[5\%/350]_E^S$

Die approbierte gedruckte Originalversion dieser Diplomarbeit ist an der TU Wien Bibliothek verfügbar
The approved original version of this thesis is available in print at TU Wien Bibliothek.

$Ti\,[5\%/600]_E^S$

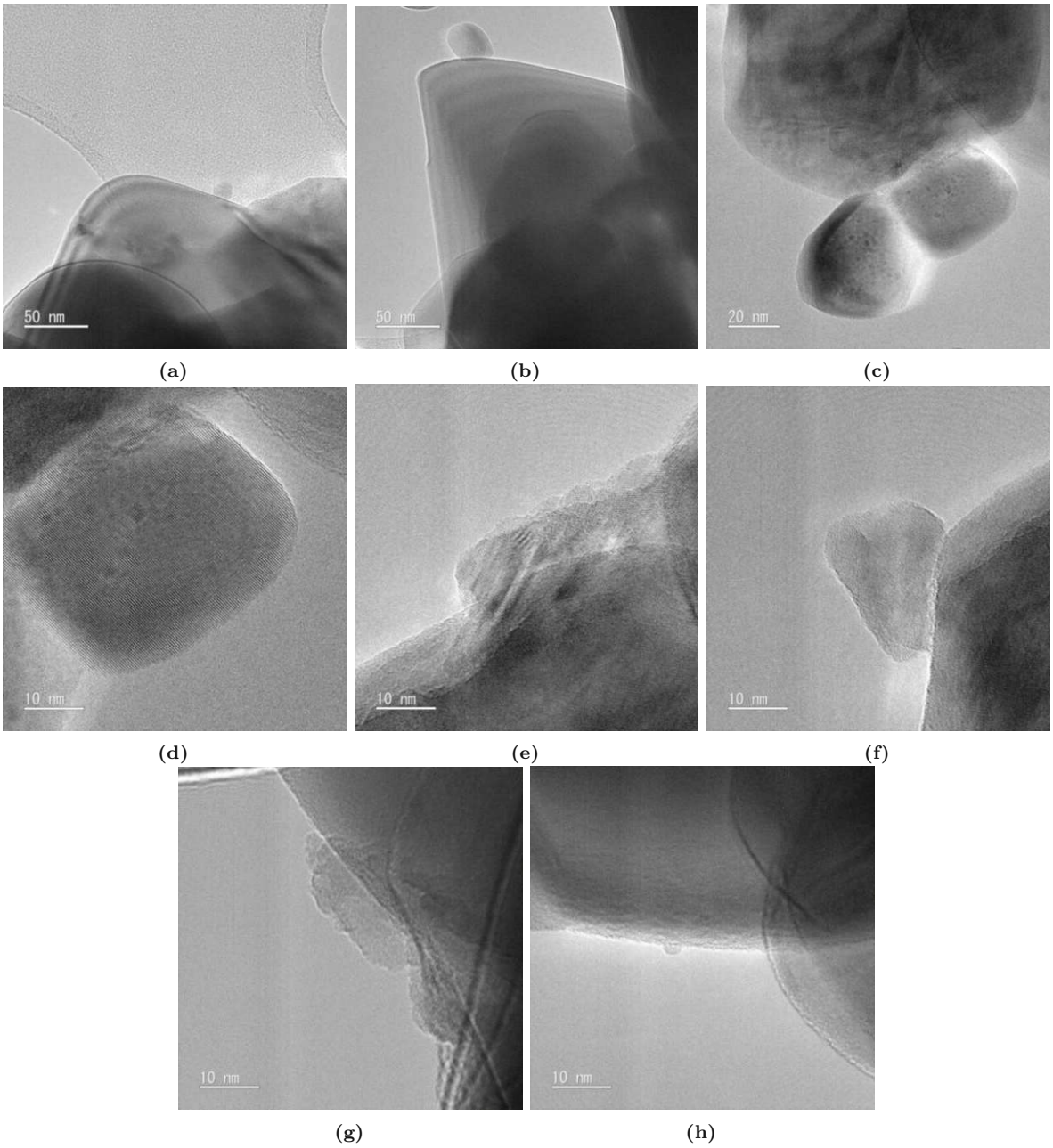

Figure 9.17: $Ti\,[5\%/600]_E^S$

Die approbierte gedruckte Originalversion dieser Diplomarbeit ist an der TU Wien Bibliothek verfügbar
The approved original version of this thesis is available in print at TU Wien Bibliothek.

$Ti\,[25\%/RT]_E^S$

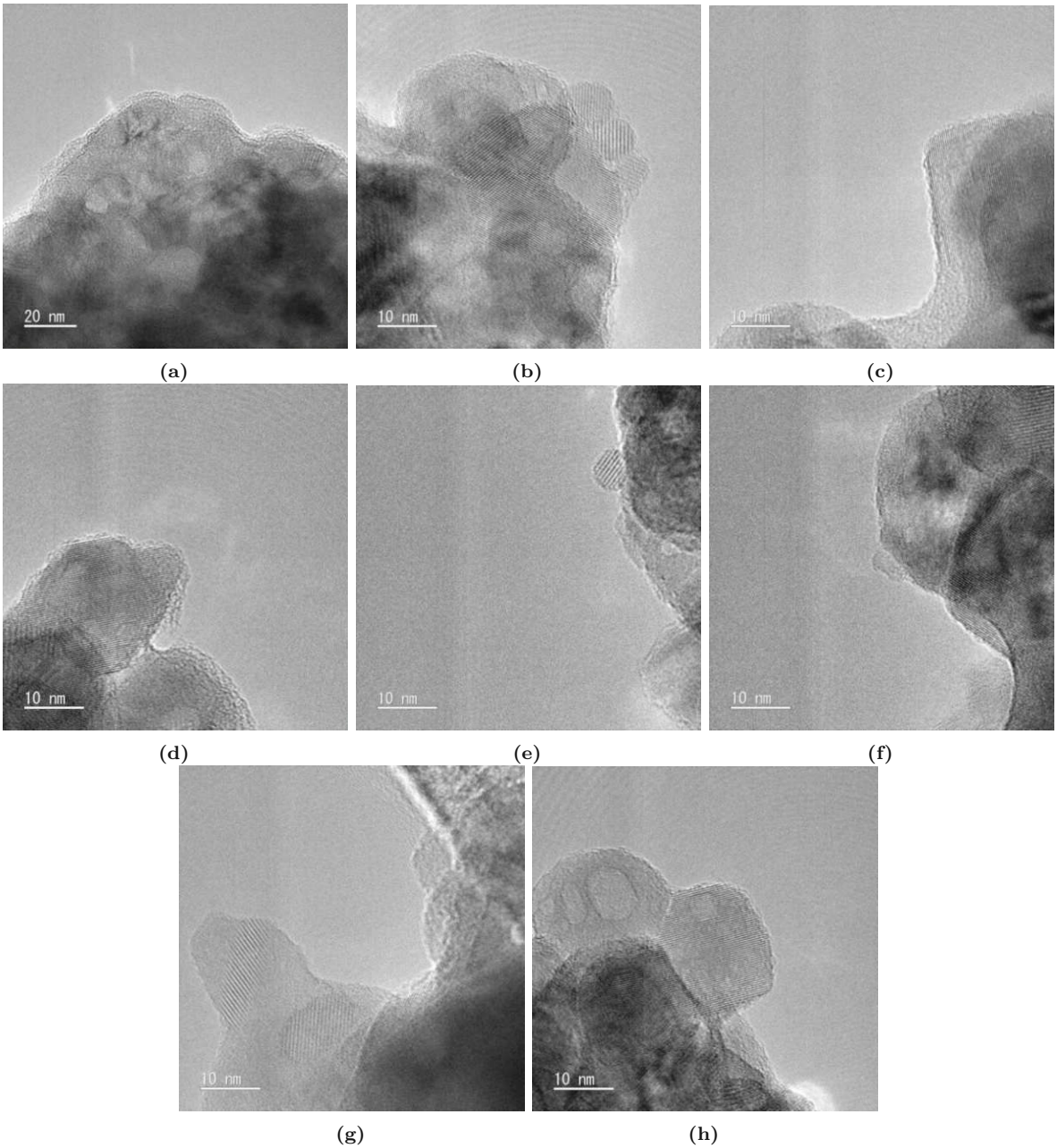

Figure 9.18: $Ti\,[25\%/RT]_E^S$

Die approbierte gedruckte Originalversion dieser Diplomarbeit ist an der TU Wien Bibliothek verfügbar
The approved original version of this thesis is available in print at TU Wien Bibliothek.

$Ti\,[25\%/350]_E^S$

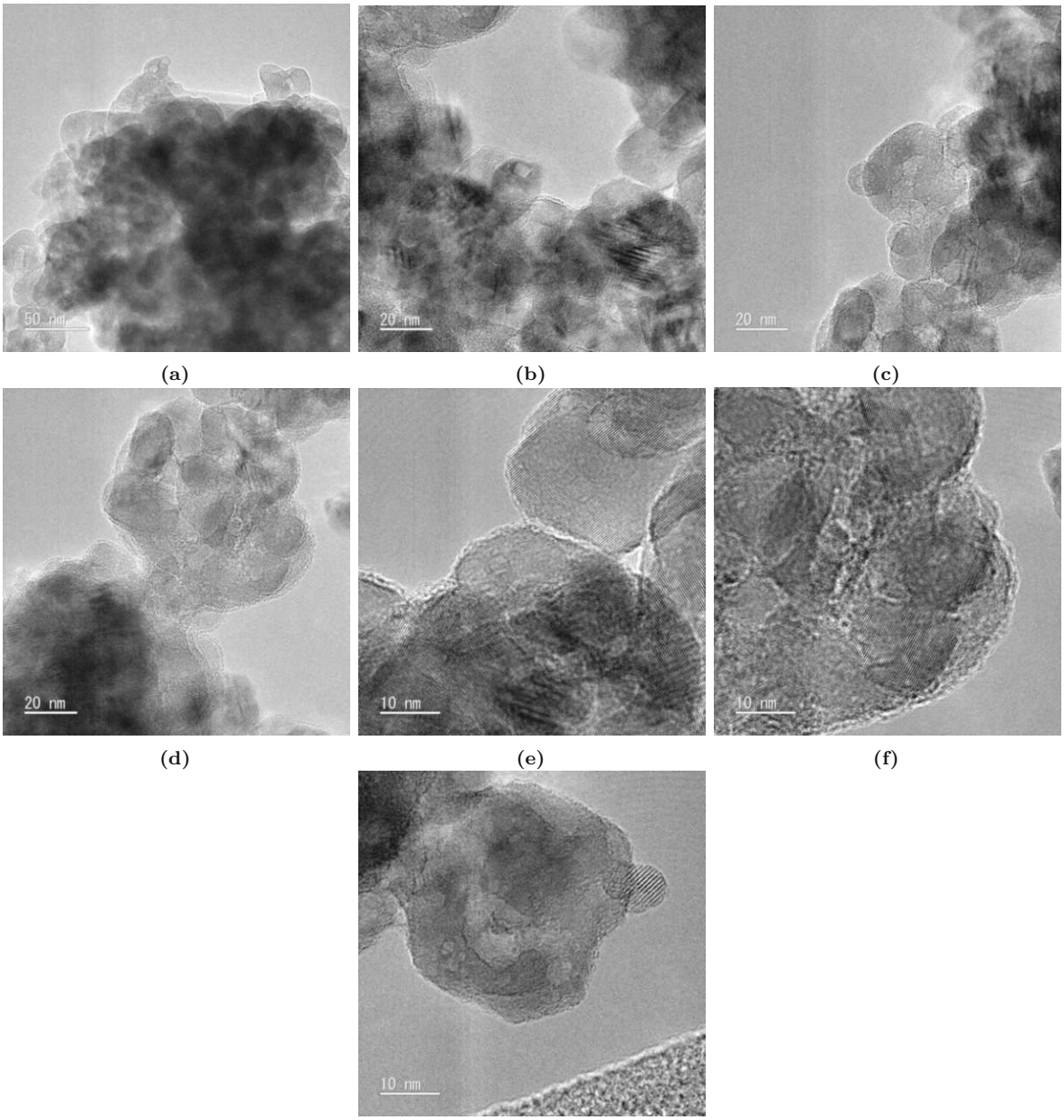

(a) (b) (c) (d) (e) (f) (g)

Figure 9.19: $Ti\,[25\%/350]_E^S$

Die approbierte gedruckte Originalversion dieser Diplomarbeit ist an der TU Wien Bibliothek verfügbar
The approved original version of this thesis is available in print at TU Wien Bibliothek.

$Ti\,[25\%/600]_E^S$

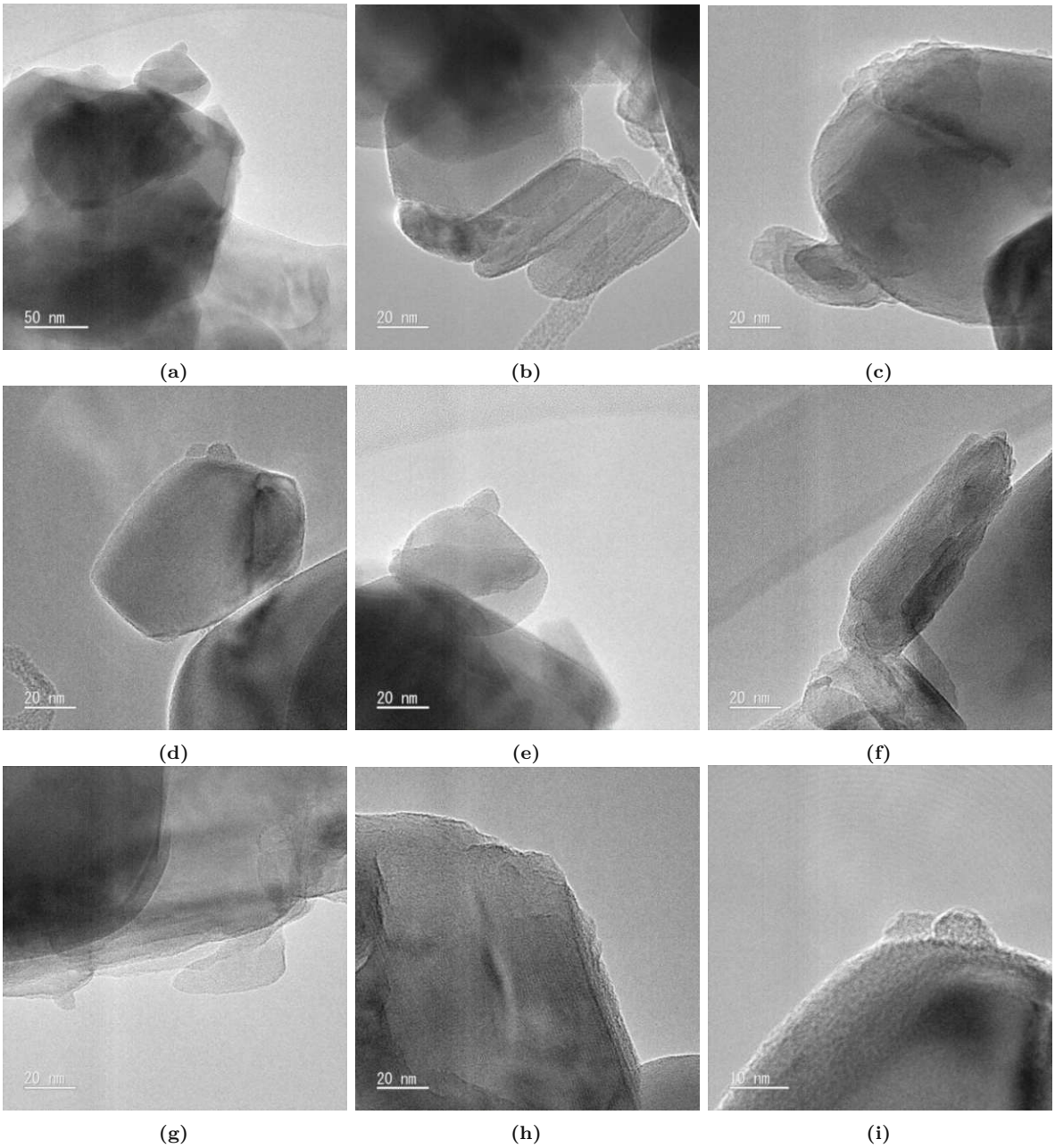

Figure 9.20: $Ti\,[25\%/600]_E^S$

Die approbierte gedruckte Originalversion dieser Diplomarbeit ist an der TU Wien Bibliothek verfügbar
The approved original version of this thesis is available in print at TU Wien Bibliothek.

9.4 XPS

$Ti\,[25\%/350]_E^S$

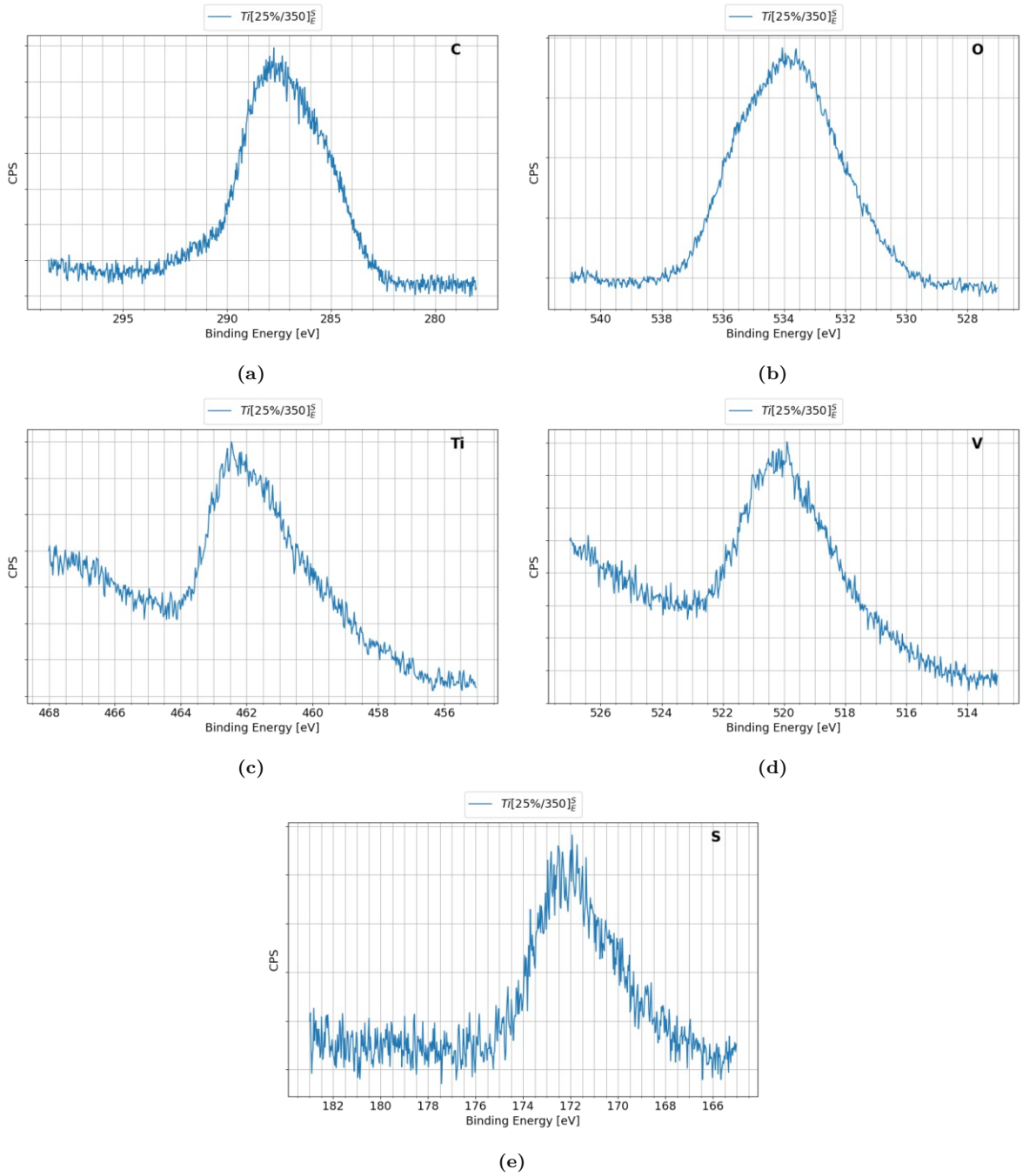

Figure 9.21: XPS spetra $Ti\,[25\%/350]_E^S$. (a) shows the binding energy region for carbon, (b) for oxygen, (c) for titanium (d) for vanadium and (e) for sulfur.

Die approbierte gedruckte Originalversion dieser Diplomarbeit ist an der TU Wien Bibliothek verfügbar
The approved original version of this thesis is available in print at TU Wien Bibliothek.

9.5 TXRF

9.5.1 Composition analysis

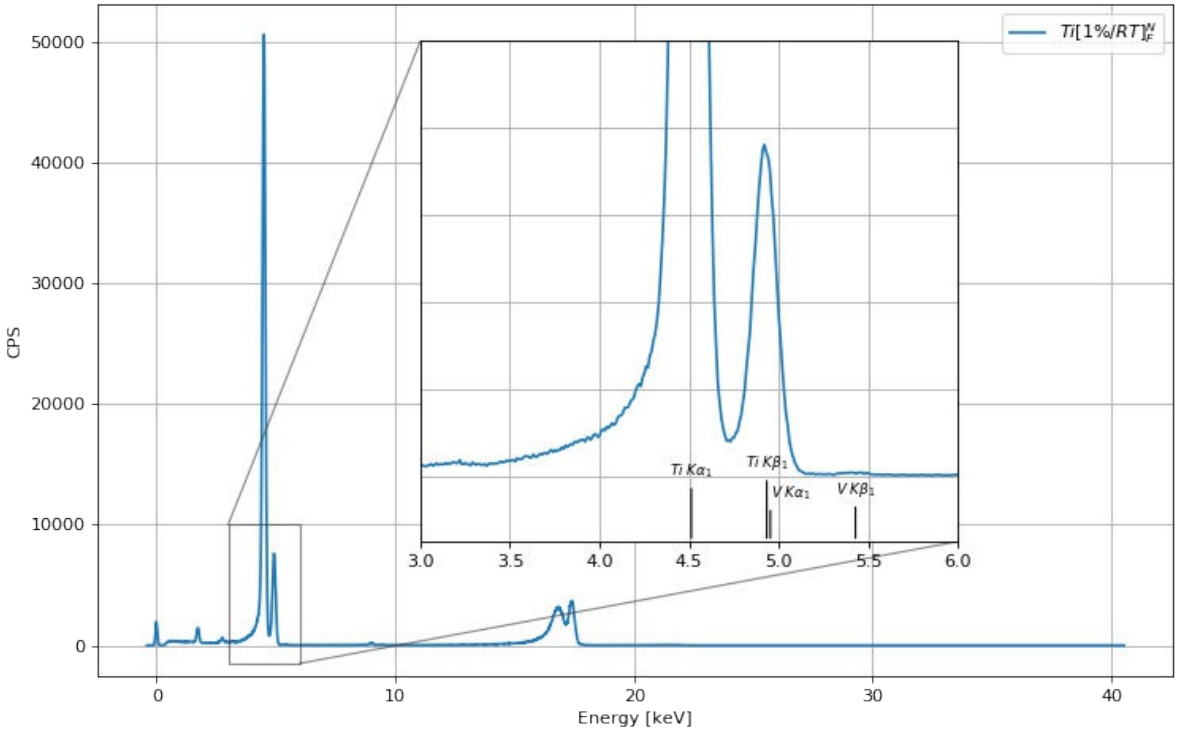

Figure 9.22: TXRF spectrum of the catalyst $Ti\,[1\%/350]_F^N$.

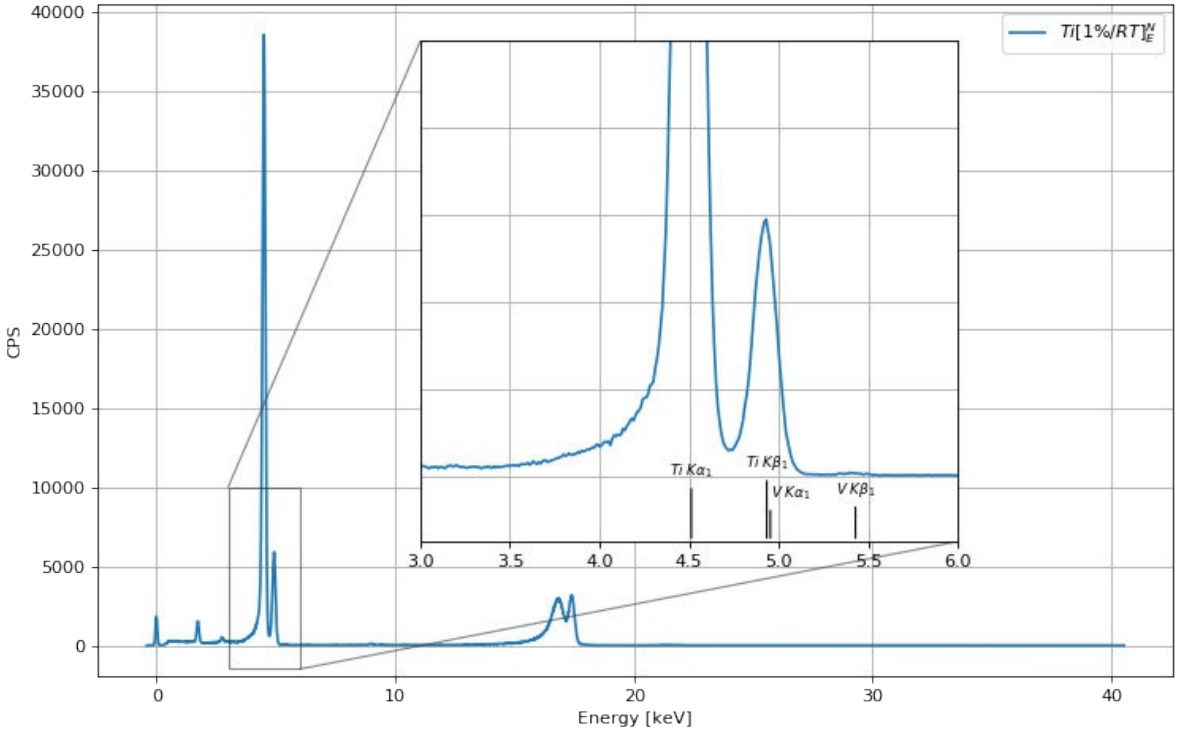

Figure 9.23: TXRF spectrum of the catalyst $Ti\,[1\%/350]_E^N$.

Die approbierte gedruckte Originalversion dieser Diplomarbeit ist an der TU Wien Bibliothek verfügbar
The approved original version of this thesis is available in print at TU Wien Bibliothek.

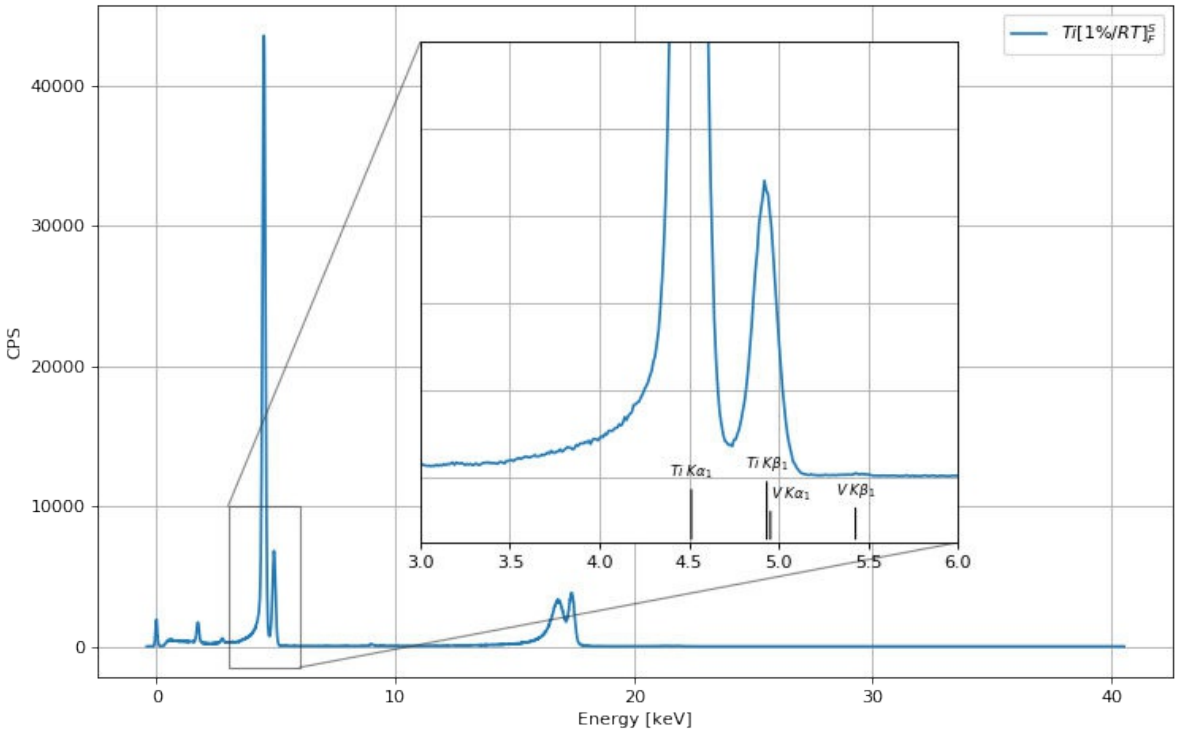

Figure 9.24: TXRF spectrum of the catalyst $Ti\,[1\%/RT]_F^S$.

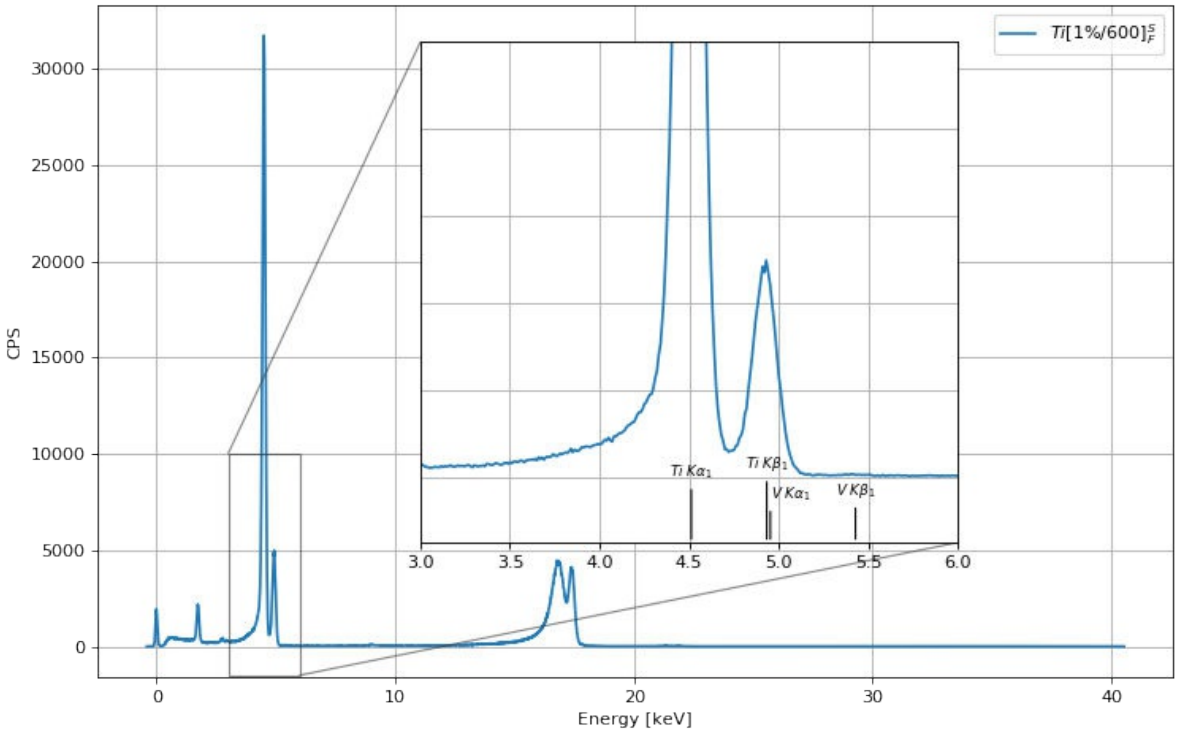

Figure 9.25: TXRF spectrum of the catalyst $Ti\,[1\%/600]_F^S$.

Die approbierte gedruckte Originalversion dieser Diplomarbeit ist an der TU Wien Bibliothek verfügbar
The approved original version of this thesis is available in print at TU Wien Bibliothek.

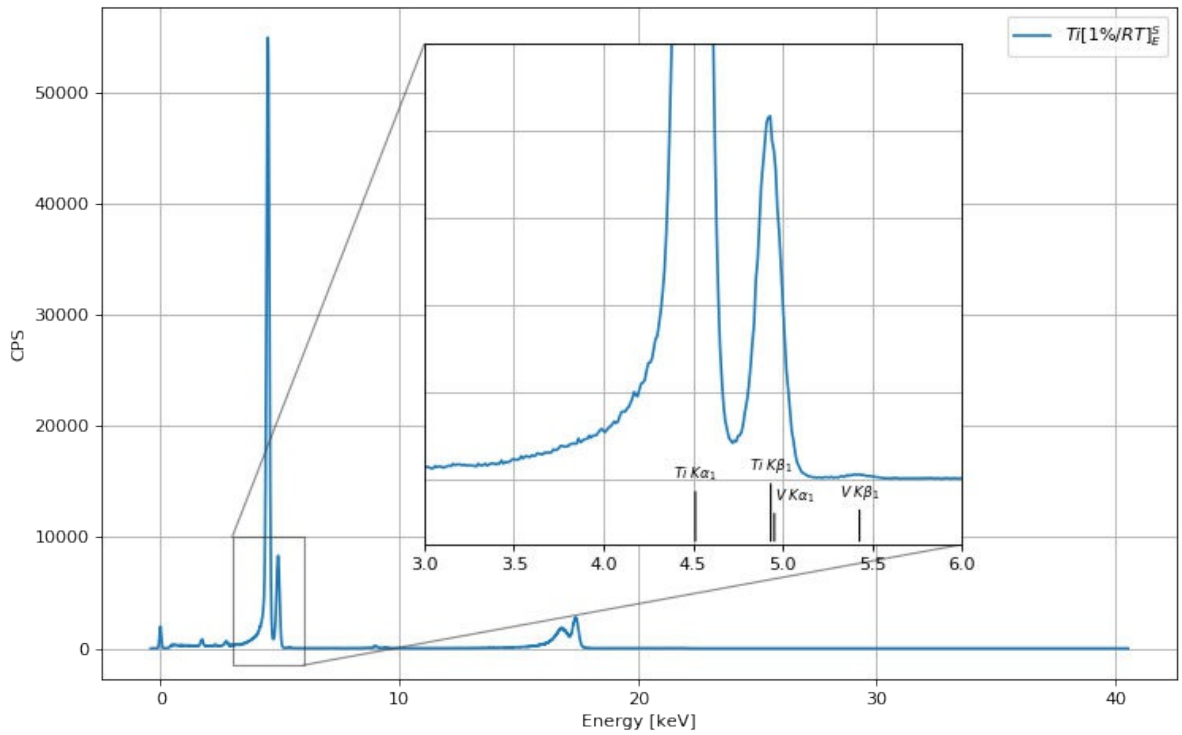

Figure 9.26: TXRF spectrum of the catalyst $Ti\,[1\%/RT]_E^S$.

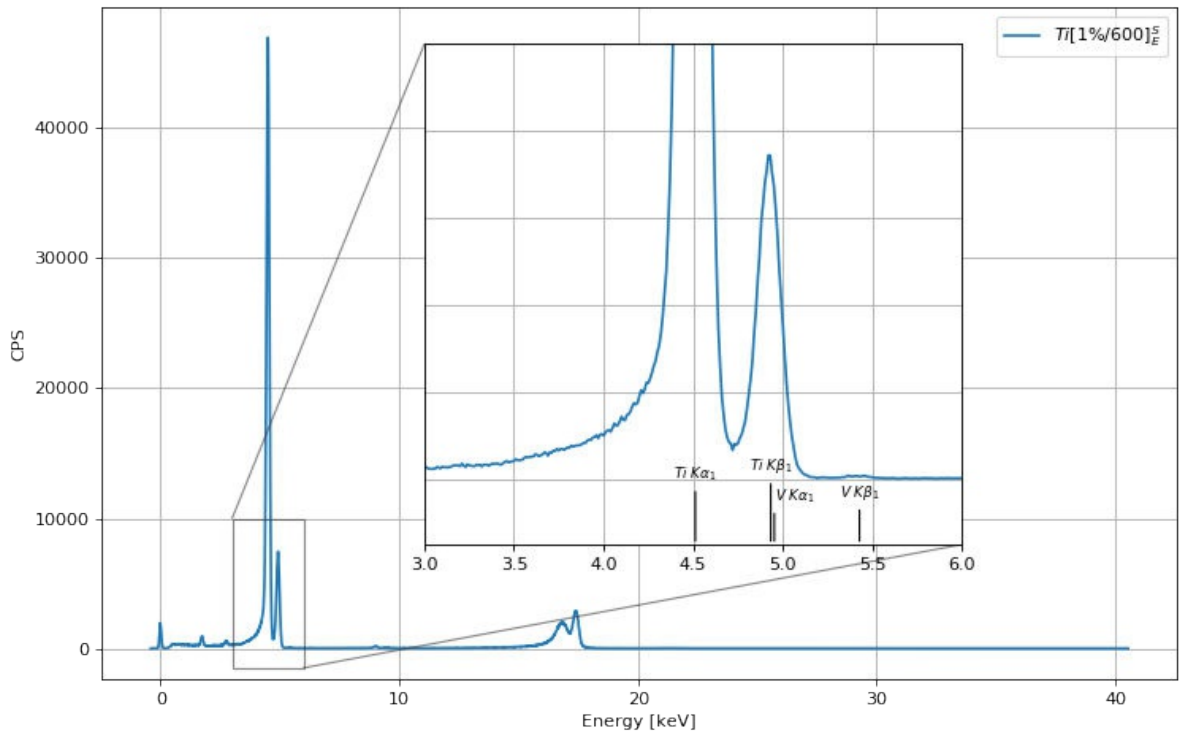

Figure 9.27: TXRF spectrum of the catalyst $Ti\,[1\%/600]_E^S$.

Die approbierte gedruckte Originalversion dieser Diplomarbeit ist an der TU Wien Bibliothek verfügbar
The approved original version of this thesis is available in print at TU Wien Bibliothek.

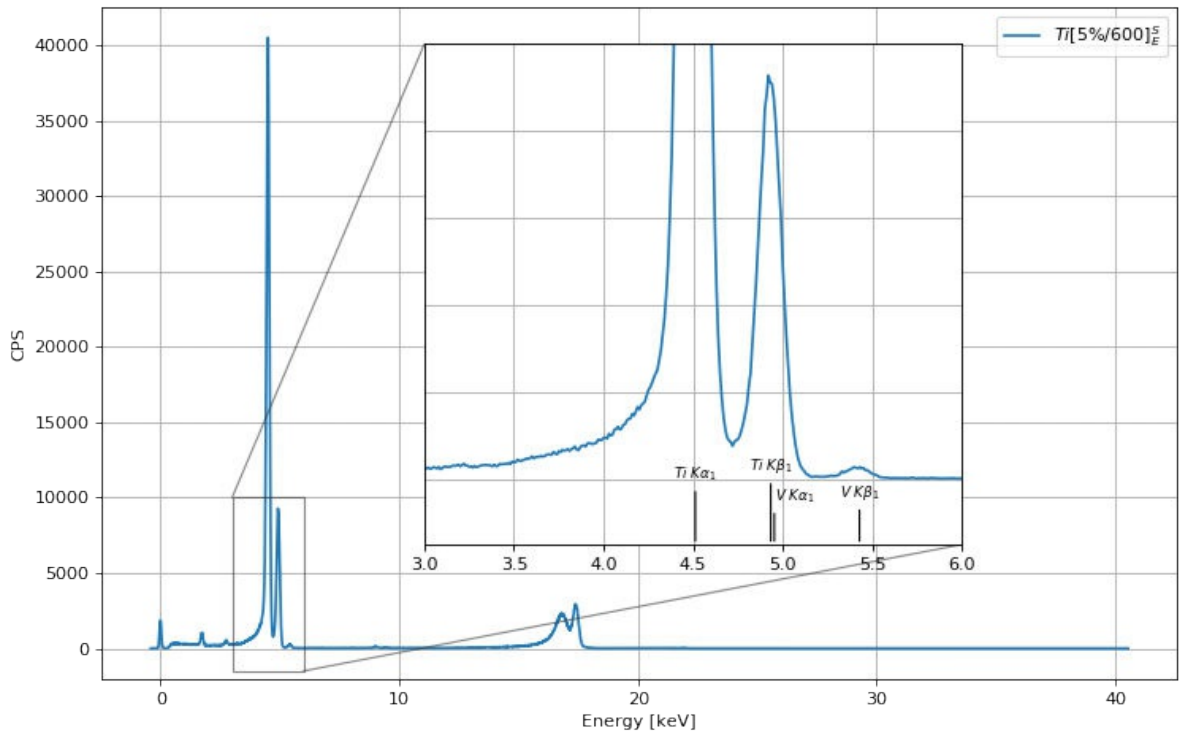

Figure 9.28: TXRF spectrum of the catalyst $Ti\,[5\%/600]_E^S$.

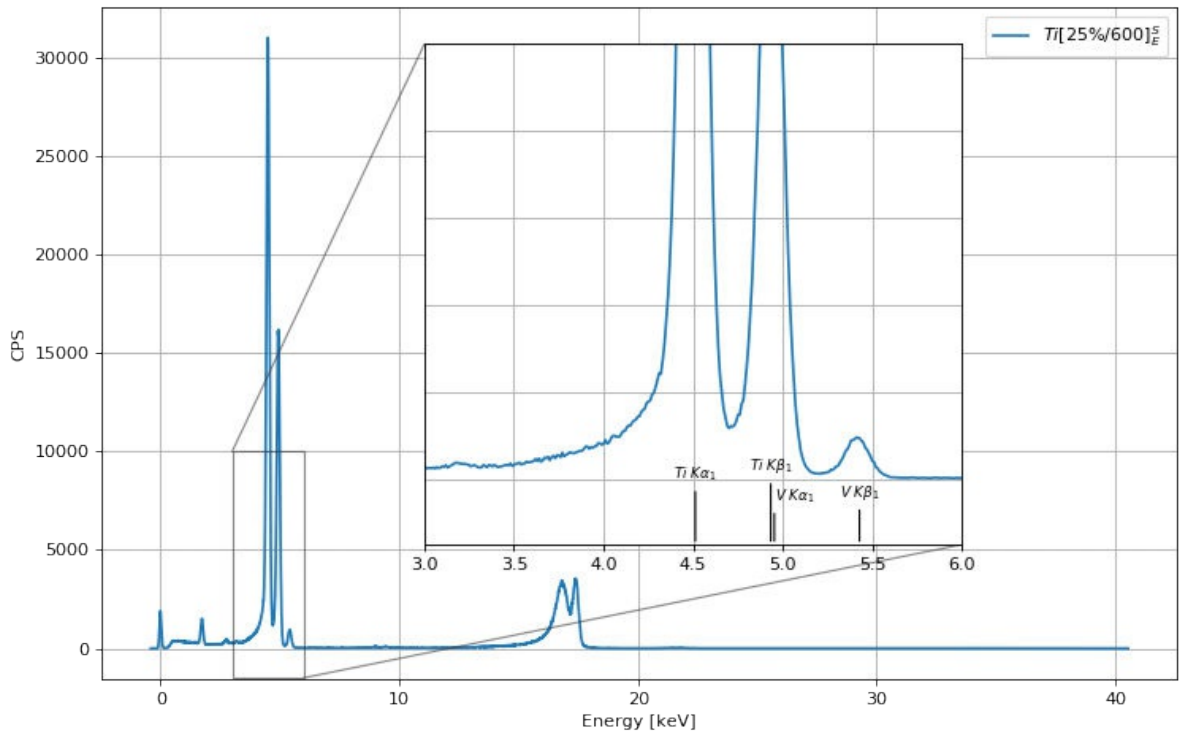

Figure 9.29: TXRF spectrum of the catalyst $Ti\,[25\%/600]_E^S$.

Die approbierte gedruckte Originalversion dieser Diplomarbeit ist an der TU Wien Bibliothek verfügbar
The approved original version of this thesis is available in print at TU Wien Bibliothek.

9.5.2 Leaching analysis

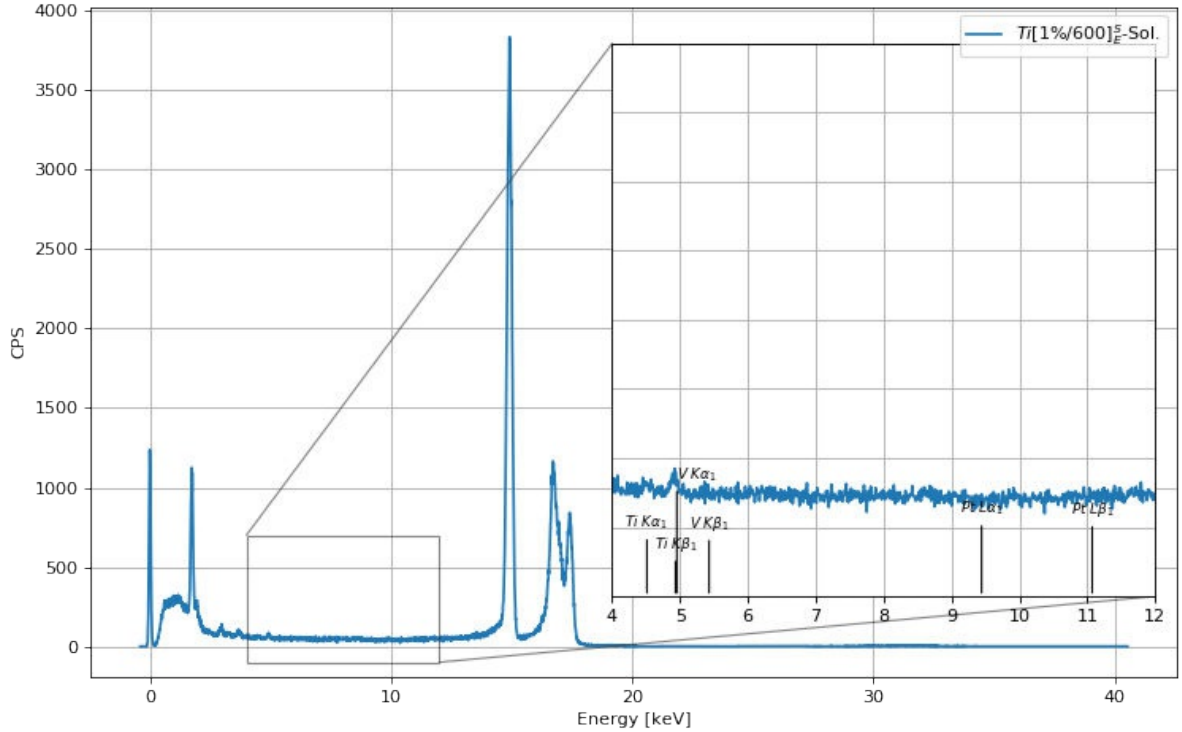

Figure 9.30: TXRF spectrum of the reaction mixture after the Vis-HER experiment of $Ti\,[1\%/600]_E^S$.

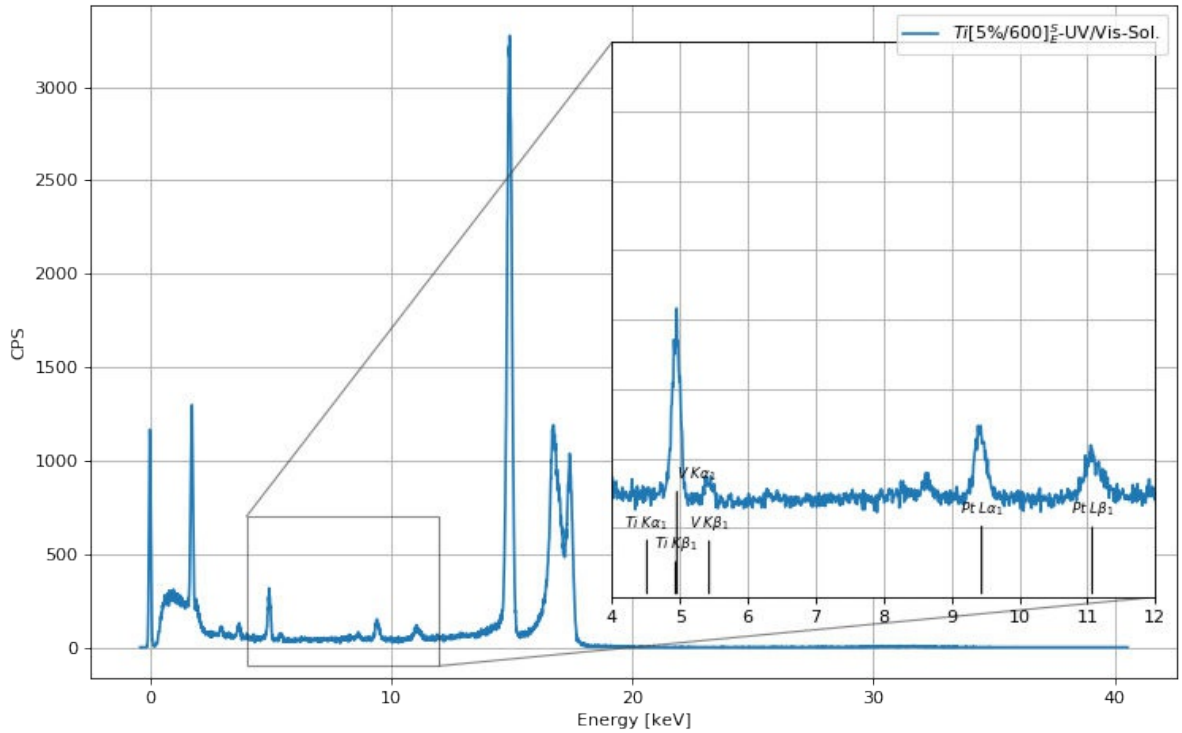

Figure 9.31: TXRF spectrum of the reaction mixture after the Vis-HER experiment of $Ti\,[1\%/600]_E^S$ (UVVis).

Die approbierte gedruckte Originalversion dieser Diplomarbeit ist an der TU Wien Bibliothek verfügbar
The approved original version of this thesis is available in print at TU Wien Bibliothek.
TU Bibliothek Your knowledge hub WIEN

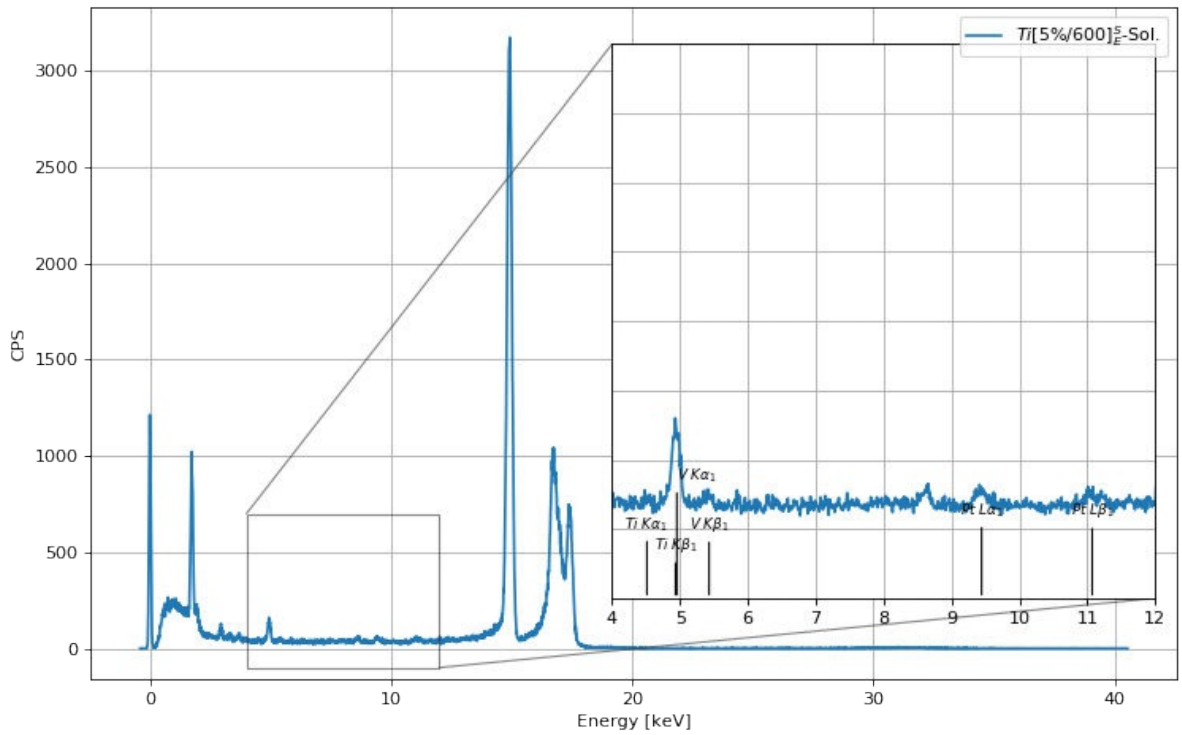

Figure 9.32: TXRF spectrum of the reaction mixture after the Vis-HER experiment of $Ti\,[5\%/600]_E^S$.

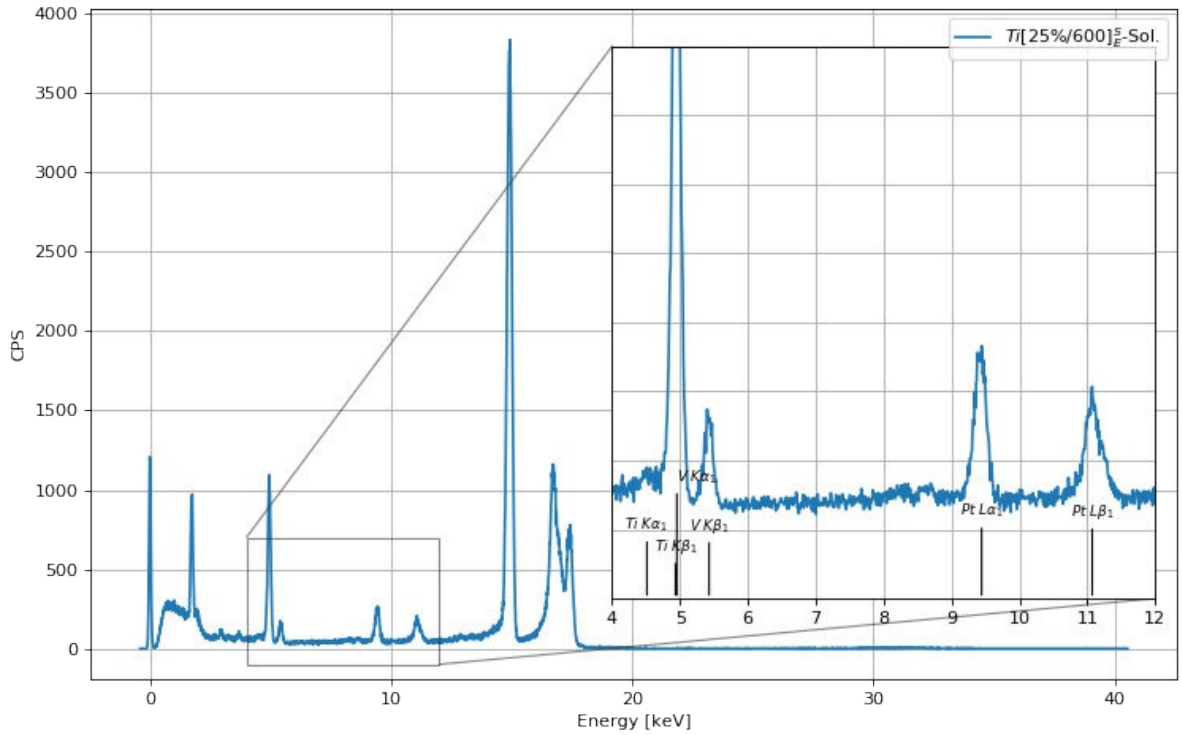

Figure 9.33: TXRF spectrum of the reaction mixture after the Vis-HER experiment of $Ti\,[25\%/600]_E^S$.

Die approbierte gedruckte Originalversion dieser Diplomarbeit ist an der TU Wien Bibliothek verfügbar
The approved original version of this thesis is available in print at TU Wien Bibliothek.

9.6 IR Spectra

Anatase

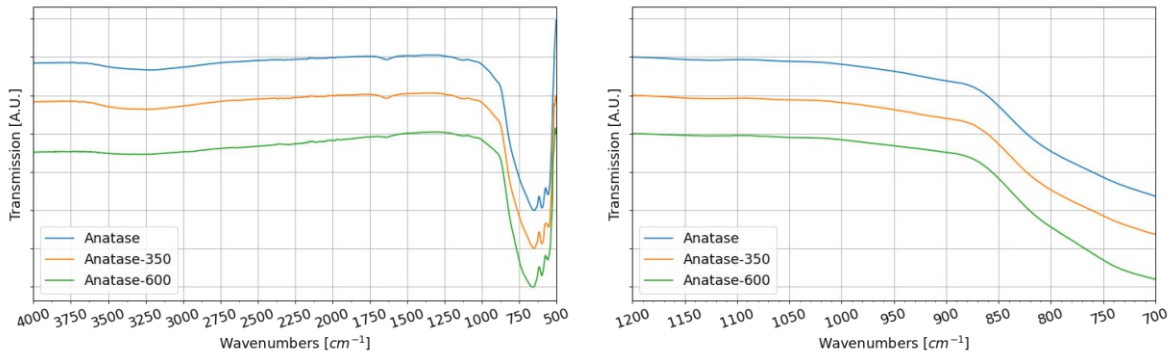

(a): Overview **(b):** Low wavenumber region

Figure 9.34: IR spectra of Anatase

$VOSO_4$

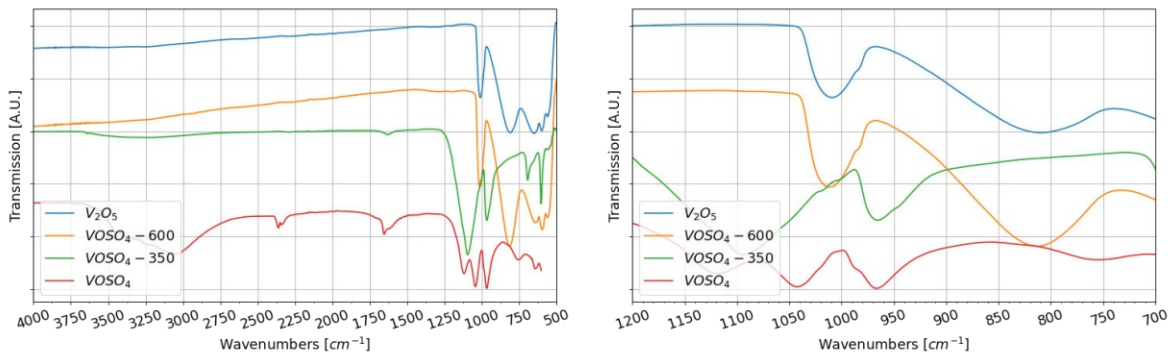

(a): Overview **(b):** Low wavenumber region

Figure 9.35: IR spectra of $VOSO_4$

NH_4VO_3

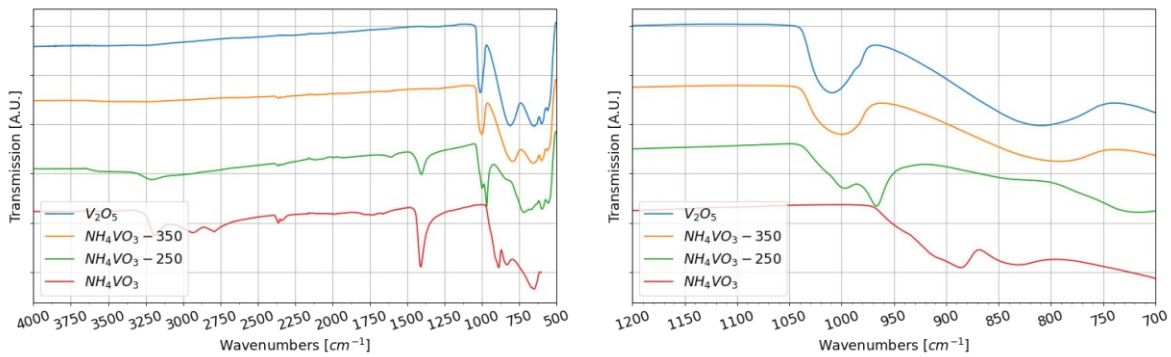

(a): Overview **(b):** Low wavenumber region

Figure 9.36: IR spectra of NH_4VO_3

Die approbierte gedruckte Originalversion dieser Diplomarbeit ist an der TU Wien Bibliothek verfügbar
The approved original version of this thesis is available in print at TU Wien Bibliothek.
TU Bibliothek Your knowledge hub WIEN

9.7 OER

To compensate the drift in the oxygen concentration, caused by small leaks in the reactor, the data was modified in such a way as to compensate for this effect. Before turning on the UV lamp (grey area), the drift was recorded for 29 min and for the last 10 min of this time period a regression line was calculated. This line was taken to be the oxygen concentration drift which was present through the whole experiment and so it was subtracted from the whole dataset. Because of this subtraction it sometimes happened that the oxygen concentration seemed to drop after the experiment, but the absolute values never showed such a drop in the oxygen concentration.

Anatase and reference samples

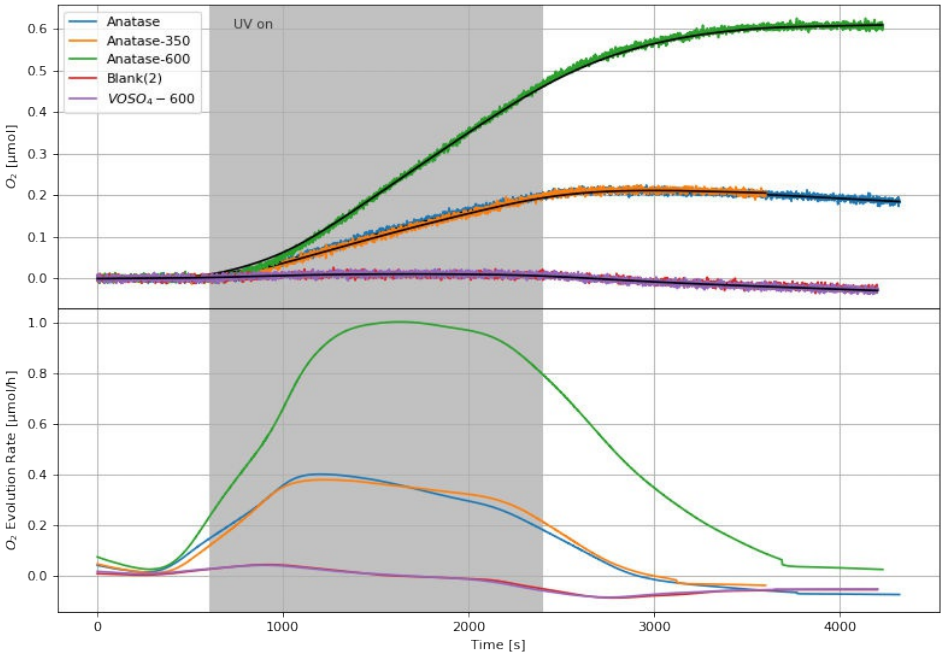

Figure 9.37: Oxygen concentrations and the first derivative of the plot for Anatase samples,Blank and $VOSO_4$-600

Die approbierte gedruckte Originalversion dieser Diplomarbeit ist an der TU Wien Bibliothek verfügbar
The approved original version of this thesis is available in print at TU Wien Bibliothek.

$Ti\,[1\%/RT]_F^N$

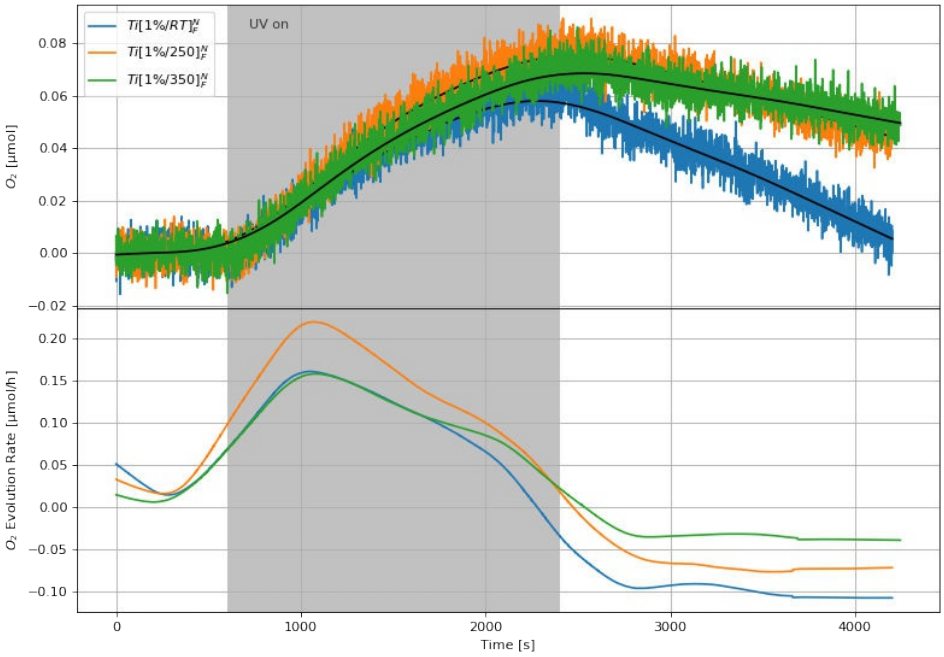

Figure 9.38: Oxygen concentrations and the first derivative of the plot for $Ti\,[1\%/RT]_F^N$

$Ti\,[1\%/RT]_E^N$

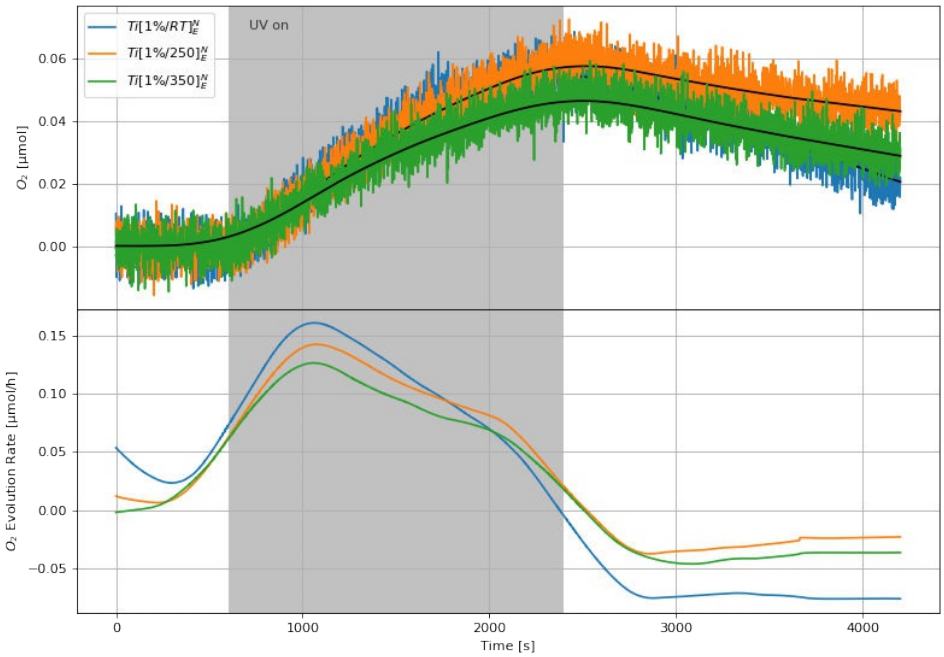

Figure 9.39: Oxygen concentrations and the first derivative of the plot for $Ti\,[1\%/RT]_E^N$

Die approbierte gedruckte Originalversion dieser Diplomarbeit ist an der TU Wien Bibliothek verfügbar
The approved original version of this thesis is available in print at TU Wien Bibliothek.

$Ti\,[1\%/RT]_F^S$

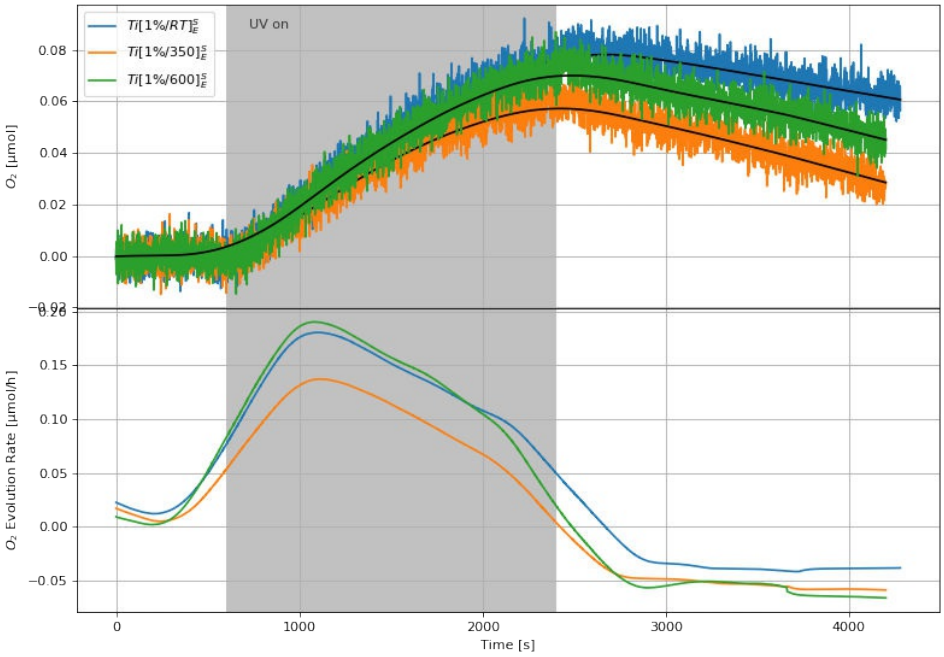

Figure 9.40: Oxygen concentrations and the first derivative of the plot for $Ti\,[1\%/RT]_F^S$

$Ti\,[1\%/RT]_E^S$

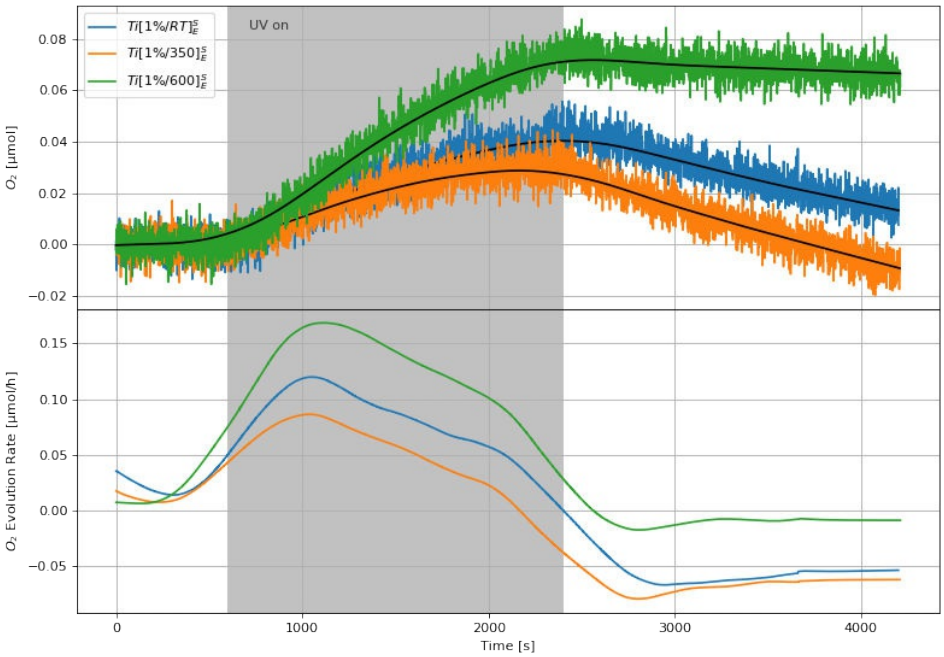

Figure 9.41: Oxygen concentrations and the first derivative of the plot for $Ti\,[1\%/RT]_E^S$

Die approbierte gedruckte Originalversion dieser Diplomarbeit ist an der TU Wien Bibliothek verfügbar
The approved original version of this thesis is available in print at TU Wien Bibliothek.

$Ti\,[5\%/RT]_E^S$

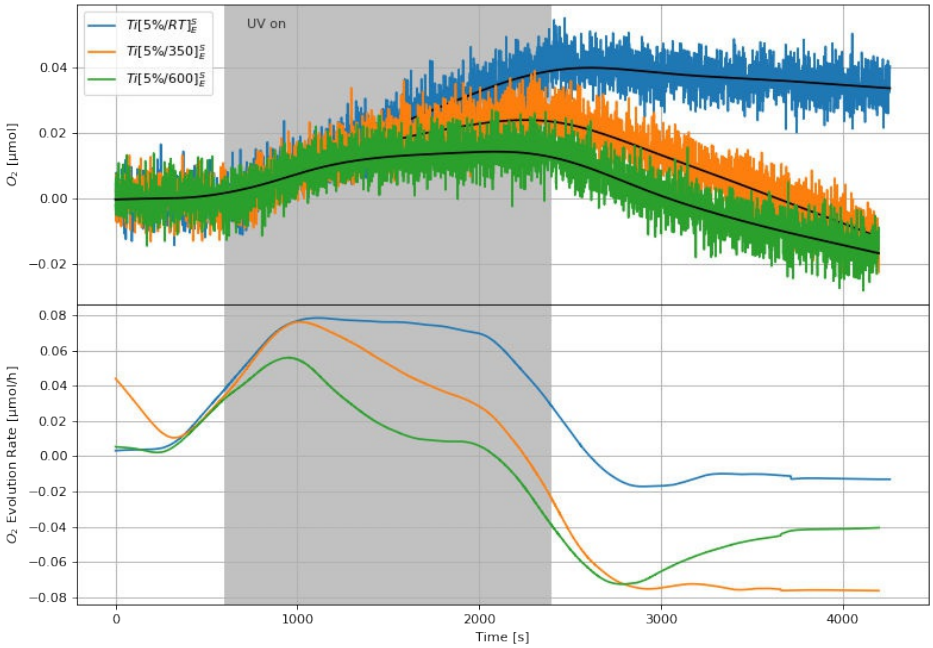

Figure 9.42: Oxygen concentrations and the first derivative of the plot for $Ti\,[5\%/RT]_E^S$

$Ti\,[25\%/RT]_E^S$

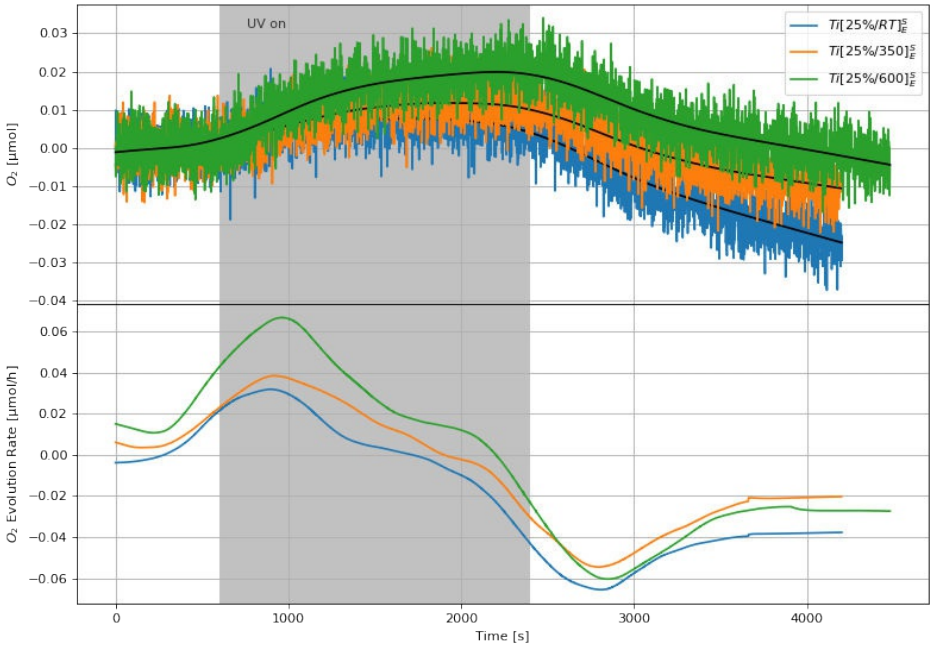

Figure 9.43: Oxygen concentrations and the first derivative of the plot for $Ti\,[25\%/RT]_E^S$

Die approbierte gedruckte Originalversion dieser Diplomarbeit ist an der TU Wien Bibliothek verfügbar
The approved original version of this thesis is available in print at TU Wien Bibliothek.

9.8 UV-HER

$Ti\,[1\%/RT]_F^N$

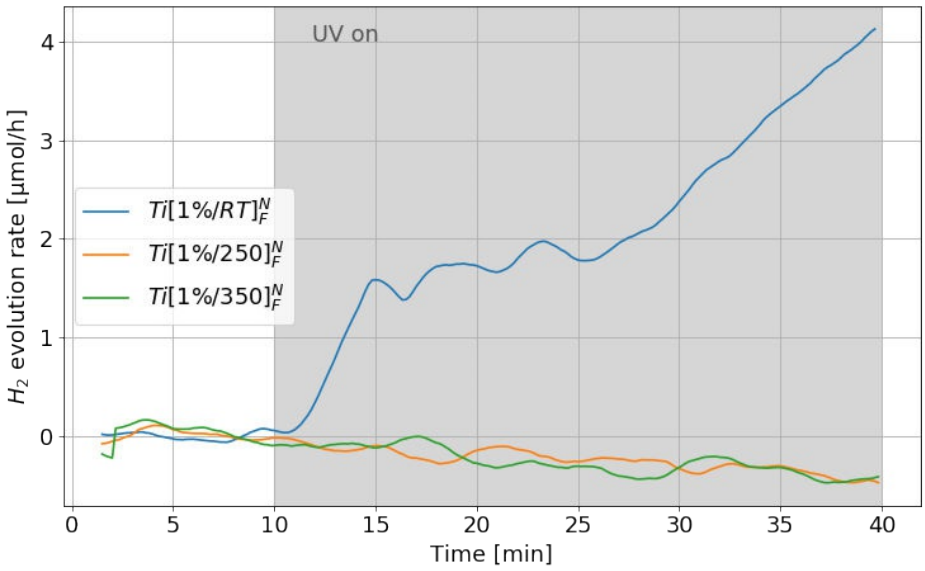

Figure 9.44: UV-HER activity of $Ti\,[1\%/RT]_F^N$

$Ti\,[1\%/RT]_E^N$

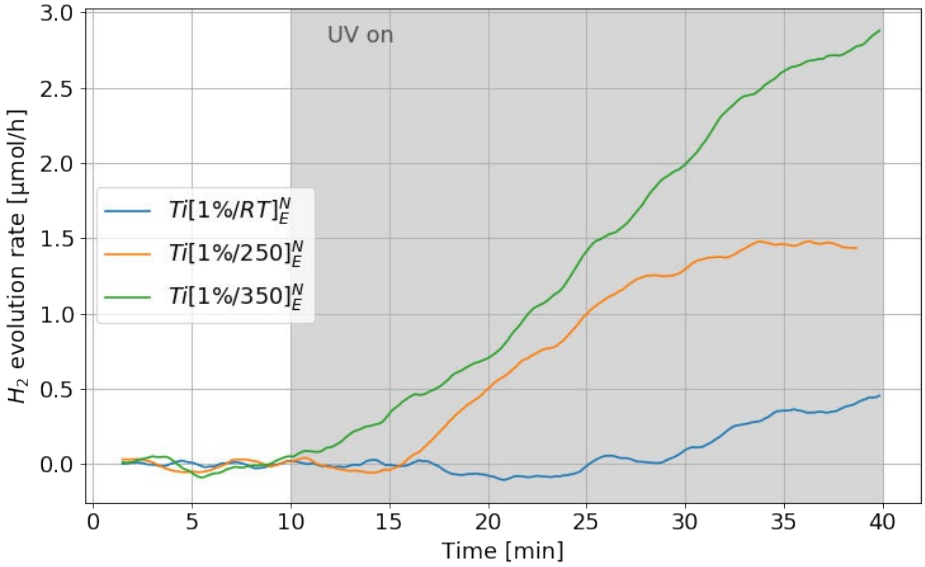

Figure 9.45: UV-HER activity of $Ti\,[1\%/RT]_E^N$

Die approbierte gedruckte Originalversion dieser Diplomarbeit ist an der TU Wien Bibliothek verfügbar
The approved original version of this thesis is available in print at TU Wien Bibliothek.

$Ti\,[1\%/RT]_F^S$

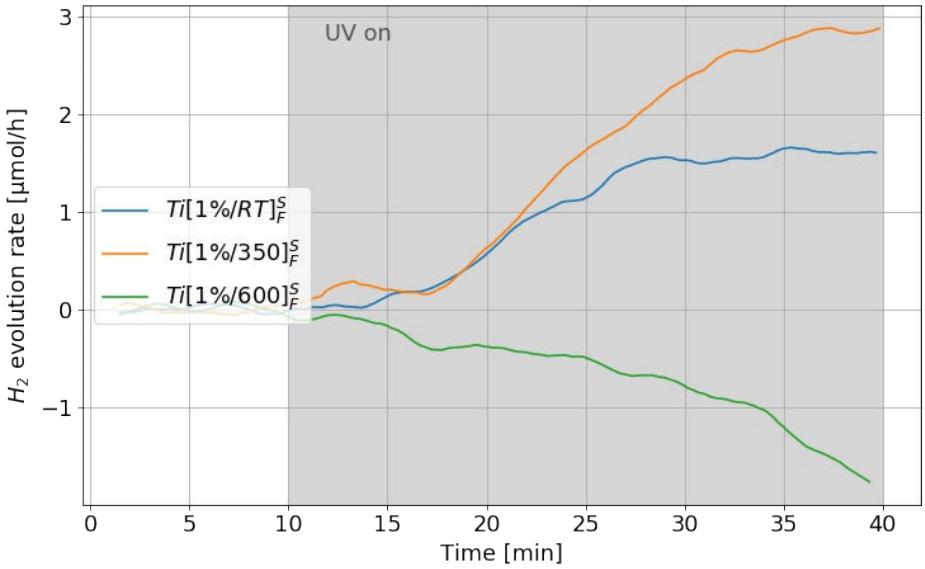

Figure 9.46: UV-HER activity of $Ti\,[1\%/RT]_F^S$

$Ti\,[1\%/RT]_E^S$

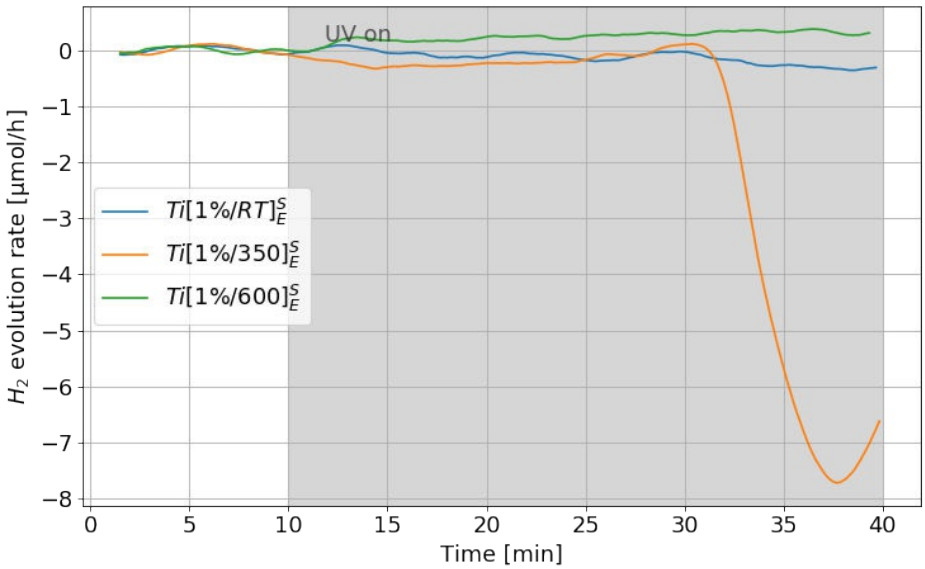

Figure 9.47: UV-HER activity of $Ti\,[1\%/RT]_E^S$

Die approbierte gedruckte Originalversion dieser Diplomarbeit ist an der TU Wien Bibliothek verfügbar
The approved original version of this thesis is available in print at TU Wien Bibliothek.

$Ti\,[5\%/RT]_E^S$

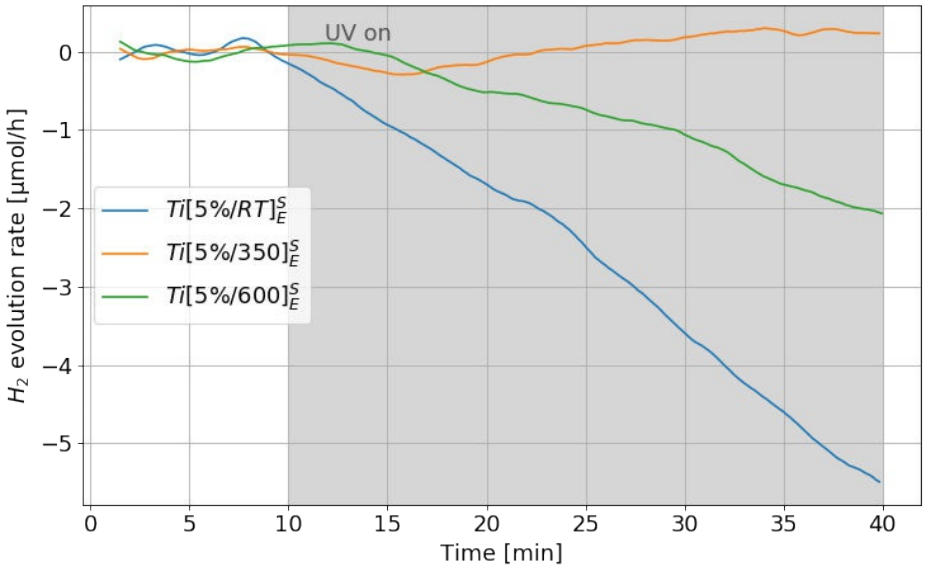

Figure 9.48: UV-HER activity of $Ti\,[5\%/RT]_E^S$

$Ti\,[25\%/RT]_E^S$

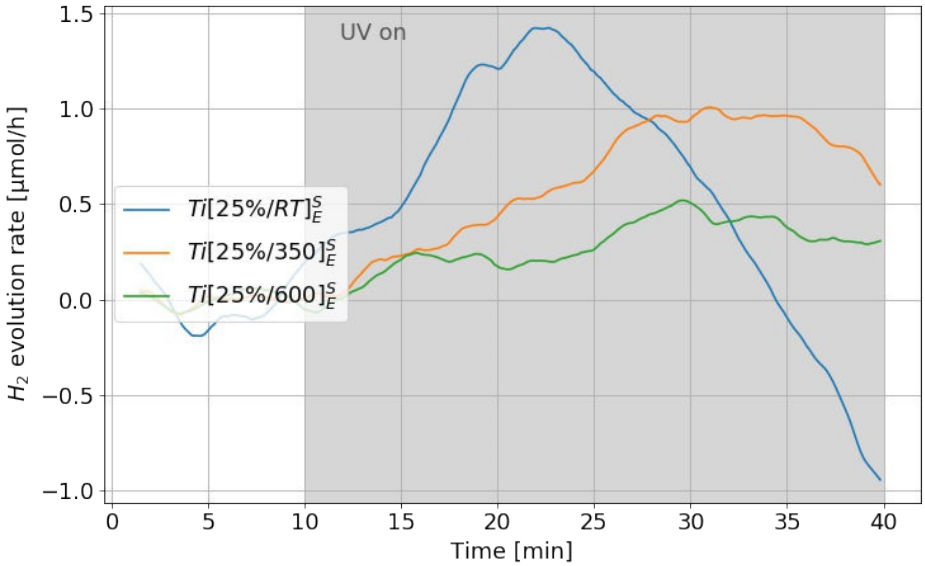

Figure 9.49: UV-HER activity of $Ti\,[25\%/RT]_E^S$

Die approbierte gedruckte Originalversion dieser Diplomarbeit ist an der TU Wien Bibliothek verfügbar
The approved original version of this thesis is available in print at TU Wien Bibliothek.

9.9 Vis-HER

9.9.1 HER experiments

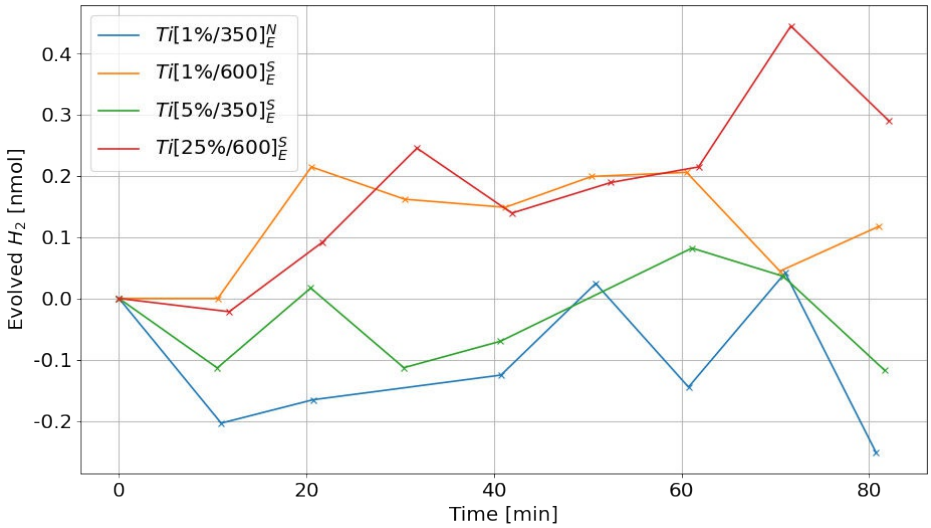

Figure 9.50: Hydrogen evolution activities for Vis-HER experiments.

Die approbierte gedruckte Originalversion dieser Diplomarbeit ist an der TU Wien Bibliothek verfügbar
The approved original version of this thesis is available in print at TU Wien Bibliothek.

9.9.2 TEM images

$Ti\,[5\%/600]_E^S$ - Visible Pt-Photodeposition

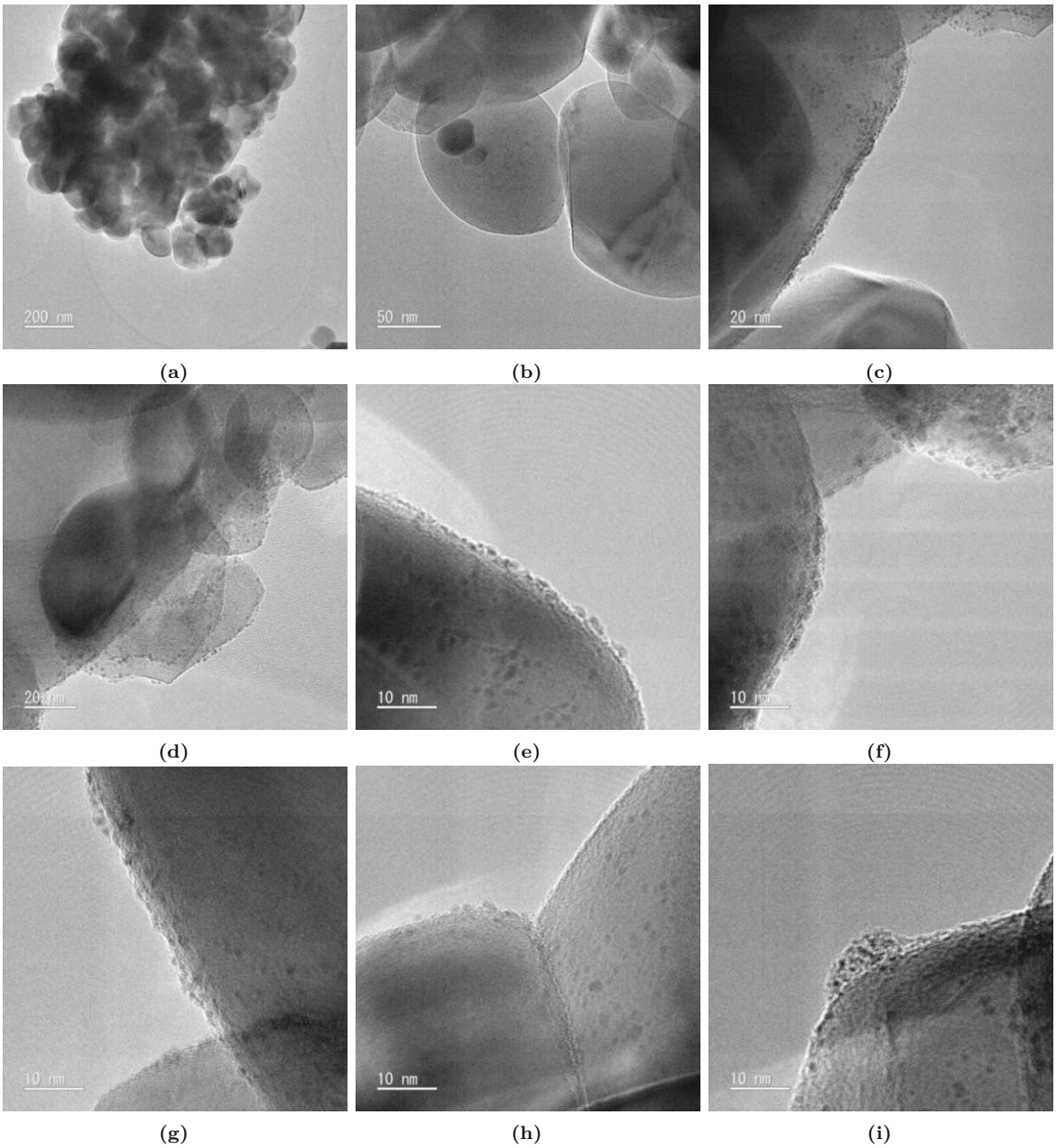

Figure 9.51: $Ti\,[5\%/600]_E^S$ after Pt Photodeposition with visible light.

Die approbierte gedruckte Originalversion dieser Diplomarbeit ist an der TU Wien Bibliothek verfügbar
The approved original version of this thesis is available in print at TU Wien Bibliothek.

$Ti\,[5\%/600]_E^S$ - UV/Vis Pt-Photodeposition

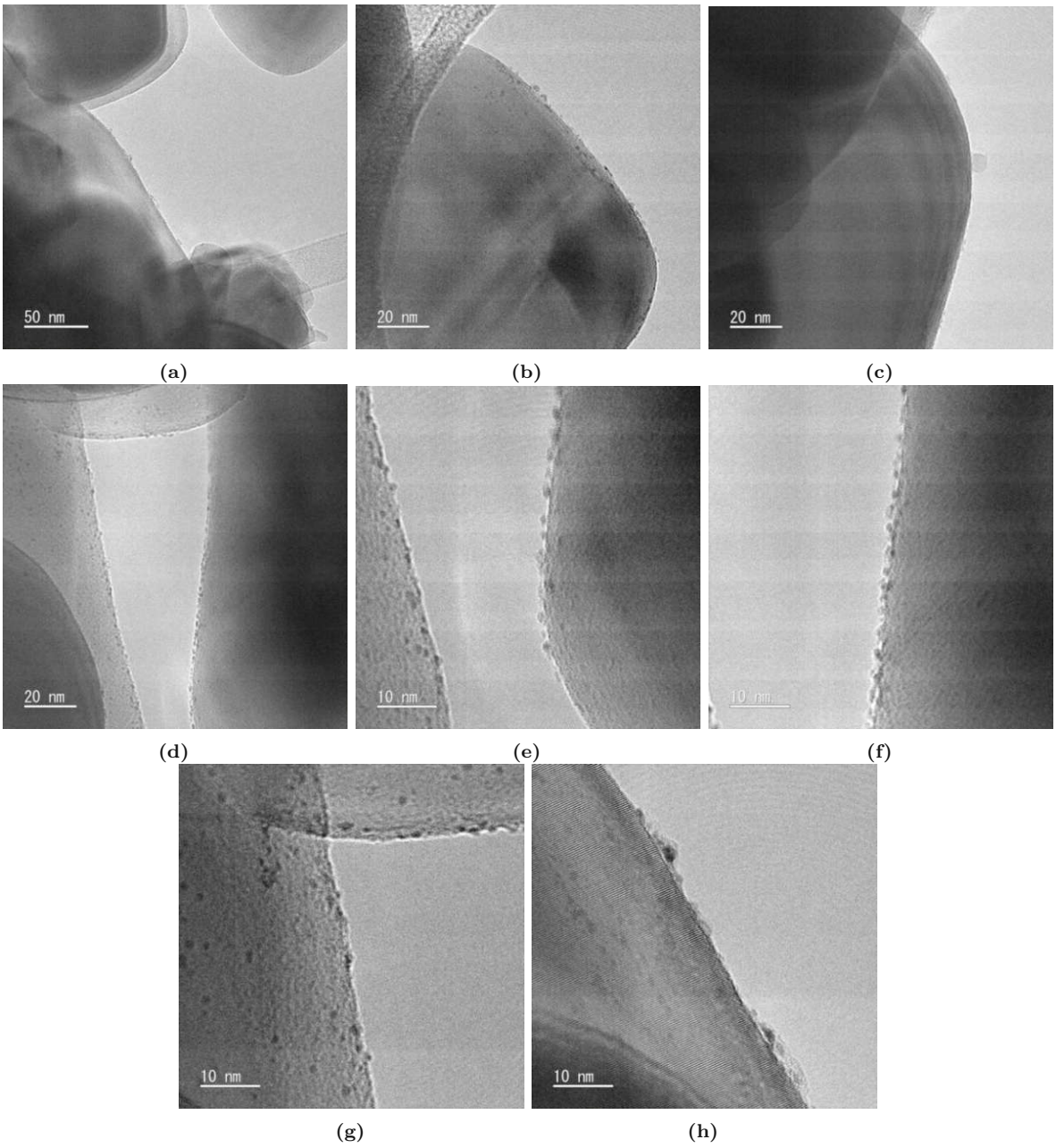

Figure 9.52: $Ti\,[5\%/600]_E^S$ after Pt Photodeposition with UV and visible light.

Die approbierte gedruckte Originalversion dieser Diplomarbeit ist an der TU Wien Bibliothek verfügbar
The approved original version of this thesis is available in print at TU Wien Bibliothek.